GEOMECHANICS OF SUBSRUFACE SAND PRODUCTION AND GAS STORAGE

A Dissertation
Presented to
The Academic Faculty

by

Jong-Won Choi

In Partial Fulfillment
of the Requirements for the Degree
Doctor of Philosophy in the
School of Civil and Environmental Engineering

Georgia Institute of Technology
May 2011

GEOMECHANICS OF SUBSRUFACE SAND PRODUCTION AND GAS STORAGE

Approved by:

Dr. Leonid N. Germanovich, Advisor
School of Civil and Environmental Engineering
Georgia Institute of Technology

Dr. Robert Lowell
School of Earth and Atmospheric Sciences
Georgia Institute of Technology

Dr. Carlos Santamarina
School of Civil and Environmental Engineering
Georgia Institute of Technology

Dr. Larry C. Murdoch
Department of Geological Sciences
Clemson University

Dr. Haying Huang
School of Civil and Environmental Engineering
Georgia Institute of Technology

Dr. Peter Van Dyke
Weatherford

Date Approved: May 6, 2011

To my wife, daughter, parents, and brother

ACKNOWLEDGEMENTS

First, I would like to express special thanks to my advisor, Dr. Leonid Germanovich, for his guidance throughout my work. Without his support and encouragement, I could not have completed this dissertation. I would also like to thank Dr. Larry Murdoch of and Dr. Peter Van Dyke, who served as co-advisers for my thesis. I am also grateful to Dr. James Castle, for his help with the second part of this thesis.

I appreciate the efforts of my thesis committee members: Dr. Leonid Germanovich, Dr. Haiying Huang, Dr. Robert Lowell, Dr. Larry Murdoch, Dr. Carlos Santamarina, and Dr. Peter Van Dyke. I received many valuable comments and suggestions from them.

I owe the completion of my studies to many people. Among them, I am grateful to Robert Hurt for his invaluable help in my experiments. I greatly appreciate the assistance and encouragement from past and present students of the Rock and Fracture Mechanics Group at the Georgia Institute of Technology: Hong Chang, Gence Genc, Devon Gwaba, Robert Hurt, Sihyun Kim, Cem Ozan, Pierre Ramondenc, Chanin Ruangthaveekoon, Youngjong Sim, and Ruiting Wu. Above all, I thank my wife, Eun-Ha Yang, for her endless support, trust, and patience. I also express my gratitude to my parents, Seung-Gon Choi and Kyung-Shin Kwon, and my brother Jong-Hyun Choi for their continuous encouragement and support.

Finally, I would like to acknowledge financial support provided by Schlumberger, Shell, National Science Foundation, and the US. Department of Energy (contract # DE-FC26-02NT41299). Itasca Consulting Group also contributed to this work by allowing me to use their numerical code *PFC*^{3D} version 3.0.

TABLE OF CONTENTS

LIST OF TABLES

LIST OF FIGURES

Page

SUMMARY

Improving methods of hydrocarbon production and developing new techniques for the creation of natural gas storage facilities are critically important for the petroleum industry. This dissertation focuses on two key topics: (1) mechanisms of sand production from petroleum reservoirs and (2) mechanical characterization of caverns created in carbonate rock formations for natural gas storage.

Sand production is the migration of solid particles together with the hydrocarbons when extracted from petroleum reservoirs. It usually occurs from wells in sandstone formations that fail in response to stress changes caused by hydrocarbon withdrawal. Sand production is generally undesirable since it causes a variety of problems ranging from significant safety risks during high-rate gas production, to the erosion of downhole equipment and surface facilities. It is widely accepted that a better understanding of the mechanics of poorly-consolidated formations is required to manage sand production; which, in turn, enables the cost effective production of gas and oil resources.

In this work, a series of large-scale laboratory experiments was conducted in fully saturated, cohesionless sand layers to model the behavior of a petroleum reservoir near a wellbore. We directly observed several key characteristics of the sand production phenomenon including the formations of a stable cavity around the wellbore and a sub-radial flow channel at the upper surface of the tested layer. The flow channel is a first-order feature that appears to be a major part of the sand production mechanism. The channel cross section is orders of magnitude larger than the particle size, and once formed, the channel becomes the dominant conduit for fluid flow and particle transport. The flow

channel developed in all of our experiments, and in all experiments, sand production continued from the developing channel after the cavity around the borehole stabilized.

Our laboratory results constitute a well constrained data set that can be used to test and calibrate numerical models employed by the petroleum industry for predicting the sand production phenomenon. Although important for practical applications, real field cases are typically much less constrained. We used scaling considerations to develop a simple analytical model, constrained by our experimental results. We also simulated the behavior of a sand layer around a wellbore using two- and three-dimensional discrete element methods. It appears that the main sand production features observed in the laboratory experiments, can indeed be reproduced by means of discrete element modeling. Numerical results indicate that the cavity surface of repose is a key factor in the sand production mechanism. In particular, the sand particles on this surface are not significantly constrained. This lack of confinement reduces the flow velocity required to remove a particle, by many orders of magnitude. Also, the mechanism of channel development in the upper fraction of the sample can be attributed to subsidence of the formation due to lateral extension when an unconstrained cavity slope appears near the wellbore. This is substantiated by the erosion process and continued production of particles from the flow channel.

The notion of the existence of this surface channel has the potential to scale up to natural reservoirs and can give insights into real-world sand production issues. It indicates a mechanism explaining why the production of particles does not cease in many petroleum reservoirs. Although the radial character of the fluid flow eventually stops sand production

from the cavity near the wellbore, the production of particles still may continue from the propagating surface (interface) flow channel.

The second topic of the thesis addresses factors affecting the geometry and, hence, the mechanical stability of caverns excavated in carbonate rock formations for natural gas storage. Storage facilities are required to store gas when supply exceeds demand during the winter months. In many places (such as New England or the Great Lakes region) where no salt domes are available to create gas storage caverns, it is possible to create cavities in limestone employing the acid injection method. In this method, carbonate rock is dissolved, while CO_2 and calcium chloride brine appear as products of the carbonate dissolution reactions. Driven by the density difference, CO_2 rises towards the ceiling whereas the brine sinks to the bottom of the cavern. A zone of mixed CO_2, acid, and brine forms near the source of acid injection, whereas the brine sinks to the bottom of the cavern.

Characterization of the cavern shape is required to understand stress changes during the cavity excavation, which can destabilize the cavern. It is also important to determine the location of the mixture-brine interface to select the place of acid injection. In this work, we propose to characterize the geometry of the cavern and the location of the mixture-brine interface by generating pressure waves in a pipe extending into the cavern, and measuring the reflected waves at various locations in another adjacent pipe. Conventional governing equations describe fluid transients in pipes loaded only by internal pressure (such as in the water hammer effect). To model the pressure wave propagation for realistic geometries, we derived new governing equations for pressure transients in pipes subjected to changes in both internal and external (confining) pressures. This is important

because the internal pressure (used in the measurement) is changing in response to the perturbation of the external pressure when the pipe is contained in the cavern filled with fluids. If the pressure in the cavern is perturbed, the perturbation creates an internal pressure wave in the submerged pipe that has a signature of the cavern geometry. We showed that the classic equations are included in our formulation as a particular case, but they have limited validity for some practically important combinations of the controlling parameters.

We linearized the governing equations and formulated appropriate boundary and initial conditions. Using a finite element method, we solved the obtained boundary value problem for a system of pipes and a cavern filled with various characteristic fluids such as aqueous acid, calcium chloride brine, and supercritical CO_2. We found that the pressure waves of moderate amplitudes would create measurable pressure pulses in the submerged pipe. Furthermore, we determined the wavelengths required for resolving the cavern diameter from the pressure history. Our results suggest that the pressure transients technique can indeed be used for characterizing the geometry of gas storage caverns and locations of fluid interfaces in the acid injection method.

CHAPTER I
INTRODUCTION

Improving methods for cost-effective hydrocarbon production and developing new techniques for the creation of gas storage facilities are critically important in the petroleum industry. This dissertation focuses on two topics: (1) mechanisms of sand production form petroleum reservoirs and (2) the mechanical characterization of caverns created in carbonate rock formations for natural gas storage.

1.1 Sand Production from Petroleum Reservoirs

Sand production refers to the inflow of solid particles from petroleum reservoirs together with hydrocarbons. Sometimes, the term "solids production" is used instead of "sand production" since chalk or coal formations may also produce solids whereas "sand production" implies only the production from weak sandstone formations [*Dusseault and Santarelli*, 1989]. Typically sand production is observed in geologically young formations with little or no cementation [*Penberthy and Shaughnessy*, 1992]. Approximately 70% percent of the petroleum reservoirs in the world are located in sandstone formations where sand production can be a potential problem [*SINTEF*, 2005].

To produce hydrocarbons, the fluid pressure in wells is maintained lower than the pressure in reservoirs, so that hydrocarbon flows toward the well due to the pressure gradient. During the production of hydrocarbon, a variety of factors may control the sand production phenomenon. Among them, the fluid flow and the change of the stress field around a well are of principal importance [*Risnes et al*., 1982].

The stress field around a well is a function of the original undisturbed stress field, stress perturbations related to well completion, and the effects of pore pressure depletion associated with sustained fluid flow in long-term production [*Risnes et al*., 1982; *Morita et al*., 1989]. In general, the change of the stress field leads to the increase in shear stress

levels and the yield of the formation around the well [*Bratli and Risnes*, 1981; *Morita et al.*, 1989; *Tronvoll et al.*, 1997].

The flow of hydrocarbons also induces hydrodynamic (seepage) forces on the formation. If the hydrodynamic force is greater than the resistance forces of a formation (e.g., cementation, frictional forces between particles, or capillary forces), the particles can be mobilized out of the formation [*Bratli and Risnes*, 1981; *Morita et al.*, 1989; *Asgian et al.*, 1995; *Charlez*, 1997; *Vaziri et al.*, 2002]. The hydrodynamic effect of the fluid flow and the change of the stress field are interrelated. For example, the change of the stress field can induce localized damage to the formation. Subsequently, the mobilization of particles may cause the increase in porosity leading to the change of the localized fluid velocity and further damage to the formation [*Vardoulakis et al.*, 1996].

Geological factors can also affect the sand production phenomenon [*Penberthy and Shaughnessy*, 1992]. The existence of a competent caprock, (i.e., a rigid impermeable layer with a higher strength) may change the outcome of the sand production. If a caprock exists over a reservoir, it resists the deflection from overburden stress [*Dusseault and Santarelli*, 1989] (Figure 1.1a). *Vaziri et al*. [2001] suggested that in this case, a stable cavity may be formed around the wellbore (Figure 1.1b). If the layer over a formation yields due to an overburden stress (Figure 1.2), the overburden deflection causes the formation to be eventually pinched off. Then, as suggested by *Dusseault and Santarelli* [1989], the cavity is unlikely to form around the wellbore.

Sand production is of great concern in the petroleum industry since it may induce a series of problems [*Penberthy and Shaughnessy*, 1992]. For example, the erosion of equipment (e.g., valves, pipes, and screens) caused by the produced particles requires the damaged equipment to be replaced much more frequently than hydrocarbon production without solids [*Penberthy and Shaughnessy*, 1992].

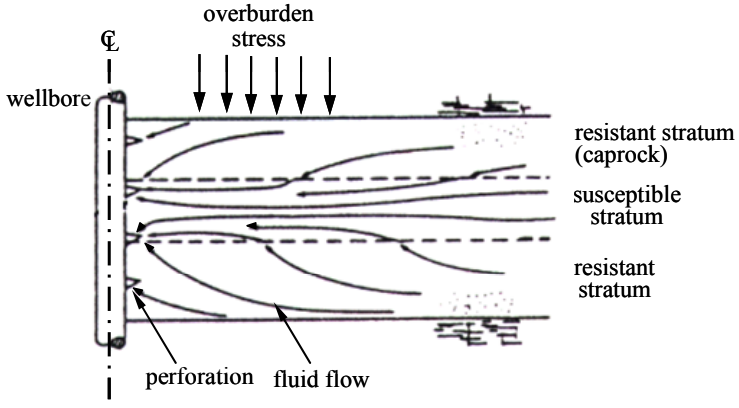

(a)

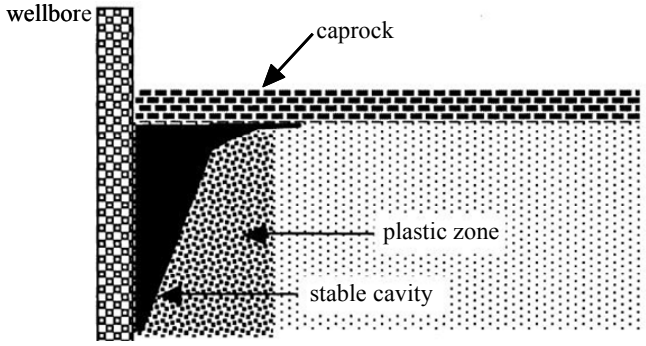

(b)

Figure 1.1 Existence of a caprock over the formation: (a) resistance of the caprock against the overburden flexure [after *Dusseault and Santarelli*, 1989] and (b) the formation of stable cavity around a wellbore [*Vaziri et al*., 2001].

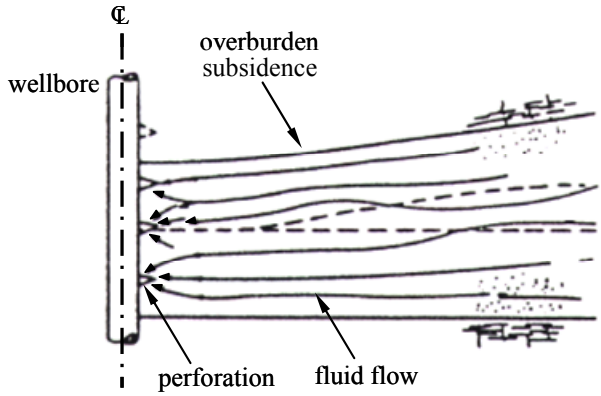

Figure 1.2 Pinch off the formation due to sand production [after *Dusseault and Santarelli*, 1989].

As solid particles are removed from a formation, the lateral constraint around a casing can be lost. The loss of the lateral constraint may lead to the buckling of the casing [*Ispas et al*., 2002].

Also, the formation of sand arches around the perforations on the surface of the casing of a well can decrease the permeability of the formation [*Bratli and Risnes*, 1981]. The formation of a stable arch creates a tight packing of sand particles, and this will act as a filter. This filter will be clogged by particles with a variety of sizes, so that the permeability of the filter will be decreased. Such a decrease in permeability may decrease the rate of petroleum production and well productivity.

If the flow velocity of fluid in a well is not sufficiently fast to transport the produced solid particles, particles will accumulate in the well. The accumulation may cause a complete shutdown of petroleum production [*Economides et al.*, 1998].

The disposal of produced solid particles can also be a problem, especially in offshore sites where environmental regulations require the solid particles to be free of oil before they are disposed. The remediation and disposal of solid particles contaminated by oil result in significant additional costs to petroleum production [*Penberthy and Shaughnessy*, 1992].

Since sand production causes the aforementioned problems, a better understanding of the sand production phenomenon is required to minimize its effect on well productivity.

Due to sand production, particles are removed from a sand formation around a well, so that the porosity of the formation is increased or cavities are created around the well. For example, assume that a cylindrical cavity is formed around a well due to the sand production. Consider a typical petroleum production rate and a typical sand production rate from this well, that is, on average 200 barrels of fluid and 10 barrels of sand per day, respectively (i.e., solid production rate constitutes 5% of the fluid production rate). If the production continues for five years from a petroleum reservoir with a thickness of 25 m and a porosity of 20%, a cylindrical cavity with a radius of 25 m will be created due to the

sand production shown schematically in Figure 1.3. This example illustrates the scale of the volume of sand that can be produced together with hydrocarbons.

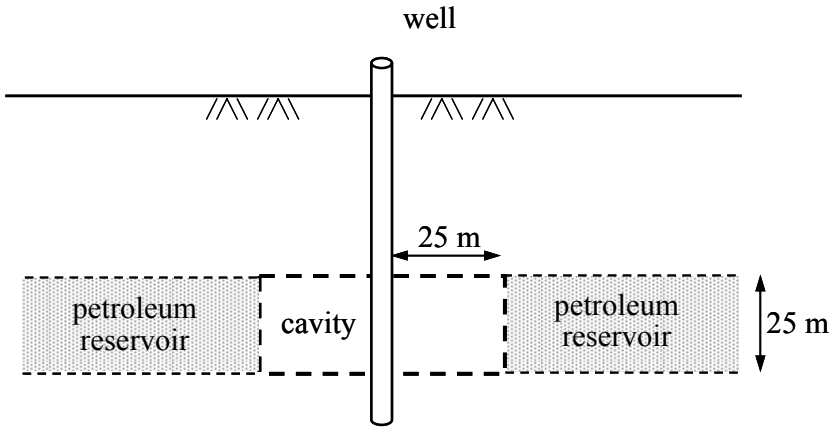

Figure 1.3 Development of cavity around a wellbore due to sand production.

To understand the phenomenon of sand production and to develop predictive capabilities, a number of mathematical models have been developed. A plastic flow model has been proposed for the application to heavy oil production [*Geilikman et al.*, 1994; *Geilikman and Dusseault*, 1997]. A different approach, the surface erosion model, was considered to take into account the motion of sand particles in the open cavities that are associated with sand production in lighter oils [*Charlez*, 1997]. Two basic geometries corresponding to these different models are shown in Figure 1.4. Figure 1.4a shows the plastic flow of disintegrated material. In the vicinity of a perforation, a region filled with disintegrated material is formed. Due to the fluid flow and the change of the confining stress, the surrounding rock fails, and the disintegrated material is "squeezed" through the perforation. Then, the material is produced together with the fluid into the wellbore (Figure 1.4a). This model is used to simulate sand production in heavy oil fields where plastic flow of disintegrated solid material (particles) occurs [e.g., *Geilikman et al*., 1994]. In the surface erosion model, shown in Figure 1.4b, a cavity is formed in the vicinity of a perforation. There still may be (and likely to be) a plastic (yielded) zone around the cavity

as it forms. To keep the diagram simple, this zone is not shown in Figure 1.4b. Due to the fluid flow, particles are eroded from the surface of the cavity, and, as a result, sand is produced into the well together with the fluid [e.g., *Charlez*, 1997].

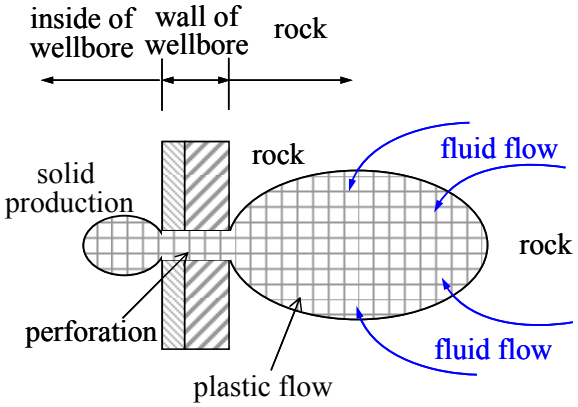

(a)

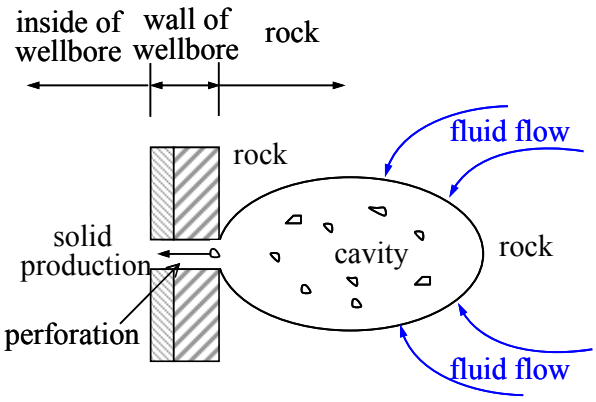

(b)

Figure 1.4 Two examples of sand production models (side view): (a) plastic flow of disintegrated material and (b) surface erosion model.

Plastic flow of disintegrated particles represents the extreme case (Figure 1.4a). This phenomenon is relatively well understood, and it has been successfully implemented in heavy-oil fields to mine hydrocarbons [e.g., *Geilkman and Dusseault*, 1997]. In other words, in heavy-oil fields such as Alberta in Canada, the sand production phenomenon is essentially utilized for hydrocarbon production. Currently, the surface erosion effect

(Figure 1.4b) is much less understood. For example, even the sand production criterion, which determines the condition when sand production starts, is not clear. For example, *Charlez* [1997] argued that hydrodynamic forces can remove particles from only a highly plastified cohesionless formation with very low effective confining stress. In this case, the surface erosion model can be applied only after a formation is plastified due to stress change.

Consider a petroleum reservoir composed of unconsolidated sand with a particle size of 0.1 mm [*Charlez*, 1997], where the initial stress around the well is 1.0 MPa [*Charlez*, 1997]. Let the inter-particle friction angle of the particles be 14° [*Charlez*, 1997], the dynamic viscosity of the fluid 0.01 Pa·sec [*Bradley*, 1987], and the permeability of the formation 10^{-13} m^2 [*Charlez*, 1997]. The radius of the well and the thickness of the reservoir are 0.1 m and 20 m, respectively [*Charlez*, 1997]. Due to the production of petroleum, sand particles around a wellbore are subject to fluid flow (Figure 1.5). Because the sand layer is unconsolidated, sand particles would be removed from the formation if the hydrodynamic force of the fluid flow were greater than the frictional resistance from the in-situ stress [e.g., *Asgian et al.*, 1995]. For a petroleum reservoir with unconsolidated sand, *Charlez* [1997] suggested that a critical fluid flow rate, Q_c, required to remove a particle around a well is (see also Sections 2.6 and 3.2)

$$Q_c = \frac{3\pi R_w k h \sigma'_{\theta\theta} \tan\varphi}{\mu d_p} \tag{1.1}$$

where R_w is the radius of the well, k is the permeability of the formation, h is the thickness of the formation, $\sigma'_{\theta\theta}$ is the effective tangential stress around the well, φ is the inter-particle fiction angle, μ is the dynamic viscosity of the fluid, and d_p is the particle diameter. Using the abovementioned values for each parameter, the fluid flow rate to remove a particle from the formation based on (1.1) is 2×10^5 barrels per day.

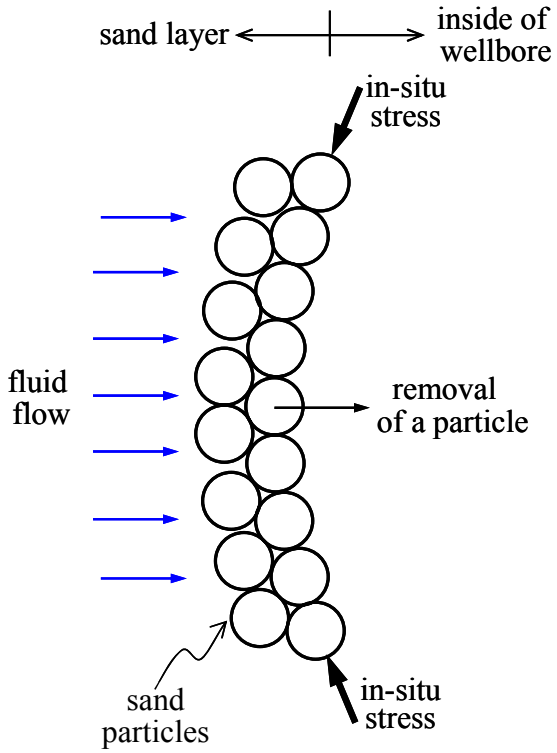

Figure 1.5 Stability of sand particles around a wellbore under the effect of fluid flow and in-situ stress [after *Charlez*, 1997].

To put this in perspective, consider that in the Duri oil field in Sumatra, Indonesia, the total production rate of fluid from 1,350 wells is 1.5×10^5 barrels per day [*Shryock et al.*, 1990]. By comparing this value (i.e., a total production rate of 1.5×10^5 barrels per day from 1,350 wells) with the calculated flow rate (i.e., 2×10^5 barrels per day) from one well based on (1.1), the production rate of fluid per well in the field is much smaller than that required to remove a particle from the formation. That is, the rate of fluid flow in the field condition results in hydrodynamic forces that are too weak to induce the removal of particles from the formation. Thus, the existing surface erosion model alone cannot describe the sand production phenomenon that commonly occurs at the Duri field [*Shryock et al.*, 1990].

It would be ideal, if the sand production phenomenon could be formulated as a boundary value problem. For example, consider a sand layer containing petroleum located between two shale layers (Figure 1.6). We must better understand the conditions on near-field boundaries (i.e., yield and/or erosion, as applicable) and in the far-field. These must be specified to formulate the relevant boundary value problems and to develop the corresponding numerical algorithms (e.g., the boundary between intact/elastic and dilated/plastic materials in Figure 1.6). Furthermore, not only the boundary condition at infinity but also the asymptotic behaviors of stresses/pressure are required for the calibration of numerical solutions. Proper boundary conditions are missing in existing models. As a first step, we suggest to consider the evolution of the relative stiffness and the corresponding redistribution of stresses as the material becomes de-cemented and removed (Figure 1.6). Note that the presence of the end-wedge in Figure 1.6 should not be minimized in stability conditions. It is the de-stabilization of this wedge by small hydrodynamic forces and/or alteration of mixed-fluid conditions that will perpetuate the sand production. In particular, this approach allows estimating both fluid flow and the sand production rates. Also, the interaction of the petroleum reservoir with the surrounding layers can be evaluated by considering the deflection of the shale layers due to overburden (Figure 1.6). This determines the distribution of vertical stress near a wellbore, which otherwise is assumed when modeling the behavior of petroleum reservoir. *Risnes et al*. [1982] assumed that the vertical stress is the same as the horizontal stress, while *Geilkman and Dusseault* [1997] used the plane strain condition (i.e., vertical strain is zero). Typically, knowing the vertical stress is important for understanding the entire boundary stress state conditions and thus for formulating realistic models for sand yield and erosion in such environments.

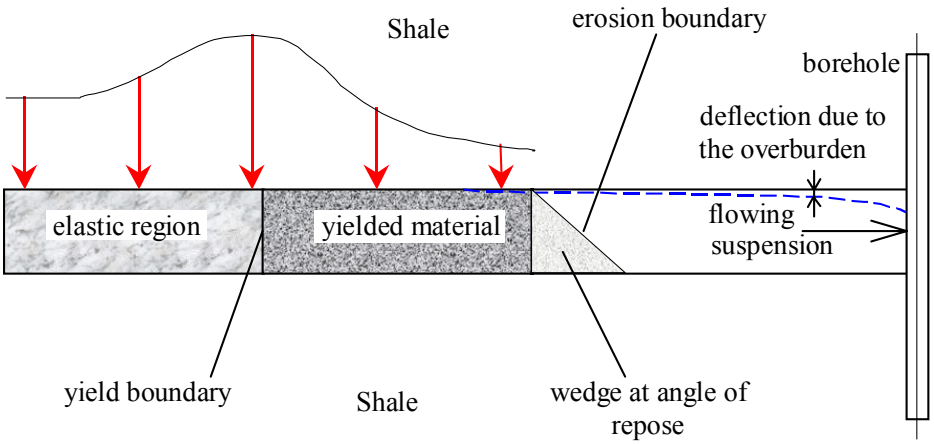

Figure 1.6 Sand-shale interaction and the effect of in-situ conditions.

Ideally, modeling the sand production phenomena should be conducted within the framework of a multi-scale approach. Conceptually this allows the consideration of geologic features such as faults, e.g., on a scale of 1000's of meters, while modeling the borehole (or its interaction with the petroleum reservoir) as a point sink at the scale of 100's of meters. At the same time, at the scale of 10's of meters, the wellbore is modeled as a linear sink/source. In each case, the larger scale model provides the proper boundary conditions for the smaller scale. The regional scale (Figure 1.7a) describes the interaction between geological formations and petroleum reservoir (that produces sand particles) in terms of compressibility and deformation. At this scale, the boreholes are not visible. Major geological features such as faults can be included. The results from this scale at a reference point (i.e., the borehole position shown by the small square in Figure 1.7a) provide the boundary conditions for the subsequent formation scale of the petroleum reservoir (Figure 1.7b). Elastic or poroelastic approaches seem adequate at the regional scale.

At the formation scale in Figure 1.7b, modeling includes only a single confined layer that produces particles. The layer is infinite and the boreholes are still not visible. Yet, the boreholes play an important role in specifying the fluid sources and sinks, and in affecting the pressure distribution in the layer. Yielding is now possible and should be

explicitly included in the model (not shown in Figure 1.7b, for simplicity). The solution at the position of the borehole from the regional scale specifies the boundary conditions at infinity at the formation scale.

At the borehole scale, shown in Figure 1.7c, the model describes the liquid and suspension flow, the particle production and migration, and the pore pressure distribution and stress state of the medium for the perforated borehole casing and the surrounding geological formation in terms of frictional flow, arching, crushing, detachment and cavity stability. Again, the solution from the previous, formation scale at the borehole position provides the boundary conditions at infinity for the borehole scale model.

A possible model of the perforation scale is shown in Figure 1.8, and includes only a single borehole perforation. However, it is important because it determines the solid-liquid interaction that, in turn, determines the removal of the particles. At this scale, the hydrodynamic effect of the fluid flow on the particles and the resistance of the assembly of particles need to be considered.

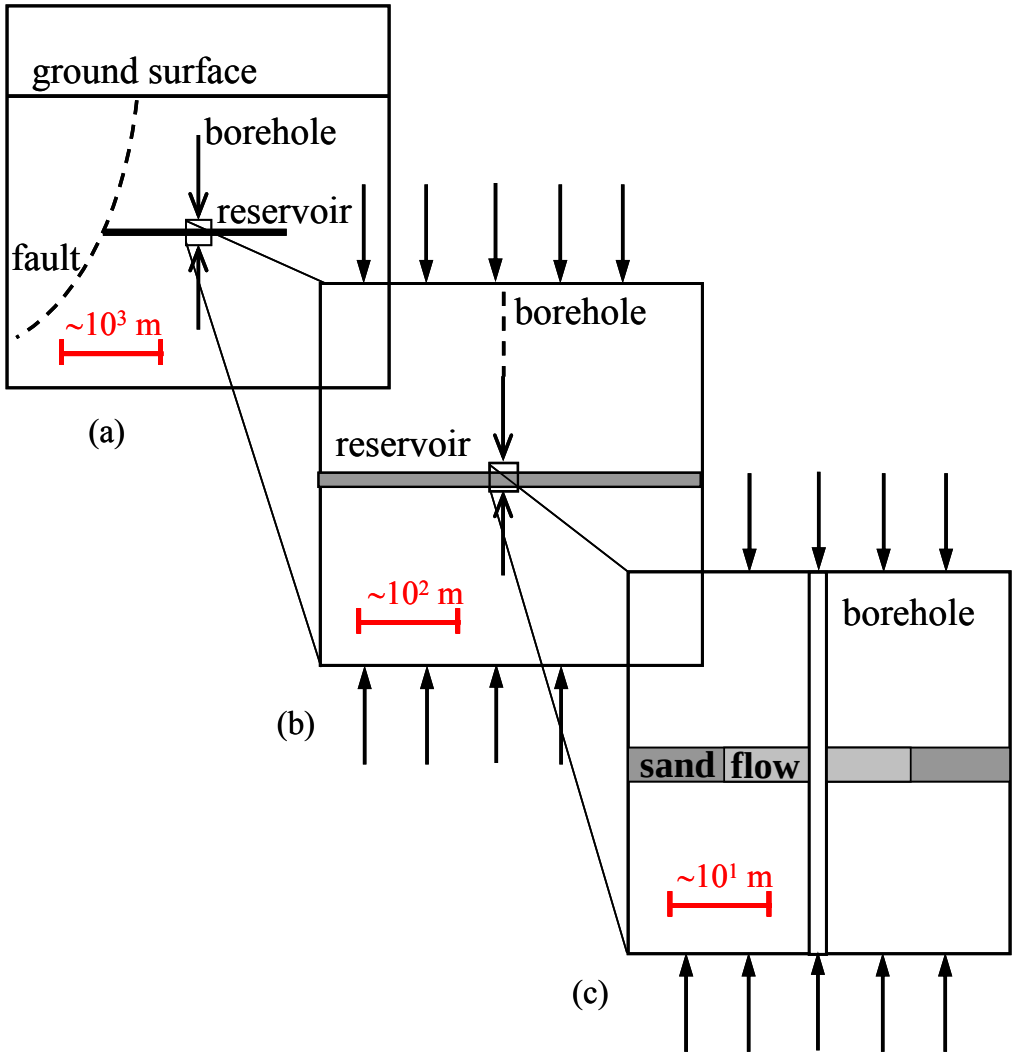

Figure 1.7 Conceptual model of the multi-scale approach: (a) regional scale, (b) formation scale, and (c) borehole scale.

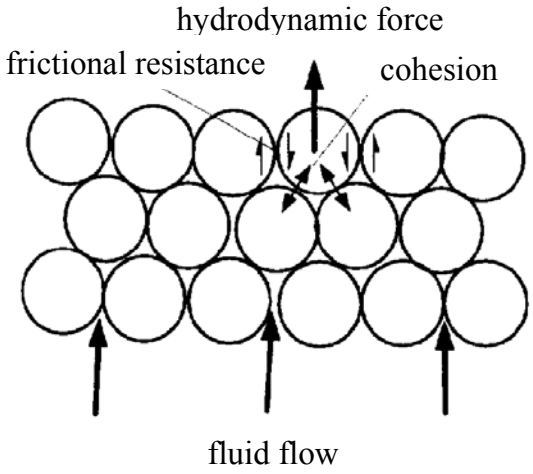

Figure 1.8 Conceptual model of the multi-scale approach at perforation scale [after *Pearson and Zazovsky*, 1997]. Particles are under the influence of hydrodynamic force due to fluid flow, and they resist such force by frictional resistance and cohesion.

In the multi-scale approach, each scale is coupled with subsequent scales, so that the behavior of a petroleum reservoir at one scale affects reservoir behavior at different scales. Thus, by adopting this multi-scale approach, one can, in principle, describe and classify the controlling processes that are involved in the particle production phenomena as well as obtain proper boundary conditions. Scaling models have a potential of determining the orders of magnitude that are involved in the particle production processes as well as the depth of their coupling at different spatial and temporal scales.

As the first step of a long-term work using the multi-scale approach, we focus on the behavior of petroleum reservoir at the borehole scale using experimental and theoretical modeling. Consideration of the borehole scale is essential in the evaluation of the interaction of the petroleum reservoir with the surrounding rock due to the production of particles (e.g., yielding of formation, disintegration and transport of particles, and evolution of erosion boundary). In the future, it is anticipated that the results from this work will be coupled with the results of modeling at the formation and regional scales. An

example of a model addressing the regional scale and reservoir-fault interaction is given by *Chanpura* [2001].

1.2 Characterization of Gas Storage Caverns

The second topic of the thesis is related to the creation of caverns in carbonate rock formations for the purpose of natural gas storage. Natural gas is the second largest energy source behind petroleum, accounting for approximately 20% of energy consumed in the United States [*EIA*, 2005]. Natural gas is used by residential, commercial, and industrial consumers as well as for power generation [*AGA*, 2005]. Natural gas consumption changes from month to month, increasing by 50% during winter [*NETL*, 2005]. In contrast, natural gas production is steady throughout the year [*NETL*, 2005]. Thus, to meet the gap between demand and supply of natural gas, surplus natural gas should be stored when supply exceeds demand. The storage of natural gas is divided into two categories: (1) compressed tanks containing natural gas in the form of a liquid, and (2) large underground storage (e.g., depleted gas reservoirs, aquifers, salt caverns, and rock caverns) [*NETL*, 2005].

Currently, liquefied natural gas (LNG) is stored in insulated tanks while waiting for re-gasification and distribution to consumers [*U.S. Department of Energy*, 2009]. This is an expensive form of storage. As a result, temporary storage of LNG adds significant cost. In addition, such facilities are also vulnerable to fire hazards. Underground storage in depleted gas reservoirs, aquifers, salt caverns, and rock caverns, can result in significantly lower storage costs as well as less vulnerability to fire hazards [*Bergman*, 1984; *Sterling*, 1993].

In the United States, most of the natural gas storage is located in depleted natural gas or oil fields close to major eastern and midwestern markets [*EIA*, 2004; *NGSA*, 2004; *NETL*, 2005]. The storage of natural gas in depleted reservoirs takes advantage of existing wells, equipment, and pipes as well as existing information about the characteristics of these reservoirs. The number of available existing depleted wells close to major markets is

limited. Furthermore, approximately 50% of the stored gas must be left as cushion gas, which may be unrecoverable [*NETL*, 2005].

Natural gas can be stored in confined aquifers by replacing water with gas using the gas injection method. Although aquifer storage accounts for substantial parts of the natural gas storage around the world, it has several disadvantages [*Dussaud*, 1989]. For most aquifers, limited amount of geological data is available [*Toelcke*, 1989]. Aquifer storage requires a large amount of unrecoverable cushion gas up to 80% of the total volume [*NGSA*, 2004]. Due to these disadvantages, aquifer storage is the least desirable among the various storage methods.

Salt caverns are also used for natural gas storage in the United States and Europe [*Hardy*, 1982; *Dussaud*, 1989; *Menzel and Schreiner*, 1989; *Oebro*, 1989; *NGSA*, 2004]. Salt caverns are created in salt formations (e.g., salt domes and salt deposits). A well is drilled into a salt formation. Fresh water is injected into the well to dissolve the salt. Then, brine is pumped out (Figure 1.9). The remaining space can be used for a gas storage. One of the main advantages of salt caverns as a natural gas storage is that the volume of cushion gas can be reduced significantly [*NGSA*, 2004]. In the United States, however, salt formations suitable for natural gas storage are limited to the Gulf Coast of Texas and Louisiana [*Bauer et al.*, 1998]. Thus, although they provide excellent storage, salt caverns are removed too far from the major markets.

Hard rock caverns have also been used for storage of compressed gas in the United States and Europe [*Froise*, 1987; *Lindblom*, 1989; *Broch*, 1989]. The hard rock caverns can be created near major markets using conventional excavation methods. Although hard rock formations are suitable for natural gas storage, the cost of creation is much higher than the cost of other underground storage methods such as cavities in salt domes produced by solution mining [*Foley*, 2006].

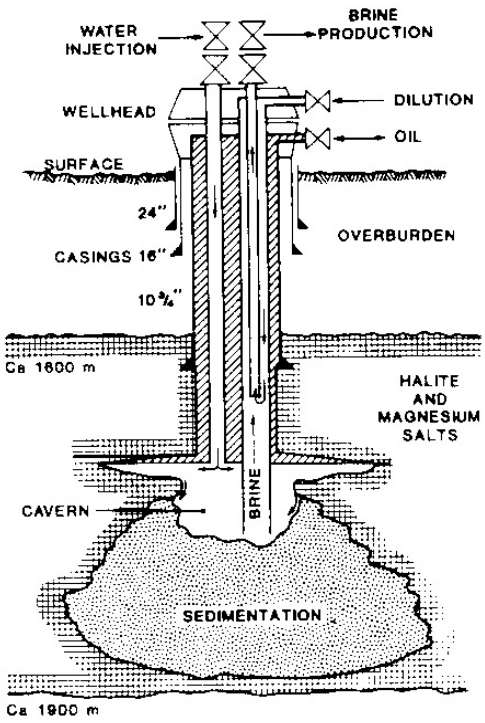

Figure 1.9 An illustration of brine solution mining [*Bartlett*, 1992].

Recently, a new method of natural gas storage has been proposed [*Castle et al.*, 2004]. The method is similar to that of salt cavern: a cavern is created in carbonate rock formation by dissolution of the formation by aqueous acid injection. This cavern can store as much as a billion cubic feet of natural gas [*Castle et al.*, 2004].

Natural gas storage in a solution-mined carbonate cavern has several advantages compared to other storage methods. Suitable carbonate rock formations for natural gas storage are more common than salt domes and depleted reservoirs in the northeastern United States [*Yang*, 2004; *Atteberry*, 2005]. Carbonate rock caverns require less cushion gas and result in less loss into the surrounding formations than those in confined aquifers and depleted reservoirs. Thus, it seems that carbonate rock caverns are economically competitive compared to other storage methods [*Castle et al.*, 2004].

One of the great concerns in the creation of gas storage caverns using the acid injection method is to maintain the cavern stability during the acid injection stage. The

cavern geometry is one of the key factors in cavern stability. In general, the geometry of underground caverns can be characterized using a sonar technique [*Goin*, 1982; *Wong*, 1996; *Reitze et al.*, 2004]. It is difficult, however, to use the sonar technique during the acid injection stage. Therefore, an alternative technique to characterize the cavern geometry during the acid injection stage is required.

Pressure wave propagation (i.e., fluid transients) has already been used to determine the geometry of hydraulic fractures [*Holzhausen and Gooch*, 1985a; 1985b; *Paige et al.*, 1992; *Soliman and Azari*, 1998]. Hydraulic fractures induce a change of hydraulic impedance during the pressure wave propagation. The hydraulic impedance is the function of a geometry of the hydraulic fractures. Hence, by generating a pressure wave and measuring the reflected or refracted waves, it may be possible to obtain the geometry of the cavern.

In this work, we investigate the possibility of using fluid transients to characterize the geometry of gas storage caverns. Since the new technique requires only the generation of a pressure wave and the measurement of the reflected and refracted waves at the wellhead, potentially it can be used during the acid injection stage.

1.3 Goals and Structure of Dissertation

Advancing methods of hydrocarbon production and developing new techniques of creation of storage facilities are critically important in the petroleum industry. This dissertation focuses on two topics: (1) mechanisms of sand production from petroleum reservoirs and (2) mechanical characterization of caverns created in carbonate rock formations for natural gas storage.

Currently, a consensus has been reached in the petroleum industry that a better understanding of the sand production phenomenon is required for optimizing petroleum production. In this work, the objectives of modeling of sand production are to:

- Build a large-scale experimental setup to simulate production of a petroleum reservoir in an unconsolidated sand formation, and to conduct a series of laboratory experiments.
- Acquire various measurements to investigate the characteristics of sand production phenomenon, and to monitor the behavior of sand formation in laboratory experiments.
- Reproduce experimental results using scale analysis and numerical modeling.

Another principal goal of this work is to investigate theoretically whether fluid transients can be used to characterize the geometry of gas storage caverns during the acid injection stage, and to suggest a new technique to analyze the field measurements for this characterization. The characterization of gas storage caverns is of great importance for maintaining the stability of the caverns. The corresponding work will be organized in the following order:

- Derive appropriate governing equations to describe transient fluid flow in pipes and caverns.
- Evaluate relevant material properties.
- Model coupled wave propagation through pipes and caverns.
- Simulate pressure histories near the wellhead by solving governing equations.
- Analyze pressure histories to obtain required information (e.g., cavern diameter and location of points of interest).

This dissertation is composed of six chapters.

Chapter I, *Introduction*, describes motivations and objectives of this work.

Chapter II, *Laboratory Experiments on Sand Production*, describes the experimental work in studying the mechanisms of sand production. A large-scale experimental setup has been built to simulate a petroleum reservoir in a unconsolidated sand formation. By monitoring the sand specimen, the behavior of the sand formation due to sand production is investigated. In addition, by measuring the production rate of sand and the inflowing pressure, the characteristics of the phenomenon are identified.

Chapter III, *Theoretical Modeling of Sand Production*, presents numerical modeling investigating the mechanisms of sand production. The experimental work discussed in Chapter II is modeled using a discrete element code. The behavior of sand formations and the characteristics of sand production phenomena are investigated by employing numerical analysis; the results of this analysis are compared to experimental observations.

Chapter IV, *Governing Equations for Gas Storage Caverns Based on Fluid Transients*, describes the governing equations for transient fluid flow in pipes. The traditionally used governing equations (often called "water hammer equations") are valid for fluid flow in a pipe loaded only by internal pressure in turbulent flow. In the field,

however, there also exists an underground cavern and a pipe loaded by both internal and external pressure. In this chapter, new governing equations for fluid flow in an underground cavern and in a pipe loaded by both internal and external pressures are developed. These equations are used in Chapter V to characterize fluid transients in gas storage caverns.

Chapter V, *Characterization of Gas Storage Caverns Using Fluid Transients*, describes the solution of the new mass and momentum balance equations. Although these equations are linearized, it is still difficult to obtain a closed-form solution with the given geometry and boundary conditions. Hence, a numerical code using the finite element method is implemented to solve these equations. Based on the results of the calculation, a technique to calculate the characteristics of cavern geometry during acid injection stage is suggested. The effect of the external pressure in a cavern on wave propagations in a brine production pipe is also investigated with appropriate boundary conditions.

Chapter VI, *Conclusions and Recommendations*, outlines the conclusions of this work. Then, based on these conclusions, it presents suggestions for further studies.

LIST OF SYMBOLS

d_p	Diameter of a particle
h	Thickness of a formation
k	Permeability of a porous medium
Q_c	Critical fluid flow rate
R_w	Radius of a well
μ	Dynamic viscosity of a fluid
$\sigma'_{\theta\theta}$	Effective tangential stress
ψ	Interparticle friction angle

References

AGA (2005), Fact sheet: overview of the U.S. Natural gas industry (2005), American Gas Association, Washington D.C., http://www.aga.org.

Asgian, M.I., P.A Cundall, and B.H.G. Brady (1995), Mechanical stability of propped hydraulic fractures: A numerical study, *Journal of Petroleum Technology*, 203-208.

Atteberry, J.T. (2005), *An assessment of carbonate formations in the Appalachian basin for gas storage using acid dissolution*, Clemson University, Clemson, SC.

Bartlett, R.W. (1992), *Solution mining: leaching and fluid recovery of materials*, Gordon and Beach Science Publishers.

Bauer, S.J., B.L. Ehgartner, B.L. Levin and J.K. Linn (1998), *Waste disposal in horizontal solution mined caverns considerations of site location, cavern stability, and development considerations*, Underground Storage Technology, Department 6113, Sandia National Laboratories, Albuquerque, NM, USA.

Bergman, S.M. (1984), Underground storage of oil and gas, *Journal of Energy Engineering*, 110, 181-190.

Bradley, H.B. (1987), *Petroleum Engineering Hand Book*, Society of Petroleum Engineers.

Bratli, R.K. and R. Risnes (1981), Stability and failure of sand arches, *SPEJ*, 236-248.

Broch, E. (1989), Use of the underground in Norway, *Proceedings of the International Conference on Storage of Gases in Rock Caverns*, Rotterdam, A.A. Balkema, Trondheim, 26-28 June 1989.

Castle, J.W., D.A. Bruce, S.E. Brame, D.A. Brooks, R.W. Falta, and L.C. Murdoch (2004), Design and feasibility of creating gas-storage caverns by using acid to dissolve carbonate rock formations, SPE 91436, *Proceedings of SPE Eastern Regional Meeting*, Charleston, WV, USA, 15-17 September, 2004.

Chanpura, R. (2001), *Fault reactivation as a result of reservoir depletion*, Ph.D. dissertation, Georgia Institute of Technology.

Charlez, P.A. (1997), *Rock Mechanics Vol. 2 Petroleum Application*, Éditions Technip, Paris.

Dussaud, M. (1989*)*, *Review of World Wide Storage Projects, in Underground Storage of Natural Gas: Theory and Practice*, edited by M.R. Tek, 23-29, Dorecht, Kluwer Academic Publishers.

Dusseault, M.B. and F.J. Santarelli (1989), A Conceptual Model for Massive Solids Production in Poorly-Consolidated Sandstones, *Rock at great depth*, edited by Maury and Fourmaintraux, 789-797.

Economides, M.J., L.T. Watters, and S. Dunn-Norman (1998), *Petroleum Well Construction,* John Wiley & Sons Ltd.

EIA (2004), *The basics of underground natural gas storage*, Energy Information Administration; Natural Gas Division, Washington D.C., http://www.eia.doe.gov/pub/oil_gas/natural_gas/analysis_publications/storagebasics/storagebasics.html.

EIA (2005), *Monthly energy review*, Energy information administration, Office of energy markets and end use: U.S. Department of Energy, Washington, D.C., http://www.eia.doe.gov/mer/pdf/mer.pdf.

Foley, J.M.S. (2006), *An analysis of cavern stability and hydraulic fractures in relation to natural gas storage in limestone formation*, MS thesis, Clemson University.

Froise, S. (1987), Hydrocarbon storage in unlined rock caverns: Norway's use and experience*, Tunneling and Underground Space Technology*, 2, 265-268.

Geilikman, M.B. and M.B. Dusseault (1997), Fluid rate enhancement from massive sand production in heavy-oil reservoirs, *Journal of Petroleum Science and Engineering*, 17, 5-18.

Geilikman, M.B., M.B. Dusseault, and F.A.L. Dullien (1994), Fluid-saturated solid flow with propagation of a yielding front, *Proceedings of the SPE/ISRM International Conference on Rock Mechanics in Petroleum Engineering*, Delft, Netherlands.

Goin, K.L. (1982), Experience in testing of a solution mined storage cavern, *Proceedings of the Annual Convention - Gas Processors Association*, Gas Processors Association, Dallas, TX, USA.

Hardy, H.R., Jr. (1982), *Basic studies associated with the design of salt caverns for the storage of pressurized fluids, in Rock Mechanics: caverns and pressure shafts*, edited by W. Wittke, 903-921, Balkema, Rotterdam.

Holzhausen, G.R. and R.P. Gooch (1985a), The effect of hydraulic fracture growth of free oscillations of wellbore pressure, *Proceedings of the 26th US Symposium on Rock Mechanics*, Rapid City, SD, USA, 26-28 Jun, 1985.

Holzhausen, G.R. and R.P. Gooch (1985b), Impedance of hydraulic fractures: its measurement and use for estimating fracture closure pressure and dimensions, SPE/DOE 13982, *Proceedings of SPE/DOE Low permeability gas reservoirs*, Denver, Colorado, 19-22 May, 1985.

Ispas, I., R.A. Bray, I.D. Palmer, and N.G. Higgs (2002), Prediction and evaluation of sanding and casing deformation in a GOM shelf well, SPE/ISRM 78236, *Proceedings of SPE/ISRM Rock Mechanics Conference*, Irving, Texas, USA, October, 2002.

Lindblom, U. (1989), The development of hydrocarbon storage in hard rock caverns, *Proceedings of the International Conference on Storage of Gases in Rock Caverns*, Rotterdam, A.A. Balkema, Trondheim, 26-28 June, 1989.

Menzel, W. and W. Schreiner (1989), Geomechanical aspects for the establishment and the operation of gas cavern stores in salt formations of the GDR, *Proceedings of the International Conference on Storage of Gases in Rock Caverns*, Rotterdam, A.A. Balkema, Trondheim.

Morita, N., D.L. Whitfill, Ø.P. Fedde, and T.H. Løvik (1989), Parametric study of sand-production prediction: Analytical approach, *SPE Production Engineering*, 4, 25-33.

NGSA (2004*), Natural Gas Supply Association*, http://www.naturalgas.org.

NETL (2005), *Transmission, Distribution & Storage: Natural Gas Storage, National Energy Technology Laboratory: Strategic Center for Natural Gas & Oil*, U.S. Department of Energy, http://www.netl.doe.gov/scngo/NaturalGas/.

Oebro, H. (1989), *Underground gas storage in Denmark - An overview, in Underground Storage of Natural Gas: Theory and Practice*, edited by M.R. Tek, 31-44, Kluwer Academic Publishers, Dorecht.

Paige, R.W., J.D.M. Roberts, L.R. Murray, and D.W. Mellor (1992), Fracture management using hydraulic impedance testing, SPE 24824, *Proceedings of the 67th annual technical conference and exhibition of the Society of Petroleum Engineers*, Washington, D.C, USA, 4-7 October, 1992.

Pearson, J.R.A. and A.F. Zazovsky (1997), A model for the transport of sand grains from a perforation during underbalance surge, SPE 38634, *Proceedings of SPE Annual Technical Conference and Exhibition*, Sand Antonio, TX, USA, 5-8 October 1997.

Penberthy, W.L. and C.M. Shaughnessy (1992*), Sand control*, SPE series on special topics, Society of Petroleum Engineers.

Reitze, A., von Tryller, H., Gaulke, K., and Schweinsberg, H.J (2004), Ultrasonic monitoring of oil and product storage caverns applying a newly developed slim sonar tool, *Proceedings of Spring 2004 Conference*, Solution mining research institute, Wichita, Kansas, USA, 18-21 April, 2004.

Risnes, R., R.K. Bratli, and P. Horsrud (1982), Sand stresses around a wellbore, *SPEJ*, 22(6), 883-898.

Shryock, S.G., S. Ahmad, J. Meloy, and J.W. Kent (1990), Gravel packing for the Duri steamflood, *SPE Production Engineering*, 5(1), 9-13.

SINTEF (2005), *Sand production and sand prediction*, http://www.sintef.no/content/page1____2750.aspx.

Soliman, M.Y. and M. Azari (1998), Effect of friction and leak-off on fracture parameters calculated from hydraulic impedance testing, *Proceedings of SPE India Oil and Gas Conference and Exhibition*, New Delhi, India, 17-19 February. 1998.

Sterling, R.L. (1993), *The Expanding Role of Rock Engineering in Developing National and Local Infrastructures, in Comprehensive Rock Engineering: Principles, Practice & Projects*, edited by J. A. Hudson, 1-27, Oxford, Pergamon Press.

Toelcke, W. (1989), *Use of Pulse Test Technique and Reservoir Simulation for Developing Aquifer Storage, in Underground Storage of Natural Gas: Theory and Practice*, edited by M.R. Tek, 159-167, Kluwer Academic Publishers, Dordrecht.

Tronvoll, J., A. Skjærstenin, and E. Papamichos (1997), Sand production: mechanical failure or hydrodynamic erosion, *International Journal of Rock Mechanics and Mining Science*, 34(3-4), 853-862.

U.S. Department of Energy (2009), *How is LNG shipped and stored?*, http://fossil.energy.gov/programs/oilgas/storage/lng/feature/howisitshipped.html.

Vardoulakis, I., M. Stavropoulou, and P. Papanastasiou (1996), Hydro-mechanical aspects of the sand production problem, *Transport in Porous Media*, 22, 225-244.

Vaziri, H.H., J.S. Jalali, and R. Islam (2001), An analytical model for stability analysis of rock layers over a circular opening, *International Journal of Solids and Structures*, 38, 3735-3757.

Vaziri, H.H., Y. Xiao, R. Islam, and A. Nouri (2002), Numerical modeling of seepage-induced sand production in oil and gas reservoirs, *Journal of Petroleum Science and Engineering*, 36, 71-86.

Wong, R.C.K. (1996), Behaviour of water-jet mined caverns in oil sand and shale, *Canadian Geotechnical Journal*, 33, 610-617.

Yang, Y. (2004), *GIS analysis of carbonate formations in six northeastern states for a suitability assessment of using new technology to develop natural gas storage*, MS thesis, Clemson University, Clemson, SC.

CHAPTER II

LABORATORY EXPERIMENTS ON SAND PRODUCTION

2.1 Introduction

In general, it is difficult to observe the sand production directly in the field. Laboratory experiments represent an alternative way to investigate this phenomenon [e.g., *Tremblay et al*., 1996]. In laboratory experiments, the production of sand particles can be observed in much better controlled conditions, than in the field. In general, the data sets obtained in laboratory are much more constrained and therefore, more suitable for the calibration of theoretical models.

Previous laboratory experiments can be divided into two categories: perforation scale (Figure 1.8) and borehole scale (Figure 1.7c). The perforation scale models the behavior of sand in the vicinity of a perforation (Figure 1.8). In a way, the famous *Terzaghi*'s [1936] trap door experiment can be viewed as a first sand production experiment at the perforation scale. *Terzaghi* [1936] found that, after opening a small hole located at the bottom of the container (filled with sand), sand particles mobilized due to gravity. Then the production of sand stopped. Hence, he concluded that a stable sand arch formed around the opening and prevented further production of sand particles.

As applied to petroleum production, *Bratli and Risnes* [1981] experimentally studied the formation of a sand arch around a hole located at the bottom of a steel cylinder that is filled with unconsolidated sand (Figure 2.1). The inner diameter and the height of the steel cylinder were 19 cm and 38 cm, respectively. The thickness of the wall was 2 cm. They used Ottawa sand with a mean particle size of 0.635 mm and crushed quartz with a mean particle size of 0.140 mm. Friction angles for Ottawa sand and crushed quartz were 38° and 36°, respectively. They filled sand into the cylinder in layers with a thickness of 2 to 3 cm, and each layer was thoroughly worked to obtain a good packing. During sand

installation, excess water was used to ensure that the water saturation of the sand sample was complete. Before conducting the experiments, water was drained through the permeable bottom plug, so that the water saturation of the sand sample was reduced to the non-drainable water content. During the experiments, they applied a vertical load using a piston (Figure 2.1a) to simulate the overburden stress. Through the top side of the cylinder, they injected air through the sand. The flow rate was increased steadily until a small amount of sand was produced suddenly. Then, the flow rate was increased further until a new amount of sand was produced. This was repeated several times until the sand pack suddenly broke down and the sand started pouring out of the opening.

The maximum radius of the sand arches varied from 1.55 cm to 2.46 cm, which exceeded the mean particle size by one to two orders of magnitude. The radius of the sand arches was calculated based on the weight of produced sand, assuming a spherical cavity. They also repeated the same experiments with crushed quartz, but this time they obtained casts by injecting gypsum through the opening to capture the existence and the shape of the cavity (Figure 2.1b). They concluded that a sand arch is formed around the opening and that the cavity created by the sand arch is stable within a certain range of fluid flow rates. In addition, they identified two types of failure modes in their experiments: shear failure due to the change of the stress field and tensile failure caused by the hydrodynamic force of the fluid.

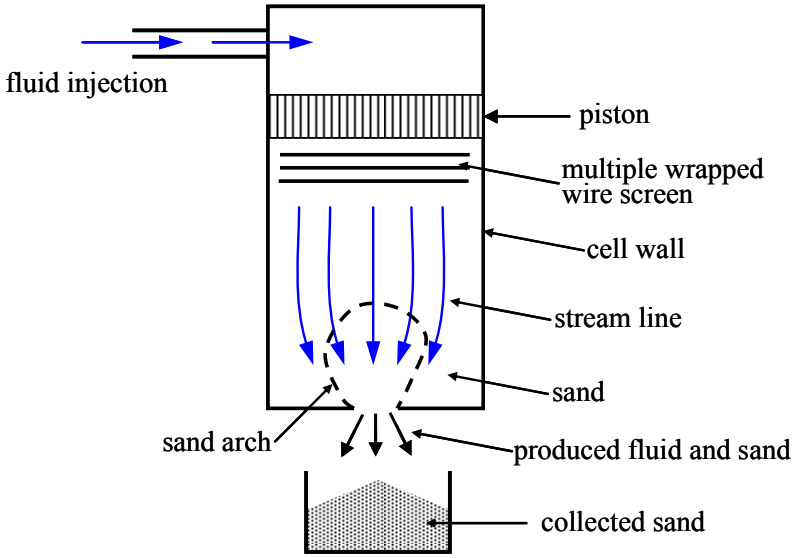

(a)

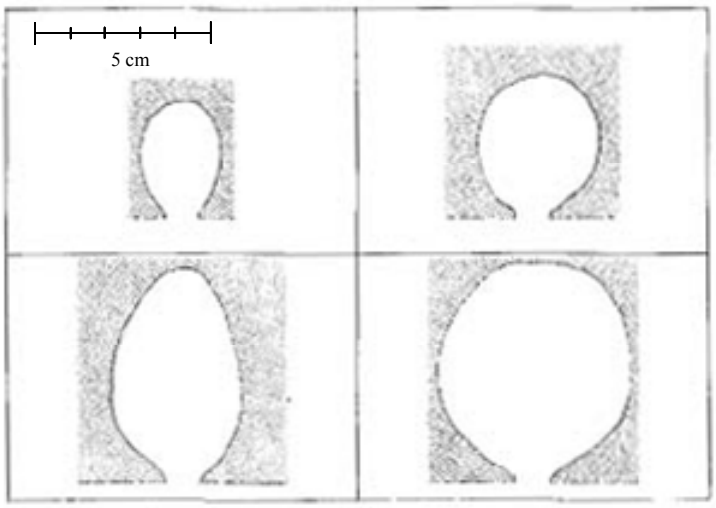

(b)

Figure 2.1 Schematic of sand arching experiment [after *Bratli and Risnes*, 1981]: (a) experimental setup and (b) profiles of cavities from the casts.

Tronvoll et al. [1997] argued that the sand production is initiated by shear failure due to the change of the stress field rather than by tensile failure caused by the fluid flow. To simulate weakly consolidated sandstone, *Tronvoll et al*. [1997] manufactured cylindrical synthetic sandstone samples (Figure 2.2). They mixed sand, sodium silicate, and water in a paste which was compacted in a casting form. Then, they injected carbon dioxide into the mixture to harden it. The material properties of the samples used in their experiments are shown in Table 2.1. Samples had dimensions of 100 mm in diameter and 150 mm in height. Each sample was placed in a pressure vessel (Figure 2.2), and loaded by confining pressure. Axial stress was applied using a loading piston located beneath the bottom plate. During the experiments, fluid was injected through a fluid inlet (Figure 2.2) and the produced sand particles were collected in the sand trap (Figure 2.2). *Tronvoll et al*. [1997] used an acoustic device (Figure 2.2) to detect failure processes, such as micro-cracking. Their goal was to identify damage in the samples, which leads to the macroscopic destabilization (e.g., shear failure), and to determine the relationship between the production of particles and the macroscopic destabilization mechanisms. *Tronvoll et al*. [1997] concluded that sand production is initiated by shear failure due to the change of the stress field and that fluid flow only facilitates the failure and transports the failed particles.

Table 2.1 Material properties of synthetic sandstone [*Tronvoll et al*., 1997]

Material Number	**Consolidation Stress (MPa)**	**Mean grain size (μm)**	**Uniaxial compressive strength (MPa)**	**Friction angle***	**Cohesion (MPa)***
I	20	250	1.6	33.1°	1.22
II	2	250	1.6	33.1°	1.22
III	2	100	1.1	31.9°	1.26
IV	2	150	1.6	32.8°	1.17

*These values are given for confining stress > 1.0 MPa.

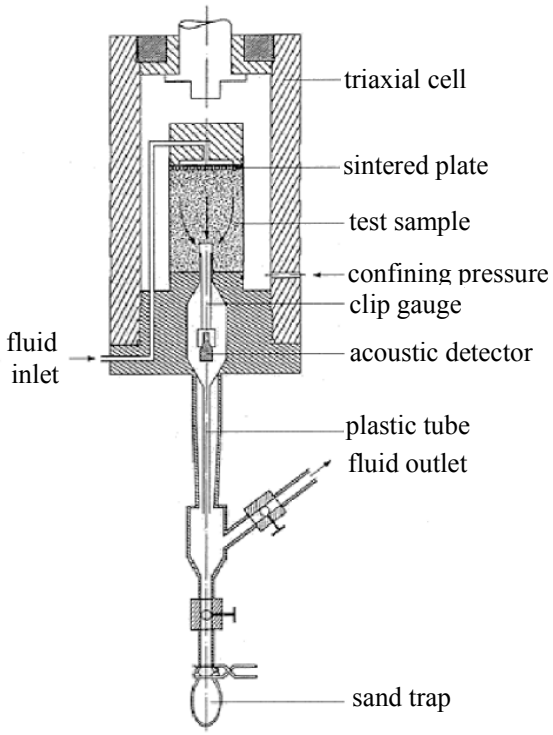

Figure 2.2 Schematic of experimental setup used by *Tronvoll et al*. [1997].

Tremblay et al. [1996; 1997] and *Tremblay and Oldakowski* [2002; 2003] investigated the interior of sand samples during sand production. *Tremblay and Oldakowski* [2002] used sand samples with an average particle size of 220 μm. The size of the cylindrical sand sample was 30 cm in diameter and 80 cm in height. The sand sample was compacted under confining stress of 27.6 MPa. The initial porosity and the initial permeability of the sand sample were 0.34 and 1.17×10^{-12} m^2, respectively. The sand sample was placed in a horizontally oriented container. Oil was injected into the sand sample (Figure 2.3a). Sand particles and fluid were produced together by lowering the fluid pressure at an outlet orifice. The produced sand particles and fluid were collected through the outlet orifice located at the opposite side of injection point. After the experiments, the interior of the sand sample was visualized using a Computed Tomography (CT) scan (Figure 2.3b). *Tremblay and Oldakowski* [2002; 2003] concluded that two channel-like zones with high porosity (called "wormholes") were formed. In their

experiments, these zones occupied almost a quarter of the sample volume (Figure 2.3b). The porosity near the wormhole did not significantly change as compared to the original state.

Walton et al. [2001] found that a "cavity" created by the perforation process is in fact a region of lower density. They simulated the perforating process using a shaped charge to create a perforation at the bottom of a cylindrical sand sample under confining pressure. Their setup is shown in Figure 2.4a. Fluid was injected through the opposite side of the sample after the perforation was created. Produced sand particles were collected together with the fluid. The interior of the sample was monitored by CT scans shown in Figure 2.4b. According to *Walton et al*. [2001], a dilated zone with a lower density was formed around the entrance of the perforation due to the removal of the particles. Its size was proportional to the fluid flow rate. In addition, they observed that there was a critical flow rate at which production of sand increased abruptly.

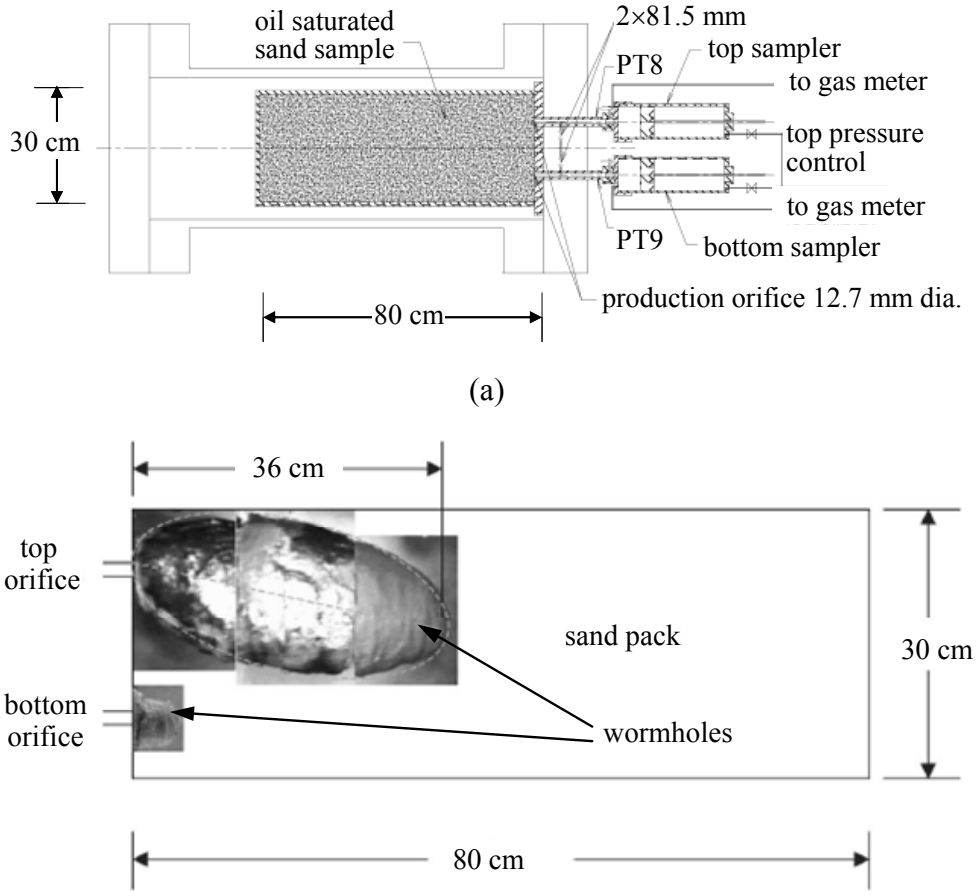

Figure 2.3 Investigation of the interior of a sand sample during sand production [after *Tremblay and Oldakowski*, 2002]: (a) experimental setup and (b) image of high porosity zone in a sand sample formed around perforations. This image was captured by CT scan.

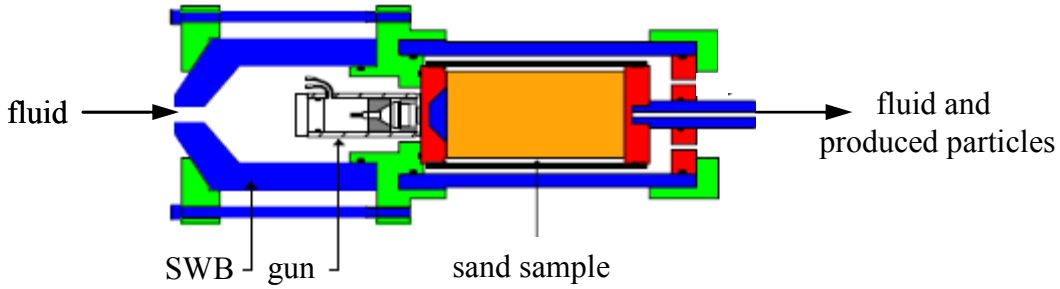

(a)

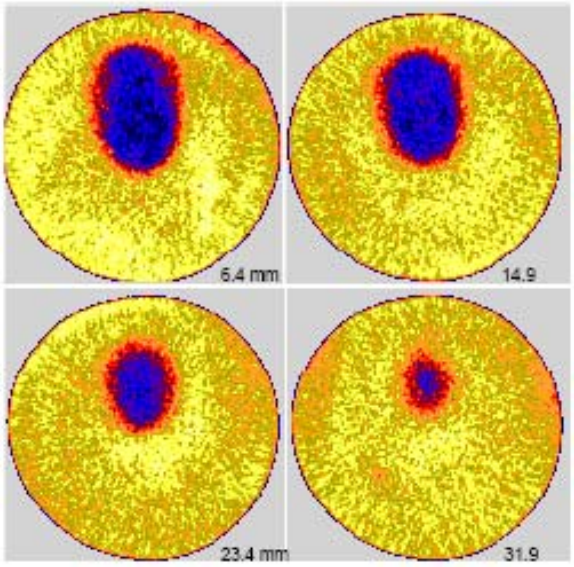

(b)

Figure 2.4 Examination of the interior of unconsolidated sand after perforation and production of particles [*Walton et al*., 2001]: (a) experimental setup and (b) cross-sectional images of CT scan. Dark area represents the dilated zone, and the number in each image is the distance of the section from the perforation.

The aforementioned laboratory experiments, at the perforation scale, show that a region of high porosity may be created in the vicinity of a perforation due to the production of particles. The main role of the fluid flow is to transport the separated particles that are failed by the stress change.

Borehole scale (Figure 1.7c) experimental models have also been used to investigate the behavior of sand formations around a borehole. *Palmer et al*. [2000] and *Vaziri et al*. [1997; 1998a; 1998b; 2000; 2002; 2003] conducted a series of centrifuge tests assuming the existence of a competent stratum over an unconsolidated petroleum reservoir and reported the results of 6 experiments. They used the centrifuge to simulate the overburden stress over the reservoir. The experimental setup was placed at the end of a 5 m radius centrifuge arm that was spun at approximately 25 times the gravitational acceleration.

The major component of their experimental setup was composed of a cylindrical container 900 mm in diameter (Figure 2.5). In the interior of the container, a sand layer was placed between two gravel layers (the authors did not specify the particle size of the gravel). A casing of 20 mm diameter was located at the center of the sand layer to simulate a wellbore. As the inflowing pressure of the fluid was maintained constant (i.e., constant pressure boundary condition), the production of the sand particles was allowed by opening the plug in the casing. The maximum head difference between the well and the outer boundary of the setup was between 26 mm and 48 mm for each experiment. They placed six linear variable differential transducers (LVDT) around the casing at various distances from the center of the wellbore to monitor the behavior of sand layer. They monitored the growth of the cavity using LVDTs. The cavity growth was triggering LVDT sensors, and their locations were correlated to the cavity size.. Since the upper part of their experimental setup was confined by a steel plate, it would be difficult to visually monitor the interface of the sand layer and the competent stratum in their experiments.

Vaziri et al. [2002; 2003] conducted two types of experiments (dimension and boundary conditions of their experimental setup are comparable to our experimental work) using homogeneous unconsolidated sand (Figure 2.6). In the first type of experiments (Figure 2.6a), a wellbore with a single slit was located at the center of the sand layer. The slit consisted of three perforations with the width of 3 mm. The arch length of each perforation was approximately 5 mm. The slit was placed near the bottom of the sand layer, so that the produced sand and fluid could drain through it. Figure 2.6b shows the second type of setup where a wellbore with evenly spaced (spacing of ~25 mm) perforations of 3 mm diameter was placed at the sample center.

The authors identified that a cavity with the shape of a frustum was formed around the wellbore (Figure 2.7). They also observed that the fluid flow rate increased due to the formation of the cavity (inlet pressure was maintained constant). In one of the two reported experiments with the single slit, they observed the formation of another kind of cavity – a surface flow channel (Figure 2.7a) [*Vaziri et al*., 2002, page 1092]. They did not observe the channel in the experiment with multiple perforations (Figure 2.7b) [*Vaziri et al*., 2002, page 1094]. They explained the formation of the flow channel in terms of the volume of produced sand. In the setup with a single slit, near the base of the sand layer, a larger amount of sand was produced, which in turn created the flow channel around the cavity. In the experimental setup with multiple perforations, the fluid flow appeared to be diverted toward the upper perforation after initiation of the cavity. This condition resulted in a smaller amount of produced sand that may not be sufficient to create a flow channel [*Vaziri et al*., 2002; 2003]. They discussed flow distribution around the cavity [*Vaziri et al*., 2002; page 1095], and the distribution in the adjacent sand can be deduced from the results of the numerical modeling [*Vaziri et al*., 2002, page 1098; see also Section 2.6.2].

According to *Vaziri et al.* [2002, page 1100], a larger amount of produced particles may have induced the flow channel formation. Because their experimental setup consists of the metal box containing sand sample, they could not monitor the sand layer during the

experiments. In particular, they were unable to observe directly the formation of the cavity in real time, although they monitored the changing cavity size using LVDTs.

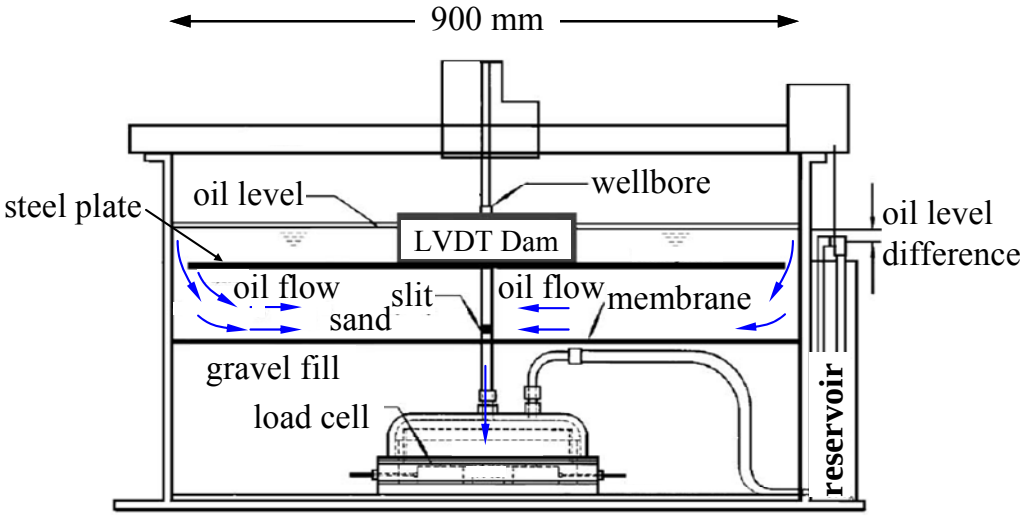

Figure 2.5 Schematic diagram of large-scale centrifuge experimental setup [after *Vaziri et al*., 2003].

Palmer et al. [2000] investigated the behavior of a weakly consolidated sandstone layer around a wellbore under a competent stratum. Two sandstone blocks with a cohesion of 350 kPa were used to simulate a sand layer around a wellbore. The sizes of small and large blocks were 0.46 m × 0.46 m × 0.46 m and 1 m × 1 m × 1 m, respectively. The simulated wellbore had four perforations. During each test, oil was pumped into the simulated wellbore to induce the production of particles. In small block test, *Palmer et al*. [2000] observed that two disturbed zones were formed around a wellbore (Figure 2.8a). These zones were interpreted as shear bands (represented by black lines in Figure 2.8a).

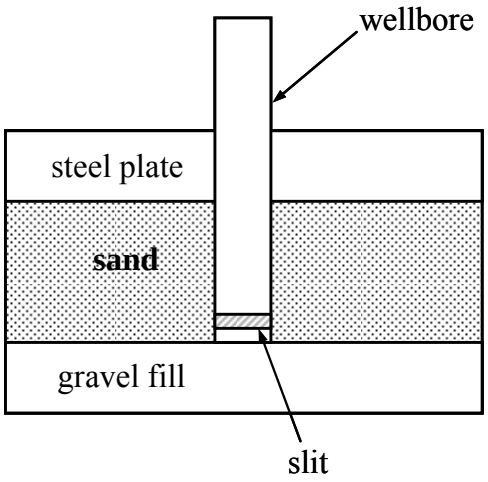

(a)

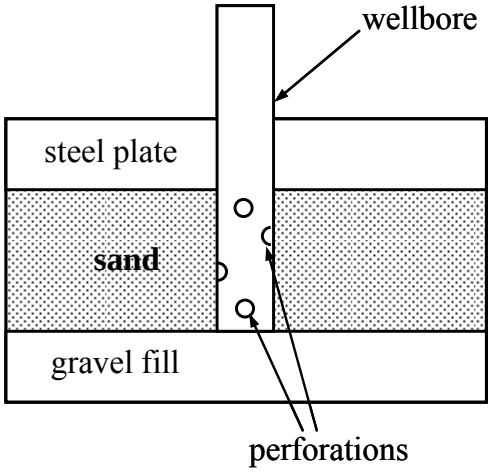

(b)

Figure 2.6 Two types of experimental setup around a wellbore employed by *Vaziri et al*. [2003]: (a) a wellbore with a slit and (b) a wellbore with evenly spaced perforations. Sample thickness is approximately 10 cm and its diameter is 90 cm. They used a 20 mm diameter casing to simulate a wellbore.

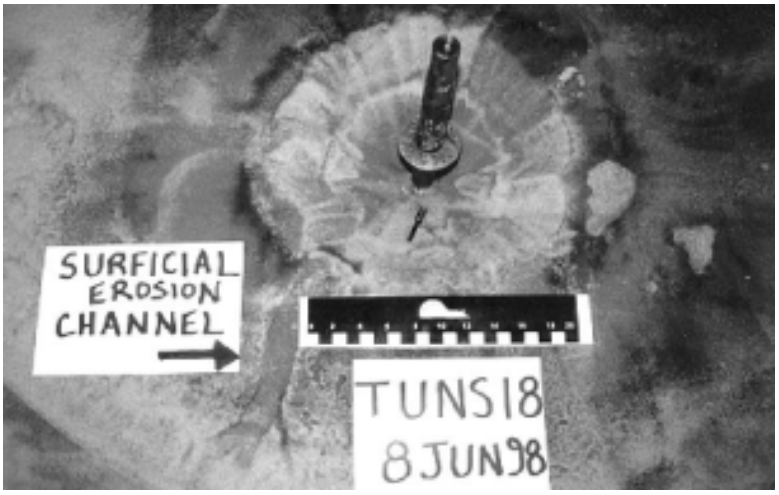

(a)

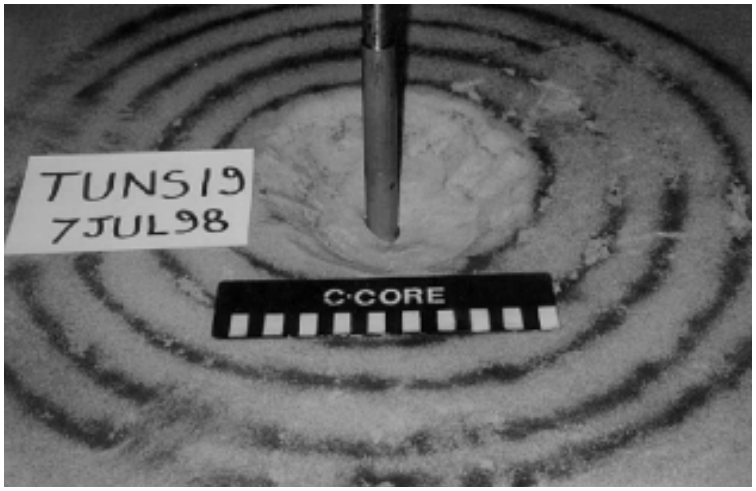

(b)

Figure 2.7 Surface of the sand layer after experiment by *Vaziri et al*. [2003]: (a) for a wellbore with a single slit (Figure 2.6a) and (b) for a wellbore with evenly spaced perforations (Figure 2.6b).

Palmer et al. [2000] reported that the physical voids were less developed. The results of the large block test (Figure 2.8b) show a similar pattern compared to that in the small block test (Figure 2.8a). That is, the disaggregated zones and layers of shear bands are dominant around the wellbore. In both experiments, the shear zone emerged from the top perforations. Sand particles were produced also only from the top perforations. *Palmer et al*. [2000] concluded that, for weakly consolidated sandstone, shear bands are much more likely to accompany sand production than empty voids, and that particle production dramatically increases the permeability of the sandstone blocks.

Van den Hoek et al. [2000] argued that cavity size correlates with the mode of the cavity failure. They used hollow, cylindrical samples that had an outer diameter of 7.8 cm and a length of 16.0 cm. The hollow cylinder samples consisted of friable Castlegate and weakly consolidated Saltwash South outcrop sandstones. Their strengths were 40 MPa and 28 MPa, respectively. For the Castlegate sandstone, the internal friction angle and cohesion were 34° and 4.5 MPa, respectively. Three different inner diameters of the samples were 0.95 cm, 1.3 cm, and 3.0 cm. During the experiments, confining stresses (5–80 MPa) and drawdown (≈5 MPa) were applied. In all experiments, the inner hole pressure was set to be zero [*Van den Hoek et al*., 2000, page 263]. According to *Van den Hoek et al*. [2000, page 264], a large cavity (e.g., wellbore) always fails in shear rather than tensile failure mode, while a sufficiently small cavity (e.g., perforation) may fail in both shear and tensile failure mode. To explain the results of their experiments, they employed a model based on the bifurcation theory. That is, shear failure around a cavity occurs due to buckling of the cavity wall. The smaller cavity diameter suppresses buckling of the cavity wall, and the walls of small cavities are less susceptible to buckling. Therefore, they are more likely to fail in tensile mode than in shear. In contrast, due to the greater susceptibility to buckling of the cavity wall, large cavities are more likely to fail in the shear failure mode.

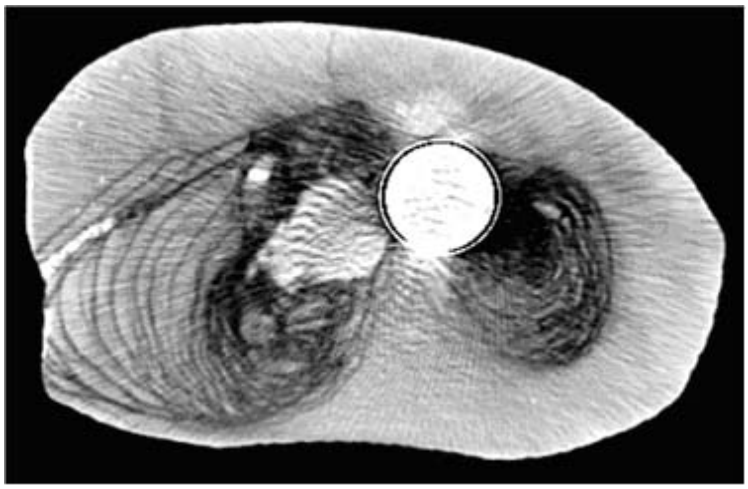

(a)

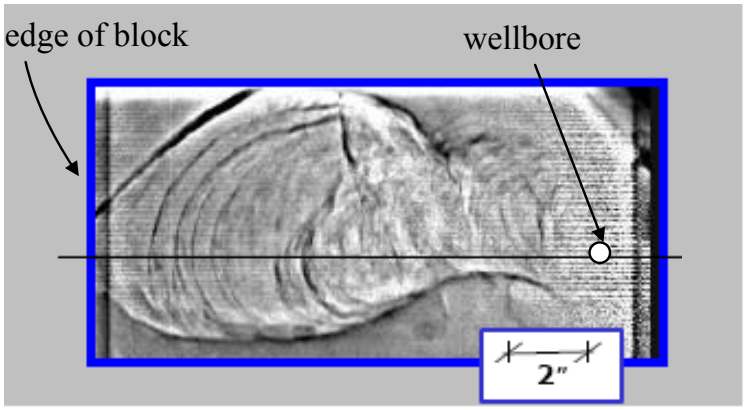

(b)

Figure 2.8 Shear bands (black lines) formed around a wellbore, (a) in the small block (0.46 m × 0.46 m × 0.46 m) (plan view) [*Palmer et al*., 2000] and (b) in the large block (1.0 m × 1.0 m × 1.0 m) (plan view) [*Palmer et al*., 2000]. These images were obtained by conducting a CT scan after the experiments.

Previous experimental work suggests that at the borehole scale, the material properties of the formation around a wellbore determine the mode of failure associated with sand production. In consolidated or weakly consolidated sand formations [e.g., *Palmer et al*., 2000], shear bands with high permeability may be formed around perforations due to the production of particles. In contrast, in unconsolidated sand formations [e.g., *Vaziri et al*., 2003], empty cavities are formed (eroded) around a wellbore, at least when a competent stratum exists above the sand layer. However, (*i*) cavity development has not clearly been monitored in experiments with unconsolidated sand [e.g., *Vaziri et al*., 2003]. Thus, (*ii*) the relationship of the cavity evolution and its impact on the characteristics of sand production has not been well understood yet. Therefore, the objectives of our work are as follows.

1. Monitor the surface of the sand layer during experiment in real time to directly observe the development of the formed cavities (if any).
2. Investigate their relationship with and their impact on the characteristics of production of particles.
3. Based on the results of the experiments, estimate a critical flow velocity required to remove particles from the formation for a better understanding of the sand production phenomena.
4. Propose a conceptual model of particle production in unconsolidated sand formations.

2.2 Laboratory Setup

A sand layer at a borehole scale (Figure 1.7c) around a borehole is simulated in this work. We built a large experimental setup containing an unconsolidated sand sample pre-saturated with water. The sand sample and water simulate an unconsolidated sand formation and fluid in a petroleum reservoir. The term "large" means that the sample size in our setup is of the order of 1 m. This experimental setup is shown in Figure 2.9a. It consists of a cylindrical chamber that contains a saturated sand specimen, stabilizing steel frames, and a sand collection tank (Figure 2.9b).

Figure 2.10 shows the major components of the cylindrical chamber: an upper transparent polycarbonate plate, a lower stainless steel plate, and a side cylindrical ring wall. The sand sample is located above an aluminum disk, which is located on top of an inflatable bladder in the chamber. The diameter of the chamber and the sand sample is chosen to reduce the role of lateral boundary effects. The inflatable bladder is used to apply vertical stress to the sand sample. Once the chamber is assembled, water is injected into the injection ports located at the boundary (perimeter) of the chamber, and the water flows toward a wellbore located at the center of the sand layer. Sand particles are produced there with the water. The produced sand particles are collected in a collection tank (Figure 2.9b).

(a)

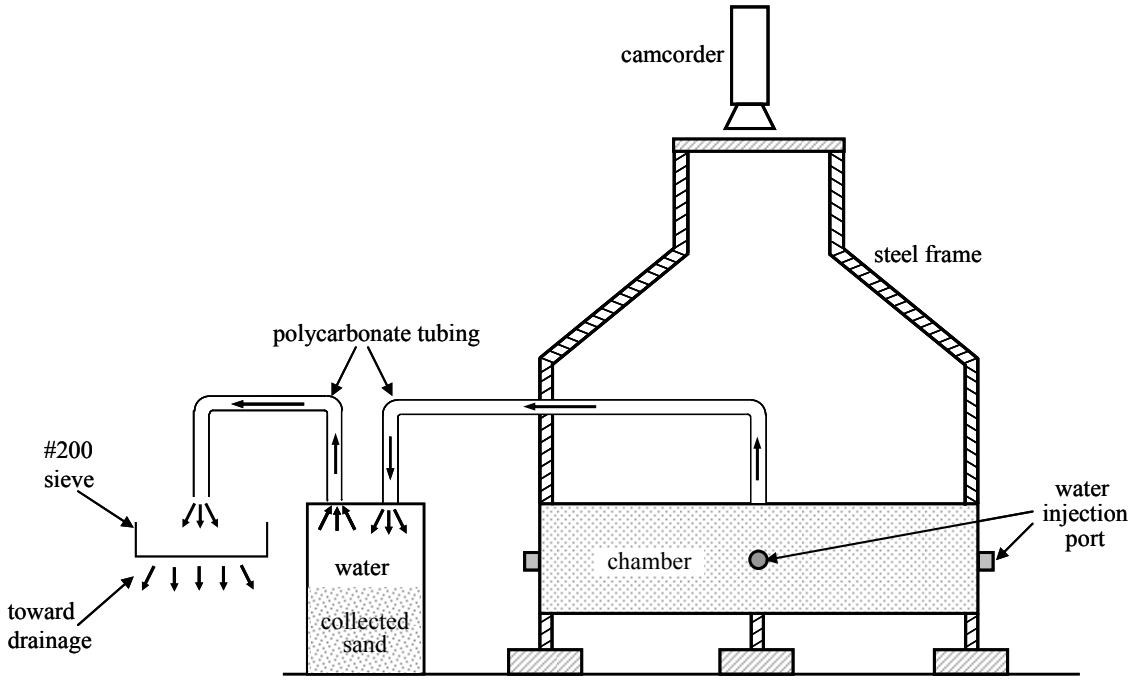

(b)

Figure 2.9 (a) Photograph and (b) schematic illustration (not to scale) of the experimental setup.

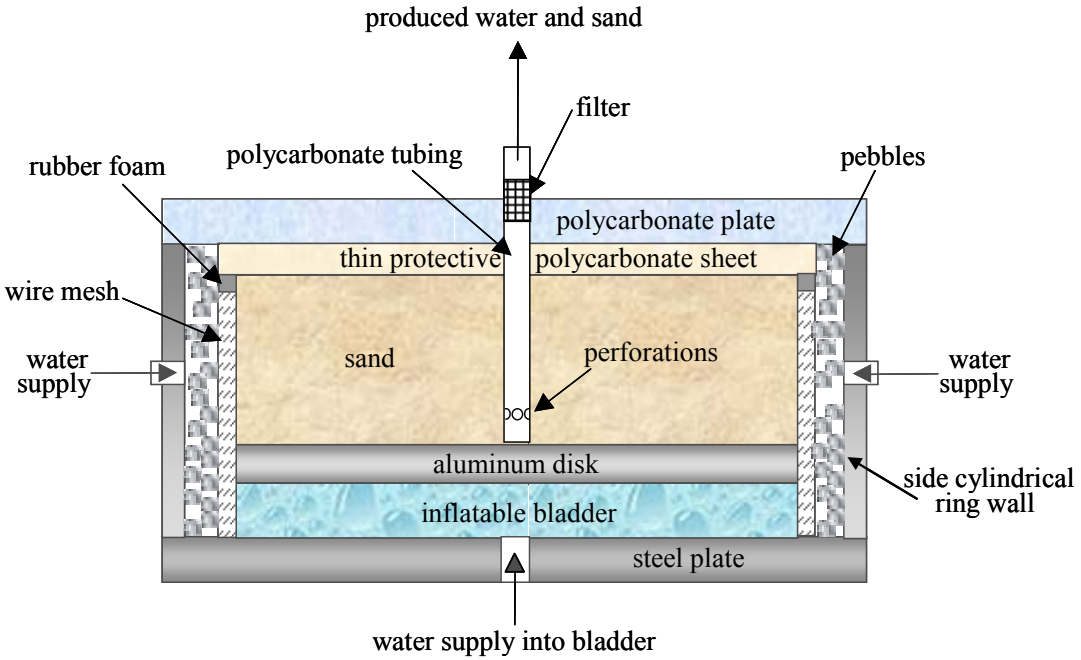

Figure 2.10 Schematic illustration of the interior of the chamber (not to scale). The filter in the polycarbonate tubing is installed only during the initial saturation of the chamber. After the initial saturation, it is removed and not used in experiments.

A typical petroleum reservoir modeled in this work is shown schematically in Figure 2.11. A sand reservoir (represented in the physical model as a sand layer) is located beneath a relatively rigid caprock such as a shale formation. As a result of fluid flow associated with hydrocarbon production, a cavity initiates around the wellbore (Figure 2.11). This geometry is somewhat duplicated in the experimental setup shown in Figure 2.12. The top of the model is a transparent polycarbonate plate (1.22 m × 1.22 m × 0.05 m), used as an upper boundary of the chamber, acts as a relatively rigid layer (Appendix A2) located above the sand layer to model the role of caprock. A key element of the experimental design is that the upper surface of the sand layer can be visualized directly through the plate during the experiments, as can be clearly seen in Figure 2.12. This is the major difference of our design compared to that of *Vaziri et al*. [1997; 1998a; 1998b;

2000; 2002; 2003]. This feature allowed us to monitor the sand production process at the edge and the surface of the sample in real time.

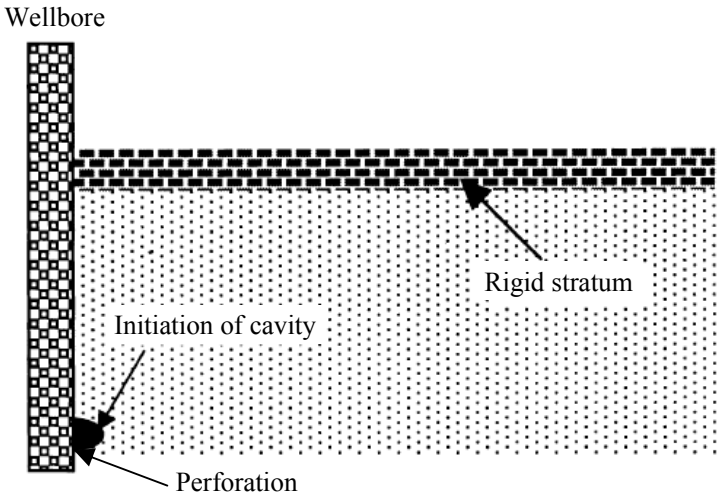

Figure 2.11 Schematic of a petroleum reservoir. Sand layer is located beneath the rigid stratum. Due to production of hydrocarbon, a cavity is initiated around the wellbore [after *Vaziri et al*., 2001].

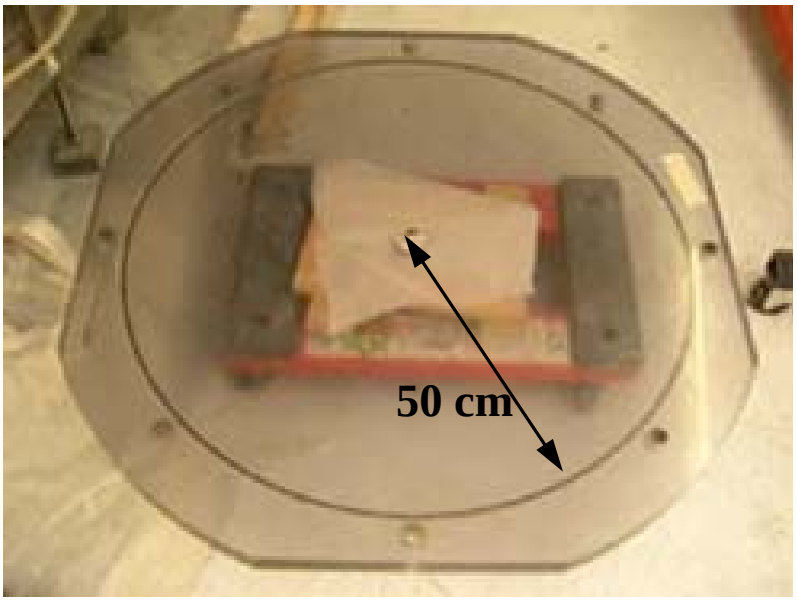

Figure 2.12 Photograph of the experimental setup showing the upper transparent polycarbonate plate.

The lower boundary of the chamber consists of a stainless steel plate, 1.22 m × 1.22 m × 0.025 m (Figure 2.13). A cylindrical steel ring is used as a lateral boundary of the chamber. It has an inner diameter of 1.07 m (3.5 ft), and a height of 0.165 m (6.5 in). Eight equidistant holes with an inner diameter of 1.58 cm (0.6 in) are drilled into the outside steel wall. T-shaped brass tube fittings are attached to each hole (Figure 2.13). The T-shaped brass tube fittings are connected to nylon tubing with an inner diameter of 1.02 cm (0.4 in). This circulation tubing system is connected to the pump that provides water into the chamber.

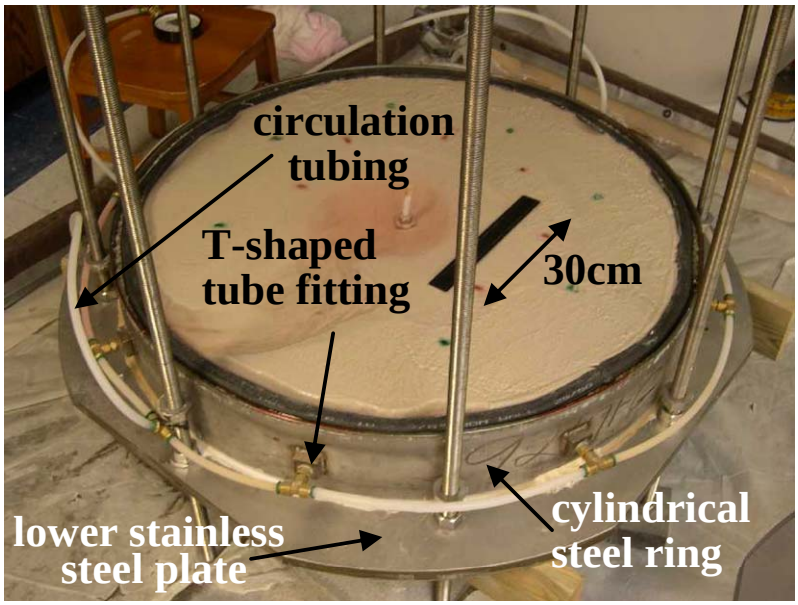

Figure 2.13 Lower steel plate and cylindrical steel ring (the black rectangle is a 30 cm long ruler to show the scale of the apparatus). The lower stainless steel plate has a diameter of 1.22 m and a thickness of 2.5 cm.

In the interior of the steel ring wall, T-shaped polycarbonate tube fittings are attached to the holes so that the water supply from the pump passes by T-shaped brass tube fittings. Then, water is injected into the chamber tangentially to obtain equal water pressure in the chamber and to protect the sand sample.

To simulate a wellbore, polycarbonate tubing with an inner diameter of 2.22 cm (0.87 in) is used (Figure 2.14a). At a distance of 1 cm from the lower end of the polycarbonate tubing, four equidistant perforations with a diameter of 6.35 mm are drilled through the wall of the polycarbonate tubing. Water and sand particles are allowed to flow through these perforations and are drained out of the chamber. The lower end of the polycarbonate tubing is attached to the lower boundary of the sand layer, i.e., the aluminum disk. Details of each part are shown in Figure 2.14b.

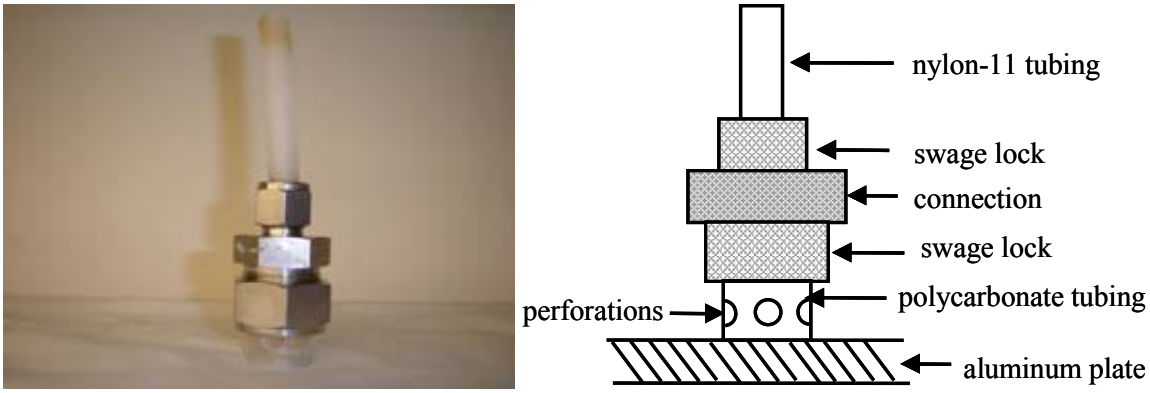

(a) (b)

Figure 2.14 Polycarbonate tubing connected to nylon-11 tubing to model wellbore: (a) photograph and (b) schematics (not to scale).

In Figure 2.14b, the polycarbonate tubing, which simulates casing in a well, is connected via a tubing adapter to nylon tubing with an inner diameter of 1.02 cm (0.4 in). This nylon tubing extends to the outside of the chamber through a hole with a diameter of 1.58 cm (0.6 in) located at the center of the upper polycarbonate plate via a tube-to-pipe adapter.

Outside the sand sample, two layers of retaining stainless steel wire mesh (fine mesh and coarse) and one layer of pebbles are placed in order to provide a lateral constraint to the sand sample and to produce a relatively uniform inflow of water into the

sample. A cross-section and a photograph of retaining wire-mesh and the pebbles are shown in Figure 2.15.

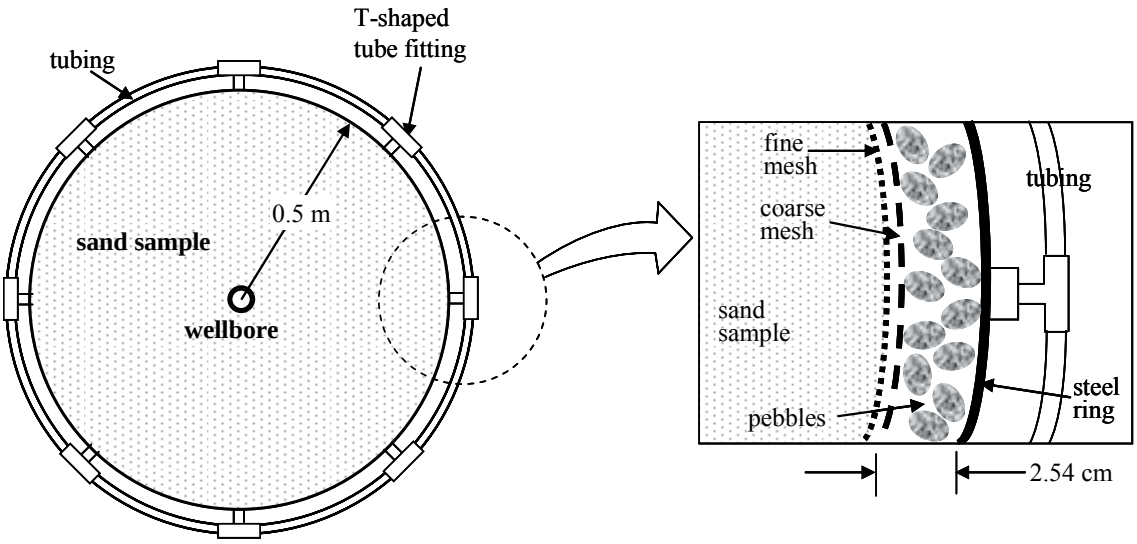

(a)

(b)

Figure 2.15 Plan view of the chamber: (a) schematics (not to scale) and (b) photograph of retaining wire-mesh and pebbles.

The fine retaining wire mesh with a mesh opening of 95 μm is placed against the sand sample (Figure 2.15). The coarse wire mesh with a mesh opening of 5 mm is located outside of the fine mesh (Figure 2.15). The fine mesh prevents the leakage of sand

particles out of the sand layer and protects the sand layer from inflowing water without lowering the hydraulic conductivity of the total system significantly. The coarse mesh provides a mechanical support for the fine mesh. The layer of marble pebbles, of mean diameter 8.0 mm, has thickness of 2.54 cm (1.0 in). The layer of marble pebbles is placed outside of the coarse mesh. The pebbles provide support to the coarse wire mesh and keep the water pressure constant around the perimeter of sand sample by providing a high-permeability zone.

In order to protect the transparent upper polycarbonate plate from abrasion by sand particles, a thin disposable transparent polycarbonate sheet with a thickness of 1.6 mm (Figure 2.16) is placed between the upper polycarbonate plate and the sand sample. In addition, this sheet prevents damage to the upper surface of the sand layer due to capillary suction when the upper polycarbonate plate is removed at the end of experiment. Such damage still may occur when the thin sheet is removed.

Figure 2.16 Thin protective polycarbonate sheet (diameter of the sheet is 1.0 m).

One side of the protective polycarbonate sheet is coated with a thin layer of sand particles. This side is in contact with the sand sample. Hence, we intend to reduce fluid flow through the gap between the sand layer and the thin protective polycarbonate sheet,

and the possibility of erosion of sand particles. Additionally, a ring of rubber foam is placed on top of the two layers of the wire mesh (Figure 2.17), to prevent the fluid flow through the boundary between the sand specimen and the thin polycarbonate sheet.

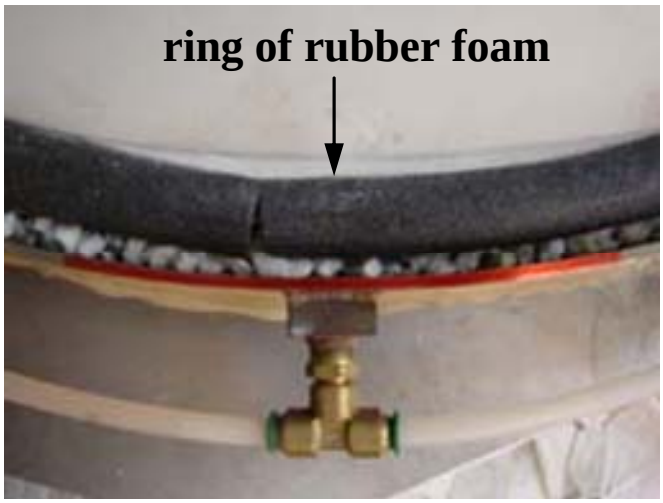

(a)

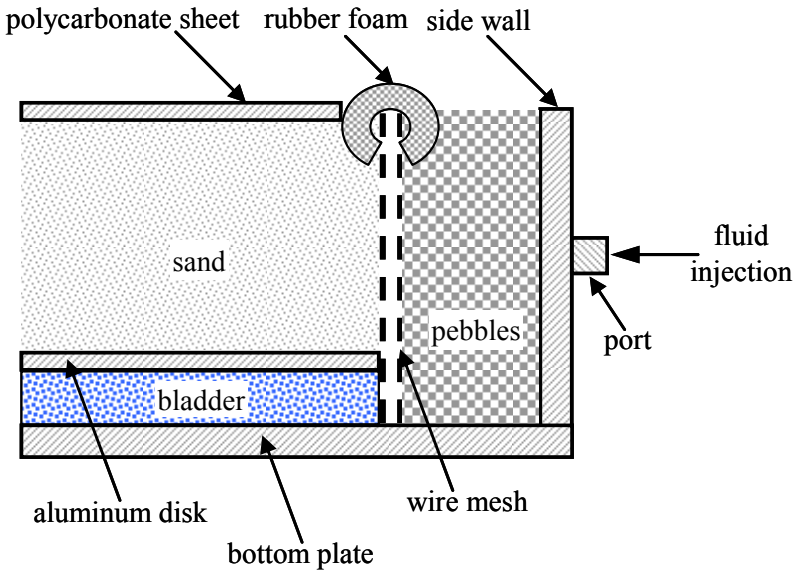

(b)

Figure 2.17 Ring of rubber foam: (a) plan view (photograph) and (b) schematic side view (not to scale).

To apply a vertical stress to the lower boundary of the sand, an inflatable rubber bladder is placed beneath the sand sample. It consists of a flexible, tear-resistant rubber membrane. Water is injected into the bladder to exert pressure onto the sand layer. The bladder has a diameter of 0.95 m and an initial height of 2.5 cm. The rubber membrane of the inflatable bladder is located above a polycarbonate ring, so that the inflatable bladder cannot inflate laterally (Figure 2.18). An aluminum disk with the same diameter as that of the sand layer and a thickness of 0.96 cm is placed between the sand layer and the inflatable bladder (Figure 2.18b). The aluminum plate moves vertically along the vertical boundary of the wire mesh (Figure 2.18b). It provides a convenient base for sample preparation and protects the bladder from sand particles. This experimental setup attempts to model a petroleum reservoir in a sand layer formation.

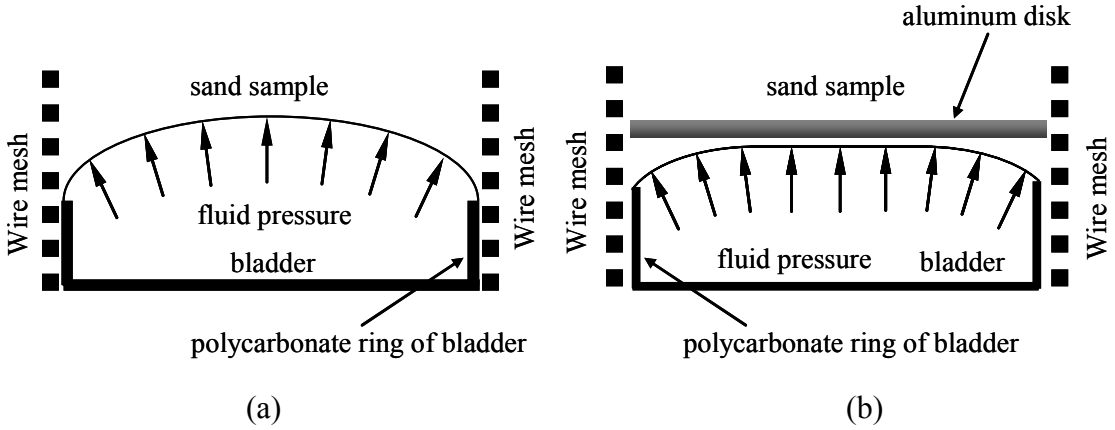

Figure 2.18 Sample-bladder deformation (side view, not to scale): (a) deformation only with a bladder and (b) effective deformation with both an aluminum disk and a bladder.

2.3 Material Properties of Sand Specimen

The physical properties of the sand specimen (Ottawa F-110) used in our experimental setup are listed in Table 2.2. A microphotograph of sand particles is shown in Figure 2.19.

Table 2.2 Physical properties of fine sand [*US Silica*, 2005]

Properties	Value
Type	Fine sand
Mineral	Quartz
Color	White
Grain	Rounded
Sphericity*	0.6
Mohs hardness**	7.0
Specific gravity	2.65
Minimum density	1.43 g/cm^3
Maximum density	1.73 g/cm^3

*$\pi^{1/3}$(6×volume of the particle)$^{2/3}$/(surface area of the particle) [e.g., *Wadel*, 1935; *Papadikis et al.*, 2010]

**Resistance of an object to scratch, defined by scratching it with another object of known hardness [*Coenraads*, 2008]

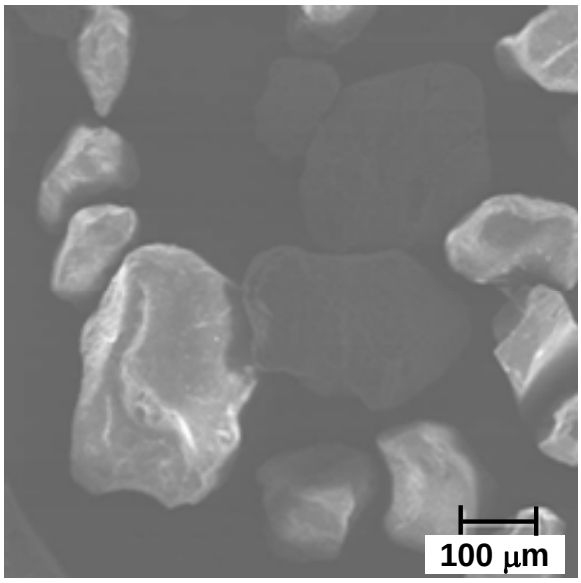

Figure 2.19 Scanning electron microscope (SEM) photograph of sand particles (Ottawa F-110) [*Chang*, 2004].

To characterize the particle size distribution of the sand sample, we used two samples and conducted sieve analyses. The results are shown in Figure 2.20. In the geotechnical literature on the particle size distribution, the uniformity coefficient, C_u, is often defined as [*Das*, 1994]

$$C_u = \frac{D_{60}}{D_{10}} \tag{2.1}$$

where D_{60} and D_{10} are the particle size on the particle size distribution curve corresponding to 60% and 10%, respectively. According to Figure 2.20, D_{60} and D_{10} are 140 μm and 80 μm, respectively. Therefore, the uniformity coefficient of the sand sample is 1.75. If the uniformity coefficient is less than 2.0, such a sample is considered to have a uniform distribution [*Lambe and Whitman*, 1979]. Thus, we conclude that our sand sample has a relatively uniform distribution (poorly graded).

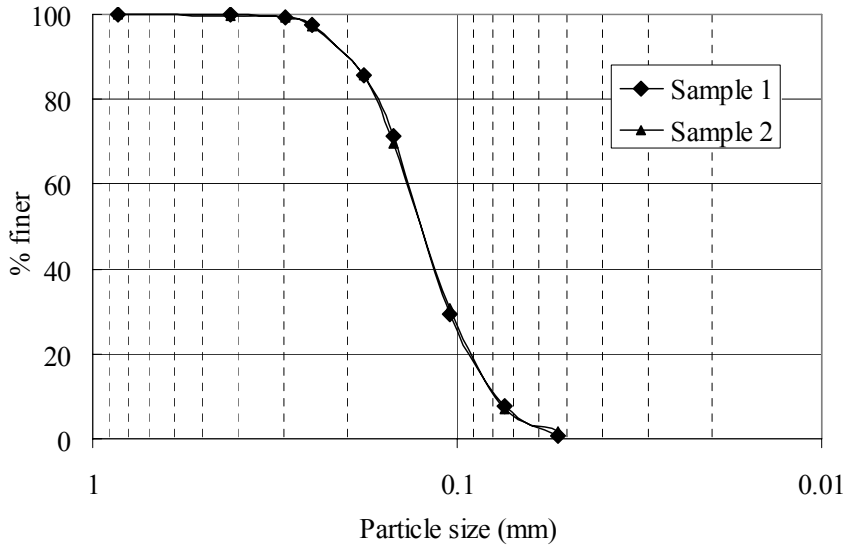

Figure 2.20 Particle sizes of sand sample (Ottawa F-110).

To measure the internal friction angle, we performed triaxial compression tests shown in Figure 2.21. The triaxial samples have a diameter of 3 cm and a height of 10 cm. We conducted four consolidated drained tests [*ASTM*, 2004] by varying the confining stress from 50 kPa to 250 kPa, which are characteristic values for the stress regime in our sand production apparatus. By opening the drainage valve, the tests were performed in drained condition. A Mohr-Coulomb diagram from the triaxial compression tests is shown in Figure 2.22. The internal friction angle of the sample was found to be approximately 32° when the confining stress was greater than 120 kPa. The internal friction angles from the literature (Table 2.3) are in agreement with our measurements.

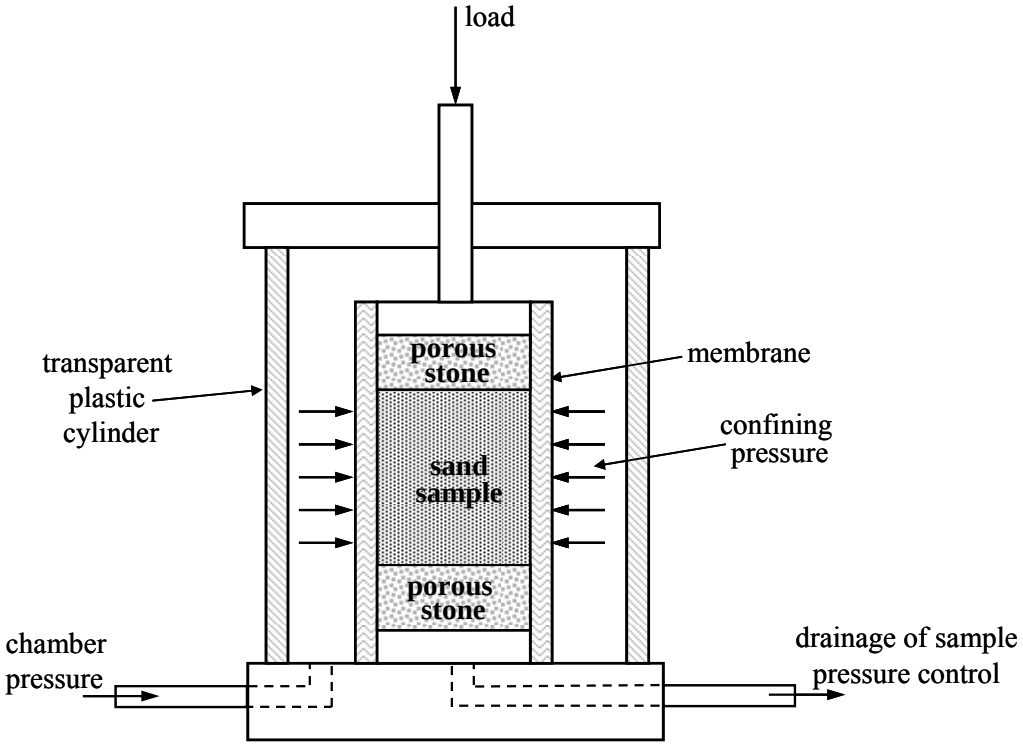

Figure 2.21 Schematics of triaxial compression test [after *Lambe and Whitman*, 1979]. The triaxial samples have a diameter of 3 cm and a height of 10 cm.

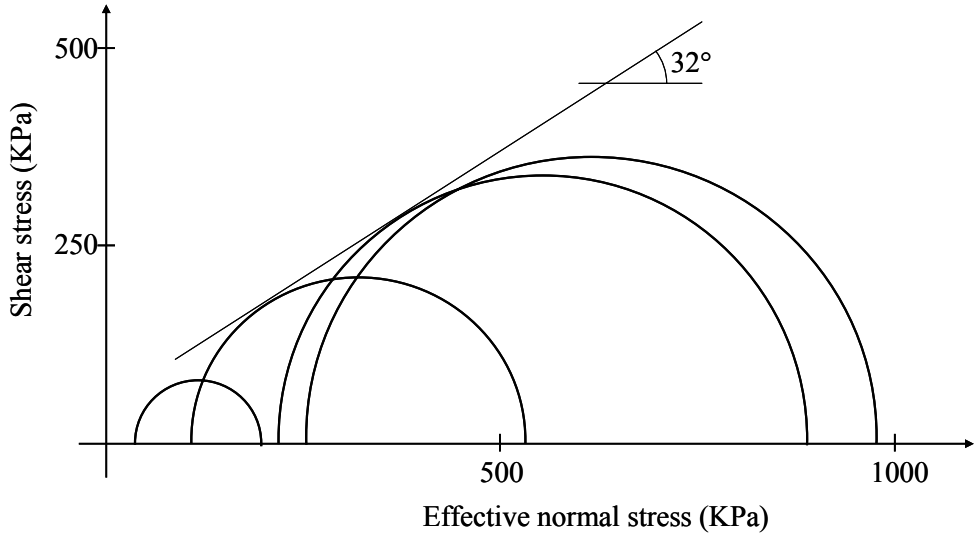

Figure 2.22 Results of drained triaxial compression tests.

Table 2.3 Internal friction angle from previous studies [*Lambe and Whitman*, 1979; *Holtz and Kovacs*, 1981]

Classification	Particle size	Density	Internal friction angle
Uniform fine to medium sand	1.7 mm – 75 μm	Medium	30° - 34°
		Dense	32° to 36°
Standard Ottawa sand	580 μm (D_{10})	Loose	28°
		Dense	35°

We also measured the repose angle of the sand sample. The repose angle is used to evaluate the effect of fluid flow on the stability of sand layer around a well (discussed in Section 2.5.3). The repose angle is frequently measured using the funnel testing method (Figure 2.23a) [e.g., *Lajeunesse et al*., 2004]. Since the sand layer is confined axisymmetrically, the repose angle is best measured using geometry that more closely matches our experiments, i.e., the shape of the cavity (Figure 2.23b).

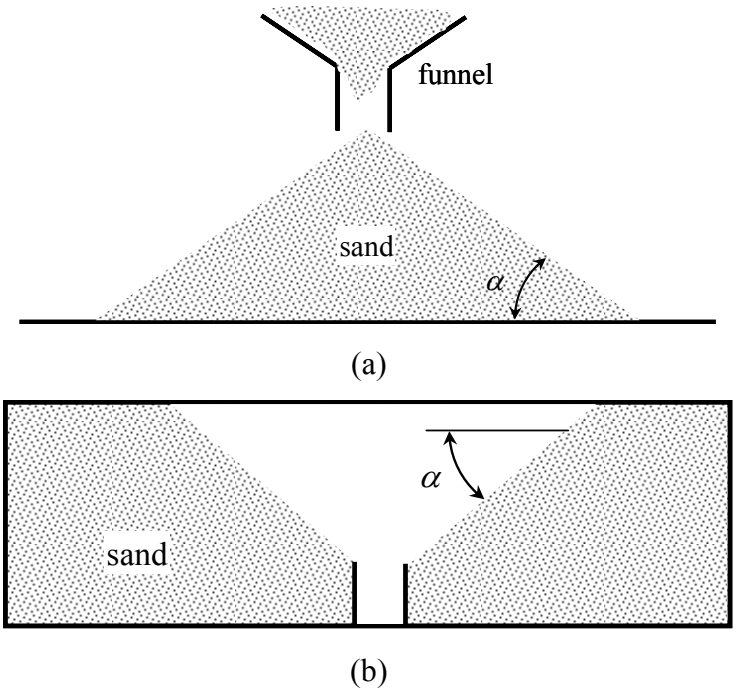

Figure 2.23 Methods of measuring repose angle α: (a) conventional funnel testing method and (b) alternative method used in this work.

The comparison of repose angles using these two methods is shown in Table 2.4. The repose angle measured using the funnel method (Figure 2.23a) is smaller than using the alternative method (Figure 2.23b). This effect of geometry and boundary condition on the measured repose angle is well known [e.g., *Zhou et al*., 2002].

Table 2.4 Measured repose angle

Test number	**Repose angle, α**	
	Funnel method (Figure 2.23a)	**Alternative method (Figure 2.23b)**
1	32°	38°
2	33°	37°

To model fluid in a reservoir, water is used instead of petroleum to reduce the complexity of the experimental procedures, although the properties of water and typical fluids from petroleum reservoirs may be quite different (Table 2.5).

Table 2.5 Properties of water and petroleum (at ~22°C and 1 atm) [*Bradley*, 1987; *Janna*, 1993]

Property	Water	Petroleum
Density	1 g/cm^3	0.82 – 0.94 g/cm^3
Dynamic viscosity	1 cP	2.0 - 80 cP (or greater)

Compared to typical petroleum, water has a slightly higher density but may have much lower viscosity. The use of water as a fluid decreases the hydrodynamic force of the fluid flow due to the decrease in viscosity. Since the confining stress of our experimental setup is rather low compared to field conditions, the difference attributed to the hydrodynamic effect from the use of water is somewhat mitigated. In general, the local pressure gradient has a greater impact on the production of particles than that of the drag force caused by fluid flow [*Charlez*, 1997]. Therefore, lower confining stress may suffice to simulate sand production if we use water as a reservoir fluid.

2.4 Experimental Procedures and Conditions

2.4.1 Experimental Procedures

To prepare the sand sample, sand was dried in an oven at a temperature of 110 °C (230 °F) for 12 hours to remove all moisture. After drying, the sand was poured into the chamber (Figure 2.9). Due to the size of the oven, the entire sand sample was divided into three batches for oven drying. Thus, the first batch and the last batch had at most time difference of 36 hours. Therefore, the first batch may have been slightly moistened due to ambient humidity while the last batch was drying. We did not observe, however, clumping of sand particles during pouring sand into the chamber and did not experience any noticeable problems during compaction.

The distribution of the density of the sand is non-uniform after pouring, and the surface of the sand sample is not smooth or flat. Thus, to create a uniform distribution of the sand density and to obtain a smooth and level upper surface, the sand sample required compaction. Due to the size of the sample (i.e., a diameter of 1.0 m and a height of 0.1 m), it was difficult to compact the sample using hammering or rodding. When one area of the sample was compacted by hammering or rodding, then the surrounding area was displaced. Hence, we compacted the sand layer by vibration with a custom-made vibration apparatus (Figure 2.24). To increase the effectiveness of the compaction, a surcharge of 3.17 kPa that corresponds to 262 kg of lead disks was applied to the vibration apparatus. Based on preliminary compaction tests, the density of the sand appeared to cease to increase significantly after compacting for 30 min.

After the sand sample was positioned, the thin protective polycarbonate sheet was placed on the upper surface of the sand. Then, the upper polycarbonate plate was placed on top of the chamber. To stabilize the upper polycarbonate plate against the pressure from

water and inflatable bladder, a stabilizing steel frame was assembled (Figure 2.9). A camcorder was attached to the stabilizing steel frame using steel rods (Figure 2.9).

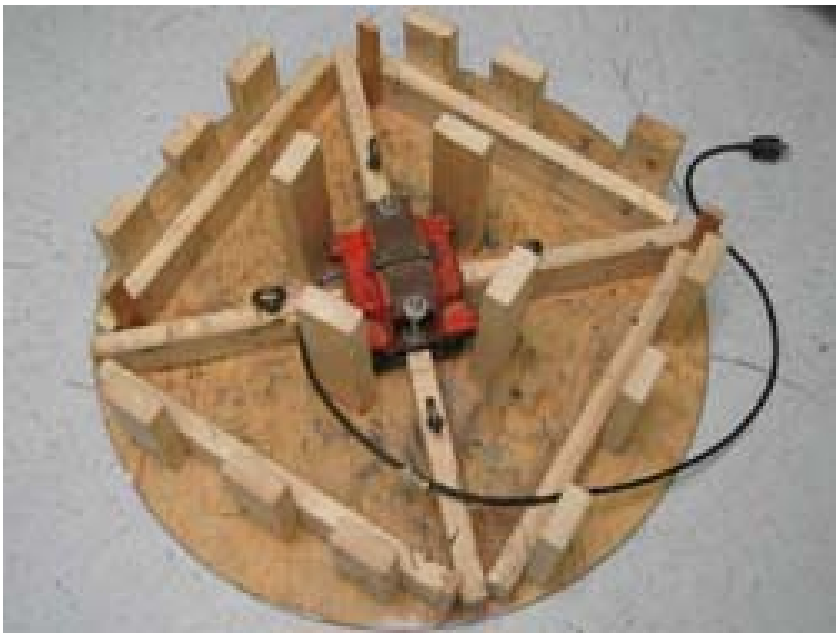

Figure 2.24 Vibration apparatus. Electric vibrator is mounted on a circular wooden plate.

Although the protective polycarbonate sheet coated with sand particles was placed between the upper polycarbonate plate and the upper surface of the sand specimen, movement of sand particles along the upper surface of the sand could still occur. Hence, dyed sand particles were placed on the upper surface of the sand layer to check the movement of sand particles on top of the sand layer.

For the first experiment (henceforth, called "base case"), we installed the temporary boundary shown in Figure 2.25a. In the interior of the boundary, we placed the original (non-colored) sand sample. Two layers of black and green sand particles are located outside of the boundary (Figure 2.25b). The black sand is located beneath the green sand. After compaction of the sand sample using a vibration table, we placed two layers of rings and two lines using sand samples dyed blue and red, respectively (Figure

2.26). We wanted to check the movement of the upper surface of the sand layer during the experiment by monitoring the rings and lines.

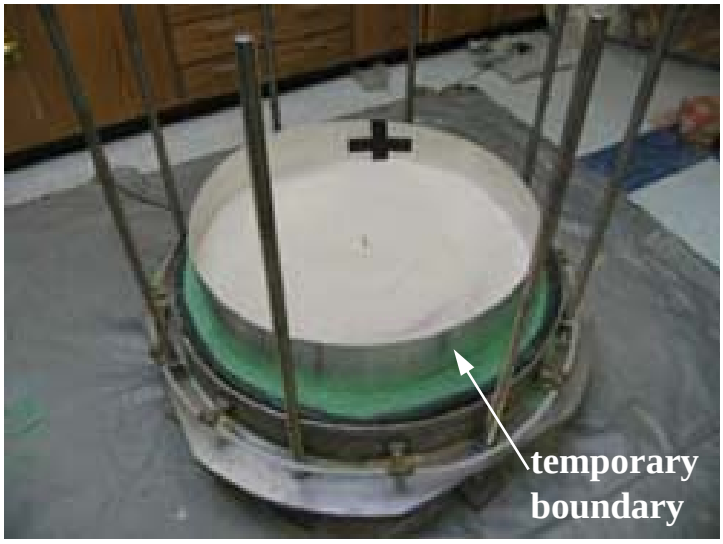

(a)

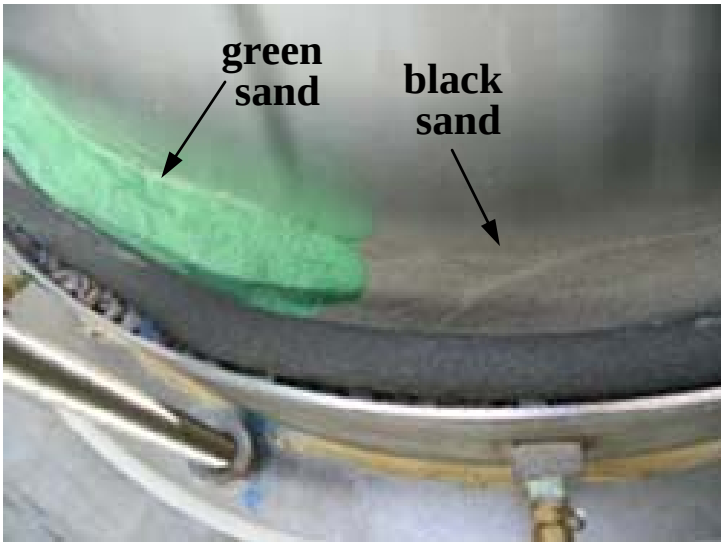

(b)

Figure 2.25 Preparation of the sand sample in base case: (a) temporary boundary to separate ordinary sand from colored sand and (b) installation of two layers of colored sand on the boundary: green sand on top and black sand on bottom.

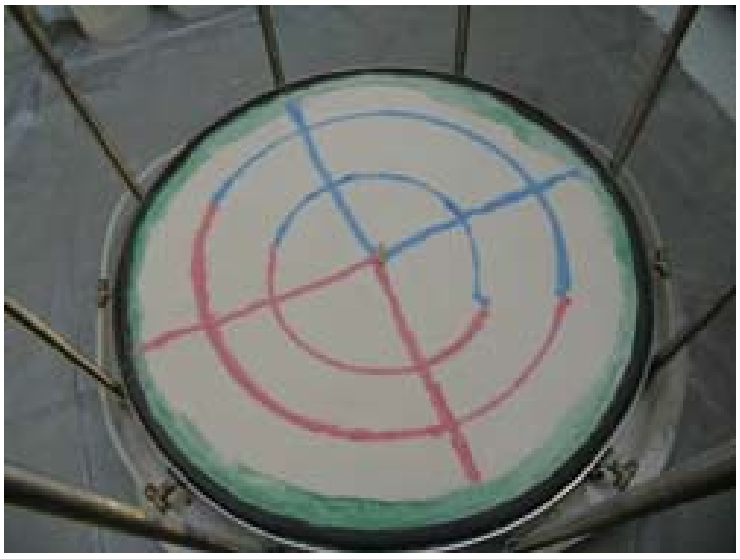

Figure 2.26 Installation of two sets of rings and lines using blue and red sand to check the movement of the upper surface of the sand layer.

For other experiments, we placed dyed sand particles in small areas (Figure 2.27a). The initial locations of the dyed sand particles were marked on the upper surface of the polycarbonate plate (Figure 2.27b). The movement of the sand particles could then be detected by comparing the location of dyed sand particles before and after the experiments. Furthermore, referencing the difference of the locations of the dyed sand after experiment compared to their original locations, would allow estimating the deformation of the sand layer.

After the setup was assembled, water was injected into the inflatable bladder to apply the vertical stress to the sand. To limit the deflection of the upper polycarbonate plate (i.e., obtained from theoretical estimates in Appendix A2), the pressure in the interior of the inflatable bladder was maintained below 34.5 kPa (5 psi) and monitored by a pressure meter connected to the bladder.

(a) (b)

Figure 2.27 Dyed sand particles placed on top of a sand layer to visualize the location of the movement of the sand layer during the experiment: (a) dyed sand particles placed on the upper surface of the sand before the experiment and (b) initial location of dyed sand particles marked on the upper surface of polycarbonate plate (a 15-cm long pen is shown for scale).

Before starting the experiment, the sand layer was saturated with water. During the saturation process, air bubbles could be entrapped in sand and in other parts of the experimental setup. To reduce the amount of entrapped air in the system, carbon dioxide (CO_2) gas was flushed through the flow system and the sand layer. For comparison, the density and solubility to water of air and CO_2 gas are listed in Table 2.6.

Table 2.6 Density and solubility to water of air and CO_2 gas at ~22°C and 1.0 atm [*Oxtoby et al*., 1990; *Lide*, 2004]

Properties	**Air**	**CO_2 gas**
Density	1.293 g/L	1.976 g/L
Solubility in water (at ~22°C)	0.023 kg/m^3	1.45 kg/m^3

The density of the CO_2 gas is greater than that of the air. Hence, as the CO_2 gas is injected into the open horizontal chamber (Figure 2.10), CO_2 displaces the air. The air flows out of the chamber through the wellbore located at the center of the sand sample. Since the solubility of the CO_2 gas in water is much greater than that of the air, CO_2 bubbles

entrapped in the interior of the sand or the rest of the setup will dissolve readily into the water. Then, the CO_2 is flushed out of the entire system. This is a well known and frequently employed technique [e.g., *Garga and Zhang*, 1997; *Lacasse and Berre*, 1988].

After flushing with CO_2 gas, the sand layer was saturated with water. Before water saturation, the polycarbonate tubing at the center of the upper polycarbonate plate was plugged with a filter with a mesh opening of 50 μm to prevent the production of sand during the water saturation (Figure 2.10). This filter was removed after the setup was completely saturated with water. Then, the sand collection tank was connected to the chamber. Finally, water was injected into the sand sample, and the produced water and sand particles were collected in the collection tank (Figure 2.9b).

After the completion of the flow experiment, the upper part of the setup was disassembled. Then, the upper polycarbonate plate and the thin protective polycarbonate sheet were removed. To preserve and measure the final geometry of the cavity and the surface channel, silicone glue was poured into the cavity and the surface channel. After solidification of the adhesive sealant, the cast of the cavity and the surface channel was removed from the sand. Its volume and shape were measured. Details are discussed in Section 2.5.

2.4.2 Experimental Conditions

The chamber in our experimental setup has a cylindrical geometry (Figure 2.9). Water and produced sand particles flow radially toward the borehole located at the center of the chamber (Figure 2.10). A vertical stress is applied to the sand specimen by injecting water into an inflatable bladder (Figure 2.10) beneath the sand layer with a pressure of 34.5 kPa. After the injection of the water, the valve to the bladder is closed, so that the volume of the water in the bladder remained constant during experiment. The pressure in the bladder is monitored with a pressure meter connected to the bladder. The lateral boundary of the bladder is constrained by a serial wire mesh/pebble layer system (Figures

2.17 and 2.18). Because the water in the bladder is effectively incompressible (for our range of conditions), the height of the bladder can be considered constant during the experiment. An upper polycarbonate plate is placed on top of the sand specimen and fixed to the main frame in the experimental setup. We did not observe any significant vertical displacement of the boundaries of the sand. The volumetric flow rate was maintained constant during each experiment. This experimental setup simulates a horizontal sand formation located under an impermeable layer (caprock).

In all of our experiments we obtained the formation of a cavity and a surface flow channel due to sand production. Among other factors affecting their formation and the development, we also investigated the effect of gravity on the behavior of the sand layer during sand production. The entire setup was inclined at slopes of 7° and 15° in addition to zero-inclination experiments such as shown in Figure 2.28. We conducted a total of eight experiments: four with zero-inclination (series 0), two with 7° inclination (series 7), and two with 15° inclination (series 15). Conditions for each experiment are given in Table 2.7, where the angle of the inclination is reflected in the experiment number. For example, test 0C represents experiment C of series 0 (with zero inclination). The maximum dry bulk density of the sand sample (Ottawa F110) was 1.72×10^{3} kg/m^{3} [*Yun*, 2005]. The relative density [e.g., *Da*s, 1994] of the sand sample was greater than 90%.

2.4.3 Measurements

The volumetric flow rate of the fluid was controlled using a flow meter with a measuring range from 1.9×10^{-3} m^{3}/sec to 19×10^{-3} m^{3}/sec. The pressure of the inflowing water was measured using a pressure meter. The locations of the flow meter and the pressure meter are shown in Figure 2.29. The pressure of the inflatable bladder was also measured by pressure meter.

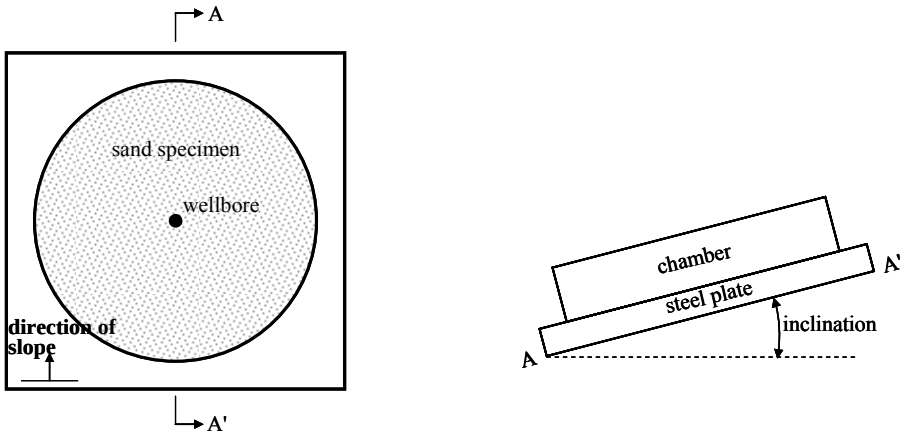

(a) (b)

Figure 2.28 Experimental setup with inclination: (a) plan and (b) side views. Direction of slope indicates the dip direction (i.e., water would flow along the direction of the arrow).

Table 2.7 Experimental conditions for experiments

Test No.	Inclination (°)	Flow rate (L/min)	Dry bulk density of sand sample (kg/m^3)
Base case	0	4.9	1.76×10^3
0A	0	4.9	1.78×10^3
7A	7	4.9	1.71×10^3
15A*	15	5.87 → 9.46	1.77×10^3
7B	7	4.9	1.72×10^3
0B	0	4.9	1.74×10^3
15B	15	4.9	1.78×10^3
0C	0	4.9	1.72×10^3

*In this experiment, the flow rate was 5.87 L/min during the first 6 hours, and 9.46 L/min after that.

In the experimental setup (Figure 2.9b), the produced water and sand particles are collected in the sand collection tank. The sand settles to the bottom of the sand collection tank and water overflows out of the tank. At the end of the polycarbonate tubing near the drainage hole, we placed a #200 sieve (opening = 75 μm) to collect sand particles from the collection tank (Figure 2.9b). For each experiment, the weight of the sand particles collected in the sieve was less than 5 g. This amount is negligible compared to the produced sand, which remains in the tank.

To visualize the upper surface of the sand through the transparent polycarbonate plate and the sand-coated protective polycarbonate sheet, we used a digital camcorder shown in Figure 2.30. The video camera was mounted above the stabilizing steel frame. With this setup, we monitored the development of the cavity and the surface channel on the upper surface of the sand specimen. By monitoring the upper surface of the chamber through the transparent polycarbonate plate (Figure 2.12) and monitoring the transparent polycarbonate tubing connecting the chamber and the sand collection tank (Figure 2.9b), we were able to directly observe the production of sand particles. We observed that for the chosen experimental parameters, the cavity and the surface channel (discussed in Section 2.5) always form within the first hour of the experiment. Hence, during the first hour of the experiment, the upper surface of the sand sample was monitored continuously. Then, after the first hour, the sample surface was recorded every 30 min. Each recording lasted approximately 1 min.

We measured the weight of the produced sand particles in the sand collection tank in real time using a scale located beneath the tank (Figure 2.30). During the experiment, unknown volume, V_s, of the produced sand is collected in the sand collection tank. The increase, W_t, in the tank weight is equal to the difference between the weight, W_s, of the produced sand and that of water displaced by the produced sand particles. In other words,

$$W_t = G_s \gamma_w V_s - \gamma_w V_s = (G_s - 1)\gamma_w V_s \tag{2.2}$$

where $G_s = 2.65$ is the specific gravity of a sand particle and $\gamma_w = 9.81$ kN/m^3 is the unit weight of water. From (2.2), the weight of the produced sand is given by

$$W_s = G_s \gamma_w V_s = \frac{G_s}{G_s - 1} W_t \tag{2.3}$$

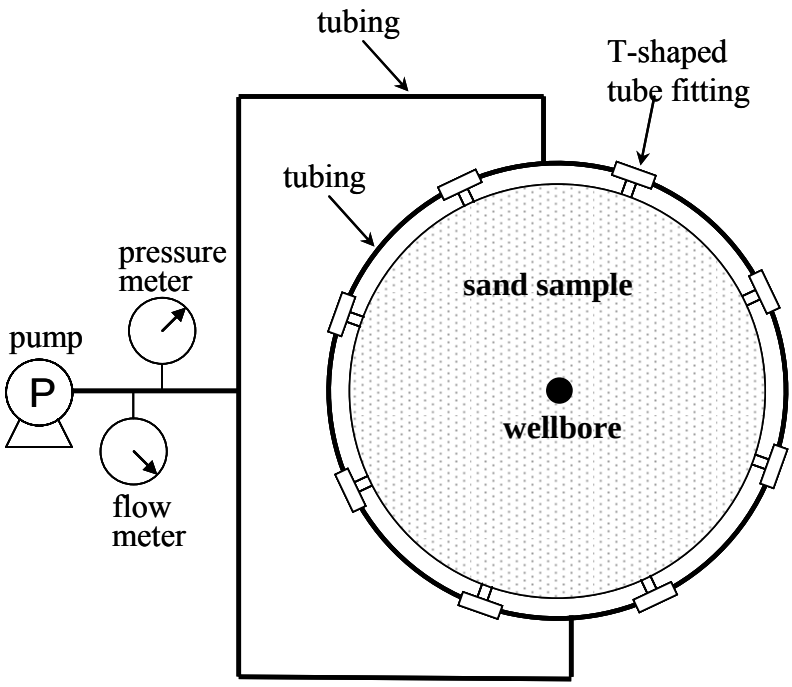

Figure 2.29 Schematic of locations of pressure meter and flow meter (plan view, not to scale).

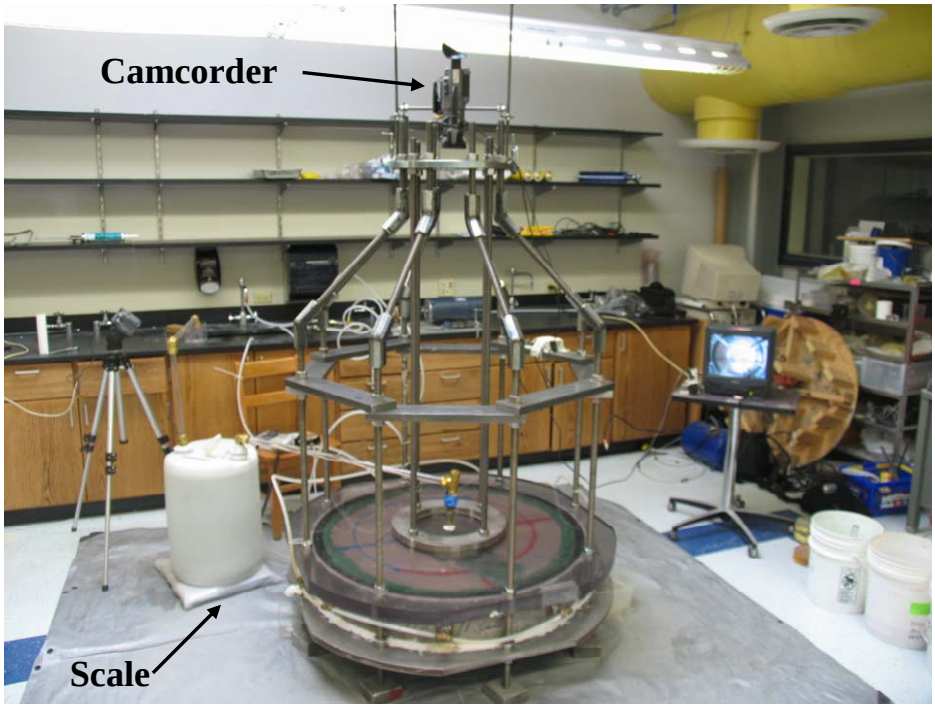

Figure 2.30 Location of scale and camcorder in the experimental setup.

2.5 Experimental Results

We conducted a total of eight experiments, not counting the preliminary experiments (that were required to develop the experimental setup). As mentioned above, we refer to the first experiment as "base case", since other experiments were conducted to verify the reproducibility of the results and to investigate deviations from the base case. In addition, a more simplified setup was used for other experiments. Specifically, we did not use the colored sand layers (rings and radial lines) on the surface of the sand sample (Figure 2.25) to improve the visualization of the surface flow channel (Section 2.4.1). Results from base case are described in Section 2.5.1 and those from other experiments are presented in Sections 2.5.2 and 2.5.3.

2.5.1 Base Case

Figures 2.26 and 2.31 show the surface of the sand sample before and after the base case experiment, respectively. Similar to *Vaziri et al*. [2002; 2003] (Figure 2.7), we observed the cavity and surface channel developed in the sample as a result of sand production. In our setup, however, we were able to directly monitor their evolution during the experiment.

Figure 2.31a shows the surface of the sand layer after the experiment. In Figure 2.31a, the colored rings and the lines located outside of the cavity are intact, which indicates that the movement of the sand particles outside of the cavity and the flow channel is not noticeable. In other words, there was no significant erosion at the upper surface of the sand sample. The shape of the cavity is close to conical and the surface flow channel is connected to the cavity (Figure 2.31b).

(a)

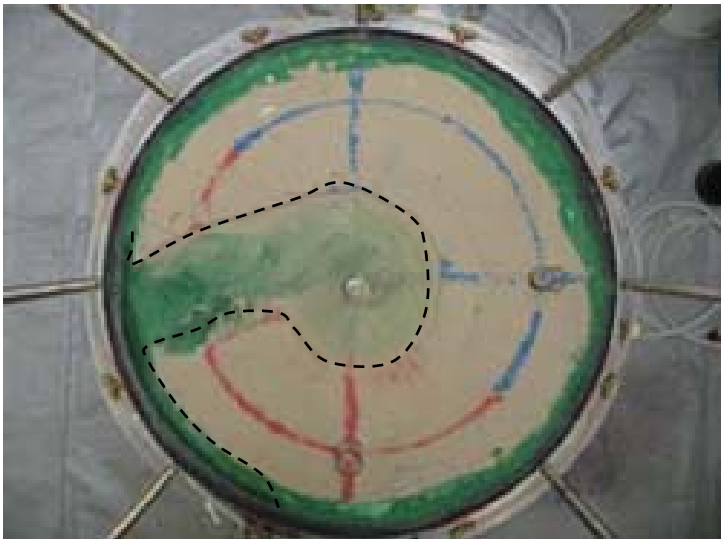

(b)

Figure 2.31 Surface of the sand layer after the base case experiment. (a) Formed cavity and surface flow channel. (b) On the same photograph, the cavity and the flow channel are shown by the dashed line. Diameter of the sand sample is 1 m.

Results of monitoring using a video camera are shown in Figures 2.32 to 2.34. Experiments began at time $t = 0$. Figure 2.32a shows the surface of the sand layer at the moment of the initiation of the surface flow channel ($t \approx 60$ sec), and Figure 2.32b shows the distortion of the inner ring of colored sand. The distortion of the ring indicates that a flow channel starts developing at that point. In Figures 2.32a and 2.32b, there are two rings: the inner and outer rings of dyed sand layers as indicated by two arrows. Comparing Figures 2.32a and 2.32b shows that when the inner ring starts deforming inwards, the outer ring remains intact. This suggests that the surface channel starts developing at the edge of the cavity and then grows towards the outer boundary of the sand layer. At 75 sec, the colored (green) sand particles originally located at the outer boundary start moving into the flow channel (Figure 2.33a). At 2 min 30 sec (Figure 2.33b), the colored (green) sand particles fully fill the flow channel. By 13 min 30 sec (Figure 2.34a), the flow channel is fully developed and maintains stable shape after that. For example, Figure 2.34b shows the surface flow channel at 29 min. Comparing Figures 2.34a and 2.34b shows that there was no change in the size of the flow channel after $t = 13$ min 30 sec.

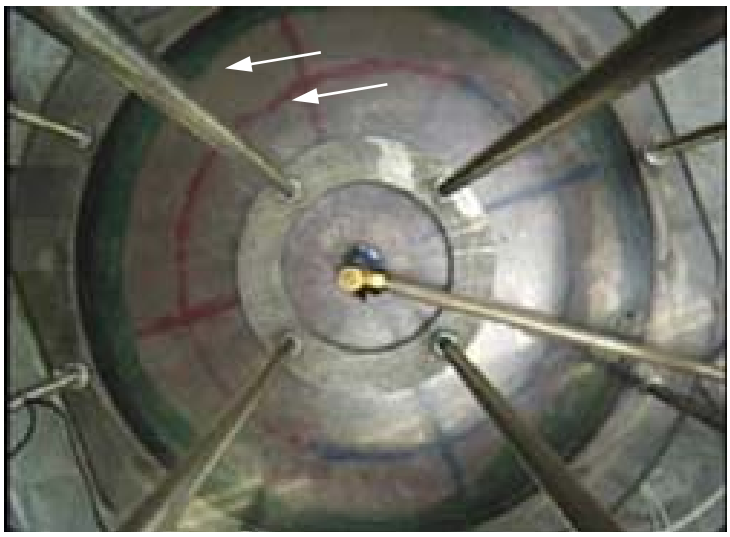

(a)

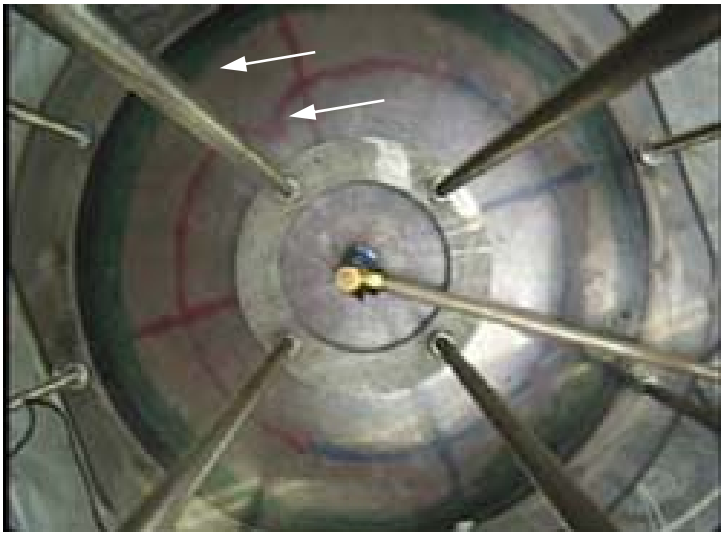

(b)

Figure 2.32 Initiation of the surface flow channel in the base case experiment: (a) 60 sec and (b) 72 sec. The white arrows point at the outer and inner rings of the dyed sand. The inner ring started deforming while outer ring remains intact.

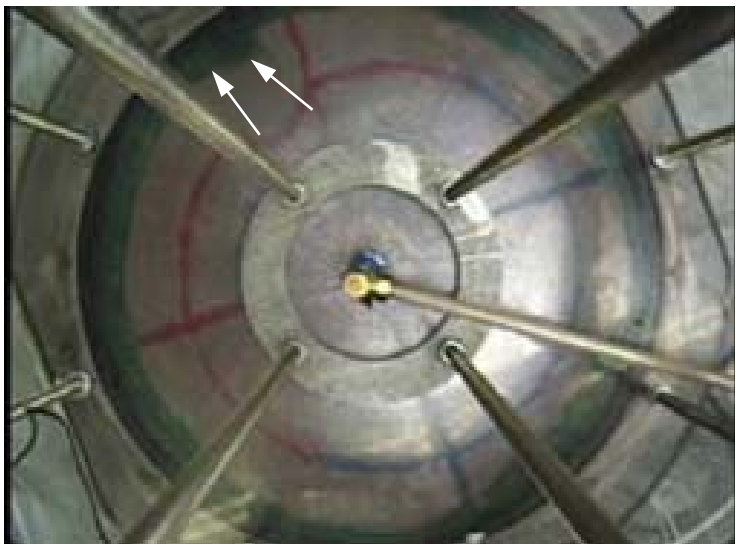

(a)

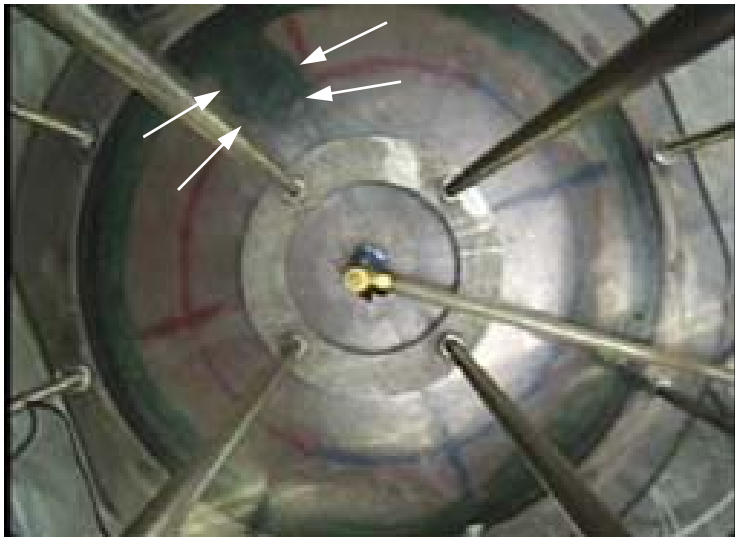

(b)

Figure 2.33 Development of the surface flow channel in the base case experiment: (a) 75 sec and (b) 2 min 30 sec. The arrows point at the influx of dyed (green) sand originally located at the outer edge of the sand sample. This represents the growth of the surface flow channel.

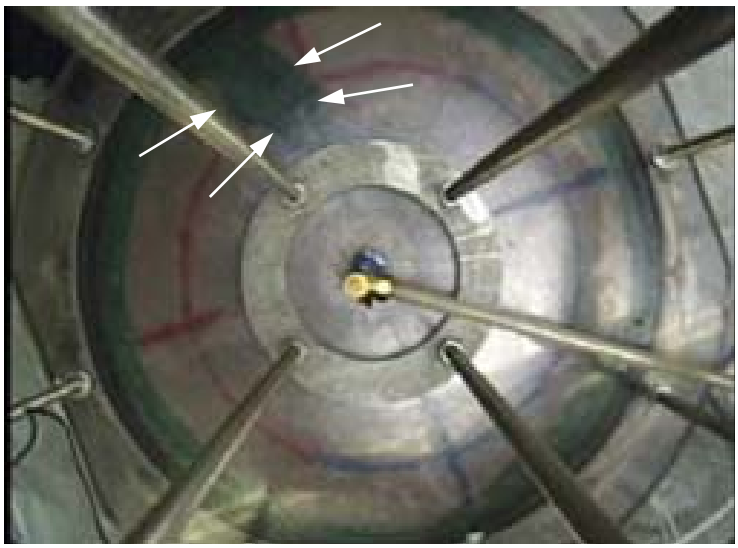

(a)

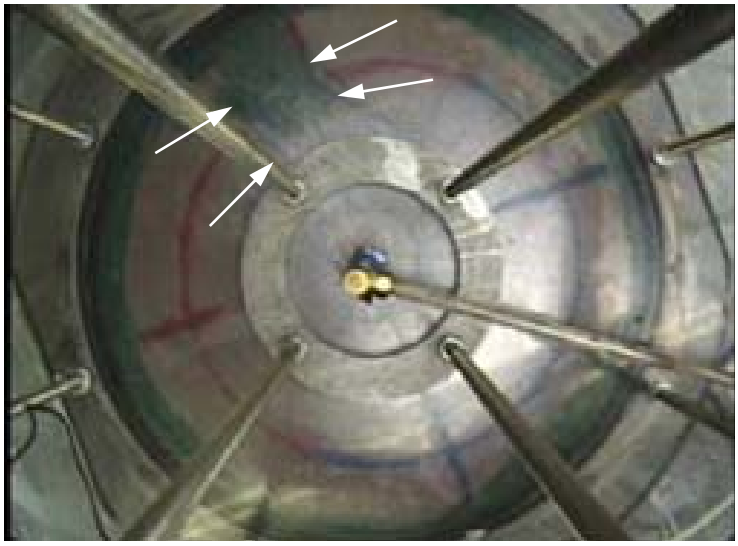

(b)

Figure 2.34 Stabilization of the surface flow channel in base case experiment: (a) 13 min 30 sec and (b) 29 min. The arrows represent the development of the surface flow channel, and the channel shapes at these moments are nearly identical.

The weight of the produced sand and inflowing pressure are shown in Figure 2.35a. Time of the initiation (Figure 2.32a) and the full development (Figure 2.34a) of the flow channel are also marked in Figures 2.35a and 2.36. The full channel development means that there was no further change of the channel size. The production of particles started in ≈1 min after the start of the experiment. At that time, the flow channel started developing (Figure 2.36). The cavity near the sample center developed and stabilized in ≈14 min after the particle production began. The weight of produced particles increased until 13 min after the start of the experiment. The flow channel was fully developed at 13 min 30 sec (Figure 2.34a). It appears that the full channel development and the end of the particle production coincide. Characteristic times recorded in the base case experiment are given in Table 2.8.

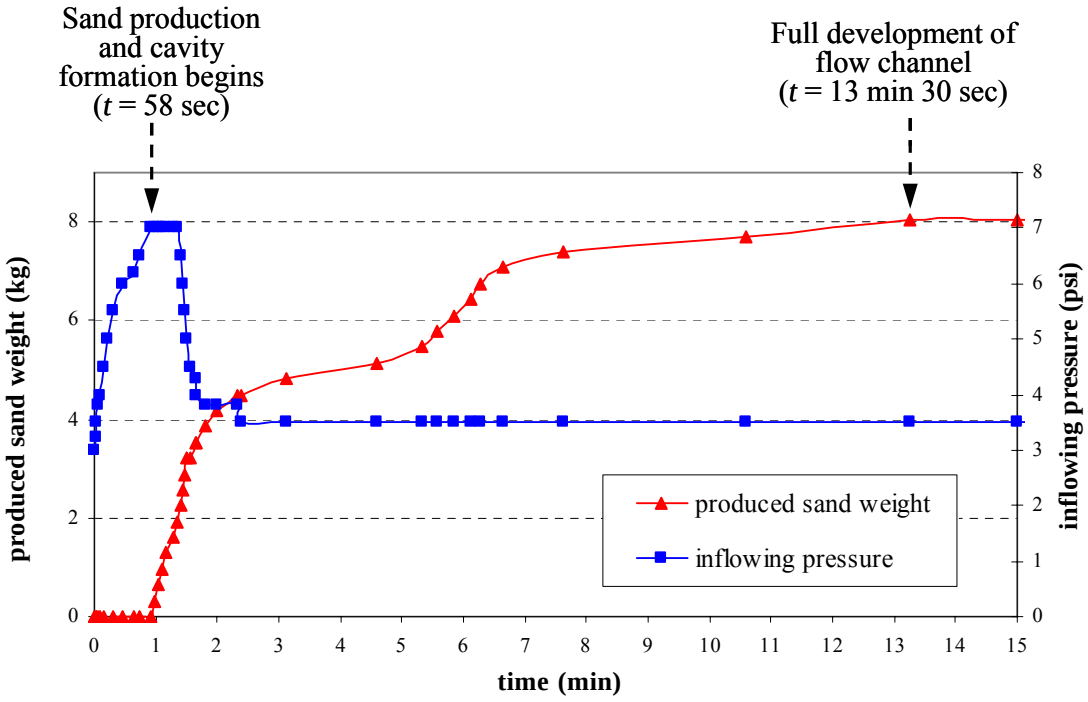

(a)

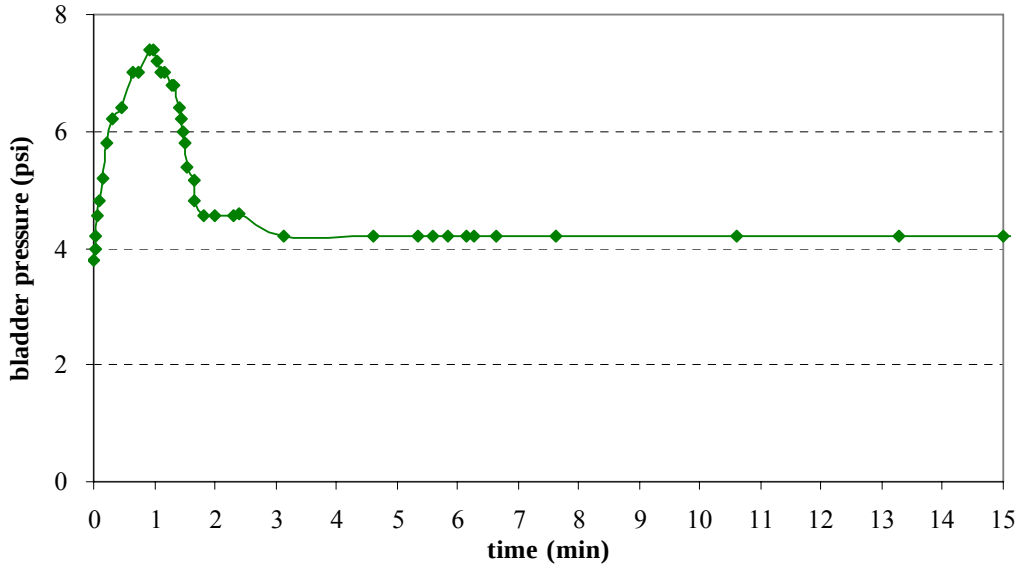

(b)

Figure 2.35 Results of the base case experiment: (a) weight of the produced sand and inflowing pressure and (b) bladder pressure as functions of times. The full development of the flow channel means that there was no further change in its size.

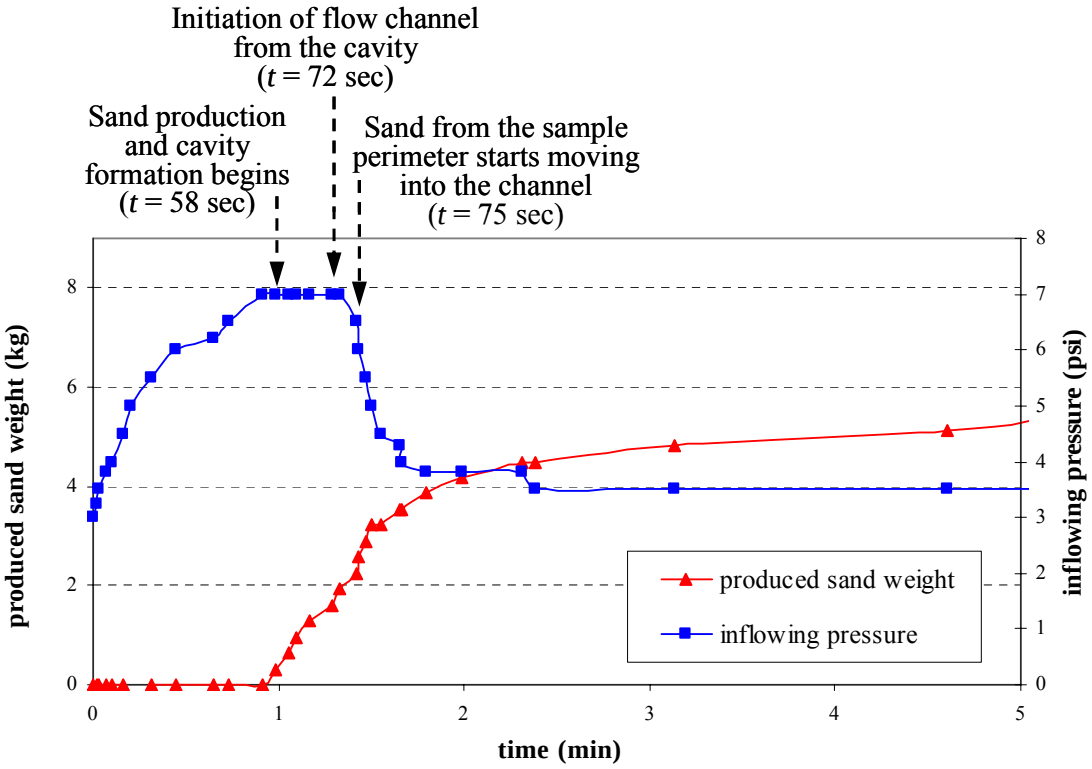

Figure 2.36 Weight of the produced sand and inflowing pressure from the base case experiment. This figure is the repetition of Figure 2.35a showing the results only for the first 5 min.

Table 2.8 Characteristic times recorded in the base case experiment

No.	Event	Time
1	Experiment begins	0
2	Sand production begins	58 sec
3	Cavity near the sample formed and stabilized	72 sec
4	Surface channel initiates at the cavity surface	72 sec
5	Channel reaches sample perimeter	75 sec
6	Sand at the sample perimeter starts inflowing into the surface channel	75 sec
7	Sand filling the channel is removed and sand production stops	13 min 30 sec

It is interesting to note that the bladder pressure history (Figure 2.35b) appears similar to inflowing pressure history (Figure 2.35a). This indicates that the increase or decrease of the inflowing pressure directly affects the pressure in the bladder.

To check the infiltration of particles through porous space and the 'piping' phenomenon [*Baghdikian et al.*, 1989; *Civan*, 2007], we collected cores of the sand layer after the experiment. For this purpose, transparent plastic tubes were inserted into the sand layer (Figure 2.37a). We extracted the core samples (Figure 2.38) by excavating the sand surrounding the tubes. In addition, by excavating the sand layer (Figure 2.37b), we were able to observe the sample cross-sections (Figures 2.39 – 2.46).

Figure 2.38 shows the four cores taken from the sand layer. Careful analysis showed no colored sand particles in the cores except for those located on the upper surface. The side sections of the excavations are shown in Figures 2.39 to 2.46. In Figures 2.39a, 2.40a, 2.41a, 2.42a, 2.43a, 2.44a, 2.45a and 2.46a, the arrows indicate that the two layers of colored sand particles do not distort into the original sand layer. Figures 2.39b, 2.40b, 2.42b, 2.43b, 2.44b, 2.45b, and 2.46b show that there are no colored sand particles in the sand layer in each section. This suggests that there is no infiltration of particles (no piping) through the interior of the sand layer. Likewise, no internal channels ('pipes') or wormholes developed in the sample. Although green colored particles can be observed in Figure 2.41b, these particles from the outer boundary were deposited after the production of the particles stopped. The region near the sample perimeter was probably fluidized during the experiment.

The absence of the particle infiltration and wormholes through the pore space can be explained by particle size distribution. As mentioned in Section 2.3, the particle size distribution of the sand sample used in this work is rather uniform. That is, the dimensions of different particles do not vary considerably, and most particles cannot penetrate into the pores of comparable size.

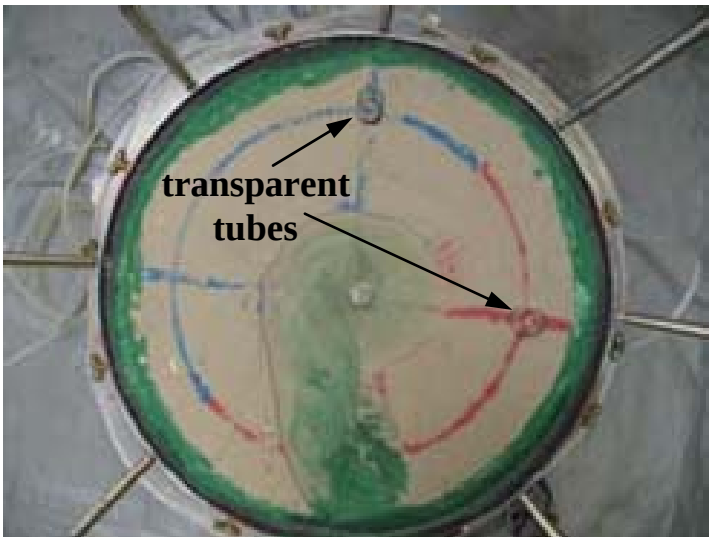

(a)

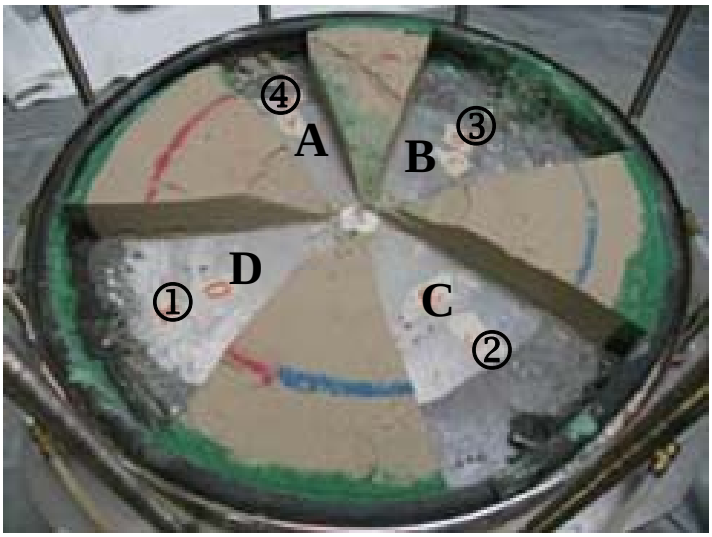

(b)

Figure 2.37 Coring of the sand sample and excavation of the sand layer to check the infiltration of particles after the base case experiment. (a) Transparent plastic tubes are inserted into the sand layer to extract cores and (b) excavation locations in the sand layer. Numbers 1 to 4 represent the location of the cores and letters A to D represent the location of the excavations. All core samples were collected 35 cm from the center of the sand layer and were located outside the cavity.

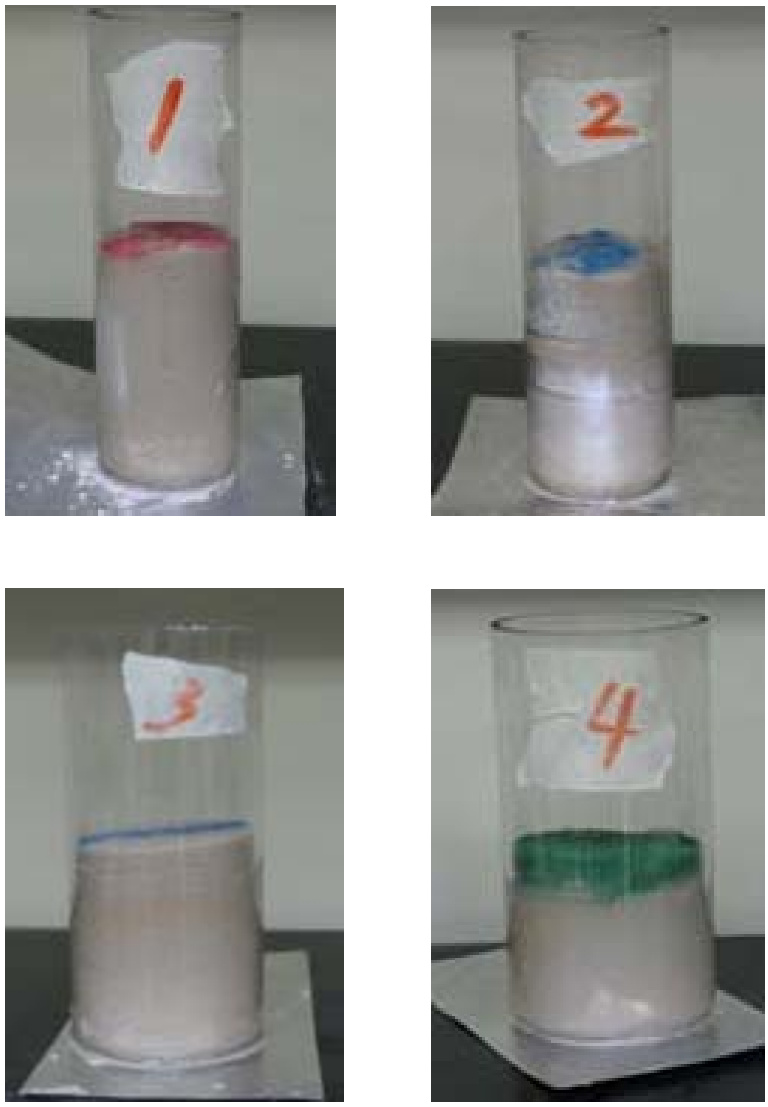

Figure 2.38 Cores taken from the sand layer. No colored sand was found in the interior of any core, which is consistent with an absence of the infiltration of particles from the layer of green particles adjacent to the outer boundary (Figure 2.25b). Numbers represent core locations in Figure 2.37b.

(a)

(b)

Figure 2.39 Excavations of the sand layer after the same experiment. (a) Section A-1 and (note the arrows) (b) the same section magnified. Arrows indicate the interface between the dyed (green) sand layer at the sample outer boundary and the non-dyed sand layer. There is no infiltration of dyed (green) sand particles into the non-dyed sand layer.

(a)

(b)

Figure 2.40 Excavations of the sand layer after the same experiment. (a) Section A-2 (note the arrows) and (b) the same section magnified. Arrows indicate the interface between the dyed (green) sand layer at the sample outer boundary and the non-dyed sand layer. There is no infiltration of dyed (green) sand particles into the non-dyed sand layer.

(a)

(b)

Figure 2.41 Excavations of the sand layer after the same experiment. (a) Section B-1 (note the arrows) and (b) the same section magnified. Arrows indicate the interface between the dyed (green) sand layer at the sample outer boundary and the non-dyed sand layer. There is no infiltration of dyed (green) sand particles into the non-dyed sand layer.

(a)

(b)

Figure 2.42 Excavations of the sand layer after the same experiment. (a) Section B-2 (note the arrows) and (b) the same section magnified. Arrows indicate the interface between the dyed (green) sand layer at the sample outer boundary and the non-dyed sand layer. There is no infiltration of dyed (green) sand particles into the non-dyed sand layer.

(a)

(b)

Figure 2.43 Excavations of the sand layer after the same experiment. (a) Section C-1 (note the arrows) and (b) the same section magnified. Arrows indicate the interface between the dyed (green) sand layer at the sample outer boundary and the non-dyed sand layer. There is no infiltration of dyed (green) sand particles into the non-dyed sand layer.

(a)

(b)

Figure 2.44 Excavations of the sand layer after the same experiment. (a) Section C-2 (note the arrows) and (b) the same section magnified. Arrows indicate the interface between the dyed (green) sand layer at the sample outer boundary and the non-dyed sand layer. There is no infiltration of dyed (green) sand particles into the non-dyed sand layer.

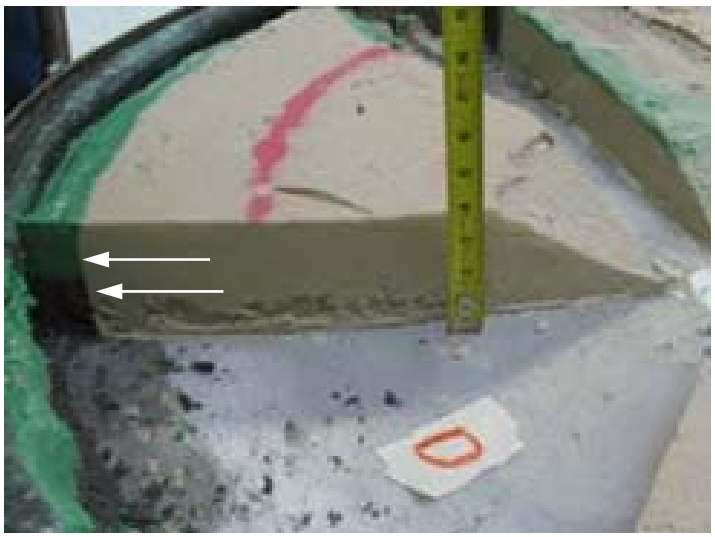

(a)

(b)

Figure 2.45 Excavations of the sand layer after the same experiment. (a) Section D-1 (note the arrows) and (b) the same section magnified. Arrows indicate the interface between the dyed (green) sand layer at the sample outer boundary and the non-dyed sand layer. There is no infiltration of dyed (green) sand particles into the non-dyed sand layer.

(a)

(b)

Figure 2.46 Excavations of the sand layer after the same experiment. (a) Section D-2 (note the arrows), and (b) the same section magnified. Arrows indicate the interface between the dyed (green) sand layer at the sample outer boundary and the non-dyed sand layer. There is no infiltration of dyed (green) sand particles into the non-dyed sand layer.

After completion of the base case experiment, we poured silicone adhesive into the cavity and the flow channel. After the adhesive cured, we measured the volume of the cast (Figure 2.47). Since the initial dry bulk density, ρ_b, of the sand sample is known (ρ_b = 1.76×10^3 kg/m^3), we can calculate the weight, W_c, of the produced sand that originally occupied the space of the cavity and the surface channel as

$$W_c = V_{cast}\rho_b g \tag{2.4}$$

where $V_{cast} = 4.4\times10^{-3}$ m^3 is the cast volume and g is the gravitational acceleration. Thus, the calculated weight of the produced sand is 7.8 kg. In the same experiment, the total amount of the produced sand found in the collection tank was 8.0 kg. Considering the error in measuring the size of the sand layer (which lead to the error in the evaluation of ρ_b), the two values agree reasonably well. Such a small difference (2.5%) also indicates that there was no significant infiltration of particles or piping in the sand layer.

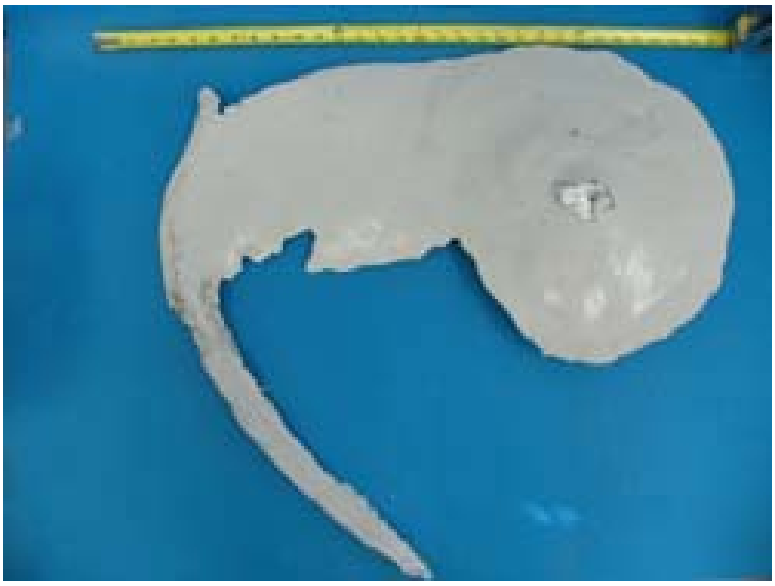

(a)

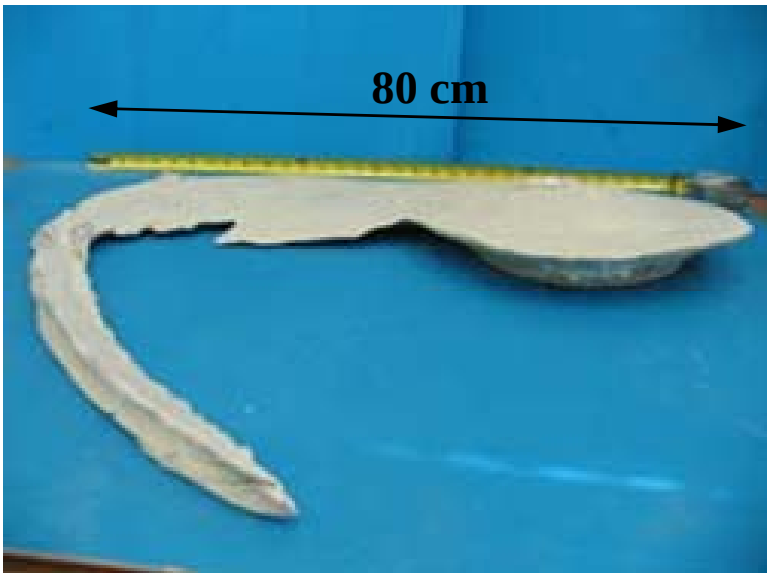

(b)

Figure 2.47 (a) Plan and (b) side views of the cast of the cavity and the flow channel in the base case experiment.

2.5.2 Inflowing Fluid Pressure and Production of Particles

During each experiment, the flow rate of the inflowing fluid (i.e., water) was controlled and maintained constant except for Test 15A. In Test 15A, the flow rate was increased after 6 hours. Flow rates for each experiment (except for the base case shown in Figure 2.35a) are shown in Figures B2.1c to B2.7c (Appendix B2). The bladder pressures are also shown in Figures B2.1c to B2.7c (Appendix B2). Similar to the base case, the bladder pressure change has the same trend as that of the inflowing pressure since the volume of the bladder is approximately constant. The pressure of the inflowing fluid was changing due to the production of sand. The histories of the inflowing fluid pressure from the seven experiments (except for base case shown in Figure 2.35b) are shown in Figures B2.1b to B2.7b in Appendix B2.

Similar to base case, we observe that, after turning on the pump, the inflowing fluid pressure increases rapidly and the production of sand particles starts within 2 min. Immediately after the beginning of the sand production, the fluid pressure reaches its maximum value. The times at which the maximum fluid pressure occurs and the sand production begins are listed in Table 2.9. After reaching its maximum value, the inflowing fluid pressure decreases and stabilizes within 20 min. Similarly, the production of particles continues for approximately 20 min. Thus, it seems that the stabilization of the inflowing fluid pressure and the stoppage of the sand production are related to each other, which is already demonstrated in the base case.

All experiments were performed for more than 6 hours, and, except for Test 15A, there was no noticeable change of the inflowing fluid pressure after 20 min. In Test 15A (Figure B2.3b), the flow rate of the fluid was stabilized within 10 min. Then, there was no further sand production. After 6 hours, the flow rate of the fluid was increased from 5.87 L/min to 9.86 L/min to induce further sand production. With the increase in the flow rate,

the increase in the inflowing fluid pressure triggered sand production again. Production of particles ceases within a minute.

Table 2.9 Times of maximum fluid pressure and beginning of sand production

Test No.	Time when maximum fluid pressure occurs (min:sec)	Time when sand production begins (min:sec)
Base case	1:17	1:00
0A	1:34	1:19
7A	1:44	1:35
15A	1:41	1:21
7B	2:30	1:55
0B	1:32	1:28
15B	1:34	1:24
0C	1:45	1:29

From the results of the experiments, we conclude that the cavity and the flow channel stabilize within certain time under a given fluid flow rate. Then, the production of the sand particles ceases, which can be determined from the monitoring the production of particles through the transparent polycarbonate tubing connecting the drainage of chamber with the sand collection tank (Figure 2.9b). These results agree with those of the series of large-scale centrifuge tests [e.g., *Palmer et al.*, 2000; *Vaziri et al*., 1997; 1998a; 1998b; 2002; 2003]. In their tests, the formation of the surface channel was observed only once, however, and they could not observe the evolution of the cavity and/or surface channel in their experimental setup. Changes in the boundary conditions (e.g., a change in fluid flow rate) may also trigger sand production. In general, the sand layer is stabilized after certain time and sand production ceases.

2.5.3 Development of Cavity and Surface Flow Channel

As a result of the production of the sand particles, similar to base case, we identified the formation of a cavity and a surface channel in every experiment. Photographs of the upper surface of the sand layer after each experiment are shown in

Figures B2.1a, B2.2a, B2.3a, B2.5a, B2.6a, and B2.7a (Appendix B2). They show that in all cases a cavity and a surface channel are formed around the wellbore.

To show that the existence of a surface flow channel is not a byproduct of the experimental setup or procedure, we considered such factors as inhomogeneity of the sand specimen and the fluid flow over the surface of the sand specimen. The inhomogeneity of the sand specimen may lead to a difference in permeability throughout the specimen. The excessive difference of the density in the sand specimen may cause the inadvertent formation of a surface flow channel. In this work, vibration compaction of the sand specimen was used to reduce such an inhomogeneity of the density along the entire specimen for all experiments, including the base case.

If the contact between the sand layer and the polycarbonate sheet is not sufficiently strong, a void can be created. This void can be a conduit to fluid flow (Figure 2.48a). Then, sand particles are removed by the erosion due to the fast fluid flow through the conduit. To prevent this phenomenon, we adopted two strategies for all experiments. First, a ring of rubber foam is placed on top of the wire meshes to prevent fluid flow occurring between the sand and the top of the chamber (Figure 2.17a). Second, the contact surface of the thin polycarbonate sheet with the sand specimen is permanently coated with sand particles (using glue) to increase the friction with the sand specimen (Figure 2.48b). In addition, to check whether there is excessive fluid flow through the boundary, dyed sand particles are placed on the surface of the sand layer (Figure 2.27a). The original location of the dyed sand particles on the upper surface of the sand sample is marked on the upper surface of the polycarbonate plate (Figure 2.27b) for all experiments except for the base case. By comparing the location of the dyed sand particles before and after the experiment, the erosion of the upper surface of sand can be checked. If there is excessive fluid flow, which may lead to severe erosion at the upper surface of sand layer, the marked particles would also be eroded.

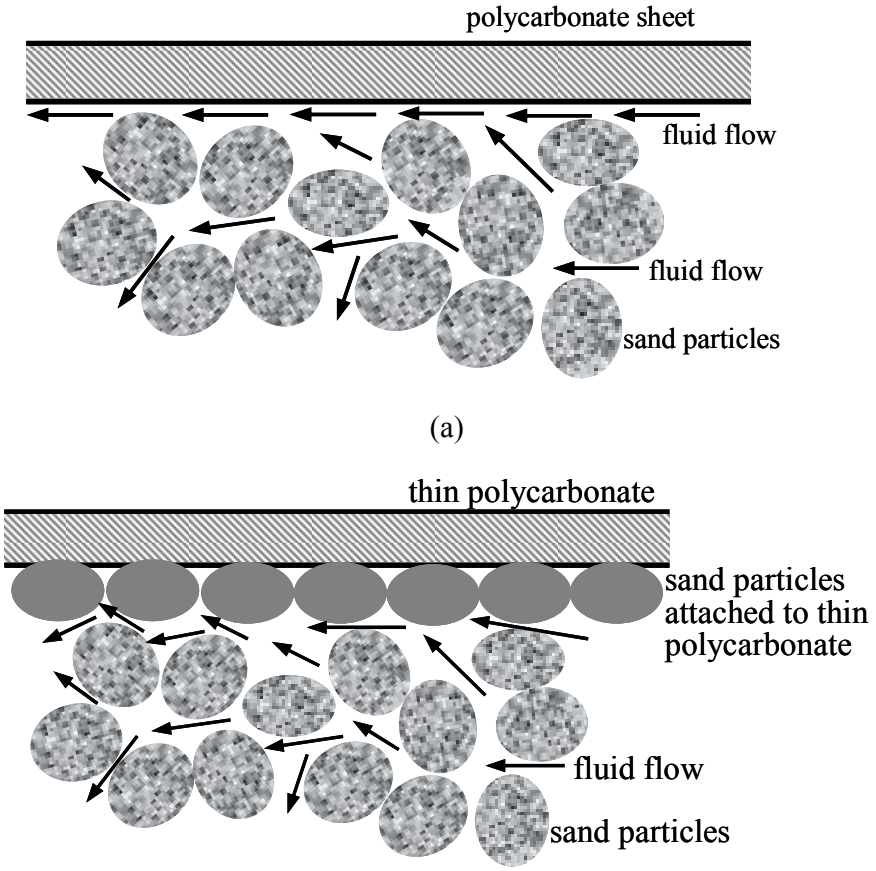

Figure 2.48 Schematic of fluid flow through the boundary between a polycarbonate sheet and a sand layer: (a) without and (b) with sand particles attached to thins polycarbonate plate.

The relative locations of colored particle spots were compared before and after the experiments in an attempt to determine if the sample was undergoing deformation. No differential movement of these spots was observed, and hence no large scale displacement in the sand layer appears to occur. In some runs dispersion of grains from the dyed sand particle spots was observed in the region close to the forming cavity and surface channel. As an example, Figure 2.49 shows photographs of the upper surfaces of sand layer of Test 0C. In Figure 2.49, we can see that the dyed sand particles are dispersed only in the region near the cavity and the surface channel.

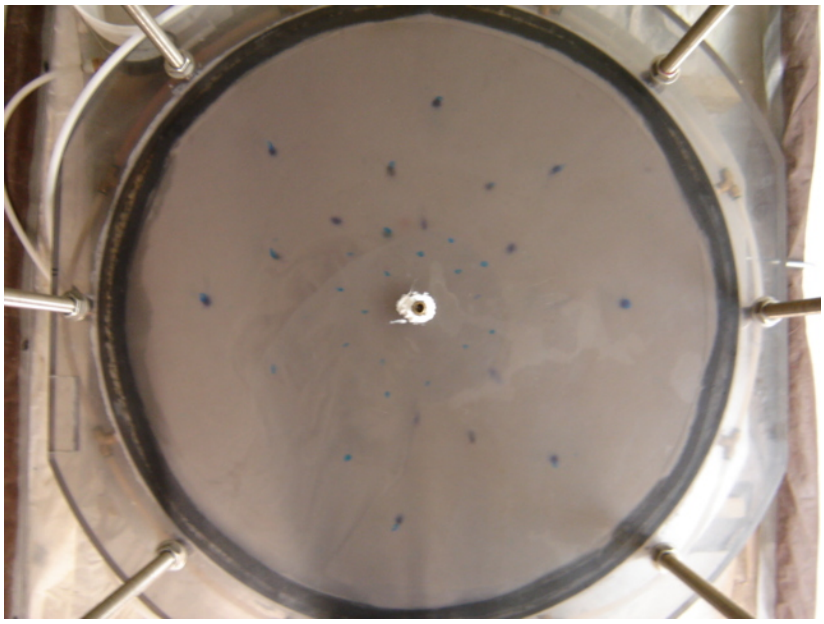

Figure 2.49 Final location of dyed particles of sand in Test 0C.

At the end of the experiment, the direction of the surface channel (i.e., the angle of the axis of the surface channel from a base line) is measured (Figure 2.50). The measured direction of the surface channel for each experiment is given in Table 2.10. The direction of the flow channel from Tests 7A, 7B, and 15B indicates that the direction of the surface channels almost coincides with the inclination of the entire setup. This implies that gravity is one of the important factors that may control the direction of the channel.

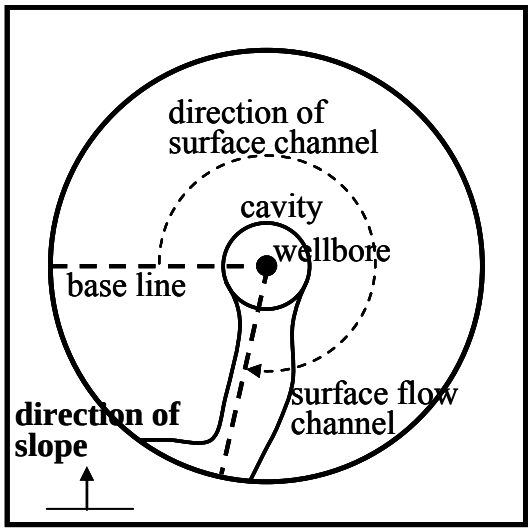

Figure 2.50 Measurement of the direction of surface channel (plan view). Direction of slope indicates the dip direction of the slope: i.e., water flows along the direction of the arrow.

Table 2.10 Direction of surface channel (slope orientation: 270° → 90°)

Test No.	Inclination (°)	Direction of channel (°)
Base case	0	290
0A	0	195
0B	0	10
0C	0	0
7A	7	93
7B	7	90 and 255
15A	15	350°
15B	15	280

In Table 2.10, however, this is not the case in Test 15A, in which no surface channel was formed until the flow rate was increased from 5.87 to 9.46 L/min. After the increase in flow rate, a surface channel was formed. Its direction is 350°, so it does not match the orientation of the inclination of the setup. These results suggest that the direction of a flow channel can also be controlled by other factors (e.g., the inhomogeneity of the sand layer). Also, it seems that the direction of the channel is arbitrary in the base case and Tests 0A, 0B, and 0C, in which the inclination of the experimental setup is zero.

This indicates that our experimental setup does not have a preferential direction for the developed surface flow channel in the case of zero-inclination.

During each experiment, the surface of the sand layer was monitored by a digital camcorder (Figure 2.30). The images captured from the videotapes are not always sufficiently clear to accurately trace the development of a cavity and surface channel. There are several reasons for the low quality of the photographs. First, the resolution of the video camera may not be sufficiently high. Second, the upper polycarbonate plate is not completely transparent. Finally, the thin polycarbonate sheet located between the polycarbonate plate and sand layer is coated with sand particles, which makes it somewhat translucent.

Therefore, digital image processing, using a computer software, Image J [*NIH*, 2004], was used to trace the development of the cavity and the surface channel. A photograph taken at a certain time after the production of sand is compared to the photograph that was taken before the sand production began. By comparing the difference between the two photographs, the development of the cavity and the surface channel can be traced. Two experiments, Tests 0A and 15B, show quite clear results. Results from these two experiments are shown in Appendix C2.

Figure C2.1a shows the upper surface before sand production for Test 0A. Comparison of the time sequence of captured images such as Figures C2.1b, C2.1d and C2.1f with Figure C2.1a enables us to detect the sequential development of the surface flow channel. The yellow arrows in the processed (difference) images in Appendix C2 indicate the location of the surface flow channel during its development. By monitoring the transparent polycarbonate tubing connecting the chamber and the sand collection tank (Figure 2.9) during experiment, we observed the start and the end of the particle production.

In Test 0A, sand production started at 79 sec. A surface flow channel was developing at 3 min (Figure C2.1c). By that time, a cavity had already formed around the

wellbore. At 9 min 20 sec (Figure C2.1e), the surface flow channel fully formed. After this, we could not detect any change in channel size. We observed that the production of sand stopped at 7 min. Based on the observation, our interpretation is that the full development of the surface flow channel is closely related to the end of the sand production. After the surface flow channel is fully developed, the inflowing flow velocity through the channel decreases. This may lead to the stabilization of sand particles on the surface of the cavity and the surface channel. The detection of the surface channel development in Test 0A was done later than that for the base case. The reasons of this later detection are that the resolution of the captured images was not sufficient and we monitored the movement of dots of dyed sand particles placed on top of a sand layer (Figure 2.27) in this test, rather than the rings of dyed sand particles (Figure 2.26) as in the base case. In Test 15B, we observed that sand production started at 84 sec and that the surface flow channel was developing at 2 min 18 sec (Figure C2.2c). Sand production stopped at 15 min, and the surface flow channel was fully formed at 30 min (Figure C2.2g). Similar to Test 0A, the images from Test 15B do not capture the exact moment of the development of the cavity.

A dye injection test was conducted for each experiment to detect the existence of wormholes in the sand layer. Dye was injected into the chamber immediately before turning off the pump. If wormholes existed in the sand layer, fluid would flow preferentially through the wormholes. Dye would remain in the sand layer after the pump is turned off. After each experiment, we tried to find the remaining dye in the sand layer, but without success. Most of dye was found in the cavity and the surface flow channel. Although injection of dye may not be the best method to detect wormholes, their absence is expected because we used sand sample with a rather uniform distribution of particles (Figure 2.20). As a result of using such distribution, not many particles can be produced from the sample interior, and the surface flow channel becomes the main conduit of fluid flow after it develops

In Appendix B2, photographs (except for the base case shown in Figure 2.31) showing the top surface of the sand sample after each experiment are presented. The shapes of the cavities from the "inclined" Tests 7A, 15A, 7B, and 15B are elliptical. In contrast, those from the "horizontal" Tests 0A, 0B, and 0C are circular. In addition, the center of the cavities for Tests 0A, 0B, and 0C is located at their centers. It is located to the upper side of the inclination for Tests 7A, 15A, 7B, and 15B. Among the eight experiments, we created six casts, including one from the base case, by pouring silicone glue into the cavity and the flow channel shown in Figure B2.8 in Appendix B2. Then, to evaluate the effect of the fluid flow on the stability of the cavity, the angle of the cavity slope was also measured. From the cast of the cavity and the surface channel, the angle of the cavity slope (β) was measured (Figure 2.51). The measured angles of the cavity slope for each case are given in Table 2.11. After removing the thin protective polycarbonate sheet, we monitored the surface of the cavity and the flow channel for each experiment. We found that there was no noticeable change in the cavity slope.

By comparing the angle of the cavity slope from the base case and from Tests 0B and 0C (Figure 2.51a) with the repose angle given in Table 2.4, we found that the repose angle is greater than the angle of the cavity slope. The repose angle is primarily controlled by gravity. In contrast, the angle of the cavity slope is mainly affected by both gravity and fluid flow. That the cavity slope has a smaller angle than the repose angle can be attributed to the hydrodynamic force applied to sand particles.

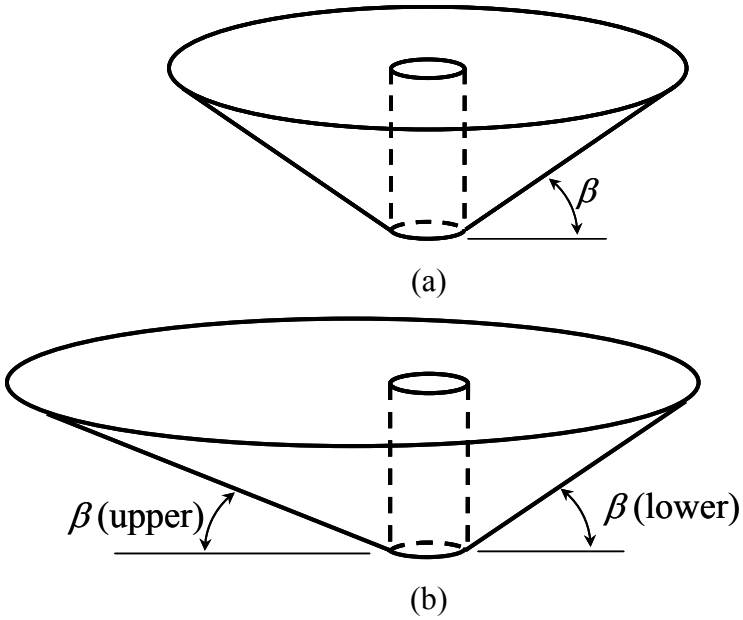

Figure 2.51 Measurement of the angle of cavity slope from a cast of cavity and surface channel: (a) from experiments with zero inclination and (b) from experiments with non-zero inclination, where "upper" and "lower" in the brackets refer to the upper and the lower side of the inclination, respectively.

Table 2.11 Measured angle of the cavity slope

Test No.	Angle of cavity slope, β (°)
Base case	32
0B	33
0C	35
15A	25.1 (upper), 40.2 (lower)
15B	24.4 (upper), 32.7 (lower)
7B	18.4 (upper), 26.6 (lower)

The angles of the cavity slope for Tests 15A, 15B, and 7B (Figure 2.51b) are also shown in Table 2.11, where "upper" and "lower" in the brackets refer to the upper and the lower side of the inclination, respectively. The mean value of the angle of the cavity slope for base case and Tests 0B and 0C is 33.3°. The difference between the mean value and the angles of the cavity slope for Tests 15A, 15B, and 7B is compared in Figure 2.52. The angle of the cavity slope at the lower side is greater than that at the upper side. This indicates that the fluid velocity at the surface of the cavity in the lower side may be less

than in the case of zero inclination. That is, because of the inclination of the experimental setup, the upper side of the cavity slope is more prone to the erosion of the particles [*Serrano et al*., 2005]. The angles of the cavity slope at both the lower and the upper sides increase with respect to the inclination. This suggests that flow velocity in the chamber increases as the inclination of the experimental setup increases. Also, the angles of the cavity slope at the upper side for Tests 15A and 15B are smaller than the mean value. Since the inclination for Test 7B is smaller than those for Tests 15A and 15B, the angle of the cavity slope at the upper side for Test 7B should be greater than those for Tests 15A and 15B. However, this is not the case. The angle of the cavity slope for Test 7B is smaller than those for Tests 15A and 15B. This result shows that other factors (e.g., inhomogeneity of the sand specimen, local fluid pressure distribution) may also affect the development of the cavity, in addition to gravity.

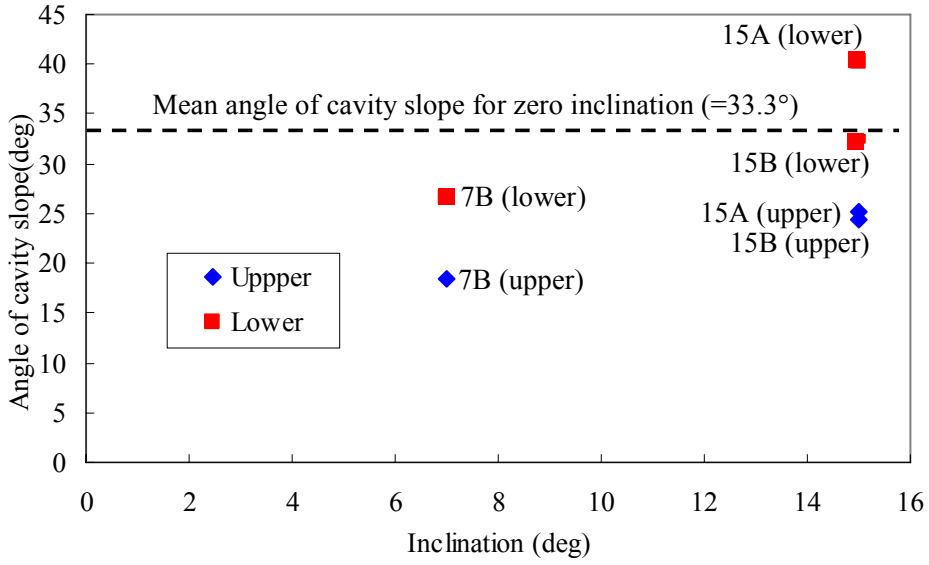

Figure 2.52 Variation of the angle of the cavity slope with respect to the inclination of the experimental setup. The upper and the lower mean the upper and the lower side of the inclination, respectively. Mean angle of cavity slope for zero inclination is a mean value from angles of cavity slope for base case and Tests 0B and 0C.

2.6 Discussion

2.6.1 Cavity Size and Flow Velocity

Our experiments showed that due to the production of sand particles, a cavity and a surface flow channel are formed (Figures 2.31a and 2.53) around the polycarbonate tubing, which represents a simulated wellbore (Figure 2.10). An example of the cast of the cavity and the surface flow channel are shown in Figure 2.47. The cavity has the shape of a frustum. The surface flow channel is connected to the side of the cavity. As reported in Section 2.5, sand production stops within 20 to 30 min after the start of the experiment, indicating that the structure of the cavity and the surface flow channel stabilize when the flow rate is constant.

The mechanism of stabilization can be explained as follows. We first assume that before the surface flow channel appears, the fluid flow pattern is axisymmetric, and that the sand layer is homogeneous. Fluid, injected through the ports around the chamber (Figure 2.9), flows radially toward the tubing located at the center of the sand layer (Figure 2.54a). We also assume the steady-state fluid flow conditions and that fluid flows approximately horizontally through the sand layer (Figure 2.54b). In this case, the fluid velocity, v, at a distance, r, from the center of the sand layer (Figure 2.55) can be expressed as

$$v = \frac{R}{r} v_0 \tag{2.5}$$

where R is the outer radius of the sand layer and v_0 is the fluid velocity at the outer boundary (Figure 2.55). This expression would be accurate in the 1-D model (Figure 2.55b) and reflects the radial character of fluid flow (Figure 2.54).

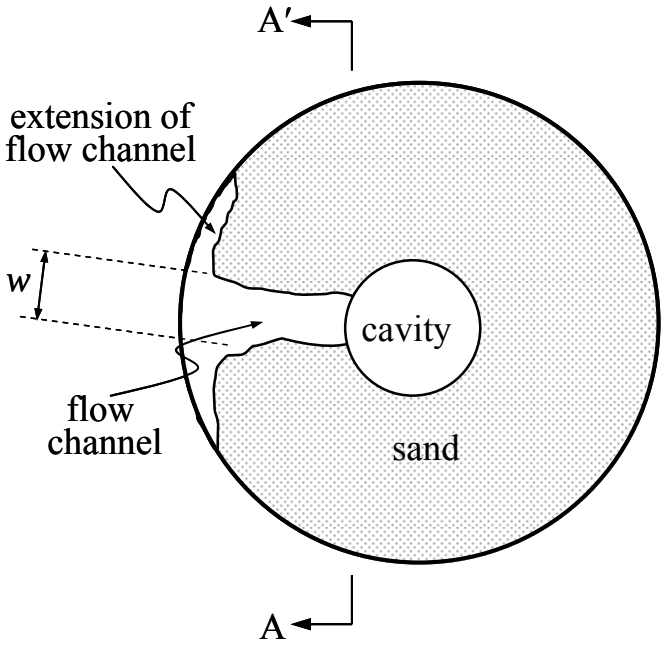

(a)

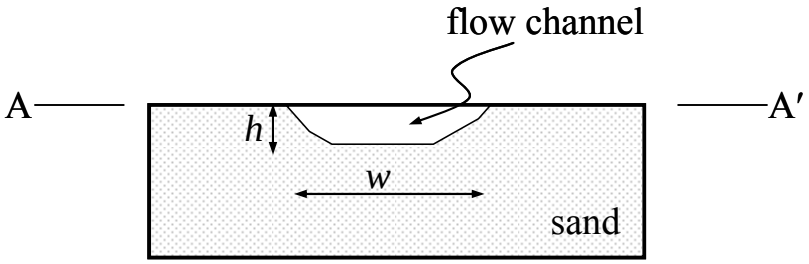

(b)

Figure 2.53 Dimension of the stabilized cavity and the surface flow channel (not to scale). (a) Sample plan view and (b) cross-sectional view of the flow channel. Extension of the flow channel in (a) probably represents a boundary effect. In the conducted experiments, the values of h~1 cm and width of w~10 cm have been consistently observed.

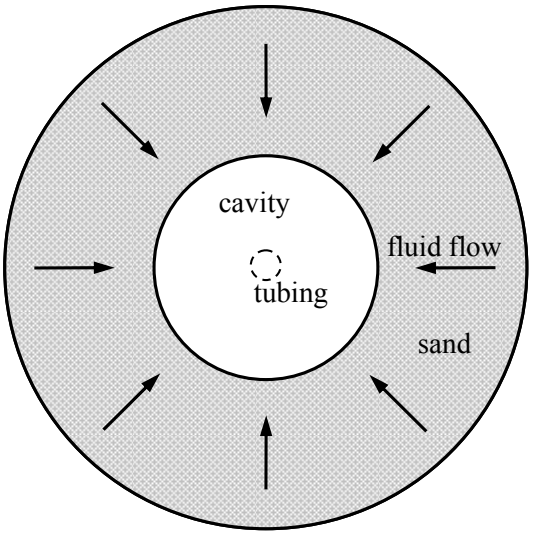

(a)

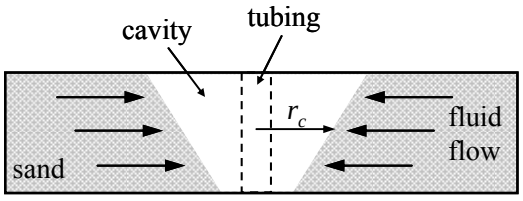

(b)

Figure 2.54 Schematic diagram of the cavity formed during a sand production experiment (not to scale): (a) plan view and (b) vertical cross-section. Prior to the appearance of the surface channel, fluid flows radially towards the center of the sand layer. Here, r_c is the cavity radius in the middle horizontal plane in the sand layer.

According to (2.5), as the size of the cavity grows, the fluid velocity at the surface of the cavity decreases. If the cavity grows beyond a certain size, the fluid velocity decreases below a critical level required to remove a sand particle from the formation. This leads to the stabilization of the cavity. Although (2.5) is only applicable to the radial fluid flow (Figure 2.55), it helps to understand the mechanism of stabilization in more realistic cases such as in conducted sand production experiments (Section 2.5), or, perhaps, in some petroleum reservoirs.

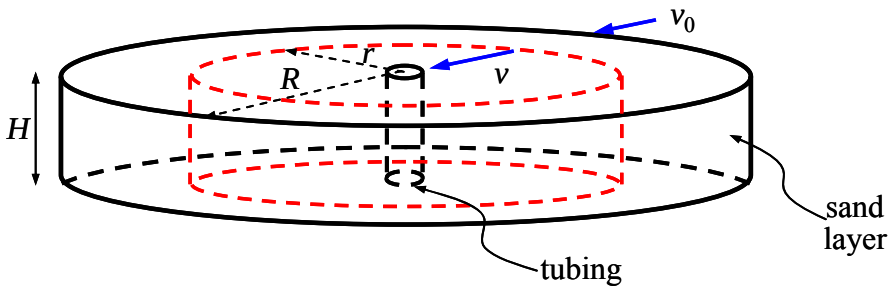

(a)

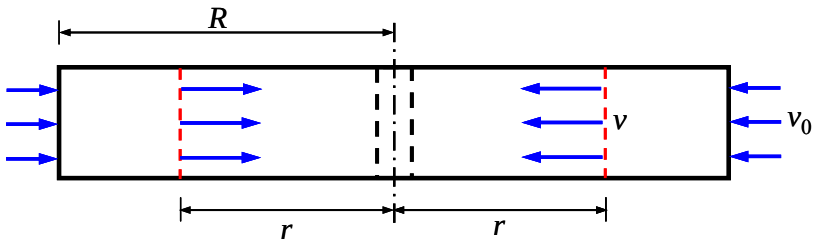

(b)

Figure 2.55 Radial effect of the fluid flow velocity change: (a) 3-D view and (b) a radial cross-section. Sand layer is shown at a moment before a cavity is formed and the drainage at the central hole is assumed uniform along its height. In such a layer with 1-D radial flow, fluid velocity $v(r)$ is defined by (2.5).

The shape of the cavity is affected by two main factors, hydrodynamic forces and inter-particle interaction, which includes friction. Hydrodynamic forces remove particles from the formation while the resistant forces (e.g., the inter-particle friction) act against the hydrodynamic forces. Hydrodynamic forces are determined by the fluid velocity [e.g., *Asgian et al*., 1995; *Charles*, 1997]. For example, particle A, shown in Figure 2.56, is loaded by the gravitational force (weight), by contact forces applied to the particle, and by the hydrodynamic force of the fluid flow. If the latter is greater than the frictional resistance, which is a part of contact forces, then particle A will be removed from the formation.

Based on this idea, consider the mechanism of sand production by cavity erosion (Figure 1.4b). The corresponding scenario is shown in Figure 1.5, where the particle is considered located on the cavity wall (Figure 2.57) before it is removed by the fluid flow towards the place of discharge (e.g., perforation). If the flow velocity is below a critical level, the particle is held in place by the friction on the contacts with other particles.

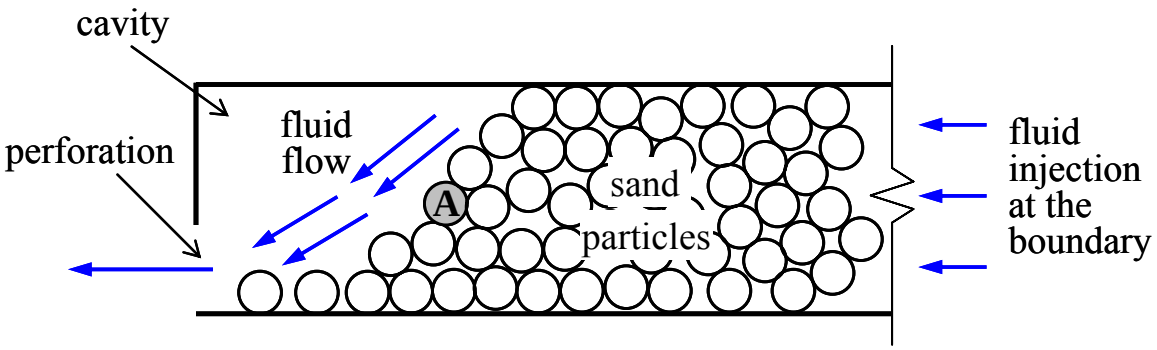

(a)

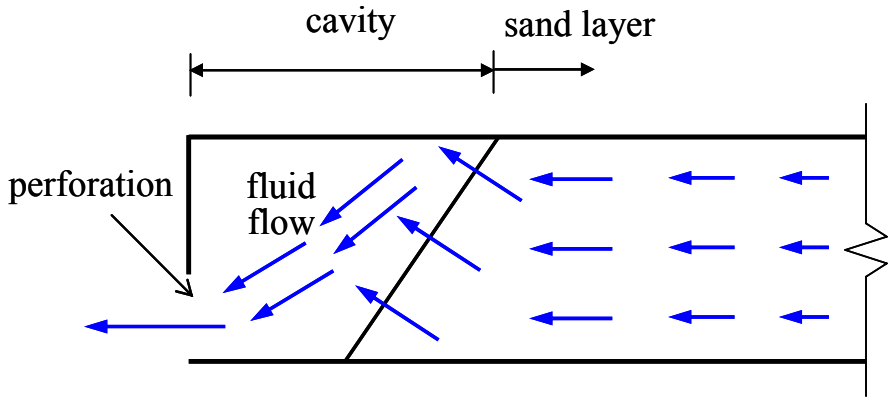

(b)

Figure 2.56 Cross-sectional view of the sand layer before the formation of the surface flow channel (not to scale): (a) the sand particle A (shaded) located at the surface of the cavity and (b) schematics of fluid flow velocities within the sand layer and the cavity. Flow velocity decreases away from the cavity due to the radial character of the fluid flow (e.g., eq. (2.5)).

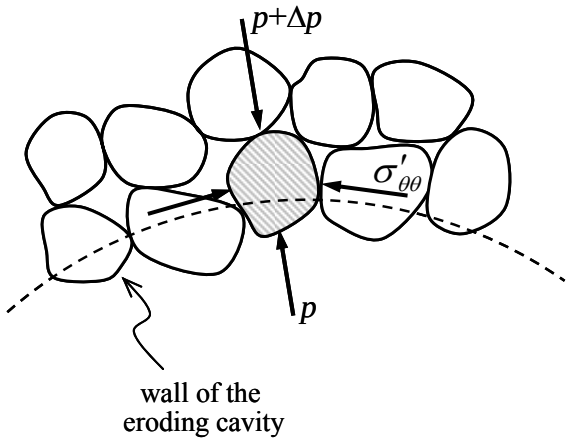

Figure 2.57 Particles located on the wall of the eroding cavity. Pressure change and tangential stress are shown schematically at the particle level. This approach assumes that forces at the particle scale can be determined from the macroscopic considerations including Darcy's law and the concept of stress.

In Figure 2.57, $\sigma'_{\theta\theta}$ is a characteristic effective stress in a cross-section to the cavity surface. It is often assumed [e.g., *Charlez*, 1997] that forces acting at the particle scale can be estimated based on macroscopic concepts such as effective stresses, Mohr-Coulomb friction, or Darcy flow. Accordingly, the friction force holding the particle in place is of the order of $\sigma'_{\theta\theta}d^2$, where d is the characteristic particle diameter. The hydrodynamic force, removing the particle, scales with $\Delta p d^2 \sim |grad(p)|d^3$, where Δp is the pressure change within the mono-particle layer adjacent to the cavity wall (Figure 2.57). From Darcy's law, $|grad(p)| \sim \mu v / k$, where μ is the dynamic viscosity of the fluid and k is the formation permeability. Therefore, $\Delta p d^2 \sim \mu v d^3 / k$, and the condition $\Delta p d^2 \approx \sigma'_{\theta\theta} d^2 \tan\psi$ of removing the particle results in the estimate of the critical flow velocity

$$v_c = \frac{k\sigma'_{\theta\theta}\tan\psi}{\mu d} \tag{2.6}$$

where $\tan\psi$ is the friction coefficient and ψ is the inter-particle friction angle. Note that v_c in (2.6) is the Darcy's velocity and the actual fluid velocity is faster.

Permeability can be estimated using the Kozeny-Carman equation [e.g., equation (5.10.18) in *Bear*, 1972]

$$k = \frac{d^2}{180}\frac{\phi^3}{(1-\phi)^2} \tag{2.7}$$

where ϕ is the porosity of the sand layer. Assuming that the dry bulk density of the sand sample ρ_b = 1.76 g/cm^3 (equal to that of the base case in Table 2.7), we calculate the bulk porosity of the dry sand sample from [e.g., *Das*, 1994]

$$\rho_b = (1-\phi)\rho_s \tag{2.8}$$

where ρ_s = 2.65 g/cm^3 is the density of sand particles (Table 2.2). From (2.8), the porosity of the sand layer is $\phi \approx 0.34$. In our experimental setup (Section 2.3), the mean diameter of the sand particles is d = 110 μm [*US Silica*, 2005] (Figure 2.19). Then, (2.7) results in the permeability of the sand layer of $k = 6.1\times10^{-12}$ m^2, which is in reasonable agreement with the value of $k \sim 10^{-12}$ m^2 measured by *Hurt* [2011] for the same material in similar conditions.

In our setup, the effective tangential stress, $\sigma'_{\theta\theta}$, around the wellbore is of the same order as the bladder pressure of ≈34.5 kPa (Section 2.2) or greater (due to the stress concentration). For the fiction coefficient, we use the order of magnitude value of $\tan\psi \approx 1$ [e.g., *Frye and Marone*, 2002]. The dynamic viscosity of fluid (water) is μ = 1 cP (Table 2.5). Then, the critical fluid velocity, calculated based on (2.6), is 1.8 m/sec.

Therefore, the critical fluid velocity, required to remove a particle and characteristic for our experimental setup, is $v_c \sim 1$ m/sec. This is three orders of magnitudes greater than the velocities (~0.1 cm/sec) observed in our experiments (Section 2.6.2). The

much higher value of the critical velocity (~1 m/sec) indicates that the hydrodynamic force, generated by the observed flow (~0.1 cm/sec), is not sufficient to remove the particles, even from a formation with such a low confining stress as was in our experiment. Thus, expression (2.6) highly overestimates the critical fluid velocity needed to remove the particles.

In the above consideration, the critical flow velocity is unrealistically high, because the hydrodynamic force is overcoming relatively high friction resistance from the neighboring particles in the stress field of $\sigma'_{\theta\theta}$. A slightly different scaling consideration based on the Stoke's experiment [e.g., *Janna*, 1993] for the hydrodynamic force is presented in Section 3.2, but conclusions are the same. Correction for the turbulent flow regime does not reduce the magnitude of the critical velocity and at the level of observed velocities, the flow regime is probably laminar (Section 3.2). Similar to *Charlez* [1997], we conclude that hydrodynamic force is unlikely to be the main mechanism of sand production even in reservoirs with low initial cementation (cohesion). The particles first need to be separated from the rock, before the fluid flow (hydrodynamic force) can carry it away.

In our experiments with fully saturated samples, the cohesion between the sand particles is practically absent. Low values of the observed critical velocities (~0.1 cm/sec) can be explained by the location of a particle, which is being removed from the slope of repose formed by sand particles on the cavity boundary. In this case, the particle is only in contact with a few neighboring particles, and $\sigma'_{\theta\theta}$ in (2.6) should be replaced by the (much smaller) gravitational load $\sim mg/d^2$, where $m \sim \rho_s d^3$. Then, the friction force acting on particle A in Figure 2.56a is relatively small and

$$v_c = \frac{Nk\rho_s g \tan\psi}{\mu} \tag{2.9}$$

where $N \sim 1-10$ is the number of contacting particles. For the values of parameters discussed above, we obtain that $v_c \sim 0.01-0.1$ cm/sec.

2.6.2 Critical Flow Velocity on the Cavity Surface

We further use our experimental results to estimate the critical fluid flow velocity, v_c, required to remove a particle from the sand layer. In our experiments, two types of structures were created in response to production of particles: a cavity and a surface flow channel (Figures 2.31 and 2.53). Since we measured their dimensions, we can now use the measurements to estimate v_c. That is, we estimate the critical velocity from the radius of the cavity and the cross-sectional area of the flow channel.

Consider the cavity slope shown in Figure 2.56a. At this stage of the experiment, the surface flow channel is not yet formed, and we assume that the fluid flow within the sand layer is laminar and approximately horizontal away from the cavity. Although the flow direction is normal to the cavity surface (Figure 2.56b), to estimate an order of magnitude of fluid velocity near the cavity slope, we still use the 1-D expression (2.5).

The direction of fluid flow in Figure 2.56b can be validated by the results of numerical analysis done by *Vaziri et al*. [2002], which are shown in Figure 2.58. To simulate their physical experiments (discussed in Section 2.1), they used a 2-D finite difference code, MODFLOW, and modeled both cases without (Figure 2.58a) and with the formed cavity (Figure 2.58b). They used boundary conditions similar to their physical model. That is, *Vaziri et al*. [2002] applied constant fluid pressure at the right end of the boundary (Figure 2.58a) while four openings were placed at the left end to simulate drainage. They found that the total flow rate (387 mm^3/sec) in the case with a cavity (Figure 2.58b) was 3.6 times greater than that (107.5 mm^3/sec) in the case without the cavity (Figure 2.58a). Also, fluid velocity inside the cavity is appreciably greater than in the sand layer (Figure 2.58b). Near the cavity slope, however, the largest magnitude of the fluid velocity (Figure 2.58b) is not too different from the 1-D case (Figure 2.58a). Hence,

the 1-D expression (2.5) appears sufficiently accurate and can be used for order-of-magnitude estimates.

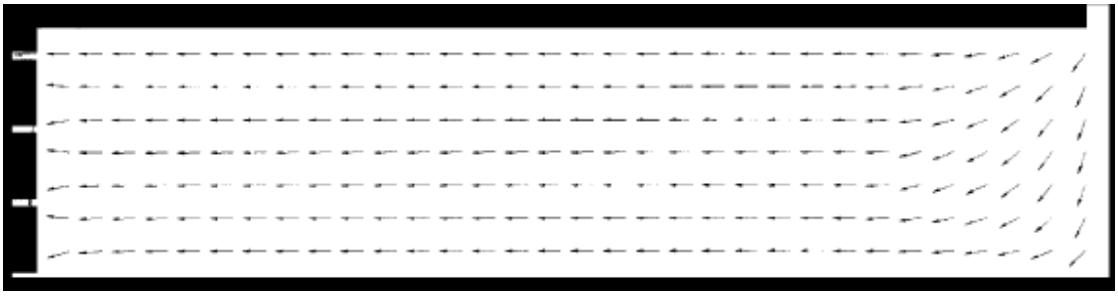

(a)

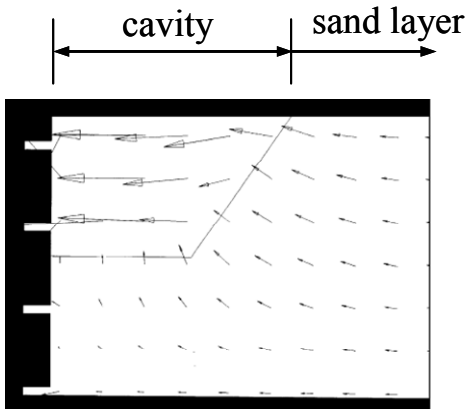

(b)

Figure 2.58 Fluid flow vectors around perforations simulating centrifuge tests (side view) [*Vaziri et al*., 2002]: (a) a case without a cavity and (b) a case with a cavity. Only the area in the cavity vicinity is shown. The fluid flow vectors on the boundary of the cavity are approximately perpendicular to its surface.

Therefore, to estimate the average critical velocity, we evaluate the flow velocity in the middle of the slope (i.e., near particle A in Figure 2.56a). We rewrite (2.5) as

$$v_c = \frac{Q}{2\pi H r_c} \tag{2.10}$$

where r_c is the cavity radius in the middle horizontal plane in the sand layer (Figure 2.54b), Q is the flow rate, and H is the height of the sand layer. In the base case (Section 2.5.1), Q = 4.9 L/min, H = 7 cm, and r_c = 11 cm. Then, (2.10) results in v_c = 0.17 cm/sec.

In the same manner, we calculate the critical velocity for Tests 0B and 0C (in which we obtained the casts of the cavity; Figure B2.8), and find v_c = 0.19 cm/sec and v_c = 0.22 cm/sec, respectively. Hence, in our experiments, the critical flow velocity was of the order of 0.1 cm/sec, which is in general agreement with the range of ~0.01–0.1 cm/sec obtained from (2.9). Given the uncertainty in the evaluation of the permeability k from (2.7) and the velocity changes along the cavity surface, such an agreement appears satisfactory. It indicates that the level of critical velocity on the surface of stable cavity is ~0.01–0.1 cm/sec, at least, in the conditions of our experiments.

2.6.3 Surface Flow Channel

Consider the stabilized cavity and assume, for simplicity, that it has a circular (conical) shape (Figure 2.54). Suppose that somewhere on the cavity surface, the fluid velocity is slightly higher than the critical velocity due to the heterogeneity of the sand sample. This means that the cavity erosion would still continue locally at this place. Based on the discussed modeling results of *Vaziri et al*. [2003] (Figure 2.58) as well as on our numerical results reported in Chapter 3 (Figure 2.59), we expect the highest velocities to be at the upper part of the slope. Therefore, the deviation of the cavity shape from a stable condition is also expected somewhere at the upper part of the slope, which indicates the beginning of the surface channel formation.

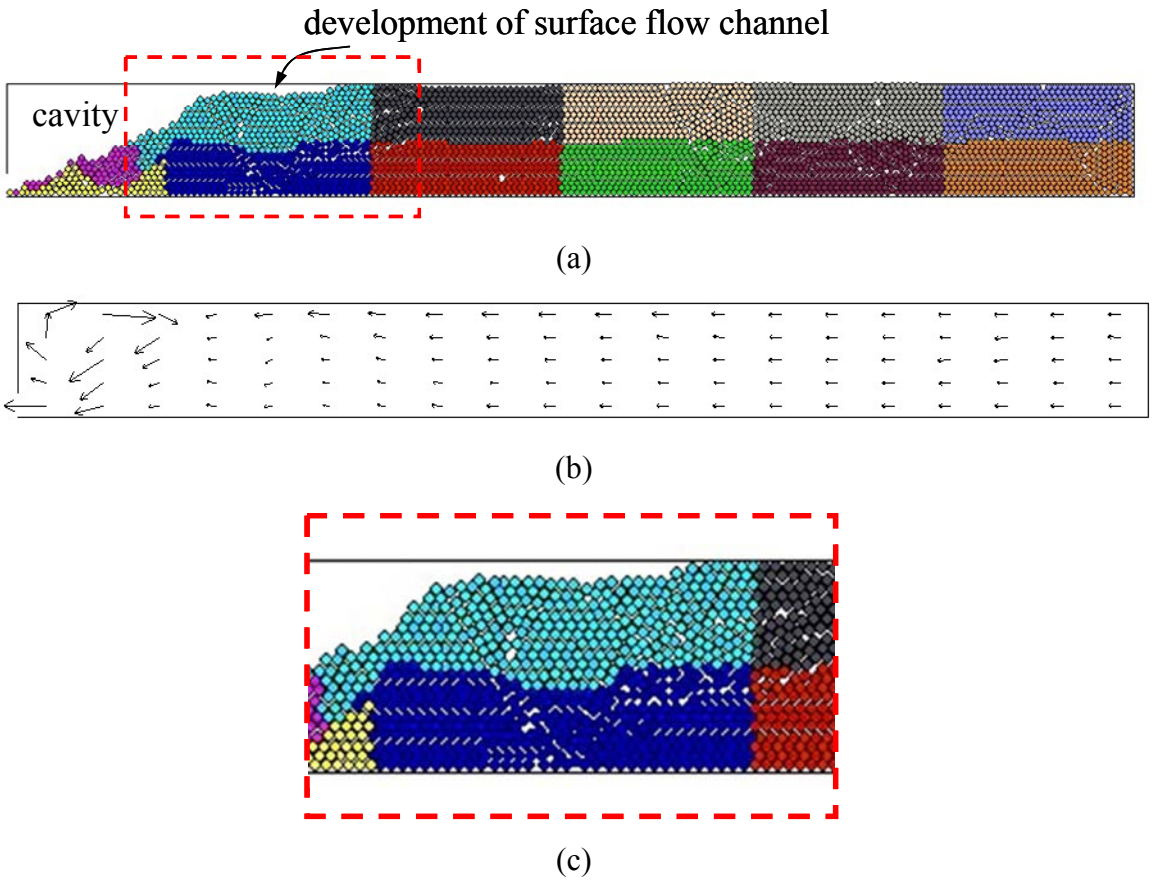

Figure 2.59 Numerical simulation with *PFC*^{2D} [*Itasca*, 2002]: (a) production of particles around a well, (b) distribution of fluid flow velocity (maximum fluid velocity is 0.01 m/sec), and (c) magnified view of the region marked with red dots in (a). These results will be explained in detail in Section 3.5.

Our numerical results (Section 3.5) also indicate that the mechanism of channel formation could be attributed to subsidence due to lateral extension of the formation. In Figure 2.59, regions in a dashed block (particularly, the blue region) spread laterally, which results in the decrease of their vertical dimension. Although this is a 2-D simulation, a similar effect may contribute to the mechanism of channel initiation in 3-D. The effect can be substantiated by production of particles from the toe of the slope and possibly from the surface at the cavity and the channel.

When the surface flow channel starts forming (Figure 2.60a), it becomes the main conduit for fluid flow, which concentrates in the channel rather than in the sand layer (Figures 2.59 and 2.61). At this stage, the radial effect of reducing velocity (e.g., eq. (2.5)) ceases, and erosion still occurs at the channel front (Figure 2.60). In other words, the geometry of the cavity surface is unstable and bifurcates in the form of the surface channel when the cavity itself stops developing due to the radial decrease of the flow velocities.

Observations (Figures 2.32-2.34 and Appendix C2) suggest that after the surface channel initiates, it continued propagating until reaching the outer boundary of the sample. At this propagation stage, the channel is filled with "moving sand" or sand slurry, so that the channel propagation can be traced by the motion of the boundary between the intact and fluidized sand. The fluidization is probably occurring at the propagation front, which leaves behind sand slurry of reduced sand concentration. For the slurry to be movable, its concentration cannot be more than ~60% [e.g., *Campbell and Forgacs*, 1990; *Coussot*, 1995; *Senapati et al*., 2009]. The slurry is removed at the end of the channel, where it intersects the cavity (Figure 2.60), by hydrodynamic force. Because the channel width does not significantly change during its propagation (Figures 2.31a and B2.1a–B2.7a), the velocity at the channel front does not decrease and it continues propagation until reaching the outer boundary of the sample.

Numerical simulations (Chapter 3 and Figure 2.59) suggest that in the case of a channel, which is not filled with particles, the direction of fluid flow through the channel is mostly parallel to its surface and only a small amount of fluid enters the channel through its bottom side (Figure 2.61b). Even though this amount may be larger for a channel filled with sand slurry, this explains why after the channel starts developing, it propagates continuously to the remote perimeter of the sand sample when the injection rate, Q, is constant. The channel development would have stopped had we decreased Q sufficiently. Fluid still would flow within the sand layer, but the flow rate would be smaller than in the forming (propagating) flow channel.

Assuming that fluid flows mainly through the cavity and the flow channel (filled with slurry or pure fluid), we estimate the flow velocity on the channel front by measuring the channel cross-sectional area (Figure 2.53).

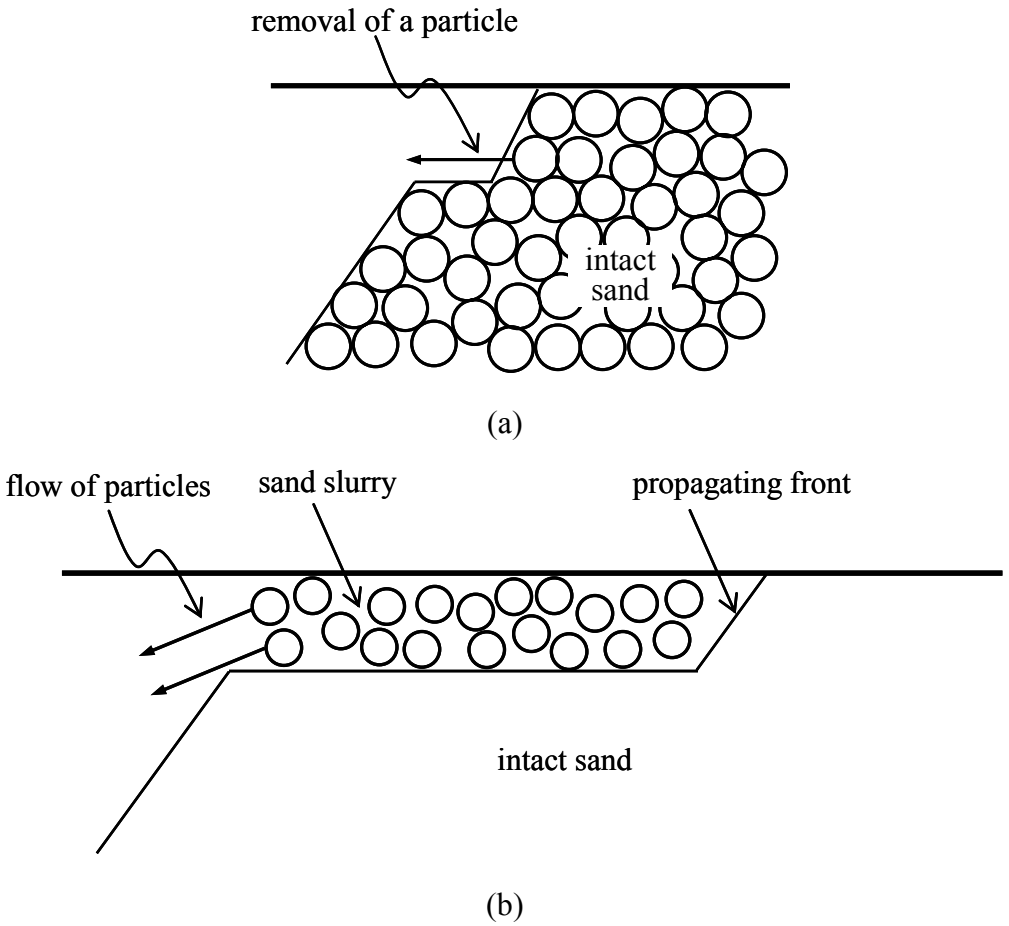

Figure 2.60 Schematics of (a) the initiation and (b) the propagation of the flow channel.

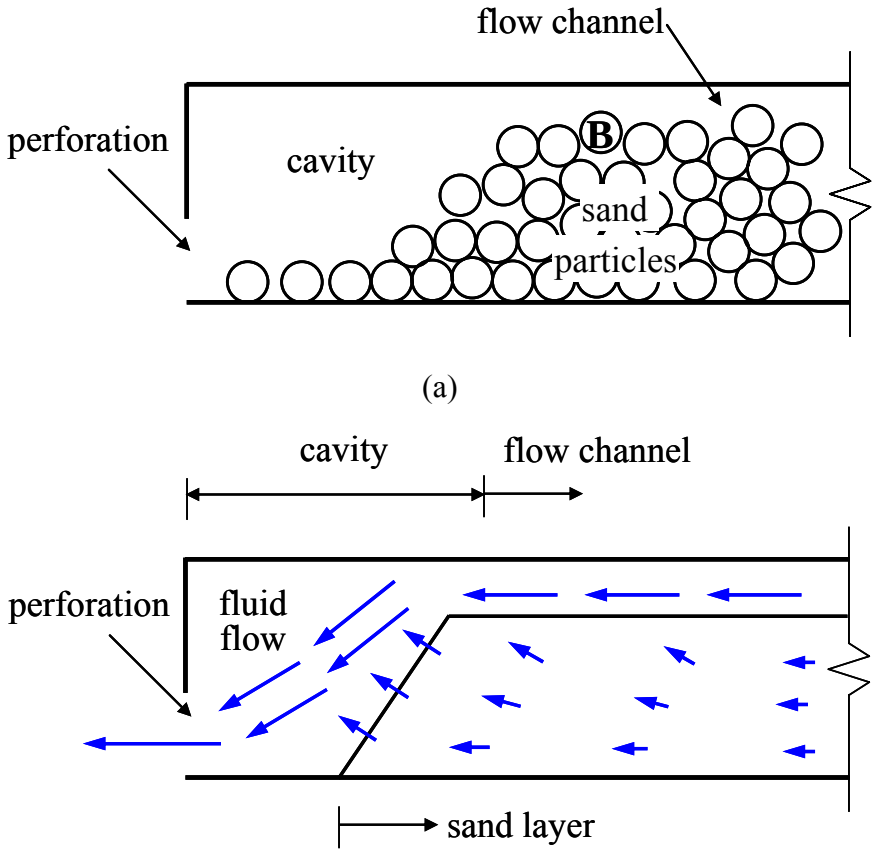

Figure 2.61 Cavity, surface flow channel, and fluid flow in the erosion case (side view, not to scale). (a) Particle B at the surface of the flow channel. (b) Fluid flow velocities within the sand layer, the cavity, and the flow channel (cartoon summarizing numerical results shown in Figures 2.58 and 2.59). Although fluid flows within the sand layer, the flow rate within the sand is much smaller than in the cavity and the flow channel. Shown arrows are not to scale.

The cross-section of the channel is shown in Figure 2.53. For the base case (Section 2.5.1), we measured $w \approx 20$ cm and $h \approx 1$ cm, where w and h are the characteristic channel width and height, respectively. Hence, the flow rate in the channel

$$v \sim \frac{Q}{wh} \tag{2.11}$$

With $Q = 4.9$ L/min (Section 2.4.2), the calculated flow rate is $v \sim 4.1$ cm/sec. In the same manner, we also calculated the channel flow velocity for all the experiments. The obtained estimates are shown in Table 2.12 and indicate that the flow velocity in the surface channel (Table 2.12) may be one to two orders of magnitude greater than before the channel formation (~0.01–0.1 cm/sec); such a difference is due to the difference in areas of $2\pi Hr_c$ (effective area of the cavity surface at $r = r_c$) and wh (the cross-sectional area of the channel) in our estimates.

It is worth noting that while expression (2.11) gives an upper estimate (because not all the fluid flows in the channel), a higher velocity at the propagation stage is, in fact, expected because at this stage, the channel is filled with the fluidized sand.

Table 2.12 Channel flow velocity estimated based on (2.11) for conducted experiments

Test No.	Width (cm)	Height (cm)	Critical flow velocity (cm/sec)
Base case	20	1	4.1
0B	15	1.5	3.6
0C	16	1	5.0
7A	20	1.2	3.4
7B	15	1.5	3.6
15A	20	1.8	4.6
15B	13	1.5	4.2

Taking into account that at this stage (Figure 2.60), the dense sand slurry transports particles through the narrow channel ($h/w \sim 10^{-1}$), the fluid velocity cannot be too low since otherwise the particles would plug the channel [e.g., *Pearson and Zazovsky*, 1997].

2.6.4 Conceptual Model

On the basis of the results of our experiments, we suggest the following conceptual model (Figure 2.62). Our laboratory observations suggest that sand production occurred in main three stages: (I) cavity formation; (II) channel initiation from the stabilized cavity; (III) channel propagation.

First, the particle production results in a cavity that forms around the borehole (stage I). As the cavity grows till it reaches the maximum size, which corresponds to the critical flow velocity, v_c, a flow channel begins forming at the edge of the cavity (Figure 2.32b). In our experiments, this happened approximately one minute after the start of the particle production (Figure 2.33a) but it may take different time in real petroleum reservoirs. The location of the surface flow channel depends on heterogeneity of the sand layer and fluid flow. As the length of the flow channel grows, it connects the outer boundary of the sand layer and the cavity surface (Figure 2.33b).

Although short (~13 min in Figure 2.34a), cavity formation is a relatively stable process that eventually ceases due to the radial effect of reducing fluid flow on the cavity surface. However, this final (largest) cavity is unstable because the fluid flow is unlikely to be homogeneous everywhere on the cavity surface and, at some place, the flow velocity exceeds the critical value. This is why cavity bifurcates in the form of the channel that starts developing from the cavity surface (stage II). Because the cavity surface slopes, the highest flow velocity is expected (and observed in numerical experiments in Figures 2.58b and 2.59) at the upper parts of the slope. Hence, the channel always developed at the surface of our sand layer – regardless of the boundary conditions on the interface with confining plate, i.e., low or high friction section. We call it 'surface' channel, although in real petroleum formations it may develop near an interface with a layer of cohesive material.

Once the channel starts growing, it continues to propagate (stage III) towards the sample perimeter. At this stage, the channel is filled by fluidized sand (slurry) and the channel formation is characterized by the propagation of the fluidization (erosion) front (Figure 2.60). Formed flow channel becomes the main conduit for fluid flow due to the difference in hydraulic conductivity between the sand layer and the flow channel. Eventually, the sand slurry, filling the channel, is transported into the central cavity and most of the injected fluid simply continues flowing through the flow channel toward the wellbore. Fluid in the sand layer also flows toward the surface of the flow channel and the cavity, although the flow rate through the sand layer would be much smaller than in the flow channel (as shown schematically in Figure 2.60).

In both cases, before the full development of the flow channel, the hydrodynamic force of the fluid flow is sufficiently large to remove particles from the surface of the channel front. In the interior of the flow channel, the fluid flow is approximately one dimensional, in contrast to the mostly radial fluid flow pattern in the sand layer (Figure 2.62). Therefore, the fluid flow may remove particles from the formation even at a distance from the center of the sand layer (Figure 2.62b) and transport the removed particles all the way towards the cavity.

The removed particles are produced into the borehole. Because, the fluid velocity through the flow channel is approximately one-dimensional (Figure 2.62a), its capacity to further erode the channel reduces because (at stage II) the normal components of the flow velocity (with respect to the channel bottom and sides) becomes too small.

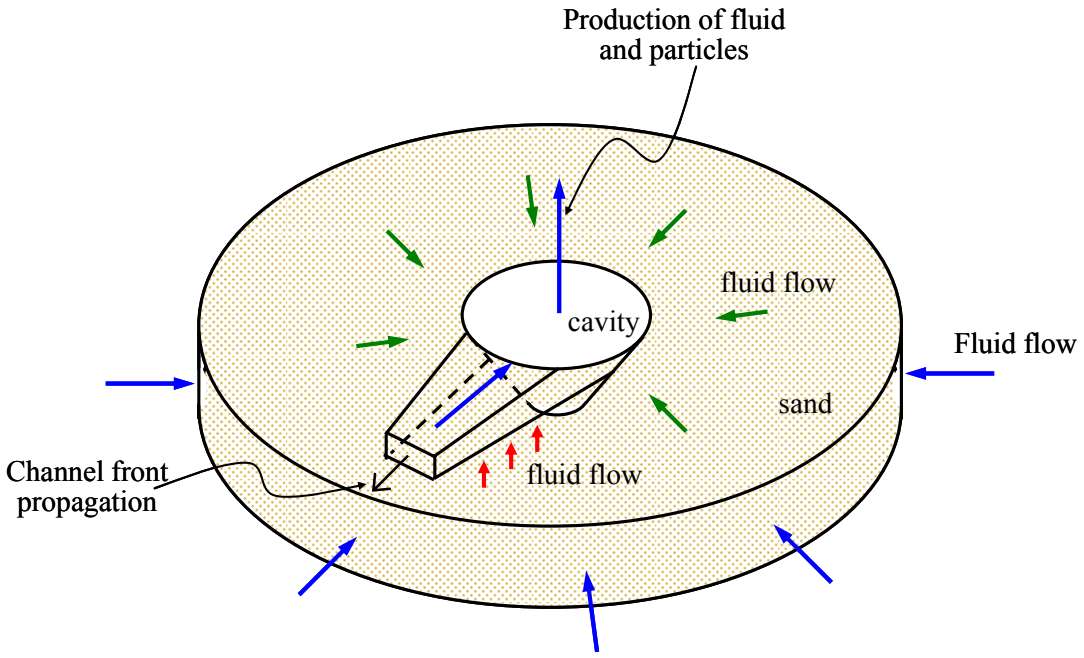

(a)

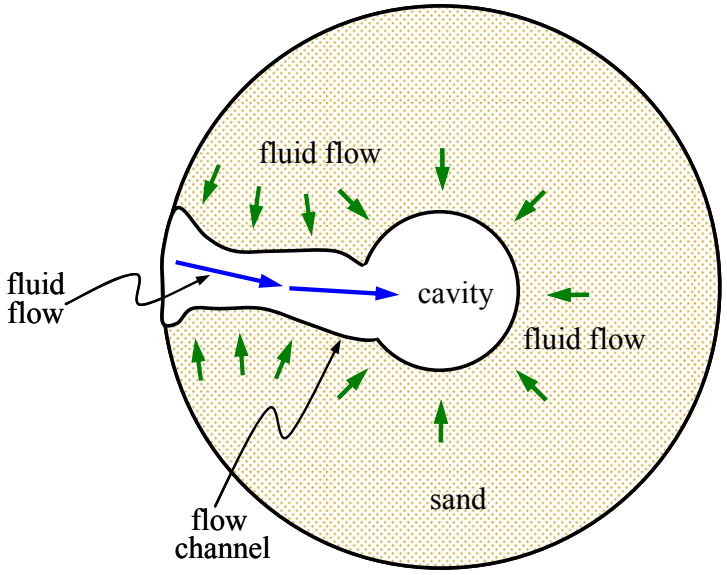

(b)

Figure 2.62 Conceptual model of sand production in conducted experiments (not to scale): (a) a 3-D schematics of a cavity–flow channel system and (b) plan view of the developed cavity and surface channel.

Consider, for example, the stability of a particle A, shown in Figure 2.56a, before the channel is initiated. The particle is located in the middle of the slope, and it starts to be separated from the formation due to hydrodynamic force of fluid flow. The direction of fluid flow is perpendicular to the surface of the cavity. After the creation of the channel, the flow rate will mostly concentrate in the channel. To remove particle B from the channel wall (Figure 2.61a), fluid must lift the particle. At this stage, however, the lifting force may not be sufficient. Hence, removal of particles stops, and fluid flow becomes steady state.

In our 2-D numerical simulations (Figure 2.59a) we did not observe high particle concentration in the channel (Figure 2.59c). This may be because our numerical resolution was not sufficiently high since the particle size in the numerical model was not small enough. It may also be, however, that the propagation of the "empty" channel (Figures 2.59a and 2.59c) represents a different possible type of the channel front that propagates (stage III) by the erosion mechanism (similar to the cavity formation at stage II). In fact, fluidization and erosion processes can be viewed as two extreme cases of the channel propagation mechanism. In the erosion case, the channel in Figure 2.62 is assumed to be filled with fluid and a small number of particles can be ignored. As a result, after a particle is separated, it does not significantly affect the erosion front and the hydrodynamic force on the remaining particles. In the fluidization case, the channel (Figure 2.62) is filled with dense sand slurry (as in Figure 2.60), affecting the stress regime on the fluidization front. The fluid velocity and hydrodynamic forces in this case are probably smaller than in the erosion case. The resolution of our experimental observations is not sufficient to determine with certainty what process actually dominates near the front of the propagating channel. In reality, the front conditions may be in between of these two extremes, but the erosion processes probably represents an upper limit for the velocity of the channel propagation.

2.7 Development of the Surface Channel

Cavity formation and the surface channel represent two most prominent features in our experiments. It is noteworthy that the formation of the surface channel occurs rather fast. Essentially, the channel propagates through the entire sample only in a few seconds (e.g., Figure 2.36 and Table 2.8). To understand this process, we consider a simple scaling based on the model of trench propagation developed by *Atkinson* [1986].

2.7.1 Atkinson's [1986] Trench Model Applied to Sand Production

Atkinson [1986] considered a 2-D, rectangular trench (slot) steadily advancing with velocity V = const in the infinite medium (Figure 2.63a). He computed the pressure distribution in the porous medium with such a trench assuming constant pressure specified on the trench surface (p_1) and at infinity (p_0). In the coordinate set (x_1, y_1), moving with the same velocity, V, the corresponding boundary value problem can be expressed as [*Atkinson*, 1986]

$$\begin{cases} \dfrac{\partial^2 P}{\partial x^2} + \alpha \dfrac{\partial P}{\partial x} + \dfrac{\partial^2 P}{\partial y^2} = 0 \\ P = 1 \quad \text{when } x < 0,\ y = \pm h \\ P = 1 \quad \text{when } x = 0,\ -1 < y < 1 \\ P = 0 \quad \text{when } r = \sqrt{x^2 + y^2} \to 0 \end{cases} \tag{2.12}$$

where

$$x = x_1 / h,\ \ y = y_1 / h \tag{2.13}$$

are the dimensionless (moving) coordinates,

$$P = \frac{p - p_0}{p_1 - p_0} \tag{2.14}$$

is the dimensionless pressure,

$$\alpha = \frac{h}{D} V \tag{2.15}$$

is the dimensionless propagation velocity,

$$D = \frac{kK}{\phi\mu} \tag{2.16}$$

is the dimensionless diffusivity (in the case when compressibility of fluid is much smaller than that of the particulate material), k is the formation permeability, ϕ is the porosity, μ is the fluid (water, in our case) viscosity, and K is the fluid bulk modulus ($1/K$ is the fluid compressibility). The first equation in (2.12) represents the pore pressure diffusion equation in steadily moving coordinates, x_1, y_1 (Figure 2.63).

Because of the symmetry, there is no fluid flow across the x_1-axis, so that

$$\frac{\partial p}{\partial y_1} = 0 \qquad (y_1 = 0,\ \ x_1 > 0) \tag{2.17}$$

Therefore, *Atkinson*'s [1986] problem also describes the propagation of the surface channel in a half-space with impermeable boundary (Figure 2.63b). In the conditions of our experiment, pressure p_1 changes along the surface channel as the fluidized slurry moves somewhat similarly to a viscous fluid. For scaling purposes, however, we consider p_1 being constant in the (semi-infinite) channel.

Because all observed channels had the height h much smaller than the width w (Figure 2.53), it seems appropriate to use a 2-D model (plane strain). In our experiments, however, the channel propagated not in a half-space (Figure 2.63b), but rather in a layer of finite thickness. Also, the pressure on the outer boundary was changing during the channel propagation (Figure 2.35), and the latter was occurring with not quite a constant rate. Yet,

Atkinson's [1986] model provides a framework for a closed form scaling that complements numerical analyses presented in Chapter 3.

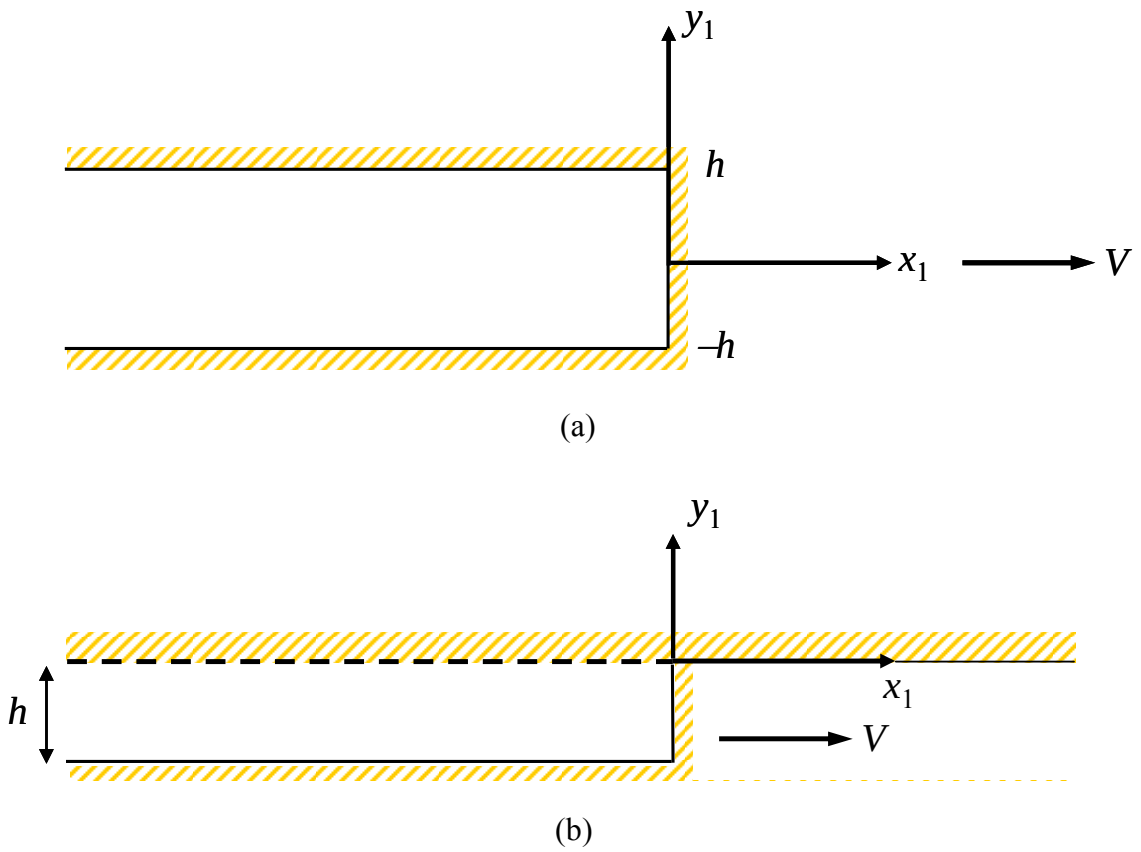

Figure 2.63 (a) Semi-infinite trench in full space and (b) semi-infinite surface channel in half-space.

2.7.2 Channel Propagation Velocity

Atkinson [1986] obtained asymptotic solutions of the boundary-value problem (2.12) for small and large values of parameter α. In the case of $\alpha << 1$, his solution can be represented in the form of [*Atkinson*, 1986]

$$P = \exp\left(-\frac{\alpha x}{2}\right)[1 + U(x, y)] \tag{2.18}$$

where

$$U(x, y) = \operatorname{Im} F(\varsigma) \tag{2.19}$$

The complex coordinate $\varsigma = \xi + i\eta$ is related to $z = x + iy$ by the Schwartz-Christoffel transformation [*Brown and Churchill*, 1996]

$$z = w(\varsigma) = -\frac{2}{\pi}\left[\varsigma\sqrt{\varsigma^2 - 1} - \ln\left[\left(\varsigma + \sqrt{\varsigma^2 - 1}\right) + \frac{\pi i}{2}\right]\right] \tag{2.20}$$

which maps the exterior of the channel on the complex plane z onto the upper half of the plane ς (Figure 2.64), and

$$F(\varsigma) = -\frac{2}{\pi}(\sqrt{2\alpha})\varsigma \tag{2.21}$$

Conformal mapping $z = w(\varsigma)$ in (2.20) is defined assuming that the logarithm has its principal value (i.e., $-\pi < \arg(\ln z) \le \pi$) and that the ς-plane has a cut from $\varsigma = -1$ to $\varsigma = 1$ lying in $z = \operatorname{Im}\varsigma < 0$ [e.g., *Atkinson*, 1986].

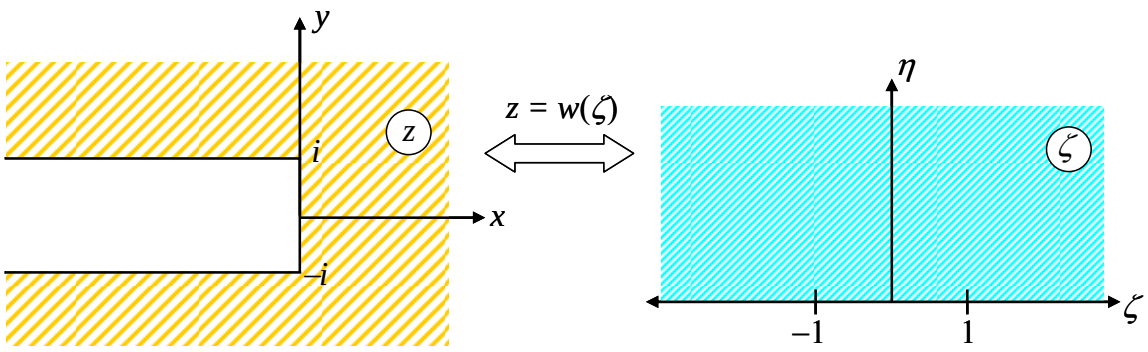

Figure 2.64 Schwartz-Christoffel transformation (2.20).

Using solution (2.18) – (2.21), we can now compare the fluid velocity to the critical fluid velocity, v_c, introduced in Section 2.6.1 and associated with the sand production. The normal component of the fluid velocity at the channel end $x = 0$ is given by the Darcy's law

$$v = -\frac{k}{\mu}\frac{\partial p}{\partial x_1} \qquad (x_1 = 0,\ -h < y_1 < h) \tag{2.22}$$

Since this velocity varies along the line $\{ x_1 = 0,\ -h < y_1 < h \}$, for scaling purposes, we use the mean velocity

$$\bar{v} = \frac{1}{2h}\int_{-h}^{h} v dy_1 \qquad (x_1 = 0,\ -h < y_1 < h) \tag{2.23}$$

which we write in dimensionless coordinates (2.13) ($x = x_1 / h,\ \ y = y_1 / h$) as

$$\bar{v} = -\frac{k(p_1 - p_0)}{2h\mu}\int_{-1}^{1}\frac{\partial U}{\partial x} dy \qquad (x = 0) \tag{2.24}$$

Here, we used expressions (2.14), (2.18), and (2.22).

Using (2.19), we further rewrite the integral in (2.24) as

$$\int_{-1}^{1}\frac{\partial U}{\partial x}dy=\int_{-1}^{1}\mathrm{Im}\frac{\partial}{\partial z}F(\varsigma)dy=-\mathrm{Re}\int_{-i}^{i}\frac{\partial}{\partial z}F(\varsigma)dz \tag{2.25}$$

where $\varsigma=w^{-1}(z)$ and we took into account that for an analytic complex function $f(z)$,

$$\frac{\partial}{\partial x}f(z)=\frac{d}{dz}f(z),\quad \int_{z=-i}^{z=i}f(z)dz=i\int_{-1}^{1}f(z)dy \tag{2.26}$$

Because $\partial F/\partial z=(\partial F/\partial\varsigma)(\partial\varsigma/\partial z)$, (2.25) becomes

$$\int_{-1}^{1}\frac{\partial U}{\partial x}dy=\mathrm{Re}\int_{-1}^{1}\frac{dF}{d\varsigma}d\varsigma=-\frac{4}{\pi}\sqrt{2\alpha} \tag{2.27}$$

where we used (2.21) and that $w(\varsigma)$ maps $\varsigma=\pm1$ onto $z=\mp i$.

Substituting (2.27) in (2.24), we find

$$\bar{v}=\frac{2k(p_1-p_0)}{\pi h\mu}\sqrt{2\alpha}+O(\alpha)\qquad(x=0) \tag{2.28}$$

and employing the particle production condition (Section 2.6.2)

$$\bar{v}=v_c \tag{2.29}$$

on the channel front, we finally represent the dimensionless velocity (2.15) of the channel propagation as

$$\alpha=\frac{1}{2}\left[\frac{\pi h\mu v_c}{2k(p_1-p_0)}\right]^2 \tag{2.30}$$

2.7.3 Comparison with Experimental Observations

In our experiments, pressure p_0 on the remote boundary corresponds to the pressure observed at the sample exterior. Per Figure 2.35, this pressure is $p_0 \approx 3\times10^4$ Pa. Pressure p_1 scales with the hydrostatic pressure corresponding to ~1 m water level in the tube we used to collect the produced sand from the center of the sand sample (Figure 2.10). Accordingly, $p_1 \approx 10^4$ Pa, so that $p_1 - p_0 \approx 2\times10^4$ Pa. As discussed in Section 2.6, the typical thickness (height) of the surface channel (Figure 2.53) is $h \sim 1$ cm. Since the critical fluid flow velocity required to remove the sand particles from the front of the propagating channel has been estimated as $v_c \sim 0.01$–0.1 cm/sec (Section 2.6.1) for permeability $k \sim 10^{-12}$ m^2 of sand sample and water viscosity $\mu = 1$ cP, we find from (2.30) that $\alpha \sim 10^{-3}$–10^{-1}. This is consistent with the asymptotic condition $\alpha << 1$ employed to obtain (2.28) and, therefore, (2.30). Furthermore, as noted by *Atkinson* [1986], based on comparison with his numerical solution, the asymptotic solution (2.18)–(2.21) has a robust way far beyond the range of its expected accuracy.

Therefore, the propagation velocity can be estimated directly from (2.15):

$$V = \frac{D\alpha}{h} \tag{2.31}$$

According to *Hurt*'s [2011] measurements of the bulk modulus of the particular material similar to our sample, $K \sim 100$ MPa in (2.16). Hence, for $k \sim 10^{-12}$ m^2, $\mu = 1$ cP, and $\phi \sim 10^{-1}$, (2.16) results in hydraulic diffusivity $D \sim 1$ m^2/sec. For $\alpha \sim 10^{-3} - 10^{-1}$ and $h \sim 1$ cm, we then obtain from (2.31) that $V \sim 10^{-1} - 10$ m/sec. This is the expected range of the channel propagation velocity consistent with the critical flow velocity $v_c \sim 0.01$–0.1 cm/sec and other parameters characteristic for our experimental setup. Since the distance L of the

channel propagation scales with the size of our sample (~1 m), the expected propagation time $t \sim 0.1–10$ sec.

Although this is a rather broad interval, it indicates that the propagation time is expected to be relatively short. Indeed, in our experiments the channel was extending from the inner cavity to the outer sample boundary only within a few seconds (e.g., Figure 2.36), which is within the obtained scaling of $t \sim 0.1–10$ sec. As follows from (2.30) and (2.31), such a short propagation time is due to the quite short propagation distance (<1 m) and, more importantly, because of the relatively high value of the hydraulic diffusivity of our sample ($D \sim 1$ m^2/sec). This can be seen directly from expression

$$V = Dh\left[\frac{\pi N \rho_s g \tan\psi}{2(p_1 - p_0)}\right]^2 \tag{2.32}$$

obtained by inserting eq. (2.9) for v_c into (2.30) and the result into (2.31). The two-orders of magnitude range for V results from the uncertainty in the number of particles $N \sim 1 - 10$, which are in contact with the particle on the surface (Figure 2.56), and the rather high values of V result from the relatively large D.

2.7.4 Discussion

Using condition (2.29) of sand production implies a small scale slope at the channel front (Figure 2.60) similar to the cavity slope (Figure 2.62). Such details, however, are beyond the resolution of the scaling condition (2.29). Even more importantly, condition (2.29) itself is based on the concept of critical flow velocity, which results from the hypothesis of erosion occurring at the channel front. While the erosion mechanism is relatively simple to scale based on the *Atkinson*'s [1986] trench model, the fluidization mechanism, as mentioned above, is also consistent with observations in our experiments (Figures 2.32, 2.33, and 2.34).

A possible fluidization condition on the channel front (Figure 2.60), can be written as

$$\sigma'_x = \sigma_x - p = 0\,,\ \sigma'_y = \sigma_y - p = 0\,,\ \sigma'_z = \sigma_z - p = 0 \tag{2.33}$$

where σ'_x, σ'_y, and σ'_z are the effective stresses. This would require solving the corresponding 3-D problem, which is beyond the scope of this work. Our scaling is still applicable, however, as we simply assumed that the channel propagates with a constant velocity. In the fluidization case, velocity v_c in (2.29) or (2.30) can be viewed as a characteristic velocity at the channel front. Employing the experimentally estimated value of $v_c \sim 0.1$ cm/sec (Sections 2.6.1 and 2.6.2) does not change the scaling results discussed in the previous section.

Employing the 2-D solution of *Atkinson* [1986] is satisfied when $h << w$, and this indeed has been observed in our experiments (e.g., Table 2.11). Our scaling is not sufficient to estimate the cross-sectional dimensions h and w (Figure 2.53) of the flow channel. The developed model, however, allowed us to obtain the rate of channel evolution consistent with the observed values of h.

2.8 Conclusions

In this work, a series of large-scale (~1 m) laboratory experiments was conducted in fully saturated, cohesionless sand layers to model the behavior of a petroleum reservoir near a wellbore. We directly observed several key characteristics of the sand production phenomenon including the formations of a stable cavity around the wellbore and a sub-radial flow channel at the upper surface of the tested layer. The flow channel is a first-order feature that appears to be a major part of the sand production mechanism. The channel cross section is orders of magnitude larger than the particle size, and once formed, the channel becomes the dominant conduit for fluid flow and particle transport. The flow channel developed in all of our experiments and in all experiments, sand production continued from the developing channel after the cavity around the borehole stabilized.

Based on scaling considerations, we developed a simple analytical model, constrained by the experimental results. This model adopts the observed erosion mechanism of the particle production, which results in a cavity forming around the borehole. As the cavity grows till it reaches the maximum size corresponding to the critical flow velocity, a flow channel begins developing at the edge of the cavity. The growing channel is filled by the fluidized sand (slurry) and the channel formation is characterized by the propagation of the fluidization front.

The notion of the existence of the flow channel has the potential to scale up to natural reservoirs and can give insights into real-world sand production issues. It indicates a mechanism explaining why the production of particles does not cease in many petroleum reservoirs. Although the radial character of the fluid flow eventually stops sand production from the cavity near the wellbore, the production of particles still may continue from the propagating surface (interface) flow channel.

LIST OF SYMBOLS AND ABBREVIATIONS

a	Plate radius
C_u	Uniform coefficient
D	Dimensionless diffusivity
D	Plate flexural rigidity
D_{10}	Particle size on the particle size distribution curve corresponding to 10%
D_{60}	Particle size on the particle size distribution curve corresponding to 60%
d	Characteristic diameter of a particle
E	Young's modulus
$f(z)$	Complex function
G_s	Specific gravity of a sand particle
g	Acceleration of gravity
H	Height of a sand layer
h	Height of the cross-section of a surface flow channel
h	Height of a trench
h	Plate thickness
K	Bulk modulus
k	Permeability of a porous medium
L	Length
M	Bending moment
N	Number of contact
P	Dimensionless pressure
p	Fluid pressure
p	Pressure

p_0	Fluid pressure at infinity
p_1	Fluid pressure at trench wall
Q	Fluid flow rate
R	Radius of a sand layer
r	Distance from the center of a sand layer
r_c	Cavity radius in the middle horizontal plane in a sand layer
t	Time
V	Velocity of a steadily advancing rectangular trench (slot)
V_{cast}	Volume of the cast of cavity and surface channel
V_s	Volume of sand particles
v	Fluid velocity
v_c	Critical fluid velocity
v_0	Fluid velocity at the outer boundary of sand layer
$\bar{v}$	Mean fluid velocity
W_c	Weight of produced sand from a cavity and a surface channel
W_s	Weight of the produced sand in the sand collection tank
W_t	Increase in the weight of a sand collection tank
w	Vertical displacement at a plate center
w	Width of the cross-section of a surface flow channel
w	Width of a trench
$w(\zeta)$	Conformal mapping of complex coordinate, ζ
z	Complex coordinates
α	Repose angle
α	Dimensionless propagation velocity

β	Angle of cavity slope
γ_w	Unit weight of water
ζ	Complex coordinates
μ	Dynamic viscosity of fluid
ν	Poisson's ratio
ρ_b	Dry bulk density of a sand sample
ρ_s	Density of a particle
$\sigma'_{\theta\theta}$	Effective tangential stress
σ'_x	Effective stress in *x*-direction
σ'_y	Effective stress in *y*-direction
σ'_z	Effective stress in *z*-direction
ϕ	Porosity
ψ	Interparticle friction angle

References

Asgian, M.I., P.A Cundall, and B.H.G. Brady (1995), Mechanical stability of propped hydraulic fractures: A numerical study, *Journal of Petroleum Technology*, 203-208.

ASTM (2004), ASTM WK3821 New test method for consolidated drained triaxial compression test for soils.

Atkinson, C. (1986), Some moving boundary problems for a generalized diffusion equation, *International Journal of Engineering Science*, 24(4), 493-512.

Baghdikian, S.Y., M.M. Sharma, and L.L. Handy (1989), Flow of clay suspension through porous medium, *Society of Petroleum Engineers Reservoir Engineering*, 4, 213-220

Bear, J. (1972), *Dynamics of fluids in porous media*, Elsevier Publishing Company, Inc.

Bradley, H.B. (1987), *Petroleum Engineering Hand Book*, Society of Petroleum Engineers.

Bratli, R.K., and R. Risnes (1981), Stability and failure of sand arches, *SPEJ*, 236-248.

Brown, J.W. and R.V. Churchill (1996), *Complex variables and applications*, McGraw-Hill, Inc.

Campbell G.A. and Forgacs, G. (1990), Viscosity of concentrated suspensions: An approach based on percolation theory, *Physical Review A*, 41, 4570 – 4573.

Chang, H. (2004), *Hydraulic fracturing in particulate materials*, Ph.D. dissertation, Georgia Institute of Technology.

Charlez, P.A. (1997), *Rock Mechanics Vol. 2 Petroleum Application*, Éditions Technip, Paris.

Civan, F. (2007), Formation damage mechanism and their phenomenological modeling – An overview, SPE 107857, *Proceedings of SPE-European Formation Damage Conference*, Scheveningen, the Netherlands, June 2007.

Coenraads, R.R. (2008), *Rocks & Fossils: A visual guide*, Firefly Book Ltd.

Coussot, P. (1995), Structural similarity and transition from Newtonian to non-Newtonian behavior for water-clay suspensions, *Physical Review Letters*, 74, 3971-3974.

Das, B.M. (1994), *Principles of geotechnical engineering*, PWS Publishing Company.

Frye, K.M. and C. Marone (2002), The effect of particle dimensionality on granular friction in laboratory shear zones, *Geophysical Research Letters*, 2(19), 22/1-4

Garga, V.K. and H. Zhang (1997), Volume changes in undrained triaxial tests on sands, *Canadian Geotechnical Journal*, 34, 762-772.

Van den Hoek, P.J., G.M.M. Hertogh, A.P. Kooijman, Ph. de Bree, C.J. Kenter, and E. Papamichos (2000), A new concept of sand production prediction: theory and laboratory experiments, *SPE Drill & Completion*, 15, 261-273.

Holz D. and W.D. Kovacs (1981), *An introduction to Geotechnical Engineering*, Prentice-Hall.

Hurt, R. (2011), *Mechanics of fluid driven fractures in rock-like materials* (in preparation), Ph.D. dissertation, Georgia Institute of Technology.

Itasca (2002), *PFC^{2D} user's guide*.

Janna, W. S. (1993), *Introduction to fluid mechanics*, International Thomson Publishing.

Lacasse, S. and T. Berre (1988), Triaxial testing methods for soils, *Advanced Triaxial Testing of Soil and Rock*, ASTM STP 977, Robert T. et al. Eds., American Society of Testing and Materials, Philadelphia, 264-289.

Lambe, T.W., and R.V. Whitman (1979), *Soil Mechanics*, John Wiley & Sons.

Lajeunesse, E., A. Mangeney-Castelnau, and J.P. Vilotte (2004), Spreading of a granular mass on a horizontal plane, *Physics of Fluids*, 16(7), 2371-2381.

Lide, D.R. (2004), *CRC handbook of Chemistry and Physics*, CRC Press LLC.

NIH (2004), *Image J*, National Institute of Health.

Oxtoby, D. W., N.H. Nachtrieb, and W.A. Freeman (1990), *Chemistry*, Saunders College Publishing.

Palmer, I. D., J.D. McLennan, and H.H. Vaziri (2000), Cavity-like completions in weak sands, SPE 58719, *Proceedings of International Symposium on Formation Damage Control*, Lafayette, Louisiana, U.S.A.

Papadikis, K., S. Gu, and A.V. Bridgwater (2010), 3D simulation of the effects of sphericity on char entrainment in fluidized beds, *Fuel Processing Technology 91*, 749-758.

Pearson, J.R.A. and A.F. Zazovsky (1997), A model for the transport of sand grains from a perforation during underbalance surge, SPE 38634, *Proceedings of SPE Annual Technical Conference and Exhibition*, San Antonio, TX, U.S.A, October, 1997.

Senapati, P.K., D. Panda, and Parida, A. (2009), Predicting Viscosity of Limestone–Water Slurry, *Journal of Minerals & Materials Characterization & Engineering*, 8(3), 203-221.

Serrano, A., C. Olalla, and J. Manzanas (2005), Stability of highly fractured infinite rock slopes with nonlinear failure criteria and nonassociated flow laws, *Canadian Geotechnical Journal*, 42, 393-411.

Terzaghi, K.V. (1936), Stress distribution in dry and in saturated sand above a yielding trap door, *Proceedings of First International Conference on Soil Mechanics and Foundation Engineering*, Harvard University, Cambridge, MA.

Tremblay, B., and K. Oldakowski (2002), Wormhole growth and interaction in a large sand pack, *Journal of Petroleum Science and Enigeering*, 34, 13-34.

Tremblay, B., and K. Oldakowski (2003), Modeling of wormhole growth in cold production, *Transport in Porous Media*, 53, 197-214.

Tremblay, B., G. Sedgwick, and K. Forshner (1996), Imaging of sand production in a horizontal sand pack by X-ray computed tomography, *SPE formation Evaluation*, 94-98.

Tremblay, B., G. Sedgwick, and K. Froshner (1997), Simulation of cold production in heavy-oil reservoirs: wormhole dynamics, *SPE Reservoir Engineering*, 110-117.

Tronvoll, J., A. Skjærstenin, and E. Papamichos (1997), Sand production: mechanical failure or hydrodynmic erosion, *International Journal of Rock Mechanics and Mining Science*, 34(3-4), 853-862.

US Silica (2005), *U. S. SILICA COMPANY PRODUCT INDEX*, US Silica.

Vaziri, H.H., J.S. Jalali, and R. Islam (2001), An analytical model for stability analysis of rock layers over a circular opening, *International Journal of Solids and Structures*, 38, 3735-3757.

Vaziri, H.H., E. Lemoine, I.D. Palmer, J. McLennan, and R. Islam (2000), How can sand production yield a several-fold increase in productivity: experimental and field data, *Proceedings of SPE Annual Conference and Exhibition*, SPE 63235.

Vaziri, H.H., E.M. Lemoine, and Y. Xiao (2002), Quantification of sand production induced improvement in productivity index, *Canadian Geotechinical Journal*, 39, 1088-1102.

Vaziri, H.H., R. Phillips, and S. Hurley (1997), Physical modeling of sand production, *International Journal of Rock Mechanics and Mining Science*, 34, 863-872.

Vaziri, H.H., S. Thallak, and R. Phillips (1998a), Centrifuge tests to identify mode of sand production and its effect on production, *International Journal of Rock Mechanics and Mining Science*, 35(4-5).

Vaziri, H.H., S. Thallak, and R. Phillips (1998b), Investigation of sand production mechanisms resulting in enhanced cold production, *Proceedings of International Society of Soil Mechanics and Foundation Engineering Centrifuge 98*, A.A. Balkema.

Vaziri, H. H., Y. Xiao, R. Islam, and E. Lemoine (2003), Physical modeling study of the influence of shale interbeds and perforation sequence on sand production, *Journal of Petroleum Science and Engineering*, 37, 11-23.

Walton, I.C., D.C. Atwood, P.M. Halleck, and L.C.B. Bianco (2001), Perforating unconsolidated sand: an experimental and theoretical investigation, SPE 71458, *Proceedings of SPE Annual Conference and Exhibition*, New Orleans, Louisiana.

Wadell, H. (1935), Volume, Shape and Roundness of Quartz Particles, *Journal of Geology*, 43, 250-280.

Yun, T.S. (2005), *Mechanical and thermal study of hydrate bearing sediments*, Ph.D. dissertation, Georgia Institute of Technology.

Zhou, Y.C., B.H. Xu, A.B. Yu, and P. Zulli (2002), An experimental and numerical study of the angle of repose of coarse spheres, *Powder Technology*, 125, 45-54.

APPENDIX A2

Deflection of a Plate

Excessive deflection of the polycarbonate plate may, in principle, result in changing the stress regime in the sand sample and, perhaps, more importantly, in creating preferential fluid pathways if permeability is affected by the deformation. Although the thick transparent polycarbonate plate (Section 2.2, Figure 2.12) is assumed to be rigid, in reality, it deflects due to the applied pressure. Thus, deflection of a circular polycarbonate plate (Figure A2.1) is estimated in this appendix. Assuming homogeneous pressure, p, applied to the plate surface, and that its edge is fixed (clamped) around the perimeter, the vertical displacement, w, at the plate center is given by [e.g., *Cook*, 1999]

$$w = \frac{pa^4}{64D} \tag{A2.1}$$

where a is the plate radius, and D is its flexural rigidity. The flexural rigidity of a circular plate is defined by [*Cook*, 1999]

$$D = \frac{Eh^3}{12(1-\nu^2)} \tag{A2.2}$$

where E is the Young's modulus of the plate material, ν is the Poisson's ratio of the plate material, and h is the plate thickness. In our experimental setup, a = 0.5 m, h = 0.05 m, and $p \approx$ 69.0 kPa (10 psi). The values of Young's modulus and Poisson's ratio of the polycarbonate plate are 2.84 GPa and 0.39, respectively [e.g., *Perry et al*., 1995]. Using (A2.1) and abovementioned value of each parameter, the calculated vertical displacement at the plate center is ≈1.9 mm. The actual displacement is probably much smaller because of the constraining action of the metal frame (Figure 2.9), which is not accounted in this estimate. For a sand sample of 10-cm thickness, the largest vertical displacement of the

plate w~1 mm, and, probably, is much smaller. Because the sand layer deforms together with the polycarbonate plate, the magnitude of the sand layer displacement and the bending moment M are connected by the following relationship:

$$M \sim D\frac{w}{a^2} \tag{A2.3}$$

The lateral strain in the plate scales as

$$\varepsilon \sim \frac{hM}{D} \tag{A2.4}$$

and inserting (A2.3) in (A2.4) results in

$$\varepsilon \sim \frac{hw}{a^2} \tag{A2.5}$$

For h~10^{-1} m, w~10^{-3} m, and a~1 m, we estimate that ε~10^{-4}. The actual strain, however, is much smaller since our estimate is conservative and does not account for the frame, which constrains the plate bending. This value indicates that the deflection of the plate can probably be neglected as such strain is unlikely to affect the sand sample in a significant way.

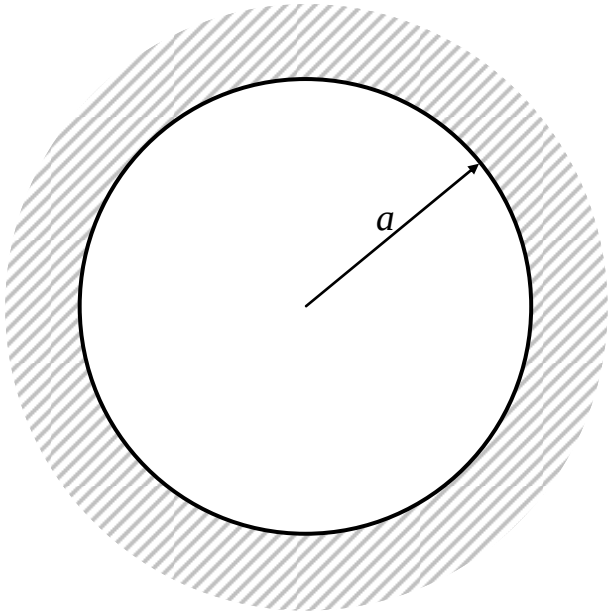

(a)

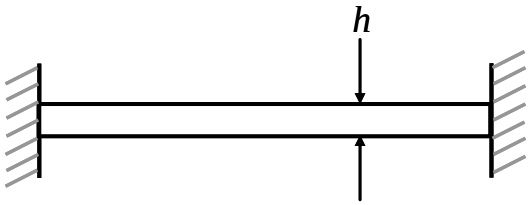

(b)

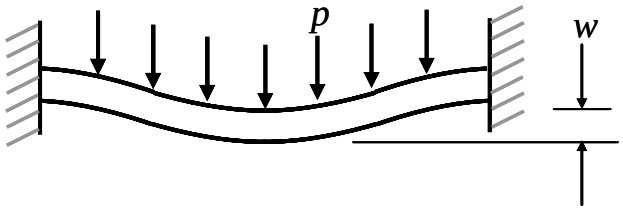

(c)

Figure A2.1 Deflection of a circular plate with fixed edges due to pressure: (a) plan view, (b) side view, and (c) deflection of the plate. Here, *a* is the radius of the plate, *h* is the thickness of the plate, *p* is pressure, and *w* is the vertical displacement of the plate.

APPENDIX B2

Results of Experiments

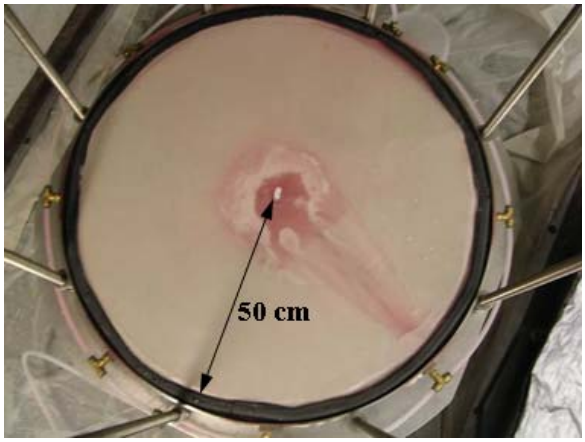

(a)

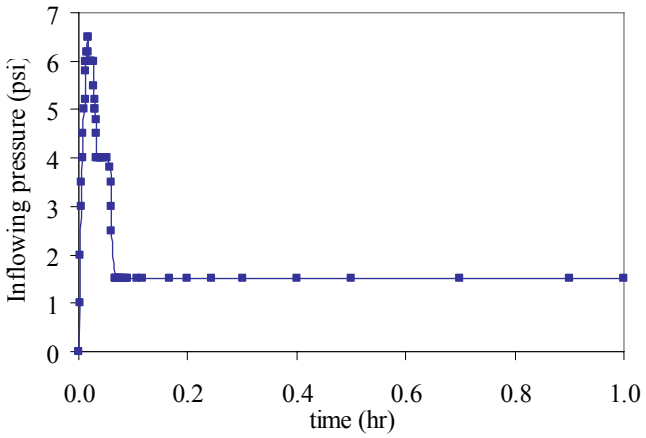

(b)

Figure B2.1 Results of experiment for Test 0A: (a) formed cavity and surface channel, (b) inflowing pressure for first one hour, (c) flow rate and bladder pressure, (d) inflowing pressure for first 10 minutes. The described events in (d) are based on the observations of the surface of the experimental setup during experiment and Figure C2.1 in Appendix C2.

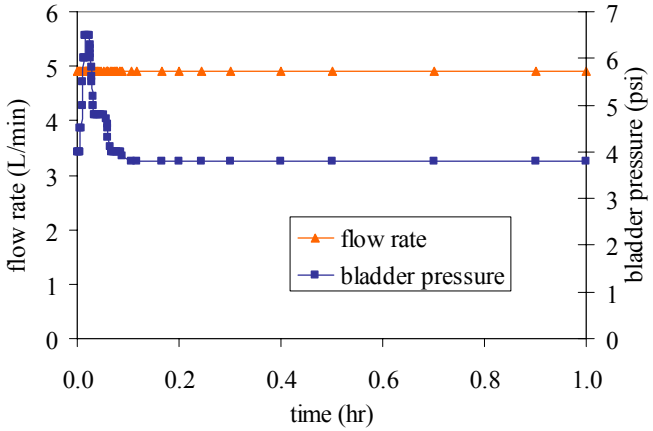

(c)

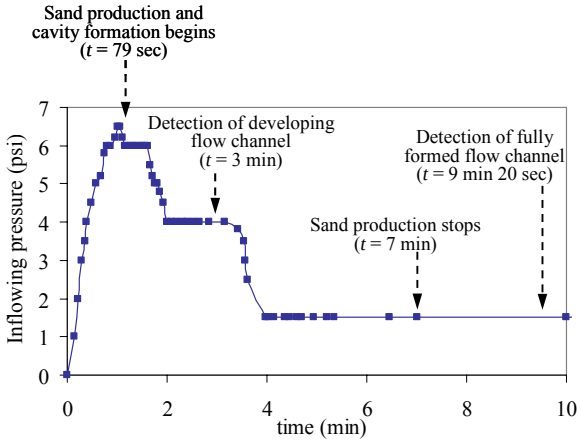

(d)

Figure B2.1 (continued).

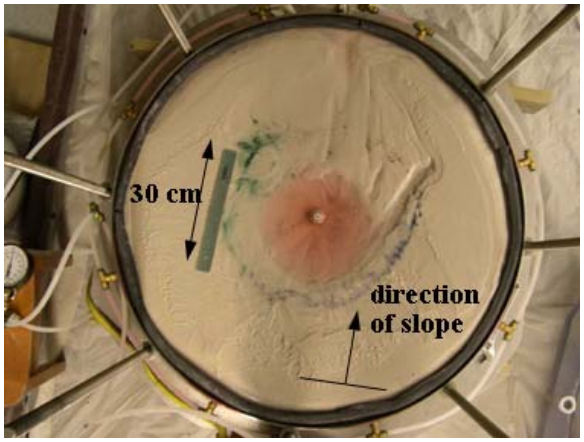

(a)

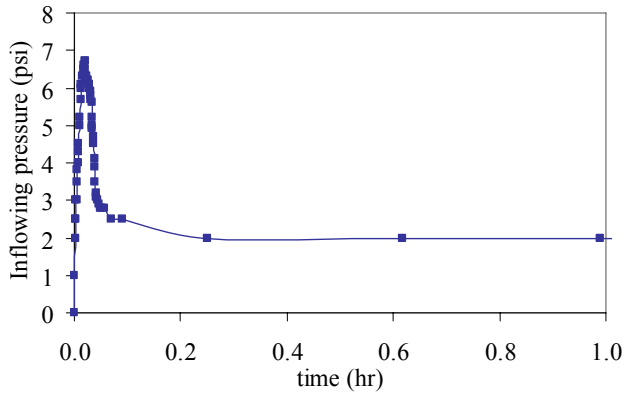

(b)

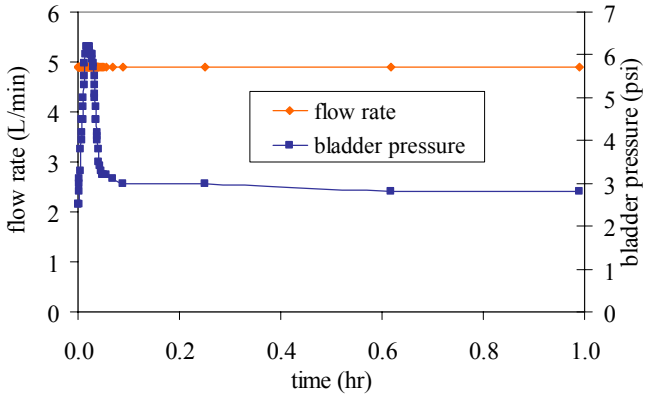

(c)

Figure B2.2 Results of experiment for Test 7A: (a) formed cavity and surface channel (the green rectangle is a 30 cm long ruler to show the scale of the apparatus), (b) inflowing pressure, and (c) flow rate and bladder pressure. Direction of slope indicates the dip direction of the slope: i.e., water flows along the direction of the arrow.

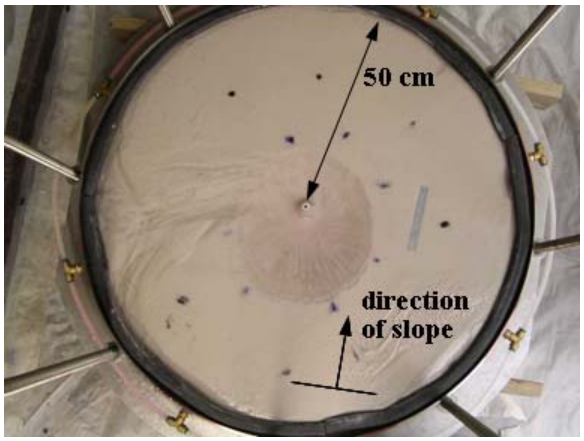

(a)

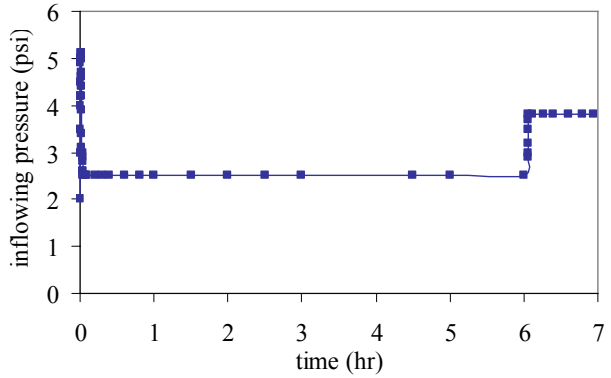

(b)

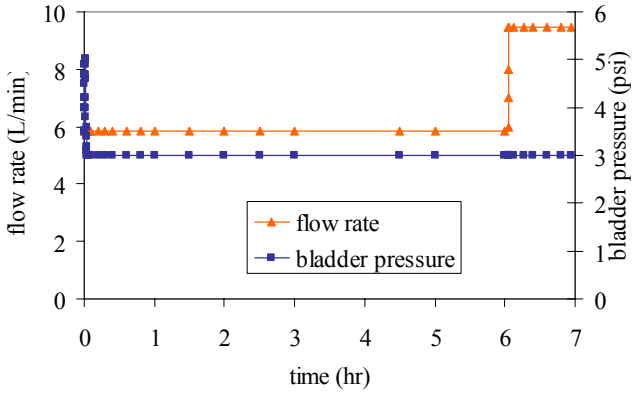

(c)

Figure B2.3 Results of experiment for Test 15A: (a) formed cavity and surface channel (the silver rectangle is a 15 cm long ruler to show the scale of the apparatus), (b) inflowing pressure, and (c) flow rate and bladder pressure. Direction of slope indicates the dip direction of the slope: i.e., water flows along the direction of the arrow.

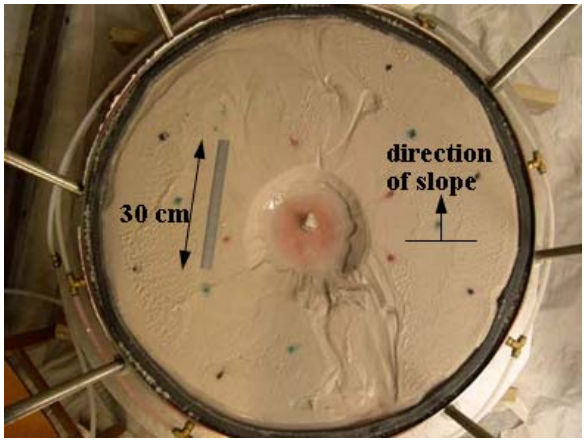

(a)

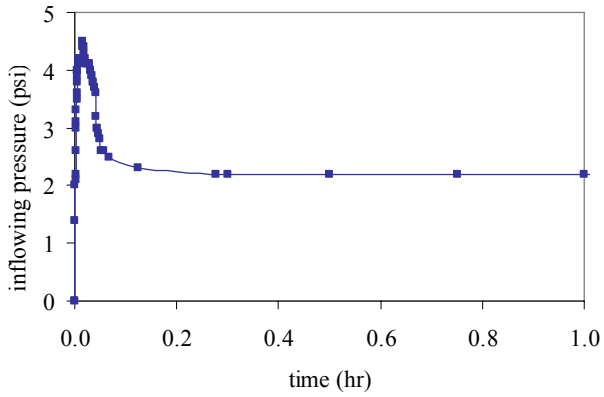

(b)

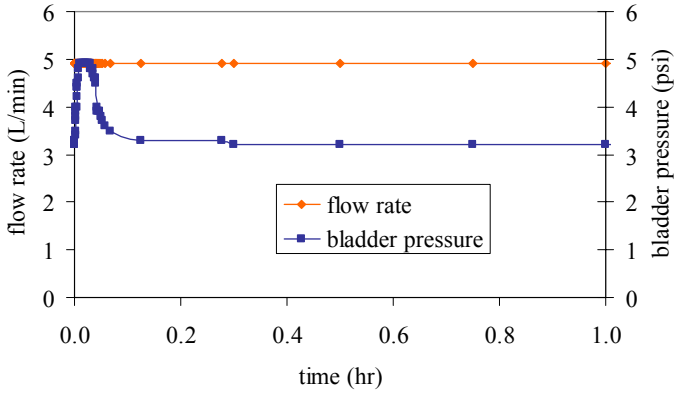

(c)

Figure B2.4 Results of experiment for Test 7B: (a) formed cavity and surface channel (the silver rectangle is a 30 cm long ruler to show the scale of the apparatus), (b) inflowing pressure, and (c) flow rate and bladder pressure. Direction of slope indicates the dip direction of the slope: i.e., water flows along the direction of the arrow.

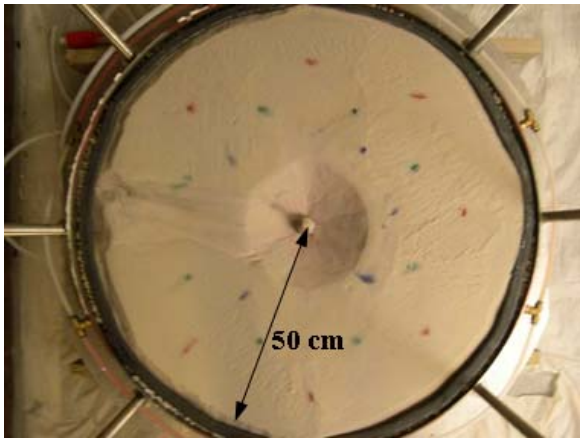

(a)

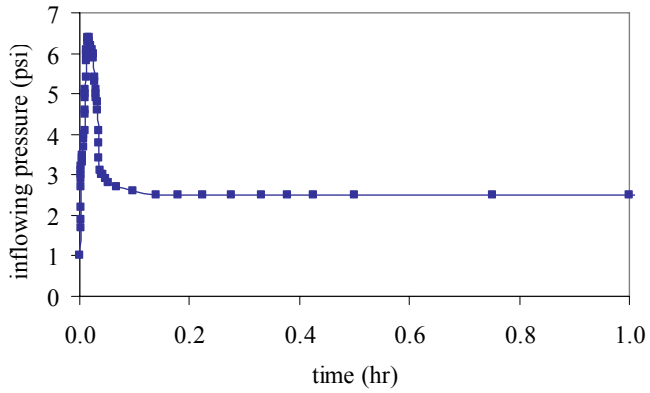

(b)

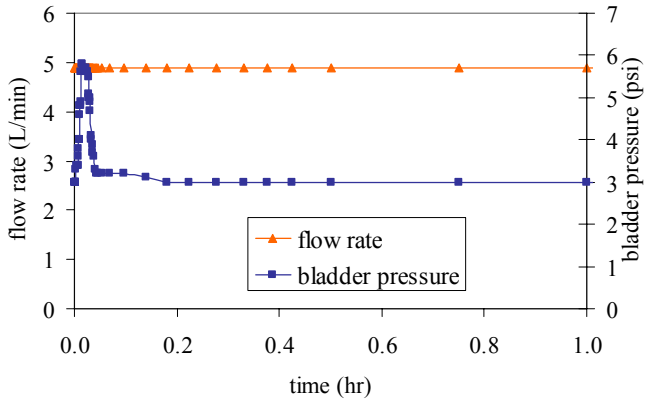

(c)

Figure B2.5 Results of experiment for Test 0B: (a) formed cavity and surface channel, (b) inflowing pressure, and (c) flow rate and bladder pressure.

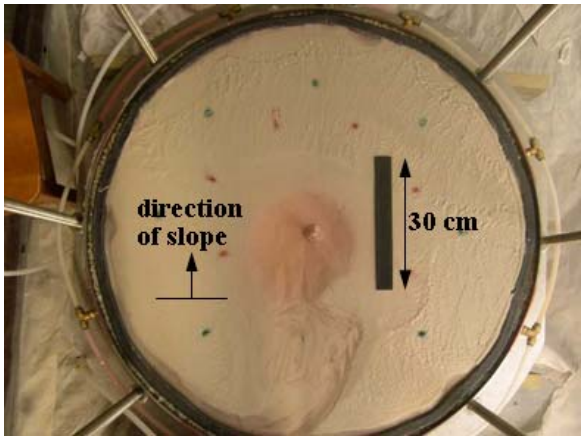

(a)

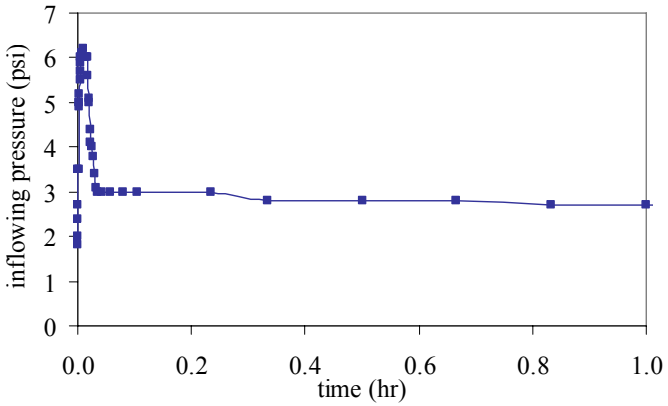

(b)

Figure B2.6 Results of experiment for Test 15B: (a) formed cavity and surface channel (the black rectangle is a 30 cm long ruler to show the scale of the apparatus), (b) inflowing pressure, (c) flow rate and bladder pressure, and (d) inflowing pressure for first 10 minutes. Direction of slope in (a) indicates the dip direction of the slope: i.e., water flows along the direction of the arrow. The described events in (d) are based on the observations of the surface of the experimental setup during experiment and Figure C2.2 in Appendix C2.

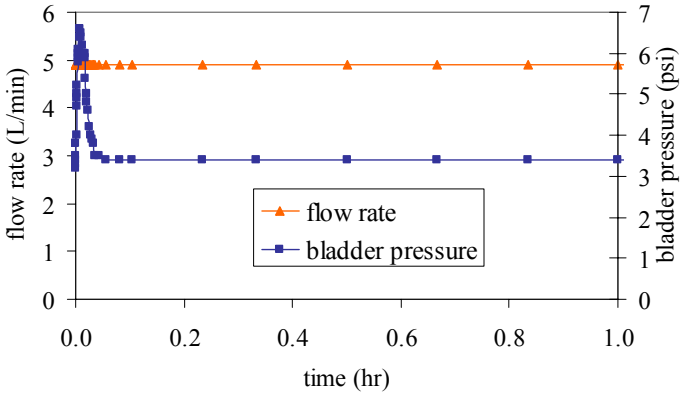

(c)

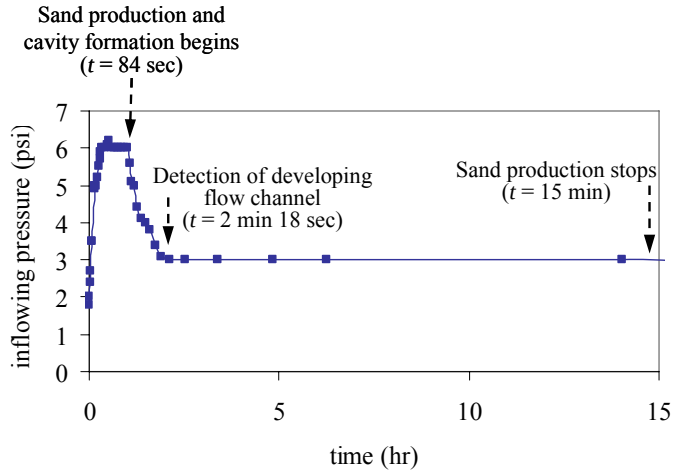

(d)

Figure B2.6 (continued).

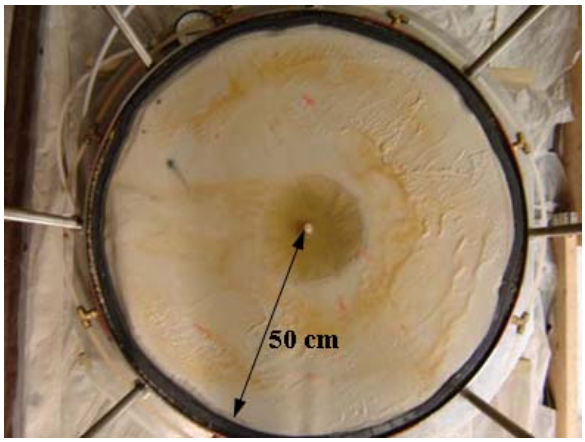

(a)

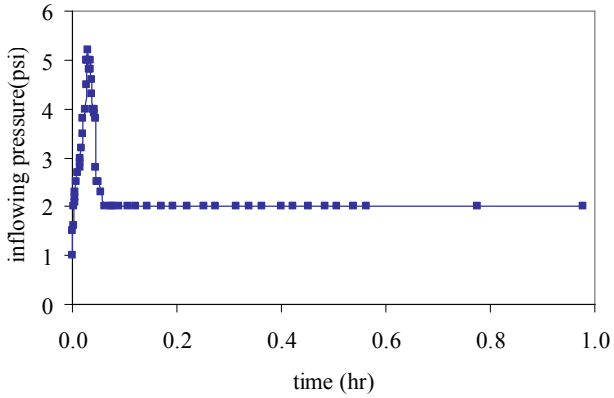

(b)

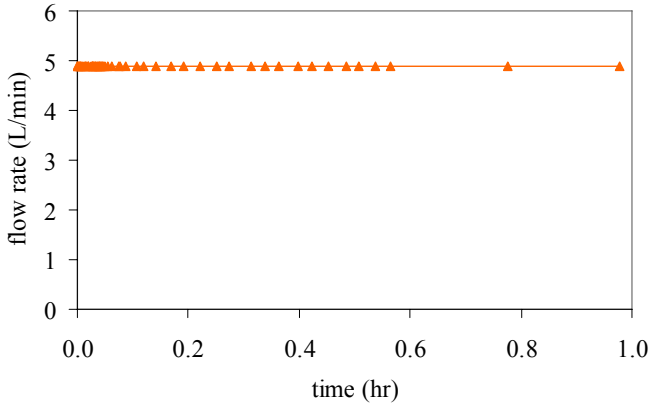

(c)

Figure B2.7 Results of experiment for Test 0C: (a) formed cavity and surface channel, (b) inflowing pressure, and (c) flow rate.

(a)

(b)

(c)

Figure B2.8 Photographs of six casts from experiments including the last one with colored sand sample: (a) base case, (b) Test 15A, (c) Test 7B, (d) Test 0B, (e) Test 15B, and (f) Test 0C.

(d)

(e)

(f)

Figure B2.8 (continued).

APPENDIX C2

Results of Experimental Technique for Sample Surface Monitoring

(a)

(b)

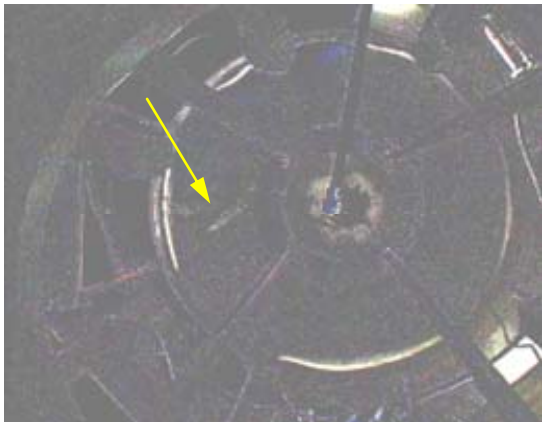

(c)

Figure C2.1 Monitoring of upper surface during experiment (Test 0A): (a) start of sand production, (b) real image of the upper surface at 3 min, (c) processed image showing the difference between (a) and (b), (d) real image of upper surface at 9 min 20 sec, (e) processed image showing the difference between (a) and (d), (f) real image of upper surface at 30 min, and (g) processed image showing the difference between (a) and (f). The yellow arrow in the processed images indicates the development and the propagation of surface flow channel. Here, (a) shows the upper surface before sand production. Thus, from the processed images by comparing a real picture with (a), we can detect the development and the propagation of the surface flow channel.

(d)

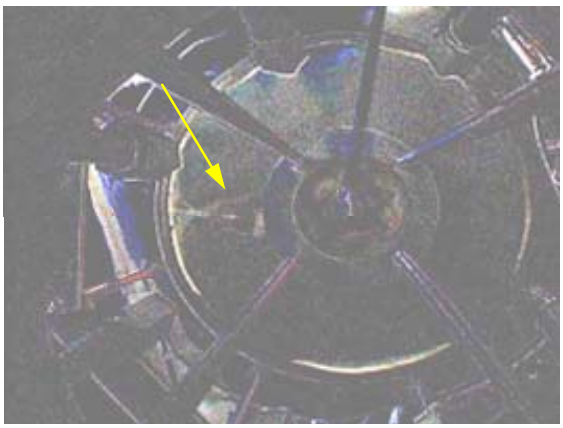

(e)

(f)

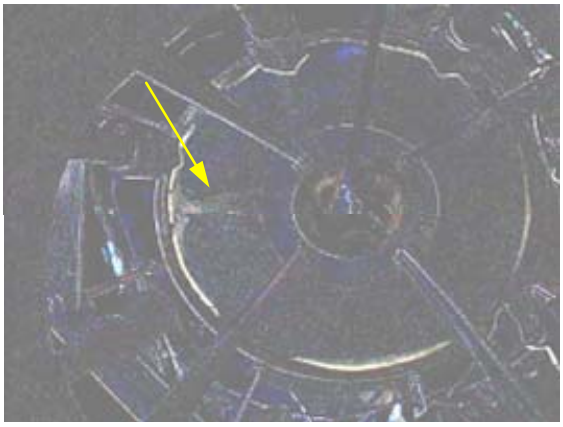

(g)

Figure C2.1 (continued)

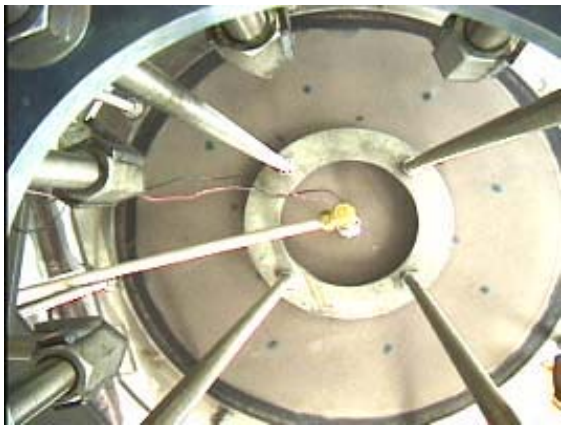

(a)

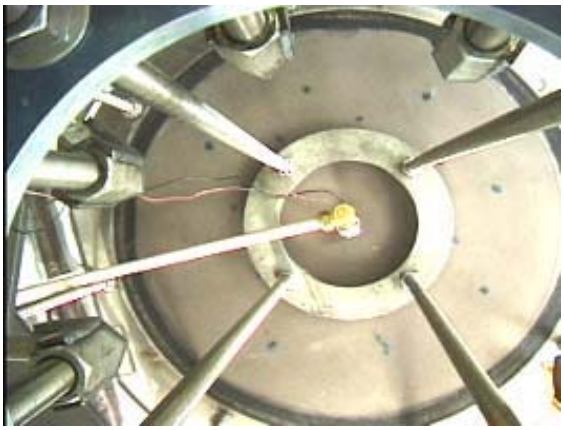

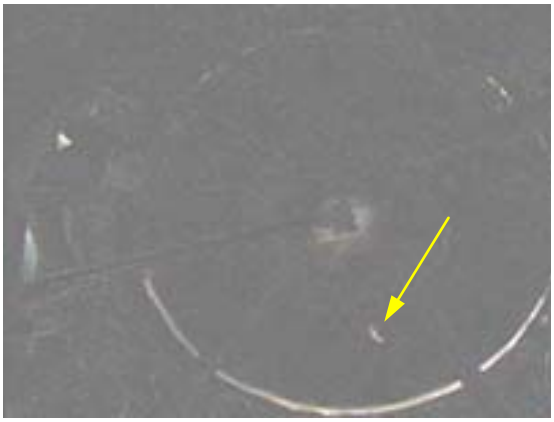

(b) (c)

Figure C2.2 Monitoring of upper surface during experiment (Test 15B): (a) start of sand production, (b) real image of the upper surface at 2 min 18 sec, (c) processed image showing the difference between (a) and (b), (d) real image of upper surface at 5 min, (e) processed image showing the difference between (a) and (d), (f) real image of upper surface at 30 min, and (g) processed image showing the difference between (a) and (f). The yellow arrow in the processed images indicates the development and the propagation of surface flow channel. Here, (a) shows the upper surface before sand production. Thus, from the processed images by comparing a real picture with (a), we can detect the development and the propagation of the surface flow channel.

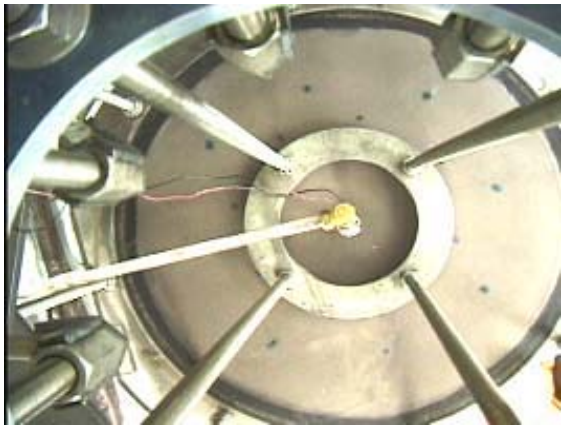

(d)

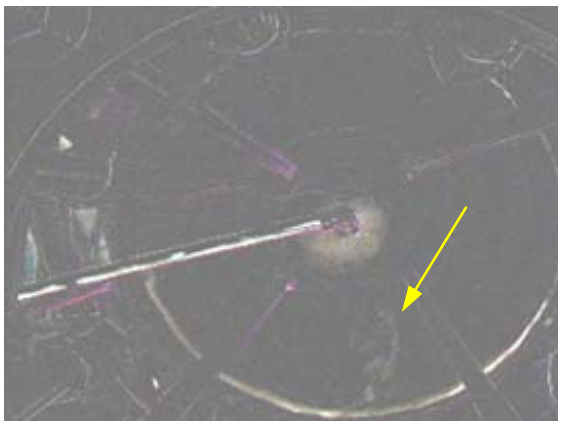

(e)

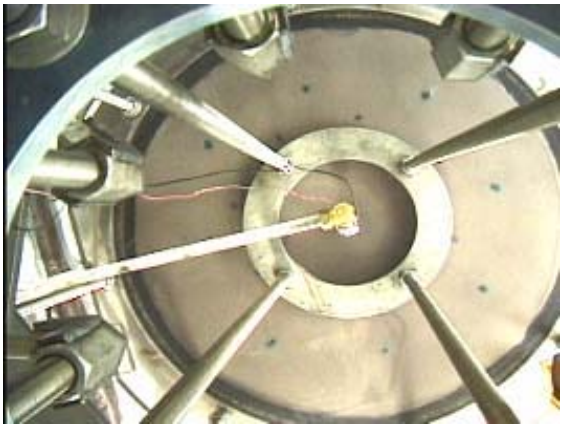

(f)

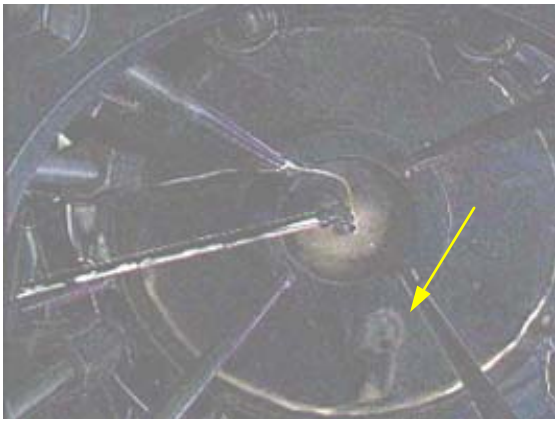

(g)

Figure C2.2 (continued)

CHAPTER III

THEORETICAL MODELING OF SAND PRODUCTION

3.1 Introduction

In this chapter, we present some theoretical results that complement our laboratory experiments on sand production reported in Chapter II. Theoretical models on sand production usually follow either a continuum or a discrete particle approach [*Dusseault and Santarelli*, 1989]. Continuum models typically describe the yield of a rock formation as a function of stresses and pore pressure. Continuum approach is appropriate for investigating the macroscopic behavior of a petroleum reservoir and requires constitutive laws to evaluate the behavior of the formation. Such models also require sand production criteria to describe the removal and transport of particles.

In addition to the constitutive laws and sand production criteria, a failure criterion is usually used to determine rock stability with respect to failure and deformation phenomena around petroleum wells [*Morita et al*., 1989a; 1989b; *Nouri et al*., 2003a; *Tronvoll et al*., 1997]. The Mohr-Coulomb failure criterion is commonly used to describe the shear failure and formation behavior around petroleum wells due to sand production [*Geilikman and Dusseault*, 1997; *Morita et al.*, 1989a; *Vaziri*, 1995]. The results of modeling using the Tresca criterion are similar to those using the Mohr-Coulomb approach [e.g., *Charlez*, 1997].

In sand production models, Mohr-Coulomb criterion has been used both in the elasto-perfect-plastic formulation [*Vaziri*, 1995] and in the approaches based on strain hardening or softening [e.g., *Nouri et al*., 2002a; 2002b; 2003a; 2003b; 2003c; 2004].

Tensile failure is usually expected in consolidated media under a high local pressure gradient near a cavity surface [e.g., *Bratili and Risnes*, 1981]. In their sand

production model, *Bratili and Risnes* [1981] described tensile failure based on the Mohr-Coulomb criterion as

$$p - \sigma_N = c \cdot \cot \Psi \tag{3.1}$$

where p is the fluid pressure, σ_N is the total normal stress, c is the cohesion of the medium, and Ψ is the internal friction angle of the medium. In (3.1) and everywhere in this chapter, tensile stresses are negative. According to (3.1), a medium will undergo failure in tension if the difference between the pore pressure and the total normal stress is greater than the material tensile strength, defined as $\sigma_t = c \cdot \cot \Psi$ (Figure 3.1a).

Vaziri et al. [2002] and *Vaziri and Xiao* [2003] asserted that the tensile strength determined from (3.1) for a particulate material may be an overestimate. Hence, they employed a modified Mohr-Coulomb failure criterion by changing envelope (3.1) in the regions of low confining stress (Figure 3.1a). In the same manner, *Nouri et al*. [2002a; 2003c] used bilinear Mohr-Coulomb envelope along with the tension cutoff decreasing the effective tensile strength of the material (Figure 3.1b).

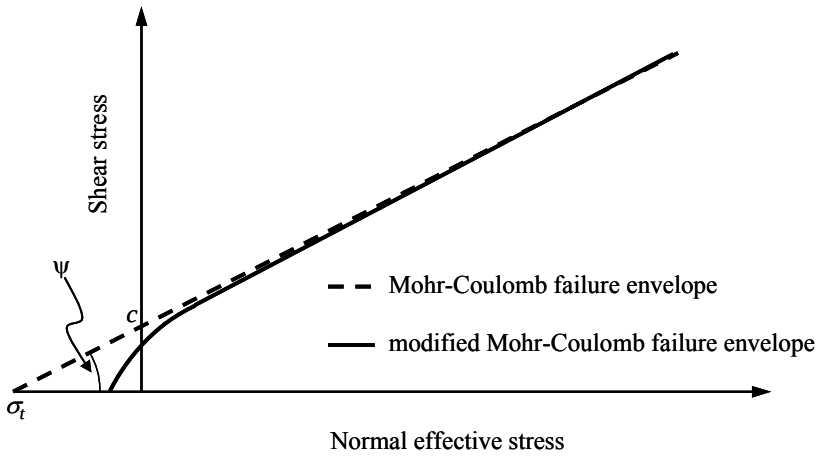

(a)

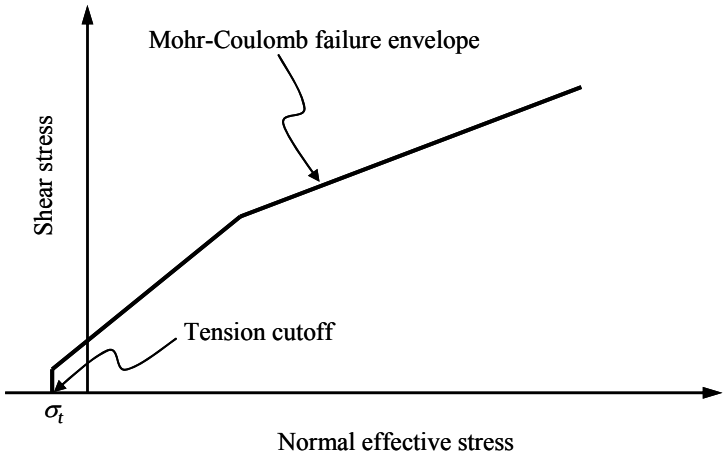

(b)

Figure 3.1 Modeling the reduced tensile strength of particulate materials: (a) modified Mohr–Coulomb criterion [after *Vaziri et al*., 2002] and (b) bilinear Mohr–Coulomb criterion with tension cutoff [after *Nouri et al*., 2003c].

In addition to the shear and tensile failure modes, *Nouri et al*. [2002a] proposed a new concept of volumetric failure. After a period of hydrocarbon production, the pore pressure in a reservoir decreases. The decrease in the pore pressure may cause an increase in the effective stress level, which in turn may lead to the collapse of pores. If sufficient void space exists in the formation, permanent volumetric deformation (distributed in space) may occur. To model the failure of the formation due to the collapse of pores, *Nouri*

et al. [2002b; 2003c] introduced a cap model coupled with the Mohr-Coulomb approach. In this model, when a stress path touches the cap shown in Figure 3.2, pores collapse, which leads to the permanent volumetric deformation.

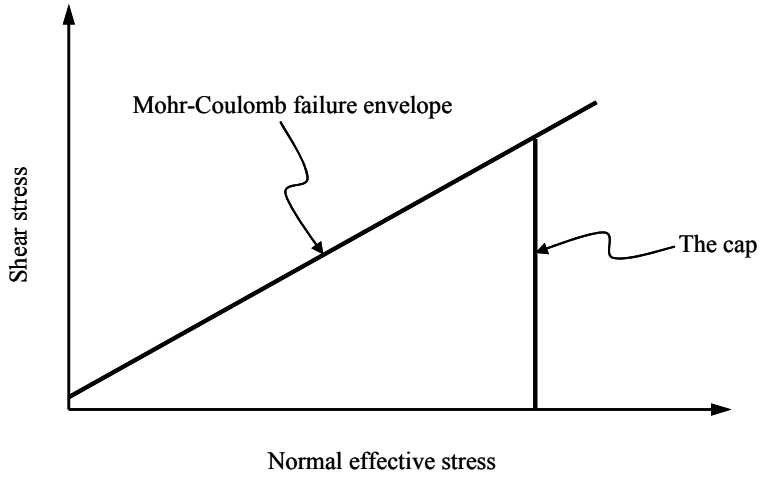

Figure 3.2 Mohr–Coulomb model with a cap [after *Nouri et al*., 2002b]. The cap is represented by a vertical line.

Since the failed particles are not necessarily produced, a sand production criterion defining how the particles are removed from a formation is needed for modeling purposes [*Morita et al*., 1989a; 1998]. *Nouri et al*. [2003a; 2003b; 2003c; 2004] assumed that production of particles occurs if material in the vicinity of a cavity fails in tension if material, which failed in shear, experiences tensile stress. They used a numerical code to model sand production problems. Specifically, *Nouri et al*. [2004] modeled a hollow cylinder compression test (Figure 3.3) using the finite difference code *FLAC* [*Itasca*, 2005].

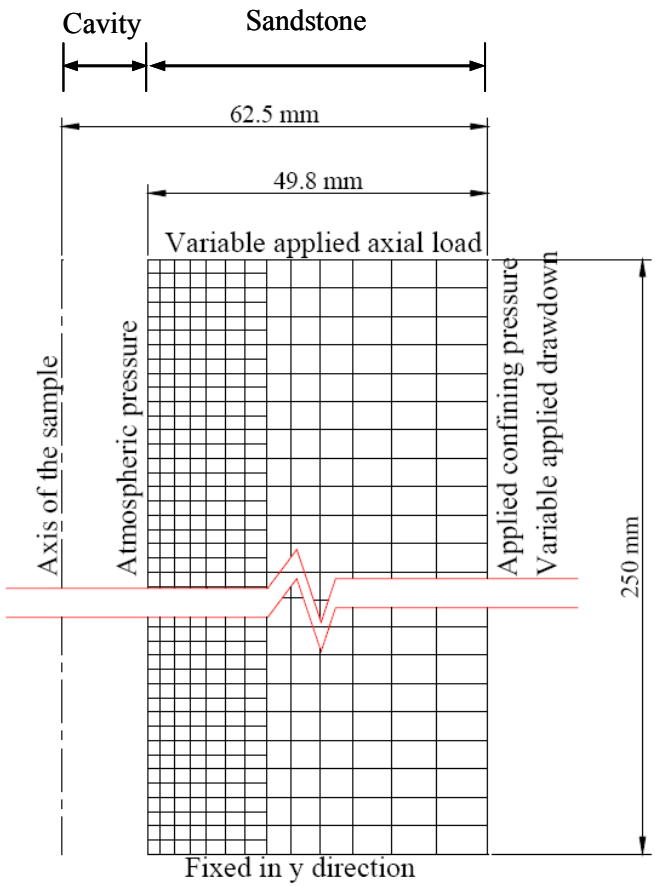

Figure 3.3 Axisymmetrical finite difference (*FLAC*) mesh and boundary conditions for modeling a hollow cylinder compression test [after *Nouri et al*., 2004].

In their simulation, as soon as a region of the model satisfies the sand production criterion, the region is entirely removed from the finite difference mesh. The particle production rate is then calculated based on the cumulative volume of the removed regions. This model assumes that all the failed particles are produced immediately and particle transport is not included in the model.

Geilikman and Dusseault [1997] and *Hoek and Geilikman* [2003] related the sand production rate to the porosity change. They assumed that, if an elastic zone transitions to plasticity, its porosity increases. Such a change in porosity corresponds to an equivalent increase in the volume of the produced particles. As mentioned in Chapter I, their goal was

to evaluate the plastic flow of disintegrated particles (Figure 1.4a) in heavy oil fields, which is beyond the scope of this work.

Papamichos and Stavropoulou [1998], *Papamichos et al*. [2001], *Stavropuolou et al*. [1998], and *Vardoulakis et al*. [1996] introduced a new constitutive equation to model the generation of eroded solid mass to calculate the sand production rate. In their model, erosion is driven by the discharge of the fluidized particles. The solid mass production rate $\dot{m}$ is given by

$$\dot{m} = \rho_s \lambda (1-\phi)\left(1-\frac{c}{c_{cr}}\right) cq \tag{3.2}$$

where ρ_s is the density of a particle, c is the transport concentration of the fluidized particles, ϕ is the porosity of the medium, c_{cr} is a critical value of c for which erosion and deposition of particles balance each other, and q is the flow rate. The parameter λ has a dimension of inverse length, and it is related to the spatial frequency of the potential erosion starter points in the solid skeleton of the porous medium. The value of the λ must be determined experimentally [*Stavropuolou et al*., 1998]. Recently, assuming low particle concentration, *Papamichos and Vardoulakis* [2005] proposed a new constitutive law and expressed the discharge velocity, q_s, of eroded particles as

$$q_s = \lambda_1 \nabla \phi \tag{3.3}$$

where λ_1 is a parameter with the dimension of squared length over time (assumed constant). The new constitutive law suggests that the eroded particle discharge follows a gradient law that enforces particles to exist from regions of increasing porosity [*Papamichos and Vardoulakis*, 2005].

The behavior of particles formed by sand production can also be modeled by using the discrete particle approach. Such production is induced by the interaction of discrete

particles in response to the changes in the stress field and the hydrodynamic forces generated by fluid flow [*Masson and Martinez*, 2000; *Ting et al*., 1989]. Thus, the discrete element method could be appropriate to model sand production phenomena. In the discrete element method, a sand formation is modeled as an assembly of particles and the behavior of each particle is coupled with the fluid flow. For example, *O'Connor et al*. [1997] modeled the behavior of sand particles in the vicinity of a perforation channel (Figure 3.4). They concluded that sand production does not occur below a critical flow rate, and that the increase in the flow rate beyond a critical value induces the instability of the formation in the vicinity of the perforation channel.

Although many theoretical models have been proposed, comparison to field observations has shown limited success, especially for poorly cemented sandstones. Existing models usually define the onset of sand production and evaluate the stability of cavities and surrounding rock formation in the vicinity of wells. The description of the volumetric production rate and its evolution is typically less successful. However, as this production rate is the parameter of greatest practical interest, formulating new models to understand the sand production phenomenon better is highly desirable [*Nouri et al*., 2004].

In this work, we model numerically the behavior of sand formation around a wellbore in order to simulate our experiments (Chapter II). Despite the inherent limitation (i.e., number of particles), the discrete element model has an advantage for modeling the interaction of particles in response to the changes in the stress field and the hydrodynamic forces generated by fluid flow. Since we obtained a well-constrained data set from laboratory experiments on sand production, we use the data for calibrating our numerical model.

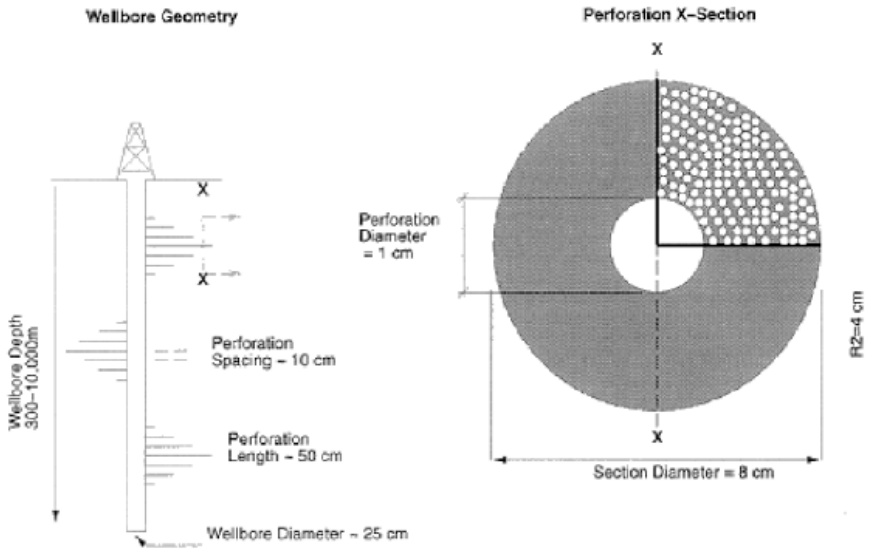

(a)

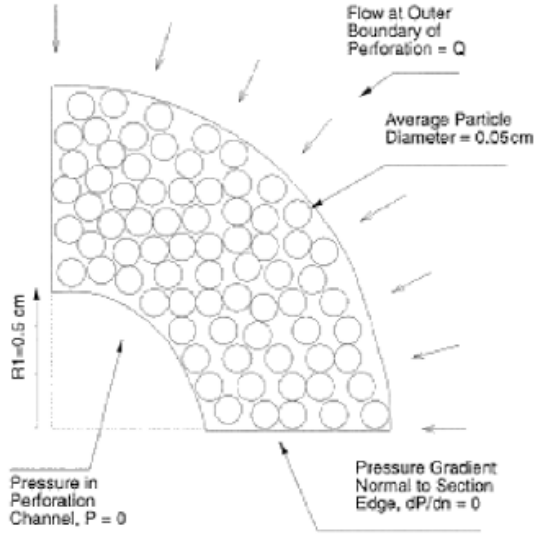

(b)

Figure 3.4 Schematic of a discrete particle model [*O'Connor et al*., 1997]: (a) wellbore and cross-section of a perforation channel and (b) geometry and boundary conditions of the discrete element model. The dimensions of the perforation channel are 1 cm in diameter and 50 cm in length. Due to symmetry, only one quarter of the cross-section of the perforation channel is modeled. Pressure in the perforation is assumed to be zero, and fluid is injected through the outer boundary toward the perforation.

3.2 Scale Analysis of Sand Production

From the results of our experiments (Chapter II), we identified the existence of a cavity and flow channel due to the production of fluid and sand particles (Figure 2.31). We also observed that there was no infiltration of particles through the interior of the sand layer (Figures 2.38 – 2.42). These observations indicate that in our experiments, the production of sand particles were directly related to the creation of the cavity and the flow channel. That is, most erosion of particles occurred on the surface of the cavity and the flow channel, and the removed particles were produced together with fluid. It appears, therefore, that the surface erosion model (Figure 1.4b) rather than plastic flow of disintegrated material (Figure 1.4a) is more appropriate to describe the behavior of unconsolidated sand layers around a well – unless the sanding condition described by *Geilikman and Dusseault* [1997] takes place. To evaluate the validity of the surface erosion model, we first conduct a simple scale analysis using a set of field data. Consider fluid flow from a petroleum reservoir into a well with parameters shown in Table 3.1.

The fluid flow rate through a perforation q_1 is given by

$$q_1 = \frac{q}{NH} \tag{3.4}$$

where q is the fluid flow rate, N is the perforation density, and H is the perforation interval (Figure 3.5). Assuming fluid velocity to be the fastest at the borehole wall, the fluid velocity at the cavity surface in the vicinity of a perforation scales as

$$v_d = \frac{q_1}{d_s^2} \tag{3.5}$$

where v_d is the Darcy's velocity at the cavity surface, and d_s is the cavity size.

Table 3.1 Parameters characteristic for reservoirs producing sand [*Bradely*, 1987; *Charlez*, 1997; *Dake*, 1978; *Economides et al*. 1998; *Kooijman et al.*, 1992]

Parameter	Symbol	Value	Petroleum unit
Permeability	k	3.65×10^{-13} m^2	365 md
Dynamic viscosity of fluid	μ	0.01 Pa·sec	10 cP
Density of fluid	ρ_f	9.81 kN/m^3	62.4 lb/ft^3
Internal friction angle	Ψ	38°	38°
Cohesive strength of medium	c	0.1 MPa	14.5 psi
Porosity	ϕ	0.26	26%
Biot poroelastic constant	β	0.8	0.8
Pressure in well	p_0	69 kPa	10 psi
Pressure in reservoir	p_f	3.4 MPa	490 psi
Stress at infinity	σ	13.8 MPa	2000 psi
Fluid production rate per well	q	1.84×10^{-4} m^3/sec	100 bbl/day
Perforation density	N	33 m^{-1}	10 ft^{-1}
Perforation interval	H	9.1 m	30 ft
Sand production cavity size	d_s	10 cm*	3.94 inch
Size of a particle	d_p	100 μm	3.94×10^{-3} inch

*Assumed value based on the field data from *Ispas et al*. [2002] and *Risnes et al*. [1982]

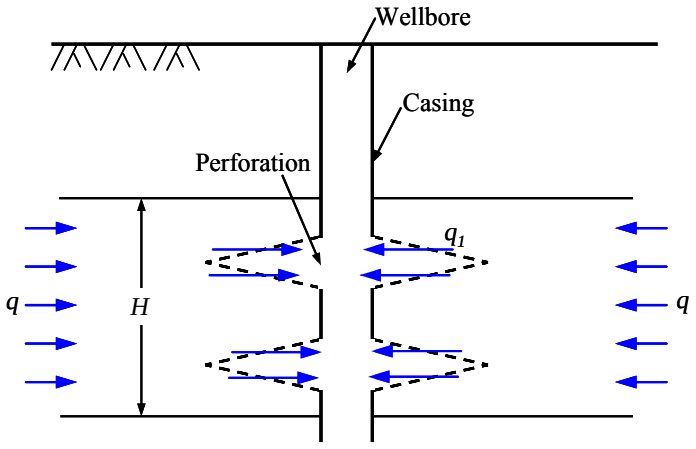

Figure 3.5 Schematic of a petroleum well, where q is the fluid flow rate (toward the well), q_l is the fluid flow rate through a perforation, and H is the perforation interval.

Fluid velocity, v_f, through the pores and Darcy's velocity are related by [*Bear*, 1972]

$$v_f = \frac{v_d}{\phi} \tag{3.6}$$

Using parameters in Table 3.1, we calculate the fluid velocity at the cavity surface to be of the order of 10^{-4} m/sec. Then, the Reynolds number of the fluid flow in a porous medium is given by [*Bear*, 1972]

$$\mathrm{Re} = \frac{\rho_f v_f d_p}{\mu} \tag{3.7}$$

where ρ_f is the fluid density, d_p is the particle diameter, and μ is the fluid dynamic viscosity. Using the porosity, particle size, and dynamic viscosity given in Table 3.1, we estimate that Re ~10^{-3}. For Re < 2000, fluid flow can be considered laminar [*Janna*, 1993]. In this case, therefore, fluid flow through this medium is classified as a laminar flow.

The hydrodynamic force of fluid flow on a particle can be represented as a function of the drag force and a force related to the pressure gradient [e.g., *Charlez*, 1997]. For laminar flow, the drag force F_d, applied to a particle, scales as [*Asgian et al.*, 1995]:

$$F_d = \alpha v_f d_p \mu \tag{3.8}$$

where α~10 (for spherical particles, its value is 3π [*Asgian et al.*, 1995]). The magnitude of the Darcy's velocity in a porous medium is given by

$$v_d = \frac{k}{\mu}|\nabla p| \tag{3.9}$$

where k is the permeability of a porous medium, and ∇p is the pressure gradient. From (3.6), (3.8), and (3.9), we obtain that

$$F_d = \frac{\alpha d_p k}{\phi} |\nabla p| \tag{3.10}$$

The part of the hydrodynamic force related to the pressure gradient F_p is estimated by [*Asgian et al.*, 1995]:

$$F_p = \gamma d_p^3 |\nabla p| \tag{3.11}$$

where γ is a constant of the order of 1 (for spherical particles, its value is $\pi/6$ [*Asgian et al.*, 1995]). Therefore, from (3.10) and (3.11), the total hydrodynamic force F_h on a particle due to the fluid flow scales as

$$F_h = F_p + F_d = \left(\frac{\alpha d_p k}{\phi} + \gamma d_p^3 \right) |\nabla p| \tag{3.12}$$

Using the Mohr-Coulomb model (3.1), we conclude that the resistance force F_r against the particle removal is

$$F_r = \beta d_p^2 [c + (\sigma - p) \tan \Psi] \tag{3.13}$$

where $\beta \sim 1$, c is the cohesion, σ is the total stress, and Ψ is the internal friction angle. In the simplest approach, if the hydrodynamic force exceeds the resistance force, the particle is removed from the medium and produced. Therefore, the condition of particle production is given by

$$F_d + F_p \geq F_r \tag{3.14}$$

and from (3.10) – (3.14), we obtain the critical pressure gradient that results in the particles being removed from the formation:

$$|\nabla p| = \frac{\beta d_p}{\left(\frac{\alpha k}{\phi} + \gamma d_p^2\right)}\left[c + (\sigma - p)\tan\Psi\right] \tag{3.15}$$

For parameter values given in Table 3.1, we obtain that the ratio of γd_p^2 to $\alpha k/\phi$ is ~10^3. This indicates that the drag component of the hydrodynamic force in (3.12) and (3.15) is negligible. Thus, (3.15) becomes

$$|\nabla p| = \frac{\beta}{\gamma d_p}\left[c + (\sigma - p)\tan\Psi\right] \tag{3.16}$$

Furthermore, given parameter values from Table 3.1, the critical pressure gradient required to remove a particle from an assembly of particles is $|\nabla p| \sim 10^2$ MPa/mm. On the other hand, an upper bound of the pressure gradient along the diameter of a particle is given by

$$|\nabla p|_{\max} = \frac{p_f - p_0}{d_p} \tag{3.17}$$

where p_f is the original fluid pressure in the reservoir, and p_0 is the fluid pressure in the well. Such a pressure gradient would occur in the porous medium if pressure in the well were instantaneously reduced from p_f to p_0. Expression (3.17) and the parameter values in Table 3.1 result in $|\nabla p|_{\max} \sim 10$ MPa/mm. Thus, the *required* pressure gradient, $|\nabla p|$, at the cavity surface (needed to remove a particle) is an order of magnitude greater than the upper limit of *available* pressure gradient, which is $< |\nabla p|_{\max}$.

Similarly, using (3.9), (3.13) and (3.17), the *required*, v, and the possible maximum *available*, $v_{\max}$, fluid velocities at the cavity surface to induce particle production are given by

$$v = \frac{k}{\mu}\frac{\beta}{\gamma d_p}\left[c + (\sigma - p)\tan\Psi\right] \tag{3.18}$$

$$v_{\max} = \frac{k}{\mu}\frac{p_f - p_0}{d_p} \tag{3.19}$$

Using parameter values from Table 3.1, we obtain that v ~10 m/sec and $v_{\max}$ ~ 1 m/sec. Similar to the pressure gradient, the fluid velocity, v, at the cavity surface, which is needed to remove a particle, is at least an order of magnitude greater than the upper limit, $v_{\max}$, of the *available* fluid velocity.

In case of an unconsolidated petroleum reservoir (with uncemented particles), the medium cohesion (c) can be considered zero (similar to the model of *Charlez* [1997] described in Sections 1.1 and 2.6). Then, using (3.17) and parameters listed in Table 3.1, we find $|\nabla p| \sim 10^2$ MPa/mm and $|\nabla p|_{\max} \sim 10$ MPa/mm. Therefore, even when c = 0, the required pressure gradient, $|\nabla p|$, is still at least an order of magnitude greater than the upper limit of available pressure gradient, $|\nabla p|_{\max}$.

From this scale analysis, we infer that the hydrodynamic forces generated by fluid flow are unlikely to remove particles directly from a yielding formation. Using slightly different consideration, *Charlez* [1997] also concluded that the critical fluid flow rate to induce removal of particles around a wellbore would be unrealistically high even in the absence of cementation between the particles. In both cases, the larger values of the fluid velocity sufficient to remove the particles resulted from the assumption that the total stress in (3.15) and (3.16) scales with the remote stress, σ. This resulted in large values of

hydrodynamic force and fluid velocity needed to remove a particle from a yielding formation. In sections 2.6 and 2.7, we suggested that formation load on the particle located near the erosion boundary may be much smaller (Figure 2.56) and determined only by the weight of the neighboring particles. This allowed us to reconcile much lower velocities observed in our experiments with the model based on consideration similar to (3.15) and (3.16). To understand the erosion process in more detail, we further employed a numerical approach to account for the removal of particles from a formation as well as transport of the removed particle due to fluid flow to adequately account for the mechanism of sand production.

3.3 Discrete Element Method (DEM)

For numerical analysis, we use the codes PFC^{2D} and PFC^{3D} [*Itasca*, 2002; 2006]. They model two- (PFC^{2D}) and three- (PFC^{3D}) dimensional behavior of stressed assemblies of particles using the discrete element method (DEM). Particle interaction is treated as a dynamic process. The dynamic behavior of particles is calculated numerically using an explicit time-stepping algorithm with a central difference scheme [*Potyondy and Cundall*, 2004].

3.3.1 Background of PFC^{2D}/PFC^{3D}

The PFC^{2D} and PFC^{3D} codes are composed of two components: particle and wall. A particle occupies a finite amount of space and interacts only at contacts or interfaces between particles or walls. The behavior of particles is modeled based on the following assumptions:

- Circular (2-D) or spherical (3-D) particles are rigid.
- At contact points, particles are allowed to overlap one another instead of becoming deformed in shape.

- The magnitude of the overlap is related to the contact force calculated using force displacement laws. All overlaps are small relative to the particle sizes.

A wall is a line (2-D) or plane (3-D) segment with arbitrarily defined contact properties to account for the interaction with the particles. The wall is typically used to apply velocity boundary conditions to assemblies of particles to provide confinement. Particles and walls interact via forces at the contacts [*Itasca*, 2002; 2006].

At the start of each calculation step, all the contacts between particles and between particles and walls are updated using the positions of particles and walls known from a previous calculation step. Then, the chosen force-displacement law is applied to each contact to update the contact force based on the relative motion between the two entities at the contact, and the contact constitutive model.

In PFC^{2D} and PFC^{3D}, the interaction between particles is determined by the contact model. In particular, a linear contact model and a Hertz-Mindlin contact model are provided. In this work, we adopted the linear contact model. The linear contact model requires normal and shear stiffnesses at the contact between two particles (Figure 3.6). In both cases, contact forces in normal and shear directions are calculated as

$$F^n = K^n u^n \tag{3.20}$$

$$F^s = -K^s u^s \tag{3.21}$$

where F is the contact force, K is the stiffness between particles at a contact with the dimension $[F/L]$, u is the relative displacement, and superscripts n and s represent the normal and shear directions, respectively.

To model shear strength between two particles, a slip model is provided in PFC^{2D} and PFC^{3D}. If the shear force between two particles remains less than a maximum allowable shear force, a force equilibrium between the two particles exists and the particles are in rest. However, the two particles will start to slip relative to each other if the shear

force exceeds the maximum allowable (critical) shear force, $F_{\max}^{s}$. The criterion of the slip is defined by

$$F_{\max}^{s} = f_{\mu}\left|F_{i}^{n}\right| \tag{3.22}$$

where f_{μ} is the interparticle friction coefficient and F_{i}^{n} is the normal contact force in i direction.

During each calculation step in the PFC^{2D} and PFC^{3D} algorithms, the contact models are used to determine the contact force between particles. Then, an equation of motion is applied to each particle to calculate its velocity and position based on the resultant force and moment from the contact model. This calculation cycle is repeated for every calculation step.

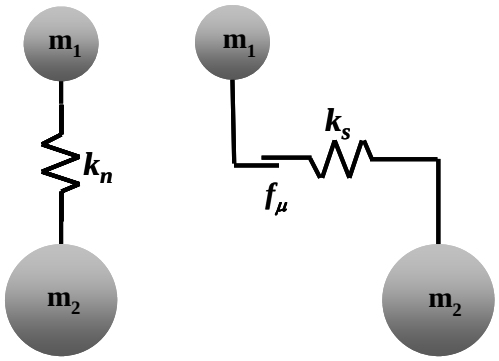

Figure 3.6 Linear contact model in PFC^{2D} and PFC^{3D}: (a) normal direction and (b) shear direction [*Itasca*, 2002; 2006]. Here, k_n is the normal stiffness, k_s is the shear stiffness, f_{μ} is the interparticle friction coefficient, and m_1 and m_2 are the mass of particles 1 and 2, respectively.

3.3.2 Fluid Flow Implementation in PFC^{2D} and PFC^{3D}

To model fluid flow through a porous medium, PFC^{2D} and PFC^{3D} adopt two approaches: "pipe" model and "fixed coarse-grid" model [*Itasca*, 2002; 2006]. The "pipe" model is typically used for material with relatively low initial porosity (e.g., granite). In this case, particles do not directly correspond to rock grains but rather provide a means to discretize the space and simulate appropriate mechanical behavior. Assembly of particles is considered a network within the "domain", which, in turn, is defined as a closed chain of particles. A "domain" denotes a closed loop in the topological sense, and is used to describe a space enclosed by a group of particles independently of the geometry. Fluid flows through "pipes" between two adjacent "domains", and a "pipe" is equivalent to a parallel-plate channel (PFC^{2D}) or a cylindrical tube (PFC^{3D}). The flow rate, q, in a pipe is given by [*Itasca*, 2002]

$$q = ka^3 \frac{p_2 - p_1}{L} \tag{3.23}$$

where k is a conductivity factor, a is the aperture, L is the length, and $p_2 - p_1$ is the pressure difference between the two adjacent domains. When fluid flows toward a domain through the surrounding pipes, the change in fluid pressure, Δp, in the "domain" is [*Itasca*, 2002]

$$\Delta p = \frac{K_f}{V_d}(\Sigma q \Delta t - \Delta V_d) \tag{3.24}$$

where K_f is the bulk modulus of fluid, V_d is the apparent volume of the domain, Σq is the summation of flow rate toward the "domain" through the surrounding "pipes", and Δt is the time step.

The coupling between fluid flow and mechanical behavior of particles is done by considering the polygonal path that joins the contacts surrounding a given domain. Then, the force vector, F_i, on a particle is given by [*Itasca*, 2002]

$$F_i = pn_i s \tag{3.25}$$

where n_i is the unit normal vector of the line joining two contact points on the particle (PFC^{2D}) or the unit normal vector of the line joining the centers of a domain and a particle (PFC^{3D}), and s is the length of the line (PFC^{2D}) or the projective area on the particle determined by the three contacting points with three neighboring particles, which comprise the domain (PFC^{3D}).

In the "fixed coarse-grid" fluid model, the void geometry in the assembly of particles is regarded as identical to the actual space between particles. This approach is considered appropriate for a rock with relatively high porosity, such as sandstone [*Itasca*, 2002]. In this case, both PFC^{2D} and PFC^{3D} consider solids as discrete particles, whereas they model fluid as a continuum [*Shimizu*, 2004]. In this work, we investigate the behavior of a sand layer with relatively high permeability and porosity. Thus, we adopt the "fixed coarse-grid" fluid approach.

To model fluid flow in the "fixed coarse-grid" fluid model, the mass continuity equation and Navier-Stokes equation are solved numerically in Eulerian Cartesian coordinates based on locally averaged quantities, i.e., averaged over each grid element. The mass continuity equation and Navier-Stokes equation for fluid phase in a fluid-solid two-phase flow model for incompressible fluid are given by

$$\frac{\partial \phi}{\partial t} = -\nabla_i (\phi v_i) \tag{3.26}$$

$$\frac{\partial (\phi v_f)}{\partial t} = -\nabla \cdot (\phi v_i v_j) - \frac{\phi}{\rho_f}\frac{\partial p}{\partial x_i} - \frac{\phi}{\rho_f}\nabla \cdot \tau_{ij} + \phi g_i + \frac{f_i}{\rho_f} \tag{3.27}$$

where v_i is the fluid velocity, τ_{ij} is the viscous stress tensor, g_i is the vector of gravitational acceleration, and f_i is the body force related to the interaction between particles and the fluid. The interaction f_i between a particle with unit volume and the fluid is given by [*Itasca*, 2002; 2006]

$$f_i = \phi \frac{\partial p}{\partial x_i} \tag{3.28}$$

where $\partial p / \partial x_i$ is the pressure gradient. Then, the total driving force F_i applied to a particle is [*Itasca*, 2002; 2006]

$$F_i = -\left(\frac{f_i}{1-\phi} + \frac{\partial p}{\partial x_i} \right) \frac{\pi}{6} d_p^3 \tag{3.29}$$

and substituting (3.28) into (3.29) results in [*Asgian et al*., 1995]

$$F_i = -\frac{1}{1-\phi} \frac{\pi}{6} \frac{\partial p}{\partial x_i} d_p^3 \tag{3.30}$$

3.3.3 Macro- vs. Micro-scale Material Properties

It is relatively straightforward to specify macro-scale material properties (e.g., Young's modulus, Poisson's ratio, internal friction angle, and cohesion) required for numerical analysis codes based on continuum mechanics because such macro-scale properties can be directly obtained from laboratory tests [*Itasca*, 2002] or used as fitting parameters in scale-dependent cases [e.g., *Murdoch and Slack*, 2002].

In a discrete element method, the micro-properties (e.g., shear and normal contact stiffnesses, and friction coefficient between particles) are typically used as input parameters. The micro-properties control the behavior of each particle and, as a result, they determine the macro-scale behavior of material. Thus, a multi-scale analysis is required to

derive the relationship between macro- and micro-scale properties [*Masson and Martinez*, 2000].

Several theoretical relationships between macro- and micro-scale properties have been suggested. For example, *Chang and Misra* [1990] derived a relationship between the normal and shear stiffnesses of particles (micro-scale) and the elastic modulus and the Poisson's ratio of a particulate medium (macro-scale). The effective Young's modulus, E, and Poisson's ratio ν have the following forms:

$$E = \frac{2R^2 N K_n}{3V}\left(\frac{2+3K_s/K_n}{4+K_s/K_n}\right),\ \nu = \frac{1-K_s/K_n}{4+K_s/K_n} \tag{3.31}$$

where R is the particle radius, N is the number of contact per particle, K_n is the normal contact stiffness with the dimension [F/L], K_s is the shear contact stiffness with the dimension [F/L], and V is the volume of packing. Using parameters, R = 0.254 mm (0.01 in), $N/V = 8.35\times10^{10}$ m^{-3} (1.37×10^{6} in^{-3}), and $K_n = 3.46\times10^{5}$ N/m (1973 lb/in), *Chang and Misra* [1990] showed that the Young's modulus increases (Figure 3.7a) while the Poisson's ratio decreases (Figure 3.7b) with increasing ratio K_s/K_n (Figure 3.7b). Their results indicate that the ratio K_s/K_n is an important parameter determining effective elastic properties of a particulate medium.

Bathurst and Rothenburg [1992] obtained similar relationships between the shear modulus, G, and the Poisson's ratio, ν, and micro-scale parameters for a 2-D disc packing:

$$G = \frac{RN\zeta K_n}{4A}\left(\frac{1+K_s/K_n}{2}\right),\ \nu = \frac{1-K_s/K_n}{3+K_s/K_n} \tag{3.32}$$

where ζ is a constant and A is the area of the assembly of particles. *Bathurst and Rothenburg* [1992] did not specify the value of ζ.

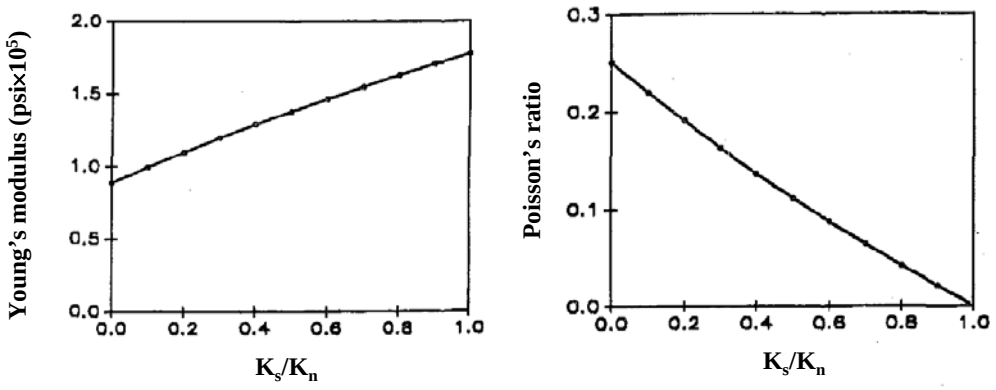

(a) (b)

Figure 3.7 (a) Young's modulus and (b) Poisson's ratio as functions of K_s/K_n [*Chang and Misra*, 1990].

Based on dimensional analysis, *Huang* [1999] suggested scaling laws

$$E = K_n \Phi_E \left(\frac{K_s}{K_n}, \phi \right), \ \nu = \Phi_\nu \left(\frac{K_s}{K_n}, \phi \right) \tag{3.33}$$

where Φ_E and Φ_ν are dimensionless functions. In the case of plain strain conditions and uniaxial loading, 2-D parameters E' and ν' are defined as [*Huang*, 1999]

$$E' = \frac{\Delta \sigma_{yy}}{\varepsilon_{yy}}, \ \nu' = -\frac{\varepsilon_{xx}}{\varepsilon_{yy}} \tag{3.34}$$

where

$$E' = \frac{E}{1-\nu^2}, \ \nu' = \frac{\nu}{1-\nu} \tag{3.35}$$

Huang [1999] conducted numerical biaxial compression tests using *PFC*^{2D} with porosity ϕ = 0.17, interparticle friction coefficient f_μ = 0.839, and radius of particles R = 1.25 mm. She showed that the scaled Young's modulus E' increases (Figure 3.8a), whereas the scaled Poisson's ratio ν' (Figure 3.8b) decreases with increasing ratio K_s/K_n. These results

are consistent with *Chang and Misra* [1990]. Thus, a particulate medium becomes stiffer as the ratio K_s/K_n increases, and ratio K_s/K_n is important parameter determining the effective elastic properties of a particulate medium.

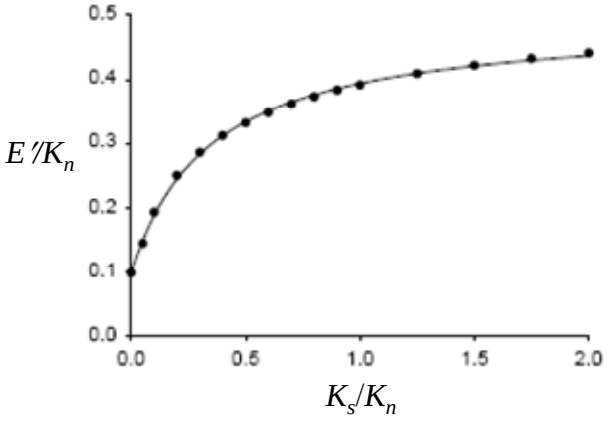

(a)

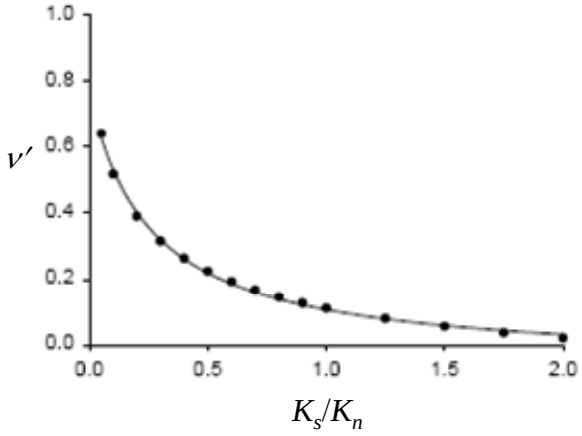

(b)

Figure 3.8 (a) Scaled Young's modulus and (b) Poisson's ratio as functions of ratio K_s/K_n for ϕ = 0.17, f_μ = 0.839, and R = 1.25 mm [*Huang*, 1999].

Skinner's [1969] experiments indicate that the internal friction angle from direct shear tests does not increase with increasing values of interparticle friction coefficient. He conducted direct shear tests using glass beads with a diameter of 1 mm and normal stress of 24.7 kPa (3.58 psi). He prepared two samples, dry and flooded with distilled water. The interparticle friction coefficient for the dry sample was 0.07, whereas that for flooded one was 0.72.

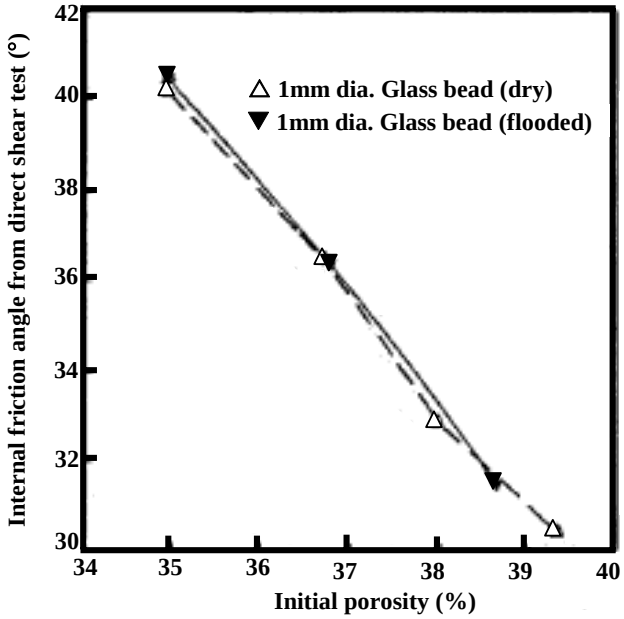

Figure 3.9 Internal friction angles from direct shear tests for dry and flooded samples as functions of the initial porosity of the samples [after *Skinner*, 1969]. Here, the interparticle friction coefficient for the dry glass bead is approximately 0.07, whereas that for the flooded sample is 0.72. Note that the internal friction angles with dry and flooded samples do not show significant difference.

Figure 3.9 shows that the internal friction angle from direct shear tests does not change significantly with respect to the interparticle friction coefficient. That is, although the interparticle friction coefficient for the flooded sample is approximately an order of magnitude greater than that for the dry one, the internal friction angles with respect to

initial porosity in Figure 3.9 for the two samples show no significant difference. The increase in the interparticle friction coefficient observed by *Skinner* [1969] in response to flooding is caused by an interlocking mechanism related to the adsorption of water molecules onto the polished mineral surface (e.g., quartz, feldspar, and calcite) [*Nascimento*, 1981]. In general, however, interparticle friction coefficient of wet particles is smaller than that of dry particles [e.g., *Silvani et al.*, 2008]. S*kinner*'s [1969] work indicates that the internal friction angle from the direct shear tests does not increase significantly with the increasing values of the interparticle friction coefficient.

Oger et al. [1998] also found that the internal friction angle is weakly dependent on the interparticle friction coefficient except in its lower range. They conducted 2-D biaxial compression tests with assemblies of disc shaped particles (Figure 3.10) with particle radii variation ranging from 10% to 40% of the mean particle radius. They described the relationship between the interparticle friction coefficient and the internal friction angle, which is presented in Figure 3.11, which shows that the internal friction angle is almost constant for the five cases (particle radii variation ranges from 10% to 40% of the mean particle radius) except when the interparticle friction coefficient is less than 0.2. This indeed indicates that the internal friction angle is weakly dependent on the interparticle friction coefficeint except in the lower range of the interparticle friction coefficient.

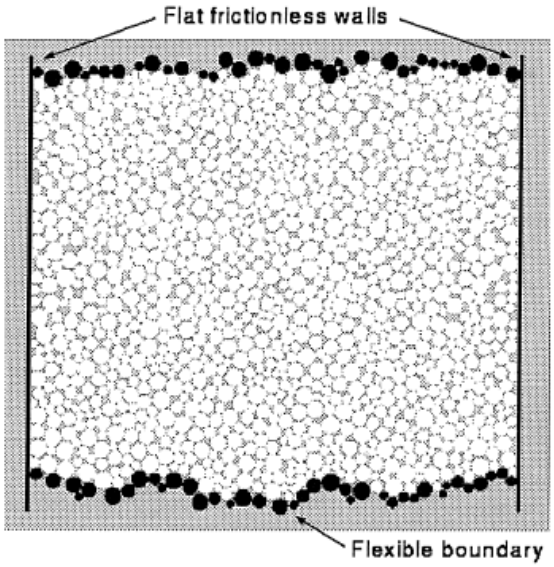

Figure 3.10 Initial configuration of the sample for biaxial compression test [*Oger et al*., 1998].

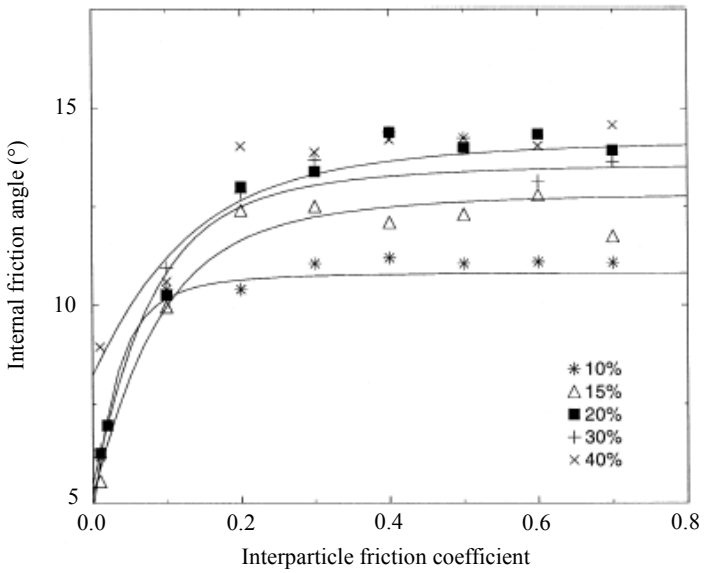

Figure 3.11 Internal friction angle with respect to interparticle friction coefficient [after *Oger et al*., 1998] using assemblies of disc shaped particles (Figure 3.10) with particle radii variation ranging from 10% to 40% of the mean particle radius. The marks represent the results of 2-D biaxial compression tests, and the solid lines are fitting curves for each case.

These are only two examples of many showing that, due to the complex nature of particulate materials, it is difficult to predict the macro-scale behavior from micro-scale properties [e.g., *Huang*, 1999; *Itasca*, 2002; *Potyondy and Autio*, 2001]. Thus, calibration processes are required to determine the relationship between macro- and micro-scale material properties. One can perform, for example, numerical tests using various sets of micro-properties and then compare the results with the desired response of the real material until both of them match [*Potyondy and Cundall*, 2004]. Biaxial tests in 2-D modeling and triaxial tests in 3-D modeling are often used as numerical tests for calibrating macroscopic properties of the modeled material [*Potyondy and Autio*, 2001; *Potyondy and Cundall*, 2004]. Mohr-Coulomb yield criteria are generally used to describe the strength of particulate materials. For the biaxial (2-D) and triaxial (3-D) tests, PFC^{2D} and PFC^{3D} provide only rigid boundary conditions. In other words, lateral boundaries are constrained by rigid walls, so that boundary condition is controlled displacement rather than constant stress. Such a displacement controlled boundary condition may excessively restrict the formation of shear band [*Kuhn*, 1995]. Thus, simulations with the displacement controlled boundary conditions may not successfully reproduce the characteristic behavior [*Kuhn*, 1995] and the material properties [*Ng*, 2004] of real particulate media.

Therefore, in this work, we used the repose angle measurements (Figure 3.12) as a calibration test instead of biaxial or triaxial tests. We found that, for the friction coefficient of 0.7, the normal stiffness of 10^6 N/m, the shear stiffness of 10^6 N/m, and the mean particle diameter of 4 mm, the repose angle of the particulate material is 20°, which is much smaller than that of real sand sample (32° – 33°) given in Table 2.4.

In general, the internal friction angle from discrete element model is significantly less than the inter- particle friction angle for real particles [*Bardet and Proubet*, 1991]. *Potyondy and Cundall* [2004] explained that this discrepancy may be due to the use of circular or spherical particles in the discrete element models. Such a discrepancy could be

reduced by using particle shapes that more closely resemble the complex-shaped and highly interlocked crystalline particles. This is beyond the scope of this work, however.

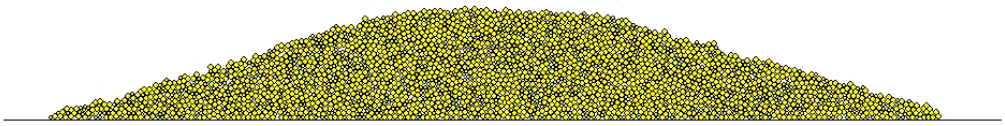

Figure 3.12 Repose angle measurement (2-D) as a calibration of the micro-scale parameters for PFC^{2D} and PFC^{3D}. The friction coefficient is 0.7, and the mean particle diameter is 4 mm.

3.4 Determination of Parameters

In our experimental setup (Chapter II), the geometry of a sand layer is a flat cylinder (layer) with a polycarbonate tubing located at the center of the layer (Figures 2.10 and 2.13). Fluid is injected at the perimeter of the layer and flows radially toward the tubing. This entire setup can be considered axisymmetric.

In our experiments (Section 2.4.1), the sand layer in the chamber has a height of ≈8 cm and a radius of 50 cm (Figure 2.26). The initial porosity is approximately 0.34. The mean particle size is 110 μm. Therefore, the estimated number of particles in the chamber is of the order of 10^{10}. From preliminary modeling, we found that it takes about one month to model 10^5 particles with a diameter of 4 mm using a computer with a 2.4 GHz CPU and 1 GB RAM for a PFC^{3D} model. Therefore, it is not feasible to model the behavior of all particles in the chamber. Thus, we only modeled a part of the experimental setup.

The calculation speed in PFC^{2D} and PFC^{3D} is also controlled by the particle sizes. The time step in mechanical calculation in PFC^{2D} and PFC^{3D} is given by [*Itasca*, 2002; 2006; *Shimizu*, 2004].

$$\Delta t = \sqrt{\frac{m}{K}} \tag{3.36}$$

where m is the mass of a particle and K is the stiffness at the contact between particles. The mass of a spherical particle is

$$m = \rho_s \frac{\pi}{6} d_p^3 \tag{3.37}$$

where ρ_s is the particle density, and d_p is the particle diameter. Hence, assuming that the stiffness and the density of a particle are constant in (3.36) and (3.37), the time step and particle diameter have the following relationship:

$$\Delta t \propto d_p^{3/2} \tag{3.38}$$

According to (3.38), as the diameter of particles increases, the total calculation time is reduced due to the increase in the time step.

To obtain a realistic calculation speed, the number of particles in the model needs to be reduced and the diameter of the particles needs to be increased. Therefore, results obtained below should be viewed as somewhat qualitative. Nevertheless, they provide an important insight in the mechanism of sand production.

3.5 Two-Dimensional Modeling

3.5.1 Model Setup

We first consider a cross-section in our experimental setup shown in Figure 3.13. In this work, 2-D particles are considered to be cylindrical. Assuming that the particle diameters are identical, the geometric arrangement of particles is close to cubic tetrahedral. Therefore, the 2-D porosity of the cross-section is approximately 0.12. Other parameters used for the 2-D modeling are shown in Table 3.2.

The boundary conditions of the model are shown in Figure 3.14. The top, bottom, and left walls have zero displacement and zero flow boundary conditions. The right wall has zero displacement boundary condition and a constant flow velocity boundary condition for the fluid. The width of the setup used for a PFC^{2D} model is 0.75 m. The radius of the sand layer in experiment is 0.5 m, but we increased the width of the model to decrease the boundary effect (without increasing the calculation speed significantly). In addition, the out-of-plane thickness of the model is unit length (1 m).

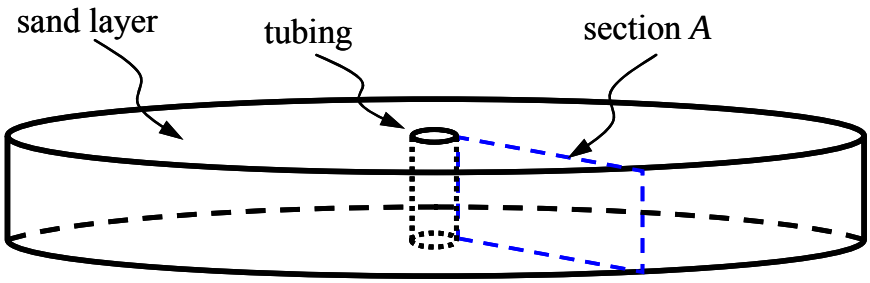

Figure 3.13 Section A in the sand layer of an experimental setup to be modeled using PFC^{2D} (not to scale).

Table 3.2 Parameters used for input data of *PFC*^{2D} model

Parameter	Value	Petroleum unit
Particle diameter	4 mm	0.157 in
Number of particles	3931	-
Initial porosity	0.12	-
Normal stiffness	10^6 N/m	-
Shear stiffness	10^6 N/m	-
Friction coefficient	0.7	-
Particle density	2650 kg/m^3	165.4 lb/ft^3
Confining stress	10 kPa	1.45 psi
Fluid density	1000 kg/m^3	62.4 lb/ft^3
Dynamic viscosity of fluid	10^{-3} Pa·sec	1 cP
Fluid injection rate	3×10^{-5} m^3/sec/m	3.2×10^{-4} ft^3/sec/ft

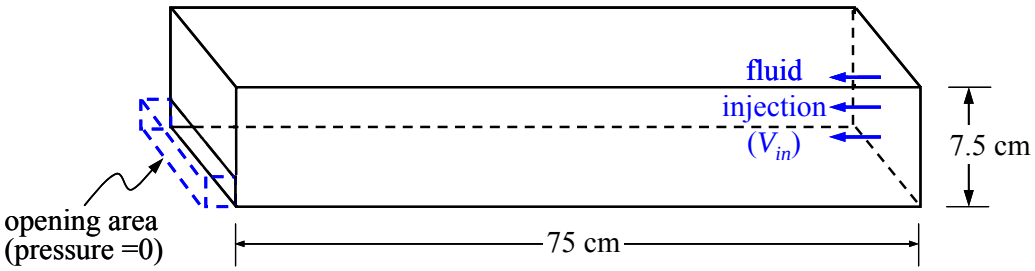

(a)

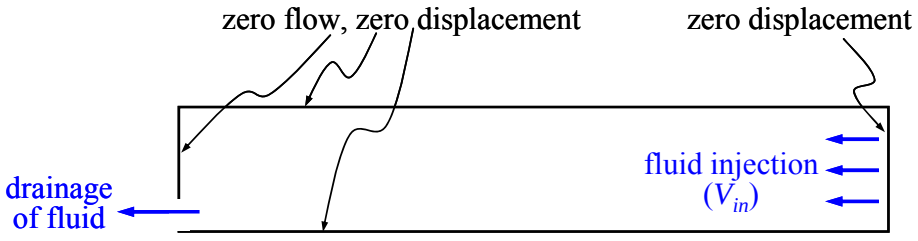

(b)

Figure 3.14 Boundary conditions for the *PFC*^{2D} model (not to scale): (a) 3-D view and (b) 2-D view. The thickness of the model in the direction out of the page is unit length (1.0 m). Fluid is injected with a velocity V_{in}. Fluid pressure in the opening area is maintained to be zero to simulate an atmospheric drainage area. Except for the right wall, the other walls have no flow boundary conditions imposed.

To simulate the experimental setup, at the right end boundary, fluid is injected with a velocity V_{in} (Table 3.2), which models the incoming flow from the pump (Figure 3.14). As in the experimental setup, the flow velocity is controlled instead of the injection pressure. At the corner of the left end, there is an opening area to simulate the perforation in the wellbore. The fluid pressure in this area is maintained to be zero to simulate the drainage area. The opening size of the drainage area is determined to be of 1.5 cm (≈4 particle diameters) in height based on the results of preliminary calculations, so that it does not induce bridging of the particles around the opening.

3.5.2 Results of Calculations

The assembly of particles at the initial state is shown in Figure 3.15. The entire domain is divided into 12 subdomains. The color of particles in each subdomain is different from each other to trace the movement of particles. At the time of 6.7 sec shown in Figure 3.16a, a cavity forms around the opening. We can observe the initiation of a surface flow channel. Figure 3.16b shows that the contact force behind the cavity apparently decreases compared to those areas located far from the drainage area. In Figure 3.16c, we show the fluid flow vectors. By comparing Figures 2.54b and 3.16c, we can see the impact of the surface flow channel on the fluid flow pattern.

Figure 3.15 Assembly of particles from the results of *PFC*^{2D} modeling at initial state. Regions 1 and 2 are the same as in Figure 3.16.

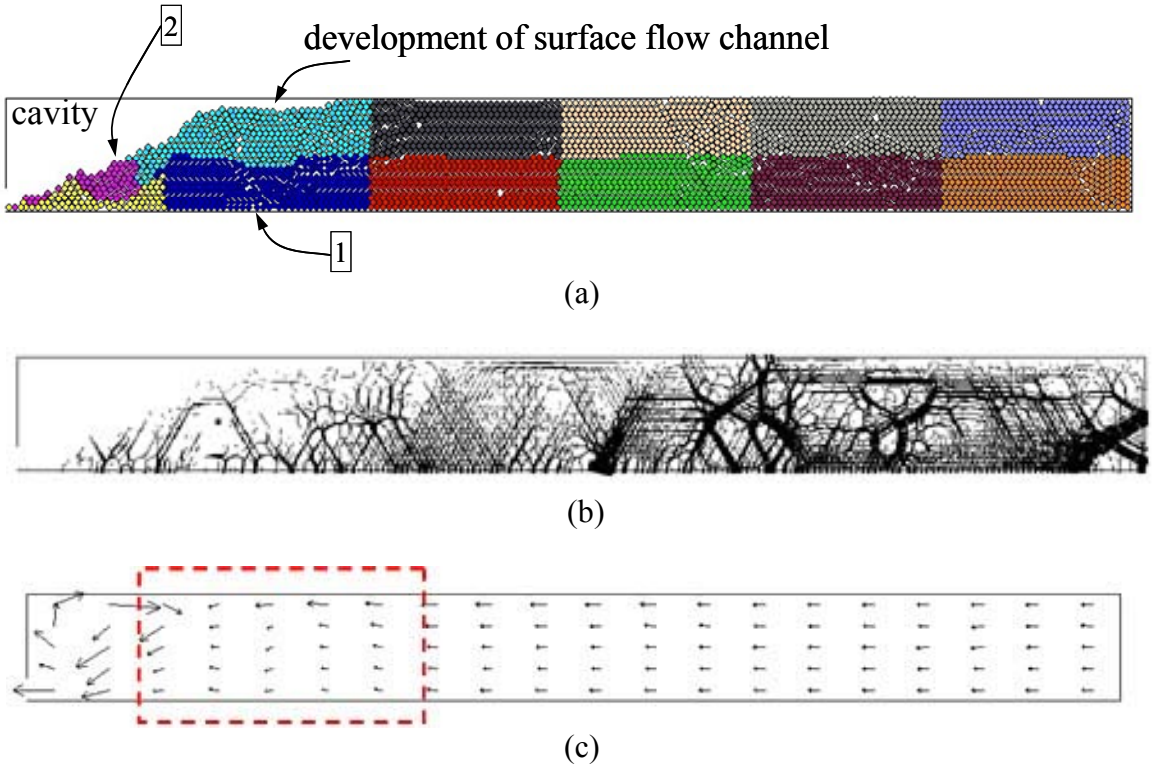

Figure 3.16 Results of *PFC*^{2D} modeling at time 6.7 sec: (a) assembly of particles, (b) contact force (maximum contact force is 5.1×10^{-2} N), and (c) fluid flow vector (maximum fluid velocity is 0.01 m/sec). Note that blue region 1 spreads laterally (compared to Figure 3.15), which results in the decrease of its vertical dimension and could be an important mechanism contributing to the channel formation.

In the container marked with dashed lines in Figure 3.16c, the magnitude of the fluid velocity in the area of the flow channel is greater than that in the particulate medium. Without flow channel (Figure 2.54b), such a concentration of flow rate does not occur. This indicates that flow channel is a main conduit for flow.

As a result of the erosion of particles and subsidence due to the lateral extension (Figure 3.16), the size of the flow channel increases and the cavity slope collapses at the time of 10.0 sec shown in Figure 3.17a. It appears (compare Figures 3.16a and 3.17a) that the collapse resembles progressive failure of the slope due to the unloading at its toe. The unloading occurs because of the preferential removal of the particles near place of fluid withdrawal. Blue region 2 in Figure 3.17a corresponds to the blue region 2 in Figure 3.16a. This region is almost intact and moved down the slope because the particles below have been removed. Although the contact force behind the cavity remains almost the same compared to that at a time of 6.7 sec (Figure 3.17b), the fluid flow concentrates in the area of the flow channel in Figure 3.17c. The concentration of fluid flow leads to the increase in fluid velocity. This may contribute to the increase of the size of the surface flow channel.

We found that this process repeats itself. That is, the formation of the surface flow channel and the collapse of the cavity continue. Therefore, the production of particles is ongoing. This indicates that the cavity and the flow channel are not stabilized. If this calculation continues, all particles would be produced out of the container. The continuation of particle production can be explained by the 3-D effect of the flow velocity. According to (2.5), the fluid velocity at a point decreases as the distance from the point to the center of the sand layer increases in the 3-D experimental setup. In 2-D modeling, however, this effect cannot be captured, and the fluid velocity does not change along the horizontal axis. That is, in the 2-D model, the fluid velocity at the surface of the cavity does not decrease as the size of the cavity increases.

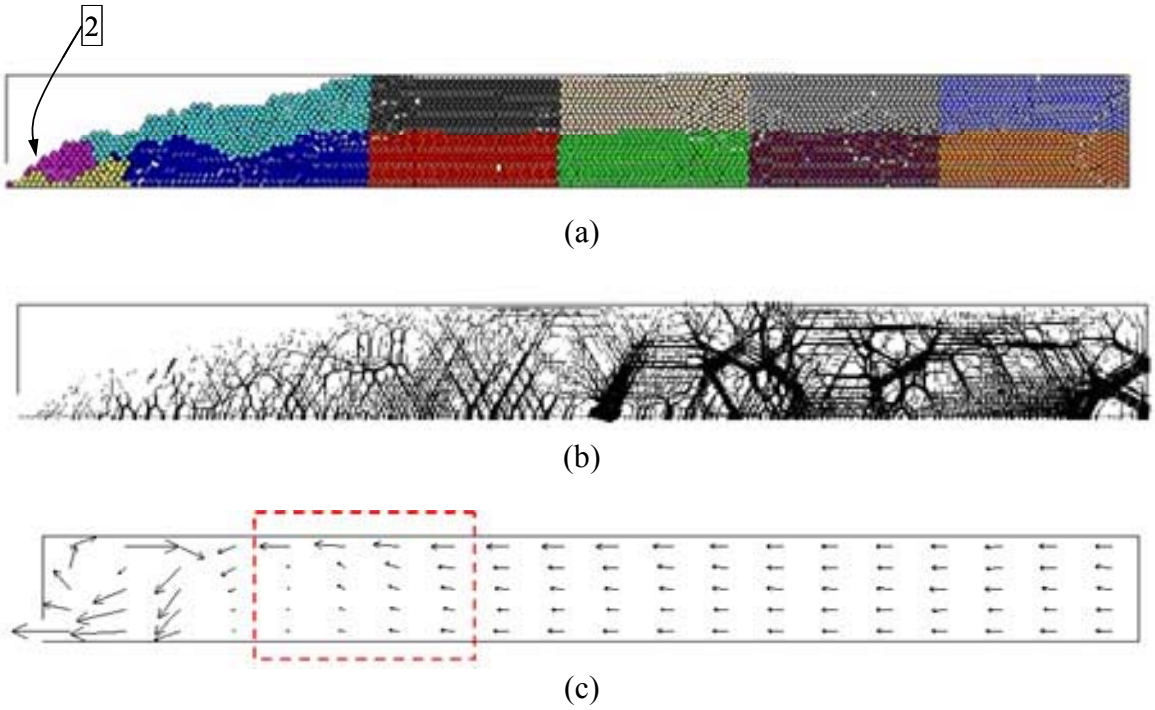

Figure 3.17 Results of *PFC*^{2D} modeling at time 10.0 sec: (a) assembly of particles, (b) contact force (maximum contact force is 4.8×10^{-2} N), and (c) fluid flow vector (maximum fluid velocity is 0.009 m/sec). A cavity and a flow channel are created due to particle production.

3.6 Three-Dimensional Modeling

3.6.1 Model Setup

To increase the speed of computations, only a portion of the sand layer is modeled here. The modeled domain is marked with dots in Figure 3.18. The domain has the shape of a rectangular parallelepiped (prism) because standard *PFC*^{3D} code does not allow using a cylindrical boundary for fluid flow modeling. We used samples with approximately 9600 (= 40×40×6) particles and placed 6 particles in the vertical direction.

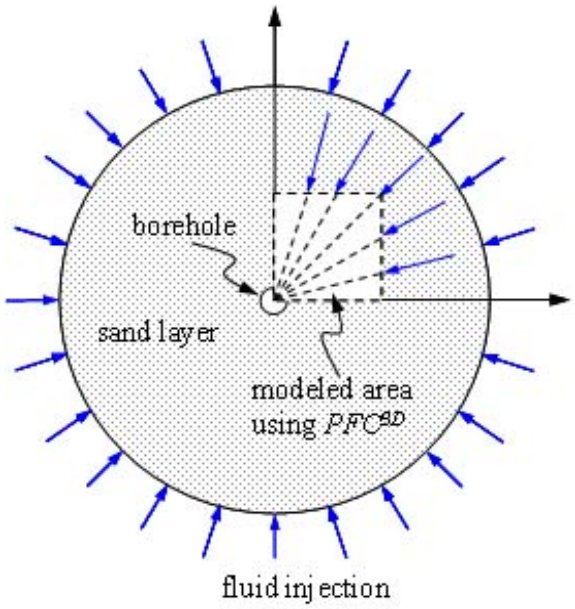

Figure 3.18 Modeled area for a *PFC*^{3D} modeling. This is a plan view of the experimental setup. A borehole is located at the center of the sand layer. Fluid is injected at the boundary of the setup. A square region marked by a dashed line is modeled in the 3-D analysis using *PFC*^{3D}. The fluid velocity at the boundary of the model is determined to consider the radial fluid flow of the experimental setup. The radius of the sand layer is 0.5 m.

To increase the calculation speed, we also upscaled the particle size as well as the size of the model instead of increasing the number of particles, i.e., the mean particle diameter and the size of the model are enlarged to 4 cm and 1.5 m× 1.5 m× 0.25 m, respectively (Figure 3.19). The particle size has a linear distribution, ranging from 3 cm to 5 cm. According to (3.38), if the diameter of the particles, d_p, is increased, the calculation time step, Δt, is also enlarged. Therefore, the calculations become faster.

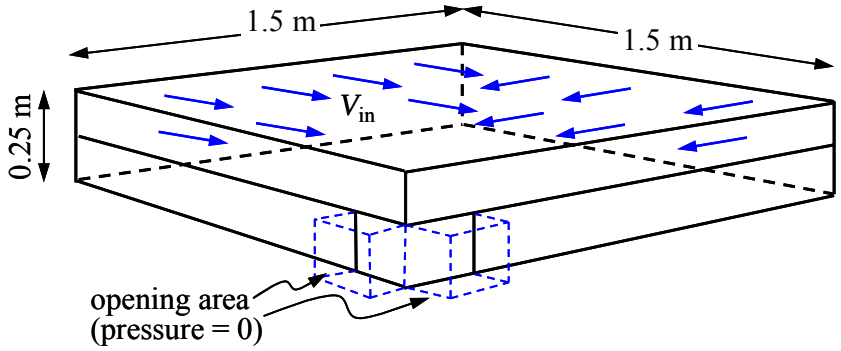

Figure 3.19 Boundary conditions in a *PFC*^{3D} model (not to scale). Fluid pressure in the opening area is maintained to be zero to simulate an atmospheric drainage area. All the walls are fixed.

The parameters used in the *PFC*^{3D} model are listed in Table 3.3. Similar to the 2-D model, in the 3-D model, the particles are contained in a container with fixed walls (i.e., with zero displacements). An opening area is placed for the drainage of the particles and the fluid (Figure 3.19). The fluid pressure in the opening area is maintained at zero. Fluid is injected with a fluid velocity V_{in} through two walls (Figure 3.19). Except for the two walls through which fluid is injected, the other walls have no flow boundary conditions imposed. In addition, to increase the frictional resistance against the hydrodynamic force of fluid flow, particles contacting the top and the bottom walls are fixed, i.e., they have zero displacement in any direction.

Table 3.3 Parameters used for input data of *PFC*^{3D} model

Parameter	Value	Petroleum unit
Particle diameter	3 – 5 cm	1.18 – 1.97 in
Number of particles	9996	-
Initial porosity	0.34	-
Normal stiffness	10^6 N/m	-
Shear stiffness	10^6 N/m	-
Friction coefficient	0.7	-
Particle density	2650 kg/m^3	165.4 lb/ft^3
Confining stress	10 kPa	1.45 psi
Fluid density	1000 kg/m^3	62.4 lb/ft^3
Dynamic viscosity of fluid	8 Pa·sec	8000 cP
Fluid injection rate	7.5×10^{-5} m^3/sec	2.6×10^{-3} ft^3/sec

Since the geometry of the *PFC*^{3D} model is a rectangular parallelepiped representing a subdomain in a circular domain (Figure 3.18), we consider the distribution of the injected fluid velocity along the parallelepiped boundaries. That is, if we inject fluid with the same fluid velocity along the circular perimeter (Figure 3.18), the fluid velocity changes radially towards the opening. Therefore, Cartesian components of the fluid velocity, shown in Figure 3.20, can be expressed as functions of the distance r from the opening as follows:

$$v_x(r) = \frac{R\sin\theta\cos\theta}{a} v_0 \tag{3.39}$$

$$v_y(r) = \frac{R\cos^2\theta}{a} v_0 \tag{3.40}$$

where $v_x(r)$ is the components of $v(r)$ in the x direction, $v_y(r)$ is the component of $v(r)$ in the y direction, θ is the polar angle shown in Figure 3.20, R is the radius of the original model (Figure 3.18), v_0 is the injected fluid velocity at distance R (Figure 3.18), and a is the side length of the container (rectangular parallelepiped; Figures 3.18-3.20).

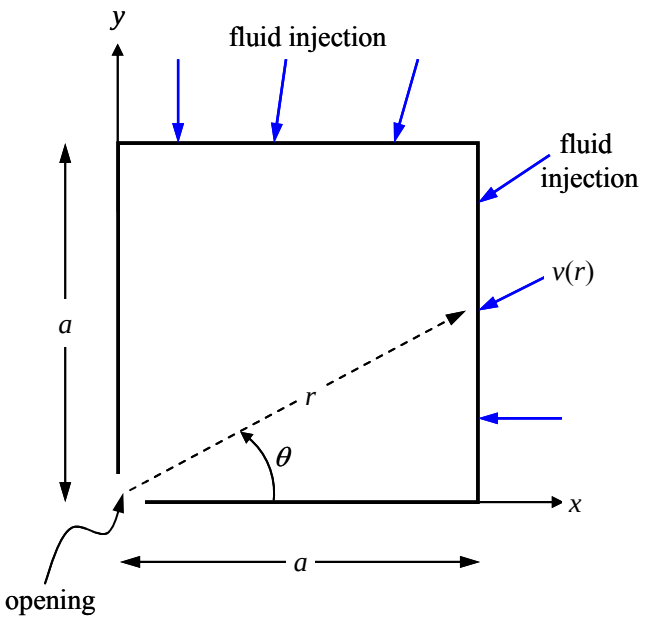

Figure 3.20 The injected fluid velocity $v(r)$ at distance r from the opening (plan view).

3.6.2 Results of Calculations

The assembly of particles at the initial state is shown in Figure 3.21. Particles located at the same height from the bottom of the model have the same color to visualize the movement of particles. Figures 3.21a and 3.21b show the plan view and the side view of the initial state of the model, respectively. We fixed particles contacting the top and the bottom walls, so that they have zero displacement in any direction to increase the frictional resistance to the hydrodynamic force of fluid flow. The existence of these particles reduces the number of available particles in the container, but makes the simulation more realistic. For comparison, we also simulated the case without the fixed layers of particles and with the boundary conditions similar to the 2-D simulations (Section 3.5). The advantage of this model is a greater number of particles and, hence, the model resolution in the vertical direction (across the particle layer).

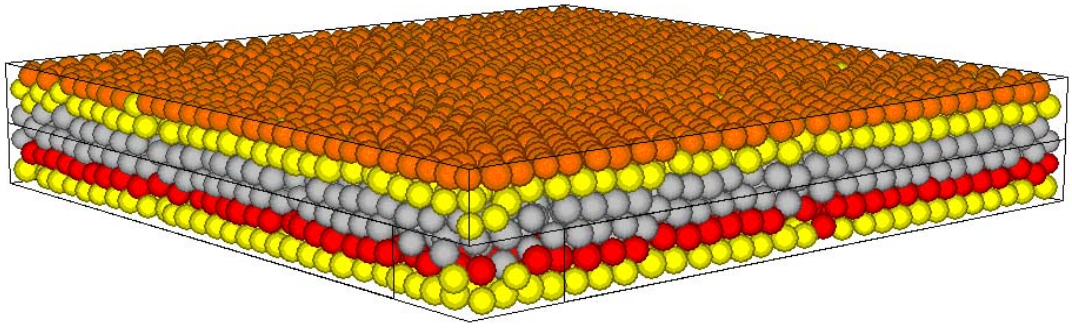

(a)

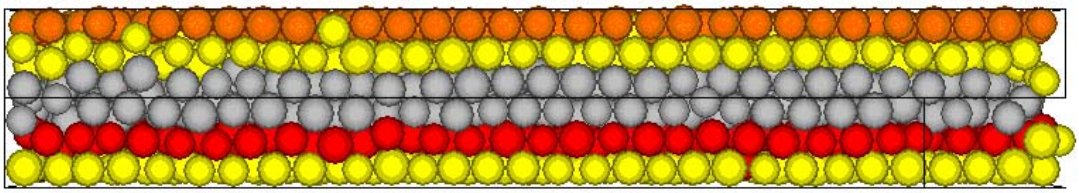

(b)

Figure 3.21 Assembly of particles at the initial state: (a) plan view and (b) side view. Particles located at top and bottom layers are fixed, such that they have zero displacement in any direction to increase frictional resistance against fluid flow.

The assembly of particles at a time of 96 sec is shown in Figure 3.22. Compared with Figure 3.21, Figure 3.22 shows that a cavity is formed around the opening due to the production of particles. The assembly of particles at a time of 110.0 sec is shown in Figure 3.23. Comparing Figure 3.23 with Figure 3.22, the size of the cavity does not change significantly. This indicates that there was no significant particle production between 96.0 sec and 110.0 sec, which may be interpreted as the decrease in production rate of particles.

Figure 3.24 shows the magnified side view in the vicinity of the opening area. As mentioned for Figures 3.22 and 3.23, a cavity is formed due to the production of particles. However, it is difficult to observe the existence of a surface flow channel (discussed in Section 2.5). Since we had to increase the particle size in order to keep the number of particles reasonably small, the particles are not sufficiently small compared to the height of the container. In Figure 3.24, we can observe that some particles lost contact with the particles contacting the top layer of the particles whose velocity is fixed as zero. It seems that such a contact loss propagates toward the interior of the assembly of particles. This tendency may be suggesting the existence of a surface flow channel propagating from the opening as observed in our experiments described in Section 2.5.

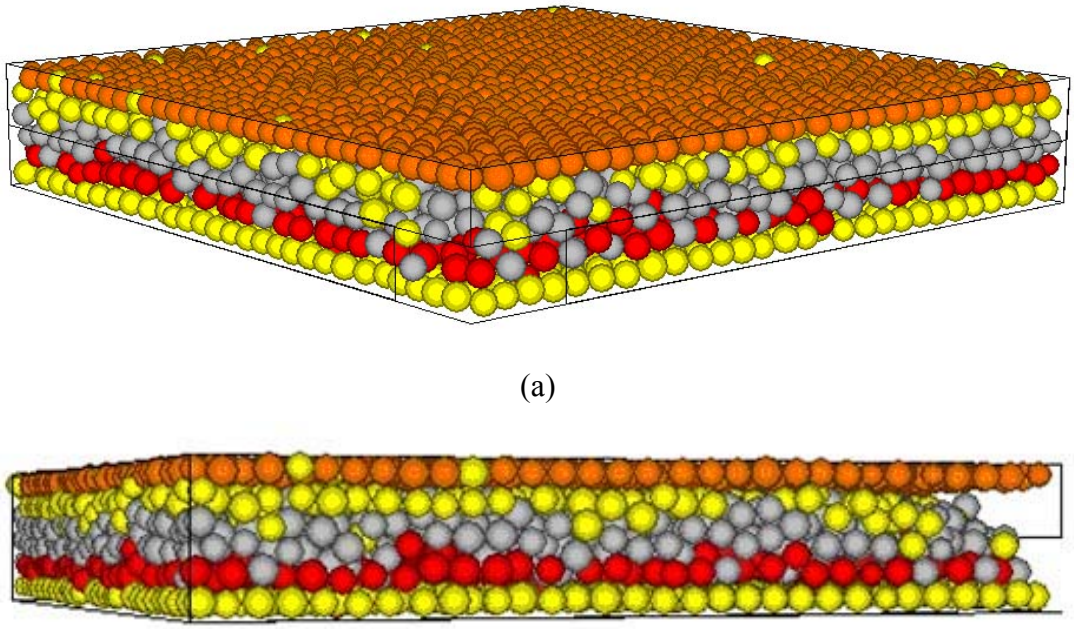

(a)

(b)

Figure 3.22 Assembly of particles at time of 96 sec: (a) plan view and (b) side view. Particles contacting the top and the bottom walls are fixed, such that they have zero displacement in any direction.

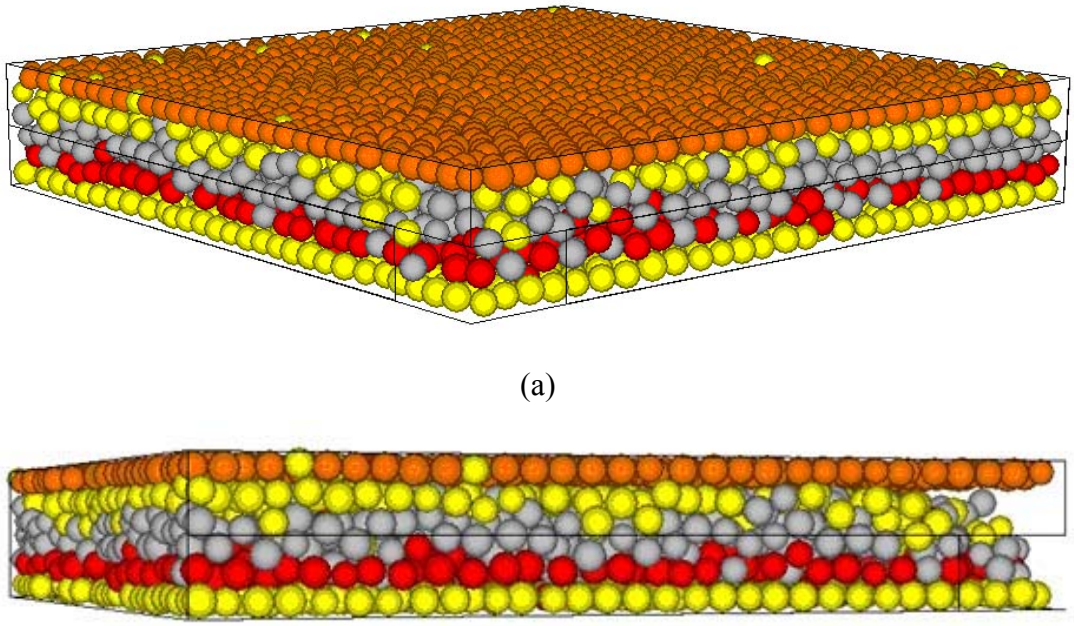

(a)

(b)

Figure 3.23 Assembly of particles at initial state at 110.0 sec: (a) plan view and (b) side view. Particles contacting the top and the bottom walls are fixed, such that they have zero displacement in any direction.

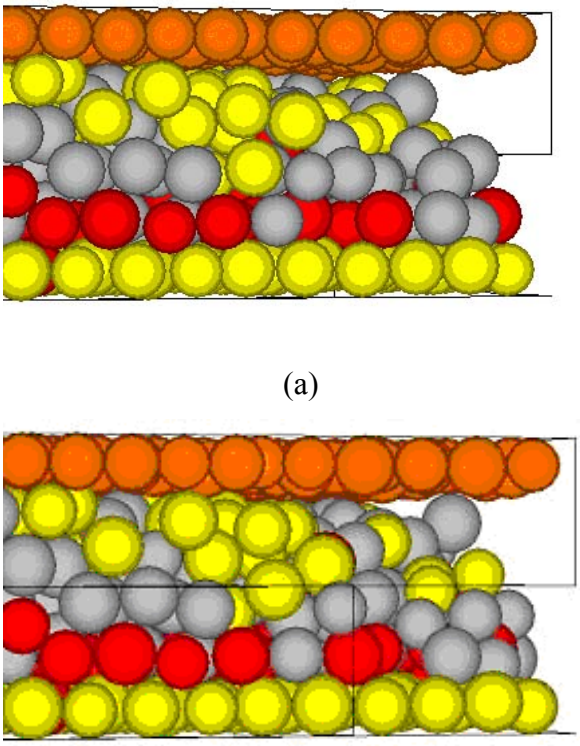

(a)

(b)

Figure 3.24 Assembly of particles with magnified side view in the vicinity of the opening area: (a) at 96 sec and (b) 110 sec.

In Figure 3.25, the contact force on a horizontal plane located in the middle of the model (at depth of 12.5 cm) is shown. Here, each bar represents the contact force between two particles. Also, the thickness of the bar corresponds to the relative magnitude of the contact force. At a time of 1.0 sec (Figure 3.25a), a zone in which particles lost their contact forces with surrounding particles is formed only in the vicinity of the opening at the right upper corner of the figure. Such a loss of the contact force may suggest that particles in this zone are fluidized.

The size of the fluidized zone increases at a time of 50.0 sec (Figure 3.25b). At a time of 96.0 sec (Figure 3.25c), the size of the fluidized zone with the shape of a quarter circle grows compared to that at a time of 50.0 sec. Comparing Figures 3.25c and 3.25d,

we observe that the size of the zone does not change dramatically. This indicates the decreasing production rate of particles, which is already observed in Figures 3.22 and 3.23. In Figure 3.25, we can identify the formation and the development of a fluidized zone, which may lead to the growth of the cavity. The cavity is more pronounced in the simulation presented in Section 3.6.3. Although due to a limited number of particles, it was difficult to capture the flow channel in this simulation, the appearance of the flow channel was registered in the simulation described in Section 3.6.3.

In Figure 3.26, we also present the side views of the contact force at different times on a vertical diagonal plane from the drainage to the diagonal corner of the container. It appears that, similar to Figure 3.25, the fluidized zone propagates towards the inside of the particulate medium.

We plotted the number of produced particles with respect to time in Figure 3.27, which shows that after 50 sec, the production rate of particles decreases. It may appear that there exist two linear dependencies, i.e., for higher and lower production rates of particles. The resolution of the model, however, does not allow making an unambiguous conclusion. Nevertheless, Figure 3.27 indicates the tendency of decreasing particle production rate. This may be an indication of the beginning of the stabilization of the particle assembly and that the particle production will eventually stop. The decrease of the particle production rate was more pronounced in another simulation (Section 3.6.3).

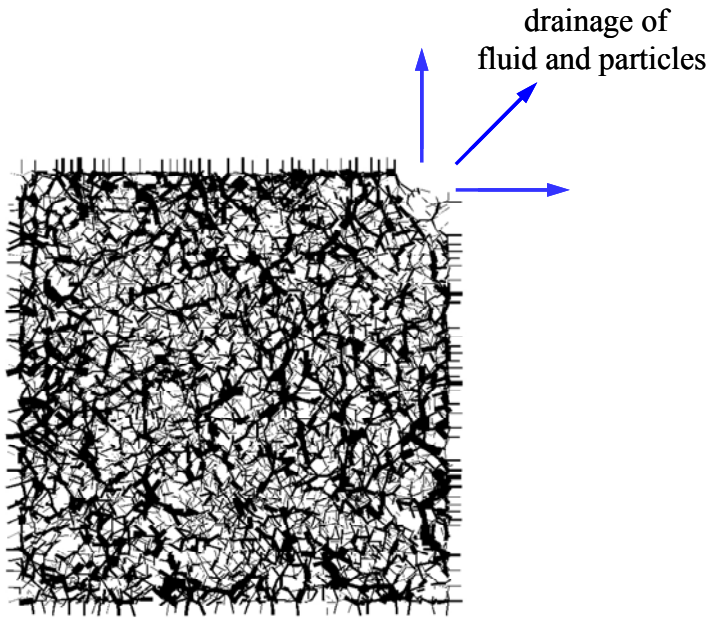

(a)

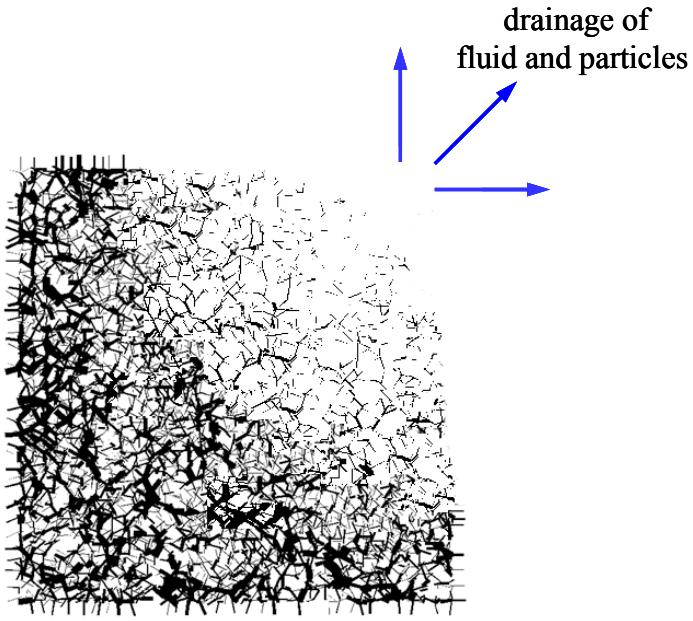

(b)

Figure 3.25 Contact force on a horizontal plane located at depth 0.125 m (plan view): (a) at 1.0 sec, (b) at 50.0 sec, (c) at 96.0 sec, and (d) at 110.0 sec. Drainage is located at the upper right corner. The thickness of the small bars denotes the relative magnitude of the contact force between particles as well as particles and walls.

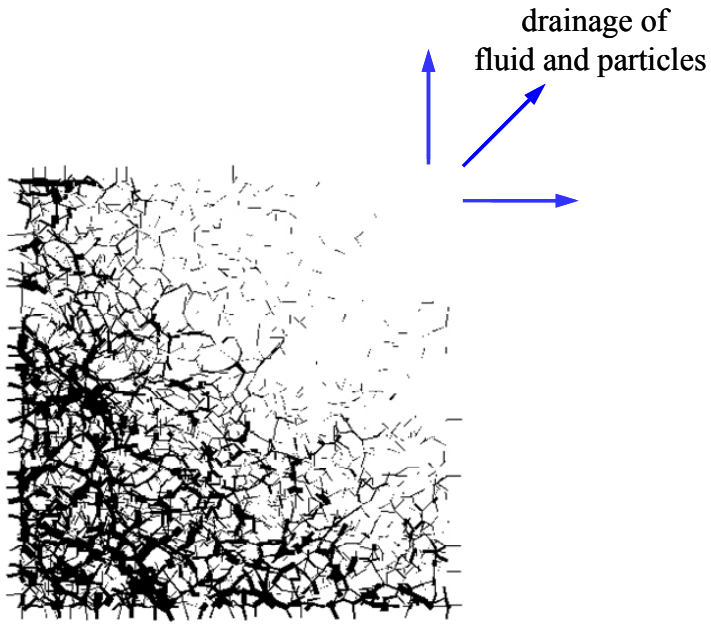

(c)

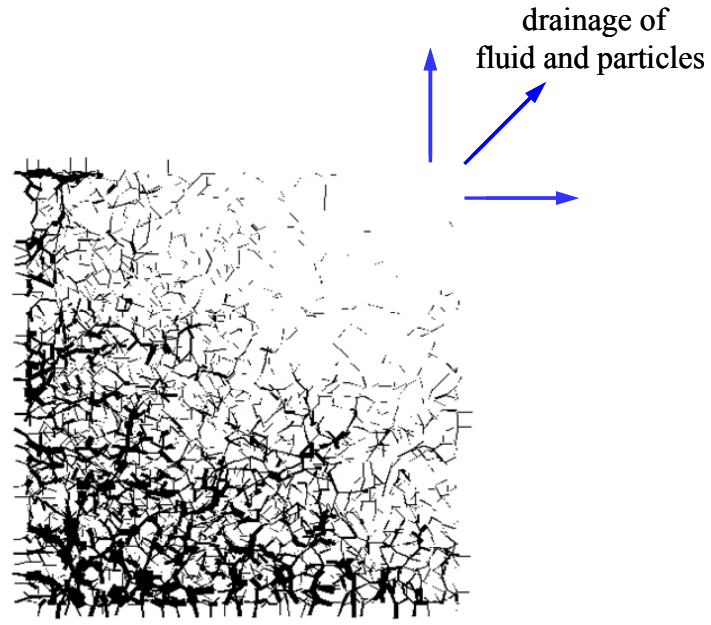

(d)

Figure 3.25 (continued).

(a)

(b)

(c)

Figure 3.26 Contact force on a diagonal vertical plane (side view): (a) at 1.0 sec, (b) at 96.0 sec, and (c) at 110.0 sec. Drainage is located at the right side. The thickness of the small bars denotes the relative magnitude of the contact force between particles as well as particles and walls.

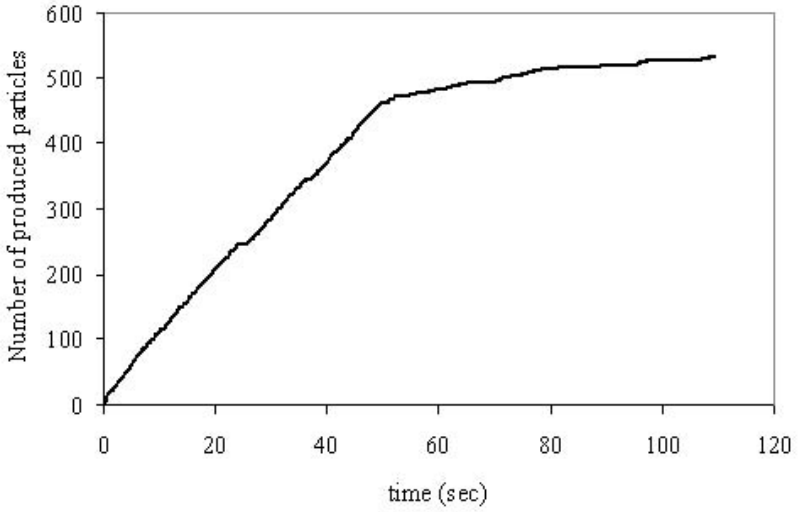

Figure 3.27 Number of produced particles with respect to time.

From Figure 3.24 and 3.27, it seems that the size of the cavity (Figure 3.24) is relatively small compared to the number of the produced particles (Figure 3.27). By assuming that the cavity has the shape of a quarter frustum shown in Figure 3.28, we can estimate the number of produced particles from the cavity.

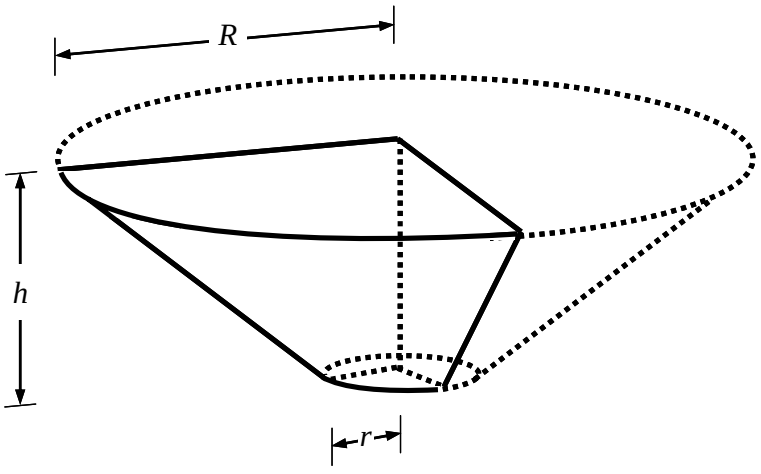

Figure 3.28 Schematic of a cavity with the shape of a quarter frustum

Since the cavity has a shape of a quarter frustum, the volume of the cavity, V_{cavity}, is given by

$$V_{cavity} = \frac{\pi}{3} h(R^2 + rR + r^2) \times \frac{1}{4} \tag{3.41}$$

where R is the upper radius, r is the lower radius, and h is the height of the frustum (Figure 3.28). Consider an assembly of particles contained in a box with a total volume of V. The volume, V_s, occupied by the particles in the total volume is

$$V_s = NV_p \tag{3.42}$$

where N is the number of particles in the total volume, and $V_p = \pi d_p^3 / 6$ is the volume of a particle with a diameter, d_p. Thus, the total volume, V, can be expressed as

$$V = \frac{1}{1-\phi} V_s \tag{3.43}$$

where ϕ is the porosity of the assembly of particles. From (3.42) and (3.43), the total number of particles in the total volume is given by

$$N = \frac{V}{\frac{1}{1-\phi} V_p} \tag{3.44}$$

Therefore, the number of the produced particles, N_c, from the cavity is

$$N_c = \frac{V_{cavity}}{\frac{1}{1-\phi_0} V_p} \tag{3.45}$$

where V_{cavity} is the volume of a cavity, and ϕ_0 is the initial porosity of the assembly of particles.

According to Figure 3.24b, R = 30 cm, r = 2.4 cm, and h = 17 cm. Also, from Table 3.3, the mean diameter of particles is 4.0 cm. With these parameters and (3.45), the number of particles from the cavity is 106. At a time of 110 sec, the total number of produced particles is 540 (Figure 3.27). The comparison of these two numbers indicates that the number of particles produced somewhere else is greater than that from the cavity. This implies that the porosity of the material adjacent to the cavity increases, which compensates for the production of particles. To verify this hypothesis, we measure the porosity of the assembly of particles at several locations (Figure 3.29a). The measurement is done at the middle depth (0.125 m) of the model assembly of particles. Then, we plot the contour of the porosity, which is presented in Figure 3.29b. The initial porosity is 0.34. Thus, the region with the porosity of 0.34 beyond the sector 3 remains intact.

Based on the contour of the porosity (Figure 3.29b), we can evaluate the number of the produced particles from each sector. We assume that the boundary of each sector has a shape of a quarter cylinder with a depth of 17 cm (= 25 cm – 2×4 cm) since the particles contacting the top and the bottom walls are fixed, such that they have zero displacement in any direction. From (3.45), the number of the produced particles, ΔN_i, from a sector i when the porosity of the sector changes from ϕ_0 to ϕ_i is given by

$$\Delta N_i = \frac{V_i}{\frac{1}{1-\phi_0}V_p} - \frac{V_i}{\frac{1}{1-\phi_i}V_p} \tag{3.46}$$

where V_i is the total volume of the sector i. The volume of each sector and the calculated number of produced particles from each sector as well as those for the cavity are presented in Table 3.4.

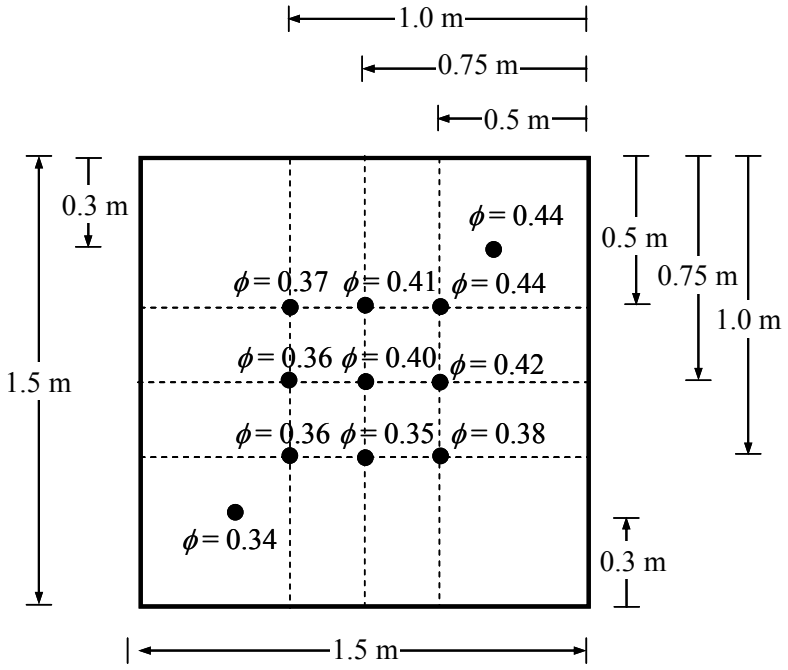

(a)

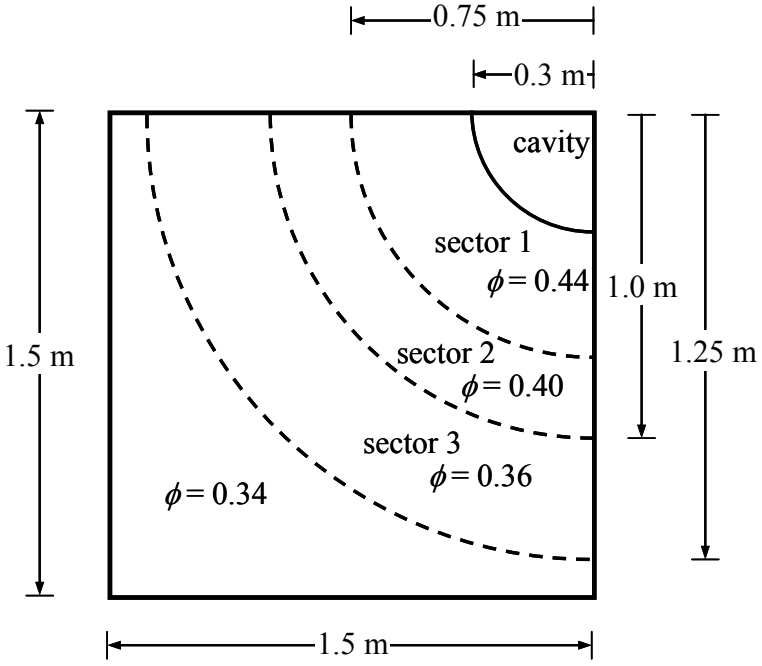

(b)

Figure 3.29 Measurement of the porosity in the assembly of particles at a time of 110 sec: (a) locations of the measurement and (b) contour of the porosity. The initial porosity is 0.34.

Table 3.4 Calculated numbers of particles from each sector shown in Figure 3.29b.

Sector	Volume (m^3)	Porosity	Number of produced particles
1	0.070	0.44	208
2	0.058	0.40	105
3	0.075	0.36	45
Cavity	0.005	-	106

According to Table 3.4, the total number of produced particle is 464. Considering the local variations of the porosity and particle size distribution (3 – 5 cm), the calculated number is close to the value 540 at the end of the simulation (Figure 3.27).

As a summary, we also compare the results of the experiments, the PFC^{2D} model and the PFC^{3D} model. The comparison is shown in Table 3.5. Experiments showed features such as the formation of a cavity, a flow channel, and stabilization of the medium. The PFC^{2D} model could reproduce the formation of the cavity and the flow channel as well as the propagation of the fluidized zone. This process, however, was not stabilized in the 2-D numerical experiments. The PFC^{3D} model could demonstrate the formation of a cavity and probably the stabilization of the medium since such 3-D effects of the fluid flow can be included naturally. Due to the limitations of the PFC^{3D} model (e.g., small number of particles and fluid cells), the flow channels cannot be clearly visualized in our simulations.

Table 3.5 Comparison of results of experiments, $\boldsymbol{PFC^{2D}}$ model and $\boldsymbol{PFC^{3D}}$ model

Features	**Experiments**	$\boldsymbol{PFC^{2D}}$ **model**	$\boldsymbol{PFC^{3D}}$ **model**
Cavity	○	○	○
Flow channel	○	○	×
Stabilization of medium	○	×	?
Propagation of fluidized zone	×	○	○

3.6.3 An Example with Different Boundary Conditions

This section presents an example of a simulation where the sample had more particles (≈12) in vertical direction with different geometry and boundary conditions. In this case, the mean particle diameter was 5 cm, and a container with dimension of 2.5 m× 2.5 m× 0.6 m (Figure 3.30) had ≈37200 particles. The initial porosity was 0.35. We placed 400 (10×10×4) fluid cells and the fluid injection rate was 0.03 m^3/sec (1.1 ft^3/sec). Fluid density was 1000 kg/m^3 and the fluid dynamic viscosity was 10 Pa·sec.

Figures 3.31 and 3.32 show a flow "channel" (removed layers) at the top of the sample. In section 3.5, which describes the results of 2-D simulation, channel appearance has been attributed mainly to the sample subsidence due to the particle withdrawal near the drainage point. This effect may also be a factor in 3-D, but the 3-D results (Figures 3.31 and 3.32) indicate the particle removal from the top quasi-planar layer ("channel") more clearly than in 2-D. The top layer of orange particles appears to be removed from the sample as a result of particle production (Figures 3.30 – 3.32). The "channel" has different geometry (Figure 3.33) than in our experiments (Chapter II), which can be attributed to the limited number of particles used in this simulation. Nevertheless, the observed "channel" indicates a possible importance of the erosion-type mechanism of the surface channel development.

The rate of particle production in this simulation decreases with time, as can be seen in Figure 3.34. The channel thickness at three different times is also presented in this figure. The rate of sand production decreases with time, which indicates that eventually both the cavity and the channel stabilize.

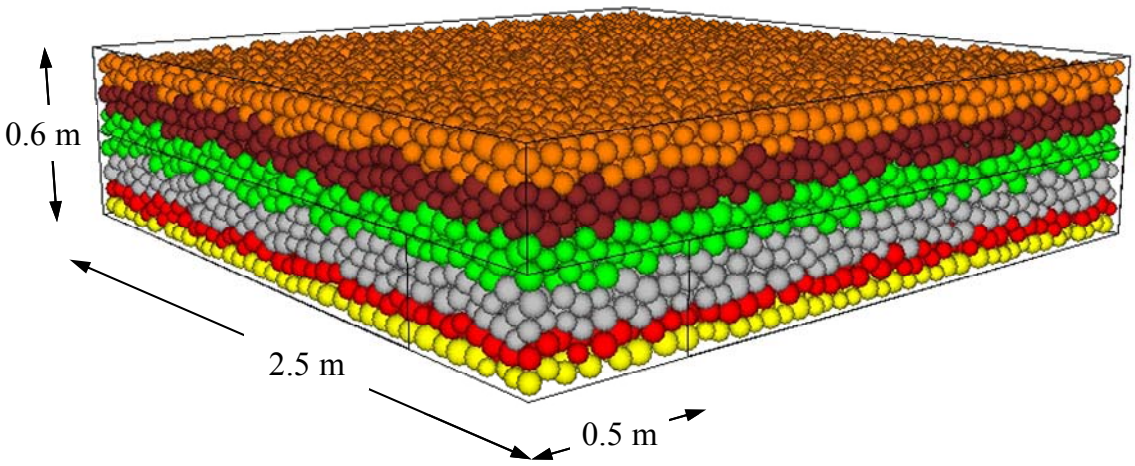

Figure 3.30 Front view of the model. In this model, there are ~37200 particles with mean particle diameter of 5 cm. The initial porosity is 0.35. Fluid velocity at drainage is 0.1 m/sec.

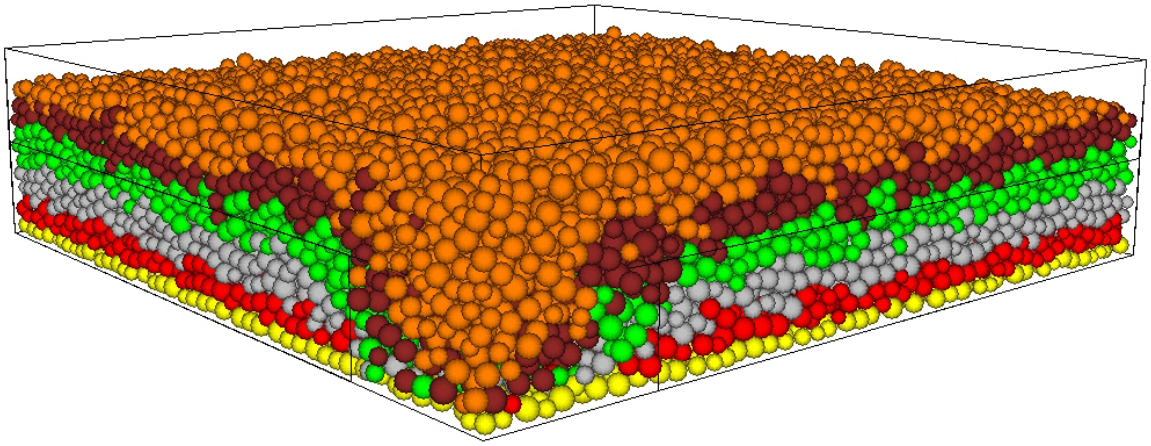

(a)

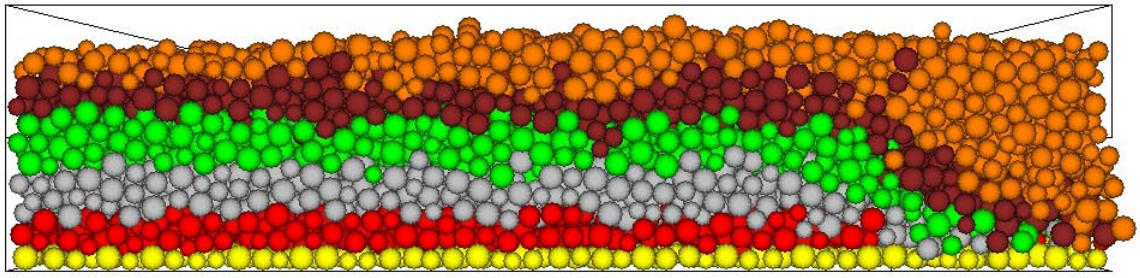

(b)

Figure 3.31 Results of modeling at 5.5 sec: (a) front view and (b) side view. At this moment, the thickness of the channel is ~0.065 m.

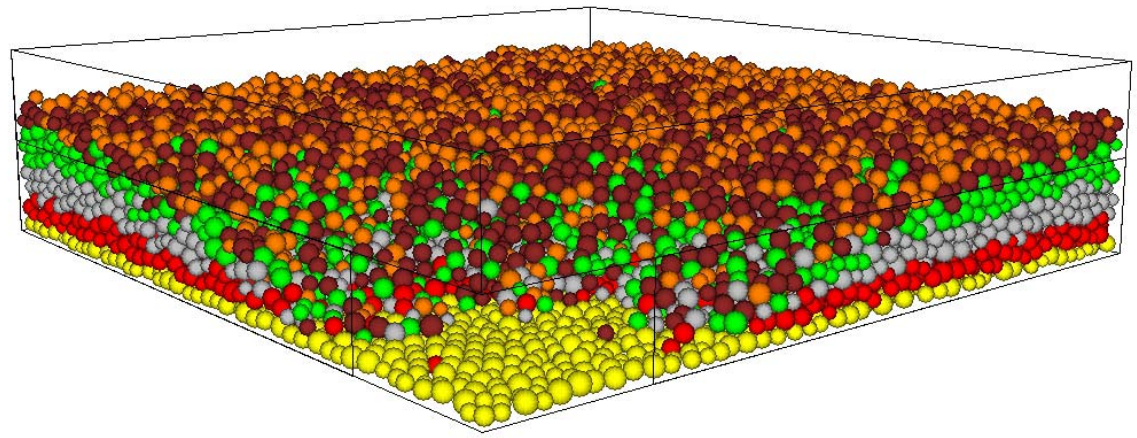

(a)

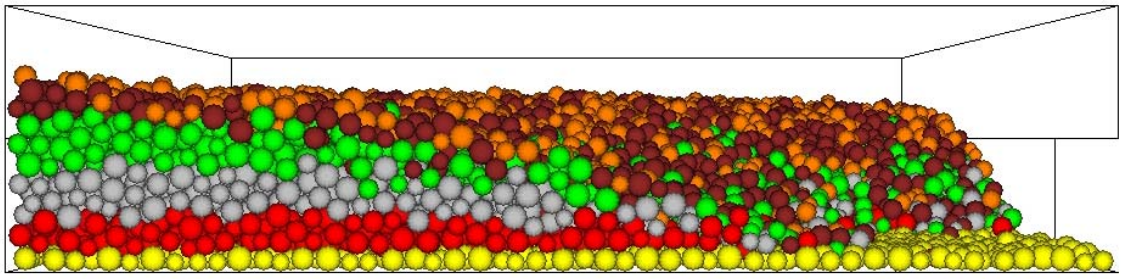

(b)

Figure 3.32 Results of model at 35.5 sec: (a) front view and (b) side view. At this moment, the thickness of the channel is ~0.176 m.

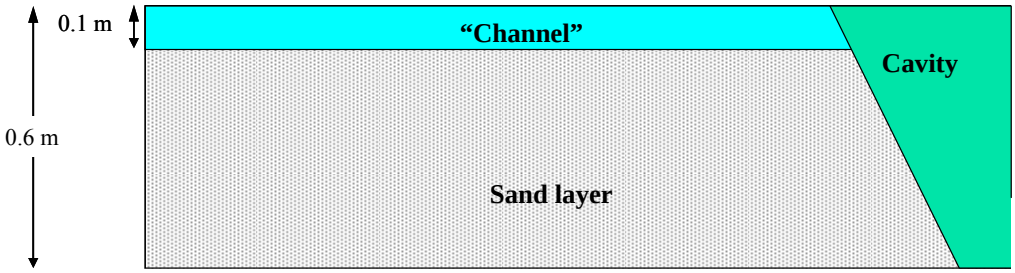

Figure 3.33 Schematic side view of the model (not to scale).

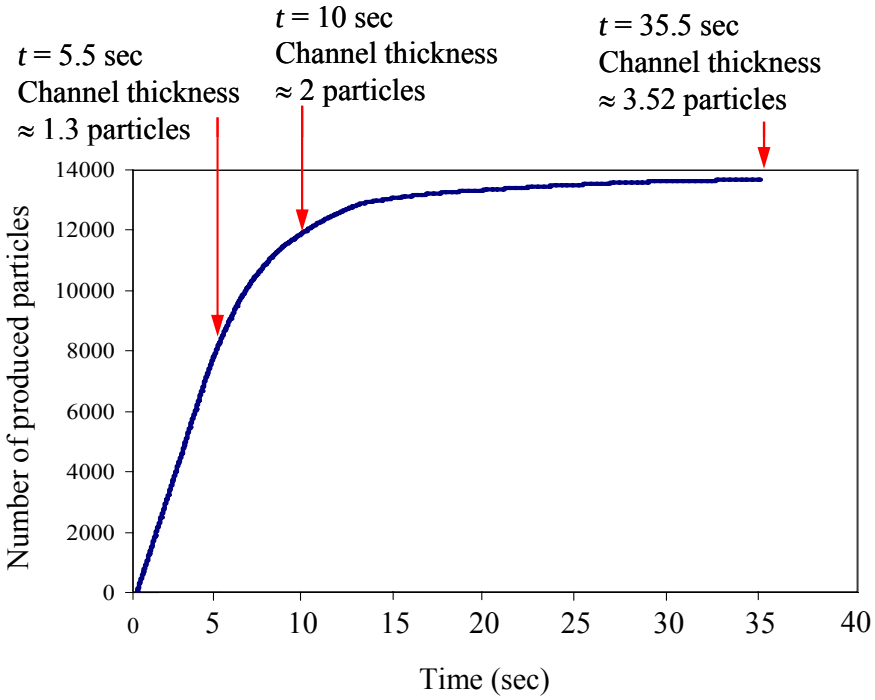

Figure 3.34 Development of the cavity and the channel at several time steps based on the size of the cavity and the channel (e.g., Figure 3.33).

3.7 Conclusions

Our laboratory results (Chapter 2) constitute a well constrained data set that can be used to test and calibrate numerical models employed by the petroleum industry for predicting the sand production phenomenon. Although important for practical applications, real field cases are typically much less constrained. In this work, we also simulated the behavior of a sand layer around a wellbore using two- and three-dimensional discrete element methods. It appears that the main sand production features observed in the laboratory experiments, can indeed be reproduced by means of discrete element modeling. Numerical results indicate that the cavity surface of repose is a key factor in the sand production mechanism. In particular, the sand particles on this surface are not significantly constrained. This lack of confinement reduces the flow velocity, required to remove a particle, by many orders of magnitude. Also, the mechanism of channel development in the upper fraction of the sample can be attributed to subsidence of the formation due to lateral extension when an unconstrained cavity slope appears near the wellbore. This is substantiated by the erosion process and continued production of particles from the flow channel.

A parametric study is required to understand particle production in more detail. Nevertheless, the conducted numerical experiments provide an important insight into the understanding of mechanisms of sand production.

LIST OF SYMBOLS AND ABBREVIATIONS

A	Cross-sectional area of an assembly of particles
a	Aperture of a crack
a	Side length of a container
C	Constant
c	Cohesion of a medium or constant
c	Transport concentration of fluidized particles
c_{cr}	Critical transport concentration of fluidized particles
d_p	Diameter of a particle
d_s	Sand cavity size for production
E	Young's modulus
E'	Scaled Young's modulus
F	Contact force
F_d	Drag force
F_h	Total hydrodynamic force on a particle
F_i	Force in *i* direction
F_i^n	Normal contact force in *i* direction
$F_{\max}^s$	Maximum allowable shear force
F_p	Pressure component of hydrodynamic force
F_r	Resistance force against the particle removal
f_i	Body force related to the interaction between particles and the fluid
f_μ	Inter-particle friction coefficient
G	Shear modulus

g	Acceleration of gravity
H	Height of a sand layer
H	Perforation interval
h	Height of a frustum
K	Stiffness between particles at a contact
K_f	Bulk modulus of a fluid
K_n	Normal contact stiffness
K_s	Shear contact stiffness
k	Permeability
k	Conductivity factor
L	Length
m	Mass of a particle
$\dot{m}$	Solid mass production rate
N	Number of contact per a particle or number of particles
N	Perforation density
ΔN_i	Number of produced particles from a sector i
n_i	Component of unit normal vector in i direction
p	Pore pressure
p_f	Pressure in reservoir
p_0	Fluid pressure in a well
q	Fluid flow rate
q_1	Fluid flow rate through a perforation
q_s	Discharge velocity of eroded particle
R	Radius of the sand layer

R	Particle radius
R	Upper radius of a frustum
Re	Reynolds number
r	Distance from the center of the sand layer
r	Lower radius of a frustum
s	Length of a line (2-D) or projected area (3-D)
Δt	Time step
u	Relative displacement
V	Fluid velocity
V	Volume of a particle packing or volume of a container
V_{cavity}	Volume of a cavity
V_d	Apparent volume of a domain in a porous medium
V_i	Total volume of the sector i
V_{in}	Injected fluid velocity
V_p	Volume of a particle
V_s	Volume occupied by sand particles
v	Required fluid velocity to induce particle erosion
v_d	Darcy's velocity at the cavity surface
v_f	Fluid velocity flowing through pores
v_i	Fluid velocity in i-direction
v_{max}	Available fluid velocities at the cavity surface
α	Constant
β	Biot poroelastic constant
γ	Constant

ε_{xx}	Strain in *x* direction
ε_{yy}	Strain in *y* direction
ζ	Micro-scale parameter for a 2-D disc packing
θ	Polar angle
λ	Constant
λ_1	Constant
μ	Dynamic viscosity of fluid
ν	Poisson's ratio of a material
ν'	Scaled Poisson's ratio of a material
ρ_f	Density of fluid
ρ_s	Density of a particle
σ	Total stress
σ	Stress at infinity
σ_N	Total normal stress
σ_{xx}	Stress in *x* direction
σ_{yy}	Stress in *y* direction
τ	Tensor of viscous stress
Φ_E	Dimensionless function
Φ_ν	Dimensionless function
ϕ	Porosity
ϕ_0	Initial porosity
Ψ	Internal friction angle

References

Asgian, M. I., P.A Cundall, and B.H.G. Brady (1995), Mechanical stability of propped hydraulic fractures: A numerical study, *Journal of Petroleum Technology*, 203-208.

Bardet, J.P. and J. Proubet (1991), A numerical investigation of the structure of persistent shear bands in granular media, *Géotechnique*, 41(4), 599-613.

Bathurst, R.J. and L. Rothenburg (1992), Investigation of micromechanical features of idealized granular assemblies using DEM, *Engineering Computations*, 9, 199-210.

Bear, J. (1972), *Dynamics of fluids in porous media*, Elsevier Publishing Company, Inc.

Bradley, H.B. (1987), *Petroleum Engineering Hand Book*, Society of Petroleum Engineers.

Bratli, R.K. and R. Risnes (1981), Stability and failure of sand arches, *SPEJ*, 236-248.

Chang, C.S. and A. Misra (1990), Packing structure and mechanical properties of granulates, *Journal of Engineering Mechanics*, 116, 1077-1093.

Charlez, P.A. (1997), *Rock Mechanics Vol. 2 Petroleum Application*, Éditions Technip, Paris.

Dake, L.P. (1978), *Fundamentals of reservoir engineering*, Elsevier.

Dusseault, M.B. and F.J. Santarelli (1989), A Conceptual Model for Massive Solids Production in Poorly-Consolidated Sandstones, *Rock at great depth*, edited by Maury and Fourmaintraux, 789-797.

Economides, M.J., L.T. Watters, and S. Dunn-Norman (1998), *Petroleum Well Construction,* John Wiley & Sons Ltd.

Geilikman, M.B. and M.B. Dusseault (1997), Fluid rate enhancement from massive sand production in heavy-oil reservoirs, *Journal of Petroleum Science and Engineering*, 17, 5-18.

Van den Hoek, P.J. and M.B. Geilikman (2003), Prediction of sand production rate in oil and gas reservoirs, *Proceedings of SPE annual technical conference and exhibition*, Denver, Colorado, U.S.A.

Huang, H. (1999), *Discrete element modeling of tool-rock interaction*, Ph.D. dissertation, The University of Minnesota.

Ispas, I., R.A. Bray, I.D. Palmer, and N.G. Higgs (2002), Prediction and evaluation of sanding and casing deformation in a GOM shelf well, SPE/ISRM 78236, *Proceedings of SPE/ISRM Rock Mechanics Conference*, Irving, Texas, USA, October, 2002.

Itasca (2002), *PFC^{2D} user's guide*.

Itasca (2005), *FLAC user's guide*.

Itasca (2006), *PFC^{3D} user's guide*.

Janna, W.S. (1993), *Introduction to fluid mechanics*, International Thomson Publishing.

Kooijman, A.P., P.M. Halleck, P. de Bree, C.A.M. Veeken, and C.J. Kenter (1992), Large-scale laboratory sand production test, *Proceedings of the 67th annual technical conference and exhibition of the Society of Petroleum Engineers*, Washing DC, SPE 24798.

Kuhn, M.R. (1995), A flexible boundary for three-dimensional DEM particle assemblies, *Engineering Computations*, 12, 175-183.

Masson, S. and J. Martinez (2000), Multiscale simulations of the mechanical behavior of an ensiled granular material, *Mechanics of Cohesive-Frictional Materials*, 5, 425-442.

Morita, N., D.L. Whitfill, Ø.P. Fedde, and T.H. Løvik (1989a), Parametric study of sand-production prediction: Analytical approach, *SPE Production Engineering*, 4, 25-33.

Morita, N., D.L. Whitfill, I. Massie, and T.W. Knudesn (1989b), Realistic sand-production prediction: Numerical approach, *SPE Production Engineering*, 4, 15-24.

Murdoch, L.C. and W.W. Slack (2002), Forms of hydraulic fractures in shallow fine-grained formations, *Journal of Geotechnical and Geoenvironmental Engineering*, 128(6), 479-487.

Nascimento, U. (1981), Lubricant and antilubricant effects of water, *Proceedings of the International Conference on Soil Mechanics and Foundation Engineering*, Stockholm, Sweden, 15-19 June, 1981.

Ng, T.T. (2004), Triaxial test simulation with Discrete Element Method and hydrostatic boundaries, *Journal of Engineering Mechanics*, 130(10), 1188-1194.

Nouri, A., M.M. Al-Darbi, H.H. Vaziri, and R. Islam (2002a), Deflection criteria for numerical assessment of the sand production potential in an openhole completion, *Energy Sources*, 24, 685-702.

Nouri, A., M.M. Al-Darbi, H.H. Vaziri, and R. Islam (2002b), A new theory and methodology for modeling sand during oil production, *Energy Sources*, 24, 995-1007.

Nouri, A., H.H. Vaziri, H. Belhaj, and R. Islam (2003a), A comprehensive approach to modeling sanding during oil production, SPE 31032, *Proceedings of SPE Latin American and Caribbean petroleum Engineering Conference*, Port-of-Spain, Trininad, West Indies, 27-30 April 2003.

Nouri, A., H.H. Vaziri, H. Belhaj, and R. Islam (2003b), Comprehensive transient modeling of sand production in horizontal wellbores, *Proceedings of SPE Annual Conference and Exhibition*, Denver, Colorado, U.S.A.

Nouri, A., H.H. Vaziri, H. Belhaj, and R. Islam (2003c), Effect of volumetric failure on sand production in oil-wellbores, *Proceedings of SPE Asia Pacific Oil and Gas Conference and Exhibition*, Jakarta, Indonesia.

Nouri, A., H.H. Vaziri, H. Belhaj, and R. Islam (2004), Sand production prediction: a new set of criteria for modeling based on large-scale transient experiments and numerical investigation, *Proceedings of SPE Annual Conference and Exhibition*, Houston, Texas, U.S.A.

O'Connor, R.M., J.R. Torczynski, D.S. Preece, J.T. Klosek, and J.R. Wiiliams (1997), Discrete element modeling of sand production, *International Journal of Rock Mechanics and Mining Science*, 34 (3-4), 213-222.

Oger, L., S.B. Savage, D. Corriveau, and M. Sayed (1998), Yield and deformation of an assembly of disks subjected to a deviatoric stress loading, *Mechanics of Materials*, 27, 189-210.

Papamichos, E. and M. Stavropoulou (1998), An erosion-mechanical model for sand production rate prediction, *International Journal of Rock Mechanics and Mining Science*, 35(4-5), Paper No. 90.

Papamichos, E. and I. Vardoulakis, J. (2005), sand erosion with a porosity diffusion law, *Computers and Geotechnics*, 32(1), 47-58.

Papamichos, E., I. Vardoulakis, J. Tronvoll, and A. Skjærstein (2001), Volumetric sand production model and experiment, *International Journal for Numerical and Analytical Method in Geomechanics*, 25, 789-808.

Potyondy, D.O. and J. Autio (2001), Bonded-particle simulations of the in-situ failure test at Olkiluoto, *Proceedings of Rock mechanics in the National Interest*, Lisse, Netherlands.

Potyondy, D.O. and P.A. Cundall (2004), A bonded-particle model for rock, *International Journal of Rock Mechanics & Mining Science*, 41, 1329-1364.

Risnes, R., R.K. Bratli, and P. Horsrud (1982), Sand arching- A case study, SPE 12948, *Proceedings of European Petroleum Conference*, London, United Kingdom, 25-28 October, 1982.

Shimizu, Y. (2004), *Fixed coarse-grid fluid scheme in PFC^{2D}*, Itasca Consulting Group Inc.

Skinner, A.E. (1969), A note on the influence of interparticle friction on the shearing strength of a random assembly of spherical particles, *Geotechnique*, 19, 150-157.

Stavropuolou, M., P. Papanastasiou, and L. Vardoulakis (1998), Coupled Wellbore Erosion and Stability Analysis, *International Journal for Numerical and Analytical Methods in Geomechanics*, 22, 749-769.

Ting, J.M., B.T. Corkum, C.R. Kauffman, and C. Greco (1989), Discrete numerical model for soil mechanics, *Journal of Geotechnical Engineering*, 115, 379-398.

Tronvoll, J., A. Skjærstenin, and E. Papamichos (1997), Sand production: mechanical failure or hydrodynamic erosion, *International Journal of Rock Mechanics and Mining Science*, 34(3-4), 853-862.

Vardoulakis, I., M. Stavropoulou, and P. Papanastasiou (1996), Hydro-mechanical aspects of the sand production problem, *Transport in Porous Media*, 22, 225-244.

Vaziri, H.H. (1995), Analytical and numerical procedures for analysis of flow-induced cavitation in porous media, *Computer & Structures*, 54, 223-238.

Vaziri, H.H. and Y. Xiao (2003), Numerical evaluation of geomechanical parameters affecting productivity index in weak rock formations – Part 2: field application, *Journal of Canadian Petroleum Technology*, 42(12), 33-38.

Vaziri, H.H., Y. Xiao, R. Islam, and A. Nouri (2002), Numerical modeling of seepage-induced sand production in oil and gas reservoirs, *Journal of Petroleum Science and Engineering*, 36, 71-86.

CHAPTER IV

GOVERNING EQUATIONS FOR GAS STORAGE CAVERNS BASED ON FLUID TRANSIENTS

4. 1 Introduction

4.1.1 Gas Storage Caverns in Carbonate Rock Formations

Natural gas is the second largest energy source after petroleum, accounting for approximately 20% of energy consumed in the United States [*EIA*, 2005]. Natural gas consumption changes from month to month, increasing by 50% during winter [*NETL*, 2005]. In contrast, natural gas production is steady throughout the year [*NETL*, 2005]. Thus, to meet the gap between demand and supply of natural gas, surplus natural gas should be stored when supply exceeds demand. Several methods have been used for the storage of natural gas such as insulated tanks, depleted gas and oil fields, salt caverns, and hard rock caverns [*EIA*, 2009].

Currently, natural gas is temporarily stored in the form of liquefied natural gas (LNG) in insulated tanks while waiting for re-gasification and distribution to consumers. This is a very expensive form of storage. As a result, temporary storage of LNG adds significant cost. For example, an LNG storage tank costs approximately \$17.0 per 10^6 BTU (British Thermal Unit) [*Powell*, 2006] by assuming that 1.0 Gallon of LNG corresponds to 89000 BTU [*Hofstrand*, 2008], whereas a depleted oil reservoir storage and a salt cavern storage cost approximately \$0.5 per 10^6 BTU and \$1.0 per 10^6 BTU, respectively [*Dietert and Pursell*, 2000]. In addition, such facilities are also vulnerable to fire hazards [*U.S. Department of Energy*, 2009]. For natural gas storage, therefore, subsurface caverns (such as solution mined salt caverns) or porous reservoirs (such as depleted gas fields or aquifers) are commonly used [*EIA*, 2009].

In the United States, most of the natural gas storage is located in depleted natural gas or oil fields close to major eastern and midwestern markets [*EIA*, 2009; *NGSA*, 2004; *NETL*, 2005]. The storage of natural gas in depleted reservoirs takes advantage of existing wells, equipment, and pipes as well as existing information about the characteristics of these reservoirs. However, the number of available existing depleted fields close to major markets is limited. Furthermore, approximately 50% of the stored gas must be left as cushion gas, which may be unrecoverable [*NETL*, 2005].

Although aquifer storage accounts for substantial parts of the natural gas storage around the world, it has several disadvantages [*Dussaud*, 1989]. For most aquifers, limited amount of geological data is available [*Toelcke*, 1989]. Aquifer storage results in a large amount of unrecoverable cushion gas that can be up to 80% of the total volume [*NGSA*, 2004]. Due to these disadvantages, aquifer storage is the least desirable among the various storage methods.

Salt caverns are also used for natural gas storage in the United States and Europe [*Hardy*, 1982; *Dussaud*, 1989; *Menzel and Schreiner*, 1989; *Oebro*, 1989; *NGSA*, 2004]. One of the main advantages of salt caverns as natural gas storage is that the volume of cushion gas can be reduced significantly [*NGSA*, 2004]. In the United States, however, salt formations suitable for natural gas storage are limited to the Gulf Coast of Texas and Louisiana [*Bauer et al*., 1998]. Thus, although they provide excellent storage, salt caverns are in general too far from the major markets.

Hard rock caverns have also been used for storage of compressed gas in the United States and Europe [*Froise*, 1987; *Lindblom*, 1989; *Broch*, 1989]. Although hard rock formations are suitable for natural gas storage, the cost of creation is much higher than that for creating cavities in salt domes [*Foley*, 2006].

Recently, a new method of natural gas storage has been proposed [*Castle et al*., 2004]. This method is similar to that for creation of a salt cavern, that is, the cavern is created in a carbonate rock formation by dissolution using aqueous acid injection. Such a

cavern can store as much as a billion cubic feet of natural gas [*Castle et al*., 2004]. Natural gas storage in a solution-mined carbonate cavern has several advantages compared to other storage methods. Suitable carbonate rock formations for natural gas storage are more common than salt domes and depleted reservoirs in the northeastern United States [*Yang*, 2004; *Atteberry*, 2005]. Carbonate rock caverns require less cushion gas and reduce loss into the surrounding formations. Thus, a gas storage cavern created by the acid injection method in a carbonate rock formation is a promising technology for storing surplus natural gas [*Castle et al*., 2004].

For the acid injection method, a well is drilled into a carbonate rock. Then, aqueous hydrochloric acid (HCl) is injected into the well to dissolve the carbonate rock formation. After pumping out the byproducts, a storage cavern is created. The two major byproducts in this chemical process are CO_2 and brine of calcium chloride ($CaCl_2$) or magnesium chloride ($MgCl_2$). The brine is pumped out of the cavern (Figure 4.1), but the pressure of CO_2, remaining in the cavern, is maintained for the sake of cavern stability.

The two major carbonate rocks suitable for gas storage caverns are limestone and dolomite [*Falta et al*., 2004]. Limestone is a sedimentary rock composed mainly of the mineral calcite (i.e., calcium carbonate, $CaCO_3$). Dolomite rock is predominantly composed of the mineral dolomite (i.e., calcium magnesium carbonate, $CaMg(CO_3)_2$). The chemical reactions of limestone and dolomite with hydrochloric acid are expressed as follows [*Falta et al*., 2004]:

$$2HCl^{aq} + CaCO_3{}^{s} \Leftrightarrow CaCl_2{}^{aq} + H_2O^{l} + CO_2{}^{sc} \quad (4.1.1)$$

$$4HCl^{aq} + CaMg(CO_3)_2{}^{s} \Leftrightarrow CaCl_2{}^{aq} + MgCl_2{}^{aq} + 2H_2O^{l} + 2CO_2{}^{sc} \quad (4.1.2)$$

where superscripts *s* indicates the solid state, *aq* the aqueous phase, *l* the liquid phase, and *sc* the supercritical state.

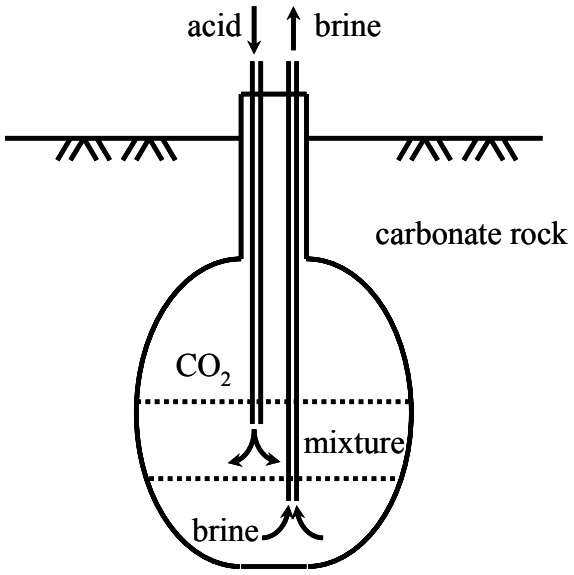

Figure 4.1 Schematic of creation of a gas storage cavern by dissolution of carbonate rock with aqueous acid (HCl) (not to scale). By injecting acid, carbonate rock is dissolved, and a cavern is created. CO_2 and brine appear as a result of the carbonate dissolution. Driven by the density difference between the two materials, CO_2 rises towards the ceiling of the cavern, whereas the brine sinks to the bottom of the cavern. A mixed zone ("mixture") of CO_2, acid, and brine forms near the place of acid injection.

According to (4.1.1) and (4.1.2), the calcium chloride in aqueous phase and magnesium chloride in aqueous phase are created from the chemical reaction. Water (H_2O) and carbon dioxide (CO_2) are the other byproducts of this reaction. Calcium and magnesium chlorides are highly soluble in water. Such dissolution results in brine of calcium or magnesium chlorides. As a reference, the solubility of sodium chloride (NaCl) in water is 0.36 g/ml at 25°C (77 °F) [*Lide*, 2004], while the solubility of calcium chloride in water is 0.81 g/ml, and that of magnesium chloride is 0.56 g/ml at 25°C (68 °F) [*Lide*, 2004]. Hence, brine is created as a byproduct of the chemical process, (4.1.1) and (4.1.2). Nevertheless, if the amount of water is not sufficient to dissolve during the chemical process, the created calcium chloride and magnesium chloride will precipitate. The physical properties of CO_2 depend on temperature and pressure. If the temperature and

pressure of CO_2 are both increased beyond the critical point, CO_2 behaves as a supercritical fluid. The supercritical fluid is a substance with both gas- and liquid-like properties. It is liquid-like because it has a much higher density than gas has, as well as gas-like because it is a still relatively compressible fluid compared to its liquid phase, although this distinction is relative [*Dean*, 1993]. The critical point of CO_2 is 31.1 °C (87.9 °F) and 7.3 MPa (1063 psi) [*Reid et al*., 1987] as shown in Figure 4.2. At this point, CO_2 density and compressibility are 320 kg/m^3 and 9.4×10^{-8} Pa^{-1}, respectively [*NIST*, 2006].

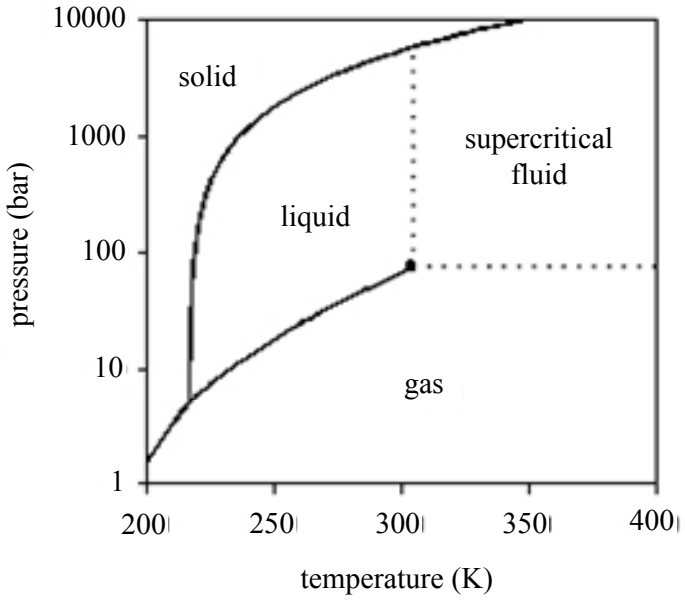

Figure 4.2 Phase diagram for CO_2. The critical point of CO_2 is 31.1 °C (87.9 °F) and 7.3 MPa (1063 psi) [*Reid et al*., 1987]. At critical point, CO_2 density and compressibility are 320 kg/m^3 and 9.4×10^{-8} Pa^{-1}, respectively [*NIST*, 2006].

For example, if a cavern is located at a depth below 1000 m (3281 ft) [e.g., *Castle et al*., 2005], the hydrostatic pressure is 9.8 MPa (given water density ρ = 1000 kg/m^3). It is quite possible that, at this depth, the temperature of the carbonate rock formation could be greater than 55°C (131°F) by assuming temperature gradient of 30°C/km [*Pruess*,

2005]. Then, CO_2 created by the chemical reaction in (4.1.1) and (4.1.2) would be in the supercritical state. In this case, since the supercritical CO_2 is not an ideal gas, its density can be calculated as [e.g., *Lake*, 1989]

$$\rho_{CO_2} = \frac{pM_{CO_2}}{ZRT} = 586 \text{ kg/m}^3 \tag{4.1.3}$$

where ρ_{CO_2} is the CO_2 density, p = 9.8 MPa is the CO_2 partial pressure, M_{CO_2} = 44.1 g/mole is the CO_2 molar mass, Z = 0.27 is the CO_2 compressibility factor, R = 8.314 J/(mol·K) is the universal gas constant [*Dake*, 1978], and T = 328 K (55°C) is the temperature of CO_2 by assuming temperature gradient of 30°C/km [*Pruess*, 2005]. If the supercritical CO_2 were an ideal gas, the value of the compressibility factor, Z, would be 1.0. Notations used in this chapter and values of some parameters are also listed in section 4.4.

In Figure 4.1, consider a cavern created by the acid injection method. If fluid pressure and temperature in the vicinity of the cavity are above the critical point of CO_2 (Figure 4.2), the phase of CO_2 should be supercritical [*Lake*, 1989]. During the acid injection, supercritical CO_2 rises up to the ceiling of the cavern. In contrast, brine is sinking to the bottom of the cavern, due to the difference in their densities. Between the CO_2 and brine layers, a layer of a mixture composed of acid (HCl), brine, and CO_2 may be formed. The physical properties of the mixture depend on the fraction of each component.

One of the great concerns for the creation of a gas storage cavern is its stability [*Foley*, 2006]. The stability of the cavern is affected by several factors that include in-situ stress, rock properties, local stratigraphy, internal pressure, cavern geometry [*Foley*, 2006]. Among these factors, the cavern geometry is the major focus of this work. The geometry of a cavern must be determined on the basis of the in-situ stress. That is, to reduce the stress concentration around the cavern, the axis ratio of the cavern must be properly chosen [*Hoek and Brown*, 1980]. Otherwise, it may lead to such undesirable effects as

rock spalling, roof buckling, surface subsidence, and even cavern collapse [*Hoek and Brown*, 1980; *Coates et al.*, 1981; *Hardy*, 1982; *Badie and Wang*, 1990; *Hu*, 1997; *Barla and Barla*, 2001].

The decision of the acid injection point is of major importance to control the geometry of a cavern. For example, if acid is injected only at a fixed depth, an excessive cavity will be formed (Figure 4.3). Since such an excessive cavity is generally not stable, it may collapse, which may compromise the stability of the entire cavern [*Foley*, 2006]. Thus, the injection depth must be changed continuously to obtain the required cavern shape.

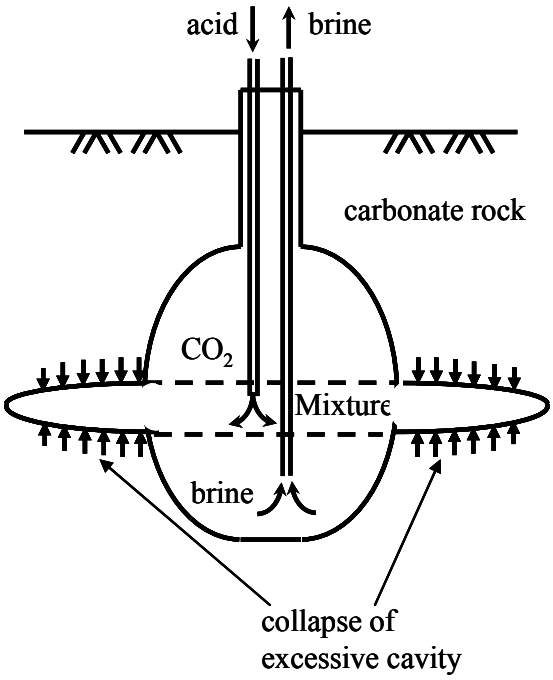

Figure 4.3 Geometry of the collapse of an unstable excessive cavity due to vertical stress (not to scale). The excessive cavity around a cavern may collapse due to confining stresses.

To control the depth of the injection point and the rate of dissolution, we need to know the location of the interface between the mixture and the brine. Most of the dissolution of the carbonate rock probably occurs in the mixture zone and adjacent areas because the concentration of acid is higher in these places.

The primary goal of this work is to utilize the method of fluid transients as a means to locate the interface as well as to characterize the geometry of the caverns for their stability.

4.1.2 Fluid Transients

Transient fluid flow refers to flow conditions that change with time [*Wylie and Streeter*, 1978]. A typical fluid transient phenomenon can be illustrated by the water hammer effect [*Wylie and Streeter*, 1978]. Consider a pipe connected to a reservoir with constant depth shown in Figure 4.4a.

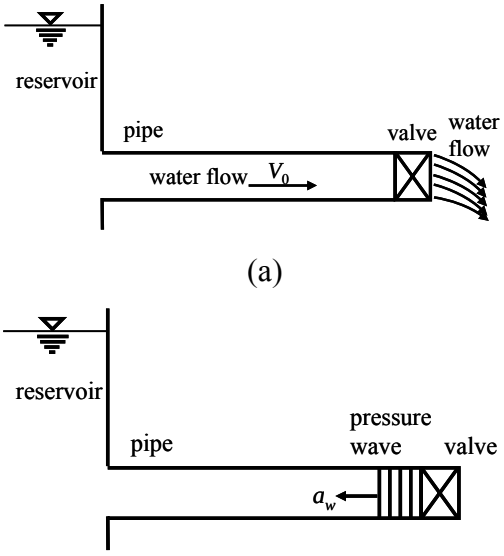

Figure 4.4 Schematic of the water hammer effect [after *Wylie and Streeter*, 1978]: (a) a closed conduit connected to a reservoir with a constant depth and a fully open outflow valve and (b) propagation of a pressure wave due to an abrupt closure of the outflow valve.

Initially, the valve at the outflow end of the pipe is open. Therefore, water flows through the pipe with a constant velocity, V_0, (Figure 4.4a). If the valve is closed suddenly, a pressure wave would be created that propagates with the wave speed, a_w, toward the reservoir [*Chaudhry*, 1987] (Figure 4.4b). In the same manner, changing a boundary condition can generate a transient pressure change in the system [*Wylie and Streeter*, 1978]. For example, injecting a controlled amount of fluid into a pipe can create pressure waves that propagate through the system.

Fluid transients have already been used to determine the characteristics of hydraulic fractures [*Holzhausen and Egan*, 1986; *Holzhausen and Gooch*, 1985a; 1985b]. By generating a wave and measuring the reflected and refracted waves at the wellhead, the reflection coefficient of the hydraulic fracture can be determined. The reflection coefficient can be expressed in terms of the hydraulic impedance of the fracture and that of the well. The hydraulic impedance of the hydraulic fracture is a function of the fracture geometry. Hence, information about the geometry of the hydraulic fracture can, in principle, be obtained from the fracture reflection coefficient. This method is generally called the Hydraulic Impedance Testing Method (HIT) [*Paige et al.*, 1992; 1995; *Soliman and Azari*, 1998].

During acid injection into a well to create gas storage caverns, however, three different fluids exist in the pipe and the cavern. Also, the geometries of such caverns are different than those of hydraulic fractures in wells in terms of pressure wave propagation. Thus, HIT cannot be directly used in this work. Instead, we model the pressure wave propagation during an acid injection stage by obtaining and solving governing equations for the transient fluid flow in a pipe-cavern system. We then conduct a series of parametric studies by changing such parameters as the cavern diameter and the location of the interface between the mixture and the brine. On this basis, one can develop a new technique based on the analysis of pressure histories measured at the wellhead. The purpose of this chapter is to formulate governing equations that will be used in Chapter 5.

Chapter 5 is to substantiate that the new technique can be utilized to characterize gas storage caverns during the acid injection stage.

4.2 Fluid Transients in the Pipe-Cavern System

The behavior of transient fluid flow in a pipe can be described by mass and momentum balance equations [e.g., *Chaudhry*, 1987]. Thus, such equations are used as the governing equations in this work. The derivation of the governing equations for transient fluid flow in a pipe is based on the following assumptions:

1. Fluid flow is one-dimensional (1-D), that is, the characteristic quantities are averaged along the pipe cross-section.
2. Hydraulic losses are quasi-steady, that is, the same losses are assumed for a steady and transient flows at a given mean velocity of a fluid.
3. The dynamic fluid-pipe interaction is neglected such that a quasi-steady pipe response to pressure changes is assumed.
4. Changes in the cross-sectional area of the pipes and the cavern due to wave propagation are relatively small.

If the length of a pipe is sufficiently long compared to the diameter of the pipe, lateral flow can usually be neglected. Therefore, we can consider fluid flow to be one dimensional [*Thompson*, 1972]. This constitutes the first assumption. Hydrodynamic losses described by the second assumption are usually characterized by the friction factor f that varies with the Reynolds number. The effects of variations of f on transient conditions are small and can typically be neglected [*Chaudhry*, 1987].

Pressure wave generated by water hammer may excite structural system by applying dynamic force to fittings where flow direction or area changes (e.g., elbows, tees, and valves). Such excitation may lead to pipe motion, which in turn can create water

hammer effect [*Wiggert et al*., 1985; *Tijsseling*; 2007]. Effect of such interactions on a cavern and pipes, transmitted by the pressure waves is beyond the scope of this work. Thus, the dynamic fluid-pipe interaction is not considered. The forth assumption will be discussed later in Section 4.3.

Conventional governing equations for transient fluid flow in a pipe (often called "water-hammer equations") [e.g., *Wiley and Streeter*, 1978; *Charudhry*, 1987] consider a pipe under internal pressure. Therefore, we need to investigate pressure wave propagation in caverns located in carbonate rock formations and pipes under both internal and external pressures. Instead of considering the general mass balance condition, it is more convenient to address separately the following three particular cases of interest. In other words, in order to characterize a cavern, pressure waves are triggered to propagate through (*i*) pipes loaded only internally and (*ii*) pipes loaded both internally and externally. Because the cavern is expected to have a large aspect ratio and be elongated in vertical direction, we model it by a "tall" cylinder (Chapter 5). Such a cavern itself can be considered as an interior of a pipe (with infinite thickness), which contains injection and production pipes (Figure 4.5).

Suppose that a flow perturbation is generated in the injection pipe near the ground surface. The corresponding pressure waves then travel along the pipe and continue downward propagating in the cavern. Due to the contrast in properties between the brine and mixture, a reflected wave is expected to propagate upwards from the interface along the cavern. At the same time, the wave transmitted through the interface continues propagating downwards. These two waves results in the perturbation or pressure in the cavern, which loads the production pipe externally. Because at this stage, the transmitted wave has not reached the cavern bottom yet and, therefore, there is no pressure perturbation propagating from the bottom inside or outside of the production pipe, the external loading of this pipe near the brine-mixture interface is the only source of pipe loading.

This loading generates pressure perturbation inside the production pipe that travels towards the place of recording above the cavern. Registering its arrival and characteristics at the place of recording may be useful for locating the position of the brine-mixture interface. More detailed consideration is given in Chapter 5, but this example shows that the internal pressure wave can be generated in a pipe by applying the external load.

In general, a pipe with a circular cross-section is a relatively rigid system with respect to the pressure perturbation applied to the outer surface of the pipe. Therefore, if the pipe is loaded by both internal and external pressures of comparable magnitude, it behaves as a rigid body, in the sense that the external pressure does not significantly affect the internal pressure wave. For example, if the pipes shown in Figure 4.5 were connected with each other, we would not need to include the effect of the external pressure. However, when the external pressure is the sole source of internal pressure waves, which propagate through the pipe, we may need to take the impact of the external pressure into account. This may be the case when a pipe made of elastic material is located in the interior of another pipe with a propagating wave.

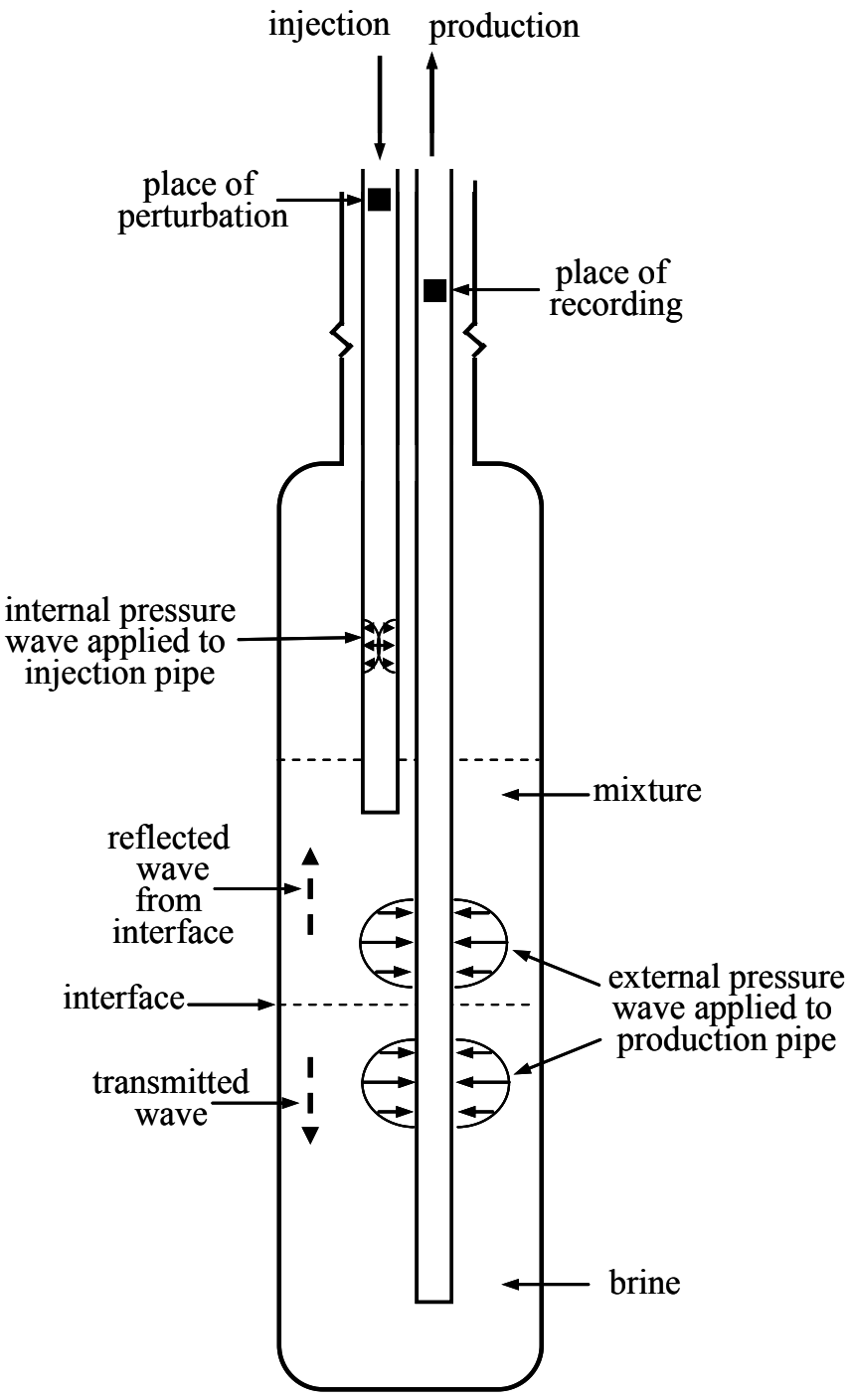

Figure 4.5 Pressure waves propagating through a pipe-cavern system due to perturbation at the top of the injection pipe.

4.3 Mass Balance Equations for Transient Fluid Flows

There are three different cases of interest for mass balance equations. The first case is fluid flow in a pipe under internal pressure. This case is required to describe the fluid flow in the pipes used for acid injection (Figure 4.5), and conventional governing equations [e.g., *Wiley and Streeter*, 1978; *Charudhry*, 1987] can describe the transient fluid flow in this case. The second case is fluid flow in a cavern. In Figure 4.5, a mixture of acid, CO_2, and brine exists in the cavern due to the chemical reactions such as (4.1.1) and (4.1.2). The third case is flow of brine out of the cavity through the production pipe. In general, the pipe used to pump out brine (Figure 4.5) is loaded both internally and externally by fluid. Since the conventional governing equations do not describe the transient fluid flow for the third case, we need to modify the mass balance equation.

4.3.1 Mass Conservation for Fluid Transients

To derive the mass balance equation for fluid flow in a pipe under internal pressure, consider a fluid flow in a pipe with elastic walls and a circular cross-section (Figure 4.6). Although this equation is well known [e.g., *Wiley and Streeter*, 1978; *Charudhry*, 1987], we rederive it here to establish the framework for the case of the pipe loaded externally and to have a clear basis for comparison. Also, the form of the mass balance equation discussed in this section, 4.3.1 is applicable to both pipes loaded internally and externally as well as flow in a cavern.

The fluid mass crossing section x_i per unit time, q_i, is

$$q_i = \rho_i A_i v_i \tag{4.3.1}$$

where ρ_i is the density of fluid, A_i is the cross-sectional area of the pipe, and v_i is the fluid velocity (i = 1, 2). Hereafter, subscripts 1 and 2 represent flow sections 1 and 2 (Figure 4.6). Fluid mass, m, between cross-section x_1 and x_2 is given by

$$m = \int_{x_1}^{x_2} \rho A dx \tag{4.3.2}$$

and the mass conservation law between x_1 and x_2 can be expressed as

$$\int_{t_1}^{t_2} \rho_1 A_1 v_1 dt - \int_{t_1}^{t_2} \rho_2 A_2 v_2 dt = \left[\int_{x_1}^{x_2} \rho A dx \right]_{t_1}^{t_2} \tag{4.3.3}$$

where t_1 and t_2 are two arbitrary moments of time ($t_1 < t_2$). The right-hand side of (4.3.3) represents the mass change between x_1 and x_2 from time t_1 to time t_2.

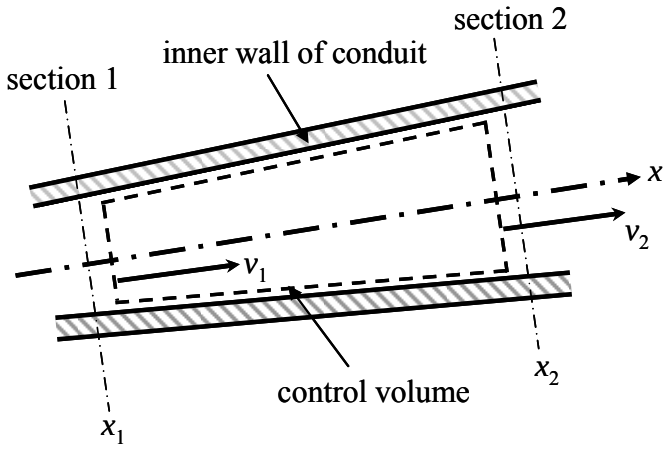

Figure 4.6 Longitudinal view of fluid flow between sections 1 and 2 in a conduit [after *Chaudhry*, 1987]. Control volume is marked with dashed lines. Fluid flow velocities through sections 1 and 2 are v_1 and v_2, respectively. Here, x is an Eulerian coordinate (fixed in space).

Expression (4.3.3) can be rewritten as

$$\int_{t_1}^{t_2}(\rho_1 A_1 v_1 - \rho_2 A_2 v_2)dt = \int_{t_1}^{t_2}\frac{d}{dt}\left[\int_{x_1}^{x_2}\rho A dx\right]dt \tag{4.3.4}$$

and because t_1 and t_2 in (4.3.4) are arbitrary, the sign of the integral with respect to t can be omitted resulting in

$$\rho_1 A_1 v_1 - \rho_2 A_2 v_2 = \int_{x_1}^{x_2}\frac{\partial}{\partial t}(\rho A)dx \tag{4.3.5}$$

Since the left-hand side in (4.3.5) can be written in the integral form

$$\rho_1 A_1 v_1 - \rho_2 A_2 v_2 = -\int_{x_1}^{x_2}\frac{\partial}{\partial x}(\rho A v)dx \tag{4.3.6}$$

and because x_1 and x_2 are also arbitrary, from (4.3.5) and (4.3.6), we have

$$\frac{\partial}{\partial t}(\rho A) + \frac{\partial}{\partial x}(\rho A v) = 0 \tag{4.3.7}$$

By arranging and collecting terms, (4.3.7) can be rewritten as

$$\frac{1}{\rho}\left(\frac{\partial \rho}{\partial t} + v\frac{\partial \rho}{\partial x}\right) + \frac{1}{A}\left(\frac{\partial A}{\partial t} + v\frac{\partial A}{\partial x}\right) + \frac{\partial v}{\partial x} = 0 \tag{4.3.8}$$

where $\rho = \rho(x,t)$, $A = A(x,t)$, and $v = v(x,t)$.

In (4.3.8), x is a Eulerian coordinate (fixed in space). Let x_0 be the corresponding Lagrangian coordinate. Specifically, a particle that is now at x was at x_0 at $t = 0$. In other words,

$$x = x(x_0, t) \tag{4.3.9}$$

so that, a material particle of fluid x_0 at time t will be located at point x defined by (4.3.9) $x(x_0, 0) = x_0$. Then, the total derivative of the fluid density is

$$\frac{d\rho}{dt} = \frac{\partial \rho}{\partial t} + v\frac{\partial \rho}{\partial x} \tag{4.3.10}$$

and the total derivative of the pipe cross-sectional area is

$$\frac{dA}{dt} = \frac{\partial A}{\partial t} + v\frac{\partial A}{\partial x} \tag{4.3.11}$$

By inserting (4.3.10) and (4.3.11) into (4.3.8), we obtain

$$\frac{1}{\rho}\frac{d\rho}{dt} + \frac{1}{A}\frac{dA}{dt} + \frac{\partial v}{\partial x} = 0 \tag{4.3.12}$$

This is the sought mass balance equation [e.g, *Wiley and Streeter*, 1978; *Charudhry*, 1987]. Below, this equation will be rewritten in more convenient form.

4.3.2 Change of the Pipe Area in Pressure Transient

For a circular pipe,

$$A(x,t) = \pi a^2(x,t) \tag{4.3.13}$$

where a is the inner radius of the pipe. By taking the total derivative of (4.3.13), we have

$$\frac{dA}{dt} = \pi \frac{da^2}{dt} = \frac{2\pi a^2}{a} \frac{da}{dt} \tag{4.3.14}$$

From time t to $t+dt$, the internal pipe radius changes from a to $a+da$ (Figure 4.7)

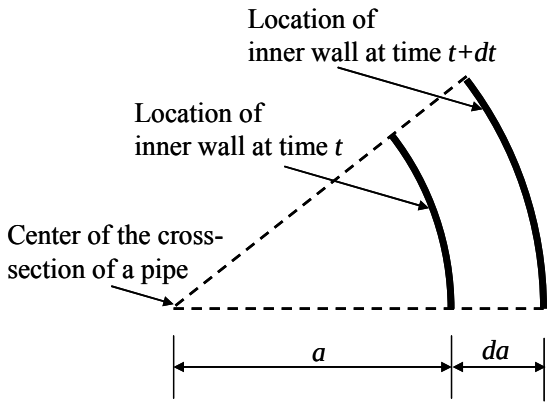

Figure 4.7 Deformation of a pipe wall from time t to time $t+dt$. At time t, radius of the pipe is a, and at time $t+dt$, it becomes $a+da$ (pipe cross-section is shown).

Therefore, the change of the tangential strain $\varepsilon_{\theta\theta}(r,x,t)$ on the pipe wall is

$$d\varepsilon_{\theta\theta} = \frac{da}{a} \qquad (r = a) \tag{4.3.15}$$

Inserting (4.3.15) into (4.3.14), we have

$$\frac{1}{A}\frac{dA}{dt} = 2\frac{d\varepsilon_{\theta\theta}}{dt} \qquad (r = a) \tag{4.3.16}$$

which is a relationship between the rate of change of pipe cross-sectional area and tangential strain rate on the pipe wall. We can use Hooke's law to connect dA/dt to the pressure change in the pipe, which will be discussed later in this section.

Consider a hollow cylinder loaded with an internal pressure (Figure 4.8). As a sign convention, tensile stresses and strains are assumed to be positive in this chapter. For both plane stress and plane strain conditions, the radial, σ_{rr}, and tangential, $\sigma_{\theta\theta}$, stresses around the cylinder are given by [*Timoshenko and Goodier*, 1970]

$$\sigma_{rr} = \frac{a^2 p}{b^2 - a^2}\left(1 - \frac{b^2}{r^2}\right), \quad \sigma_{\theta\theta} = \frac{a^2 p}{b^2 - a^2}\left(1 + \frac{b^2}{r^2}\right) \tag{4.3.17}$$

where a is the inner radius of the cylinder, b is the outer radius, p is the internal pressure, and r is the radial distance from the center of the cylinder (Figure 4.8).

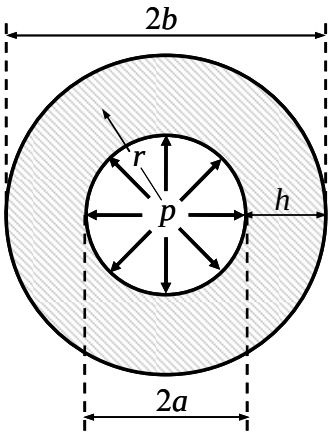

Figure 4.8 Cross-section of a hollow cylinder loaded by internal pressure p. Inner and outer radii of the cylinder are a and b, respectively. The thickness $b - a$ of the cylinder is denoted by h (i.e., $h = b - a$).

For a thin-walled cylinder, the wall thickness $h = b - a << a$. Therefore, expression (4.3.17) can be rewritten as

$$\sigma_{rr} = \frac{ap}{2h} O\left(\frac{h}{a}\right), \quad \sigma_{\theta\theta} = \frac{ap}{2h}\left[2 + O\left(\frac{h}{a}\right)\right] \qquad (h << a) \qquad (4.3.18)$$

which implies that

$$|\sigma_{\theta\theta}| >> |\sigma_{rr}| \qquad (h << a,\ a \le r \le b) \qquad (4.3.19)$$

Below we consider two end-member cases of loading conditions along the pipe, that is, (*i*) plane stress and (*ii*) plane strain deformations in the *x*-direction. In the case of plane stress condition, axial stress $\sigma_{xx} = 0$, and Hooke's law for the tangential strain, $\varepsilon_{\theta\theta}$, is given by [*Timoshenko and Goodier*, 1970]

$$\varepsilon_{\theta\theta} = \frac{1}{E}[\sigma_{\theta\theta} - \nu(\sigma_{rr} + \sigma_{xx})] \qquad (4.3.20)$$

where E is the Young's modulus of the pipe material, and ν is the Poisson's ratio of the pipe material. Inserting (4.3.18) into (4.3.20) results in

$$\varepsilon_{\theta\theta} = \frac{1}{E}\frac{ap}{2h}\left[2 + O\left(\frac{h}{a}\right)\right] \qquad (h << a) \qquad (4.3.21)$$

which is independent of r in the leading term.

For plane strain condition, axial strain $\varepsilon_{xx} = 0$ and Hooke's law for $\varepsilon_{\theta\theta}$ can be written as [*Timoshenko and Goodier*, 1970]

$$\varepsilon_{\theta\theta} = \frac{1}{E}\left[(1-\nu^2)\sigma_{\theta\theta} - \nu(1+\nu)\sigma_{rr}\right] \qquad (4.3.22)$$

Using (4.3.18) with (4.3.22) results in

$$\varepsilon_{\theta\theta} = \frac{1-\nu^2}{E}\frac{ap}{2h}\left[2 + O\left(\frac{h}{a}\right)\right] \qquad (h << a) \qquad (4.3.23)$$

which is also independent of r in the leading term.

Combining expressions (4.3.21) and (4.3.23) and keeping only the leading terms, we write

$$\varepsilon_{\theta\theta} = C\frac{pD}{2Eh} \qquad (h << D) \qquad (4.3.24)$$

where $D = 2a$ is the internal diameter of the pipe (Figure 4.8). Here, the constant

$$C = \begin{cases} 1, & \text{plane stress} \\ 1-\nu^2, & \text{plane strain} \end{cases} \qquad (h << D) \qquad (4.3.25)$$

Taking the time derivative of both sides in (4.3.24), we have

$$\frac{d\varepsilon_{\theta\theta}}{dt} = \frac{C}{2Eh}\frac{d}{dt}(pD) \qquad (4.3.26)$$

Since $D = 2a$, (4.3.15) can be rewritten as $dD/dt = Dd\varepsilon_{\theta\theta}/dt$, and from (4.3.26), we obtain

$$\frac{d\varepsilon_{\theta\theta}}{dt} = \frac{C}{2Eh}\left[pD\frac{d\varepsilon_{\theta\theta}}{dt} + D\frac{dp}{dt}\right] \qquad (4.3.27)$$

which is equivalent to

$$\frac{d\varepsilon_{\theta\theta}}{dt} = \frac{\frac{CD}{2Eh}}{1-\frac{CpD}{2Eh}}\frac{dp}{dt} \tag{4.3.28}$$

Finally, from (4.3.28) and (4.3.16), we obtain the rate of change of the pipe area in the pressure transients

$$\frac{1}{A}\frac{dA}{dt} = \frac{2}{\frac{2Eh}{CD}-p}\frac{dp}{dt} \qquad (h << D) \tag{4.3.29}$$

expressed through the rate of pressure change (dp/dt), properties of the pipe material (E, C), and pipe geometry (h, D).

4.3.3 Mass Balance Equation for a Pipe Loaded Internally

The bulk modulus, K_0, of a fluid is defined by

$$dp = K_0\frac{d\rho}{\rho} \tag{4.3.30}$$

and we further consider fluids (liquids) with constant K_0. For liquids with constant bulk modulus, K_0, the pressure-density relationship is obtained by integrating (4.3.30):

$$p - p_0 = K_0 \ln\left(\frac{\rho}{\rho_0}\right) \tag{4.3.31}$$

where ρ_0 is the density of fluid at the initial pressure, p_0. Since (4.3.30) is valid for arbitrary x and t, we have

$$\frac{1}{\rho}\frac{d\rho}{dt} = \frac{1}{K_0}\frac{dp}{dt} \tag{4.3.32}$$

By inserting (4.3.29) and (4.3.32) into (4.3.12), we obtain the mass balance equation for a thin-walled pipe loaded internally:

$$\frac{\partial v}{\partial x}+\left(\frac{1}{K_0}+\frac{2}{\dfrac{2Eh}{CD}-p}\right)\frac{dp}{dt}=0 \qquad (h<<D) \qquad (4.3.33)$$

Suppose now that the pressure perturbation, p, in the pipe is not too high, that is,

$$p<<p_c=\frac{2Eh}{CD} \qquad (4.3.34)$$

where $p_c = 2Eh/(CD)$ is the characteristic pressure. If condition (4.3.34) is satisfied, that is, $p << p_c$, then equation (4.3.33) can be further simplified:

$$\frac{\partial v}{\partial x}+\left(\frac{1}{K_0}+\frac{1}{\dfrac{Eh}{CD}}\right)\frac{dp}{dt}=0 \qquad (h<<D,\ \ p<<p_c) \qquad (4.3.35)$$

In this form, the coefficient at dp/dt is independent of p, and it is customary to introduce the parameter a_w, which is called the wave speed in a fluid in a pipe. This parameter is defined by

$$a_w^2=\frac{K_0/\rho_0}{1+\dfrac{K_0CD}{Eh}}=\frac{a_0^2}{1+\dfrac{K_0CD}{Eh}} \qquad (4.3.36)$$

so that using the total derivative $dp/dt=\partial p/\partial t+v\partial p/\partial x$, we rewrite (4.3.35) as

$$\frac{\partial p}{\partial t} + v\frac{\partial p}{\partial x} + \rho_0 a_w^2 \frac{\partial v}{\partial x} = 0 \quad (h << D,\ \ p << p_c) \qquad (4.3.37)$$

In (4.3.36), $a_0 = (K_0 / \rho_0)^{1/2}$ is the sound wave speed in the liquid with the bulk modulus K_0 [*Browne*, 1999]. As can be seen from (4.3.36), $a_w < a_0$, that is, the pipe-liquid interaction reduces the speed of propagation of waves of this type (sound wave speed, a_0, remains the same).

Equation (4.3.37) represents the mass balance condition for the transient fluid flow in a thin-walled pipe loaded by small internal pressure perturbations [e.g., *Streeter and Wylie*, 1967].

4.3.4 Mass Balance Equation for Fluid Flow in a Cavern

The mass balance equation for a fluid flow in a cavern can be obtained similarly, but at another extreme of a pipe with infinitely thick wall. Specifically, consider a thick-walled cylinder such that its external diameter is much greater than internal, so that $b >> a$ in (4.3.17). Hence, the stress distribution around the cavern can be written as

$$\begin{aligned} \frac{\sigma_{rr}}{p} &= \frac{a^2}{b^2} - \frac{a^2}{r^2}\left[1 + \frac{a^2}{b^2}\right] + O\left(\frac{a^4}{b^4}\right) \\ \frac{\sigma_{\theta\theta}}{p} &= \frac{a^2}{b^2} + \frac{a^2}{r^2}\left[1 + \frac{a^2}{b^2}\right] + O\left(\frac{a^4}{b^4}\right) \end{aligned}, \qquad (b >> a) \qquad (4.3.38)$$

From (4.3.38), the radial and tangential stresses on the wall of the cavern are given by the well known expressions [e.g., *Timoshenko and Goodier*, 1970]

$$\sigma_{rr} = -p\ ,\ \sigma_{\theta\theta} = p + O\left(\frac{a^2}{b^2}\right) \quad (r = a,\ \ b >> a) \quad (4.3.39)$$

where we did not keep $O(a^4/b^4)$ in σ_{xx} because on the cavity wall $\sigma_{xx} = 0$ exactly due to the boundary condition (and as can be seen from (4.3.17)).

In the case of plane stress deformation, $\sigma_{xx} = 0$ exactly by definition. In plane strain, $\sigma_{xx} = \nu(\sigma_{rr} + \sigma_{\theta\theta})$. Therefore, the axial stress on the hole boundary

$$\sigma_{xx} = \begin{cases} 0, & \text{plane stress} \\ O\left(\dfrac{a^2}{b^2}\right), & \text{plane strain} \end{cases} \qquad (r = a,\ b >> a) \qquad (4.3.40)$$

Hence, in the limit of $b \to \infty$, the axial stress, σ_{xx}, is zero for both plane stress and plane strain conditions. Inserting (4.3.39) and (4.3.40) into Hooke's law (4.3.20) and keeping only the leading term gives the tangential strain around the cavern:

$$\varepsilon_{\theta\theta} = \frac{1+\nu}{E} p \qquad (r = a,\ b >> a) \qquad (4.3.41)$$

Hence, the rate of tangential strain on the cavern wall is given by

$$\frac{d\varepsilon_{\theta\theta}}{dt} = \frac{1+\nu}{E}\frac{dp}{dt} \qquad (r = a,\ b >> a) \qquad (4.3.42)$$

Because $\varepsilon_{\theta\theta}$ is the tangential strain on the internal wall of the pipe, (4.3.16) is valid for a pipe of arbitrary thickness. Therefore, it is applicable to the case under consideration ($b >> a$ or $b \to \infty$). Hence, from (4.3.42) and (4.3.16), we have

$$\frac{1}{A}\frac{dA}{dt} = 2\frac{1+\nu}{E}\frac{dp}{dt} \qquad (r = a,\ b >> a) \qquad (4.3.43)$$

and inserting (4.3.32) and (4.3.43) into the general mass balance equation (4.3.12), we arrive at

$$\frac{\partial p}{\partial t} + v\frac{\partial p}{\partial x} + \frac{K_0}{1 + K_0 \dfrac{2(1+\nu)}{E}}\frac{\partial v}{\partial x} = 0 \qquad (r = a,\ b >> a) \qquad (4.3.44)$$

Similar to (4.3.36), define the parameter of the wave speed, a_w, in a fluid in the cavern as [*Throely*, 1991; *Tijsseling*, 2007]

$$a_w^2 = \frac{K_0 / \rho_0}{1 + \dfrac{K_0}{G}} = \frac{a_0^2}{1 + \dfrac{K_0}{G}} \qquad (4.3.45)$$

where $G = E/[2(1+\nu)]$ is the shear modulus of the host material around a cavern and, as before, $a_0 = (K_0 / \rho_0)^{1/2}$ is the sound wave speed in the fluid ($a_w < a_0$). Then, (4.3.44) can be written in the general form [*Throely*, 1991; *Tijsseling*, 2007]

$$\frac{\partial p}{\partial t} + v\frac{\partial p}{\partial x} + \rho_0 a_w^2 \frac{\partial v}{\partial x} = 0 \qquad (4.3.46)$$

Expressions (4.3.37) and (4.3.46) are the mass balance equations for transient fluid flow in a pipe and a cavern, respectively. We can see that they have the same form except for the definition of a_w.

4.3.5 Mass Balance Equation for a Pipe Loaded Externally

Finally, consider a cylinder that is loaded not only by internal, p, but also by external, p_e, pressures (Figure 4.9). In this case, the radial and tangential stresses in the cylinder are given by [*Timoshenko and Goodier*, 1970]

$$\sigma_{rr} = \frac{a^2 b^2 (p_e - p)}{b^2 - a^2} \frac{1}{r^2} + \frac{a^2 p - b^2 p_e}{b^2 - a^2} \tag{4.3.47}$$

$$\sigma_{\theta\theta} = -\frac{a^2 b^2 (p_e - p)}{b^2 - a^2} \frac{1}{r^2} + \frac{a^2 p - b^2 p_e}{b^2 - a^2} \tag{4.3.48}$$

Similar to (4.3.24), the tangential strain in a thin-walled cylinder is obtained by considering the case of $h = a - b << a = D/2$ and substituting by stresses in the Hooke's law (4.3.20) and (4.3.22). We then have

$$\varepsilon_{\theta\theta} = C \frac{(p - p_e) D}{2Eh} \qquad (h << D) \tag{4.3.49}$$

which is also independent of r (in the leading term). As in (4.3.24), coefficient C in (4.3.49) is expressed by (4.3.25).

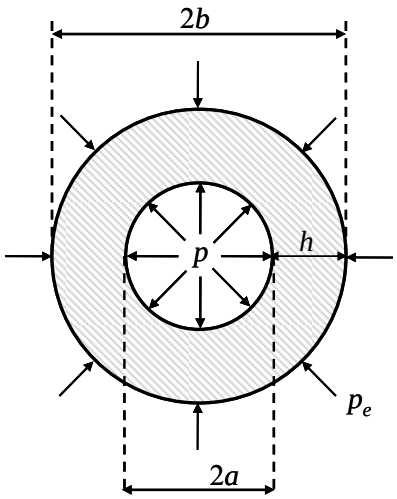

Figure 4.9 Cross-section of a cylinder loaded by internal pressure p and external pressure p_e. The inner and outer radii of the cylinder are a and b, respectively. The thickness of the cylinder is denoted by h.

Inserting (4.3.49) into (4.3.26) obtains

$$\frac{d\varepsilon_{\theta\theta}}{dt} = \frac{\frac{CD}{2Eh}}{1-\frac{C\Delta pD}{2Eh}}\left(\frac{dp}{dt} - \frac{dp_e}{dt}\right) \qquad (h << D) \qquad (4.3.50)$$

where $\Delta p = p - p_e$. Then, from (4.3.16) and (4.3.50), we have

$$\frac{1}{A}\frac{dA}{dt} = \frac{2}{\frac{2Eh}{CD} - \Delta p}\left(\frac{dp}{dt} - \frac{dp_e}{dt}\right) \qquad (h << D) \qquad (4.3.51)$$

and inserting (4.3.32) and (4.3.51) into (4.3.12) results in the mass balance equation for a thin-walled cylinder loaded both by internal and external pressures:

$$\frac{\partial v}{\partial x} + \left(\frac{1}{K_0} + \frac{2}{\frac{2Eh}{CD} - \Delta p}\right)\frac{dp}{dt} = \frac{2}{\frac{2Eh}{CD} - \Delta p}\frac{dp_e}{dt} \qquad (h << D) \qquad (4.3.52)$$

If the pressure difference is not too large and satisfies the condition

$$\Delta p = p - p_e << \Delta p_c = \frac{2Eh}{CD} \qquad (4.3.53)$$

where $\Delta p_c = p_c - p_e = 2Eh/(cD)$ is the characteristic pressure difference, then, (4.3.52) simplifies as

$$\frac{\partial v}{\partial x} + \frac{1}{K_0}\left(1 + \frac{CDK_0}{Eh}\right)\frac{dp}{dt} = \frac{CD}{Eh}\frac{dp_e}{dt} \quad (h << D,\ \Delta p << \Delta p_c) \quad (4.3.54)$$

Using the same definition (4.3.36) of the wave speed, a_w, in a pipe with liquid, (4.3.54) can be expressed as

$$\frac{dp}{dt} + \rho_0 a_w^2 \frac{\partial v}{\partial x} = \rho_0 a_w^2 \frac{CD}{Eh} \frac{dp_e}{dt} \qquad (h << D,\ \Delta p << \Delta p_c) \quad (4.3.55)$$

Finally, introduce the coefficient of

$$c_1 = \rho_0 a_w \frac{CD}{Eh} = \frac{1}{1 + \dfrac{hE}{K_0 CD}} \quad (4.3.56)$$

and (4.3.55) rewrite as

$$\frac{dp}{dt} + \rho_0 a_w{}^2 \frac{\partial v}{\partial x} = c_1 \frac{dp_e}{dt} \qquad (h << D,\ \Delta p << \Delta p_c) \quad (4.3.57)$$

or

$$\frac{\partial p}{\partial t} + v\frac{\partial p}{\partial x} + \rho_0 a_w{}^2 \frac{\partial v}{\partial x} = c_1 \left(\frac{\partial p_e}{\partial t} + v\frac{\partial p_e}{\partial x} \right) \quad (h << D,\ \Delta p << \Delta p_c) \quad (4.3.58)$$

Expression (4.3.58) is the mass balance equation for transient fluid flow in a thin-walled pipe loaded by both internal and external pressures. Compared to conventional equation (4.3.37), it has non-zero right hand side related to the rate (dp_e/dt) of change of the exterior pressure, p_e. If this rate is small (or zero, i.e., $dp_e/dt = 0$), or if coefficient c_1 is small, (4.3.58) reduces to (4.3.37) and the effect of the external pressure is negligible.

Typically, for a metal pipe with liquid $E/K_0 \sim 10^2$, e.g., $E = 200\times10^9$ Pa for steel [*Gere and Timoshenko*, 1992] and $K_0 = 2.35\times10^9$ Pa for water [*Levy et al.*, 2000], and $h/D < 10^{-1}$ ($D = 4.0$ cm and $h = 5.0$ mm), so that (4.3.56) gives $c_1 \sim 10^{-1}$ or $c_1 < 10^{-1}$ (since $C \sim$

1). Therefore, when dp/dt and dp_e/dt are of the same order, the effect of the external pressure in (4.3.58) can be ignored (since c_1 is small). If, however, the internal pressure perturbations are generated by changing the external pressure, the right-hand side in (4.3.58) becomes the essential term and should be kept even when c_1 is small. Otherwise, no internal perturbation will be induced in the system.

Let us assume that the magnitude of a pressure wave propagating through a pipe-cavern system is 10^6 MPa and its period is 1.0 sec. We can estimate the change in the pipe cross-sectional area using (4.3.29). With the abovementioned parameters, $A = 1.26\times10^{-3}$ m^2 and $\frac{2Eh}{CD} - p = 5\times10^{10}$ Pa in (4.3.29). Because $dp/dt = 2\times10^6$ MPa/sec, eq. (4.3.29) gives the change in the cavern cross-sectional area $dA = 6.4\times10^{-8}$ m^2 during the half period (0.5 sec) of the pressure wave. Thus, $dA/A = 5.1\times10^{-5}$. In the same manner, we can also estimate the change in the cross-sectional area of a cavern due to wave propagation using (4.3.43). The values of typical carbonate rock's Young's modulus and Poisson's ratio are 56×10^9 Pa and 0.3, respectively [*Goodman*, 1989]. Then, by assuming the cavern diameter to be 1.0 m, the cavern cross-section area scales as $A = 0.79$ m^2 while $\frac{1+\nu}{E} = 2.3\times10^{-11}$ Pa^{-1} in (4.3.43). Then, according to this equation, when the rate of pressure change $dp/dt = 2\times10^6$ MPa/sec, $dA = 3.7\times10^{-5}$ m^2 during the half period (0.5 sec) of the pressure wave. Thus, $dA/A = 4.6\times10^{-5}$. These estimates indicate that the changes in the cross-sectional area of a pipe and a cavern would be relatively small. Thus, we can conclude that the forth assumption in Section 4.2 is valid.

4.4 Momentum Balance Equations for Transient Fluid Flow

In this section, we consider the momentum balance equation for transient fluid flow in a pipe. To derive a momentum balance equation, consider fluid flow in the pipe (Figure 4.10). The cylinder shown in this figure represents the control volume, and x is the Eulerian coordinate (that is, fixed in space). Integrating the second law of Newton, $F = d(mv)/dt$ expresses the momentum conservation in terms of the force impulse:

$$\int_{t_1}^{t_2} F dt = [mv]_{t=t_1} - [mv]_{t=t_2} \tag{4.4.1}$$

where F is the resultant force applied to the fluid in the control volume, mv is the total momentum of the fluid in the control volume, and t_1, t_2 are arbitrary moments of time.

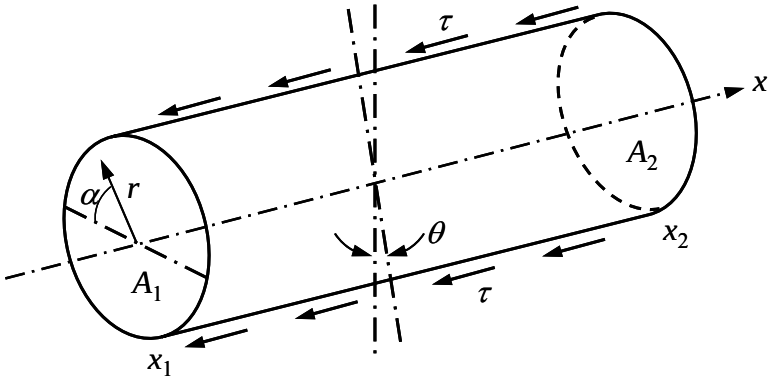

Figure 4.10 A control volume of fluid flowing in a pipe. Pressure and flow velocity at a point on a cross-section are functions of the radial distance, r, from the center of the cross-section of the pipe and the angle, α, from a horizontal line, respectively. Here, θ is the inclination of the pipe, τ is the shear traction from friction with fluid on the pipe walls, and A_i (i = 1, 2) is the cross-sectional area of the pipe at cross-section i.

The force impulse of the pressure tractions on the sides $x = x_1$ and $x = x_2$ of the control volume (Figure 4.10) is given by

$$I_p = \int_{t_1}^{t_2} [\int_{A_1} p(x_1, r, \alpha, t) dA - \int_{A_2} p(x_2, r, \alpha, t) dA] dt \tag{4.4.2}$$

where r is the radial distance from the center of the pipe cross-section, α is the angle from a horizontal line, and A_i is the cross-sectional area of the pipe at cross-section x_i (i = 1, 2) (Figure 4.10). The contribution from the gravitational force to the force impulse is given by

$$I_g = -g \sin\theta \int_{t_1}^{t_2} [\int_V \rho(x, r, \alpha, t) dV] dt \tag{4.4.3}$$

where g is the acceleration of gravity and V is the volume of the domain. Friction on the pipe surface caused by fluid flow contributes to force impulse in (4.4.1) by

$$I_f = -\int_{t_1}^{t_2} [\int_{x_1}^{x_2} \bar{\tau}(x, t) 2\pi a dx] dt \tag{4.4.4}$$

where

$$\bar{\tau}(x, t) = \frac{1}{2\pi} \int_0^{2\pi} \tau(x, \alpha, t) d\alpha \tag{4.4.5}$$

and τ is the shear traction $\tau(x, \alpha, t)$ on the internal surface of the pipe averaged over the interface perimeter of cross-section x, and a is the radius of the pipe cross-section. Hereafter, we consider small load perturbations and assume the pipe cross-section remains circular. In this case, the perturbations of the pipe radius are small ($da/a << 1$).

The right-hand side of (4.4.1) can be written as

$$
\begin{aligned}
[mv]_{t=t_1} - [mv]_{t=t_2} &= \int_V \rho(x,r,\alpha,t_1)v(x,r,\alpha,t_1)dV - \int_V \rho(x,r,\alpha,t_2)v(x,r,\alpha,t_2)dV \\
&= \int_{t_1}^{t_2}\left[\frac{d}{dt}\int_V \rho(x,r,\alpha,t)v(x,r,\alpha,t)dV\right]dt
\end{aligned}
\tag{4.4.6}
$$

Then, inserting (4.4.2) - (4.4.6) into (4.4.1) and eliminating the time integral, we obtain

$$
\begin{aligned}
&\int_{A_1} p(x_1,r,\alpha,t)dA - \int_{A_2} p(x_2,r,\alpha,t)dA - \left[\int_{t_2}^{t_1} \bar{\tau}(x,t)2\pi a dx\right] - \\
&- g\sin\theta \int_V \rho(x,r,\alpha,t)dV = \frac{d}{dt}\int_V \rho(x,r,\alpha,t)v(x,r,\alpha,t)dV
\end{aligned}
\tag{4.4.7}
$$

Now, introduce the average pressure in a cross-section,

$$
\bar{p}(x,t) = \frac{1}{\pi a^2}\int_A p(x,r,\alpha,t)dA \tag{4.4.8}
$$

the average flux of momentum through a cross-section,

$$
\bar{q}(x,t) = \frac{1}{\pi a^2}\int_A \rho(x,r,\alpha,t)v(x,r,\alpha,t)dA \tag{4.4.9}
$$

and the average density in a cross-section

$$
\bar{\rho}(x,t) = \frac{1}{\pi a^2}\int_A \rho(x,r,\alpha,t)dA \tag{4.4.10}
$$

Then, inserting (4.4.8) into (4.4.7) results in

$$\pi a^2\left[\bar{p}(x_1,t)-\bar{p}(x_2,t)\right]-2\pi a\int_{x_1}^{x_2}\bar{\tau}(x,t)dx-g\sin\theta\int_{x_1}^{x_2}dx\int_A\rho(x,r,\alpha,t)dA$$
$$=\frac{d}{dt}\int_{x_1}^{x_2}dx\int_A\rho(x,r,\alpha,t)v(x,r,\alpha,t)dA \tag{4.4.11}$$

In general, $a(x,t)$ is not constant. However, for small load perturbation, the change, Δa of the pipe radius, a, is also small ($\Delta a/a << 1$). We further consider a constant accounting for Δa value only after the higher order terms in the expression below. Therefore, combining (4.4.9) and (4.4.10) into (4.4.11), we obtain

$$\bar{p}(x_1,t)-\bar{p}(x_2,t)-\frac{2}{a}\int_{x_1}^{x_2}\bar{\tau}dx-g\sin\theta\int_{x_1}^{x_2}\bar{\rho}(x,t)dx=\frac{d}{dt}\int_{x_1}^{x_2}\bar{q}(x,t)dx \tag{4.4.12}$$

The first two terms in (4.4.12) can be rewritten as

$$\bar{p}(x_1,t)-\bar{p}(x_2,t)=-\int_{x_1}^{x_2}\frac{\partial}{\partial x}\bar{p}(x,t)dx \tag{4.4.13}$$

Inserting (4.4.13) into (4.4.12) obtains

$$-\int_{x_1}^{x_2}\frac{\partial}{\partial x}\bar{p}(x,t)dx-\frac{2}{a}\int_{x_1}^{x_2}\bar{\tau}(x,t)dx-g\sin\theta\int_{x_1}^{x_2}\bar{\rho}(x,t)dx=\frac{d}{dt}\int_{x_1}^{x_2}\bar{q}(x,t)dx \tag{4.4.14}$$

or, after eliminating the integrals in (4.4.14),

$$-\frac{\partial \bar{p}}{\partial x}-\frac{2}{a}\bar{\tau}-\bar{\rho}g\sin\theta=\frac{\partial \bar{q}}{\partial t} \tag{4.4.15}$$

where $\bar{p}=\bar{p}(x,t)$, $\bar{\tau}=\bar{\tau}(x,t)$, $\bar{\rho}=\bar{\rho}(x,t)$, and $\bar{q}=\bar{q}(x,t)$.

For an incompressible fluid,

$$\bar{q}=\rho\bar{v} \tag{4.4.16}$$

where

$$\bar{v}(x,t)=\frac{1}{\pi a^2}\int_A v(x,r,\alpha,t)dA \tag{4.4.17}$$

is the average velocity through the cross-section $A(x,t)$. In general, however,

$$\bar{q}=\overline{\rho v}\neq\bar{\rho}\cdot\bar{v} \tag{4.4.18}$$

and we further express the density of the fluid as a sum of the average density, $\bar{\rho}$, and the density perturbation, ρ_1:

$$\rho(x,r,\alpha,t)=\bar{\rho}(x,t)+\rho_1(x,r,\alpha,t) \tag{4.4.19}$$

Then, from (4.4.9), we have

$$\bar{q}(x,t)=\frac{1}{\pi a^2}\int_A[\bar{\rho}(x,t)+\rho_1(x,r,\alpha,t)]v(x,r,\alpha,t)dA \tag{4.4.20}$$

or, using definition (4.4.17) of the average velocity,

$$\bar{q}(x,t)=\bar{\rho}(x,t)\bar{v}(x,t)+\frac{1}{\pi a^2}\int_A\rho_1(x,r,\alpha,t)v(x,r,\alpha,t)dA \tag{4.4.21}$$

Since v has the same sign in each pipe cross-section, we can use the mean value theorem [e.g., *Bartle*, 2000] for the integral in (4.4.21):

$$\int_A \rho_1(x,r,\alpha,t)v(x,r,\alpha,t)dA = \rho_1^*(x,t)\int_A v(x,r,\alpha,t)dA \qquad (4.4.22)$$

where $\rho_1^*(x,t) = \rho_1(x,r_*,\alpha_*,t)$ is a value of the density perturbation at some point (r_*,α_*) in cross-section $A(x,t)$. Then, inserting (4.4.17) and (4.4.22) into (4.4.21) results in

$$\overline{q}(x,t) = \overline{\rho}(x,t)\overline{v}(x,t) + \rho_1^*(x,t)\overline{v}(x,t) = [\overline{\rho}(x,t) + \rho_1^*(x,t)]\overline{v}(x,t) \qquad (4.4.23)$$

For a slightly compressible fluid, it can be assumed that

$$\frac{\rho_1^*(x,t)}{\overline{\rho}(x,t)} << 1 \qquad (4.4.24)$$

We further consider only flows for which condition (4.4.24) is satisfied. For such flows, (4.4.23) becomes

$$\overline{q}(x,t) = \overline{\rho}(x,t)\overline{v}(x,t) \qquad (4.4.25)$$

and (4.4.15) can be written as

$$\frac{\partial(\overline{\rho}\cdot\overline{v})}{\partial t} + \frac{\partial \overline{p}}{\partial x} + \overline{\rho}g\sin\theta + \frac{2}{a}\overline{\tau} = 0 \qquad (\rho_1^* << \overline{\rho}) \qquad (4.4.26)$$

where the average shear traction $\overline{\tau}$ on the pipe wall is often represented by [*Janna*, 1993].

$$\bar{\tau} = \frac{f}{8}\overline{\rho v}|\bar{v}| \tag{4.4.27}$$

where f is the Darcy-Weisbach friction factor, $\bar{v}|\bar{v}|$ is used instead of $\bar{v}^2$ to consider fluid flows both in the x-axis (Figure 4.10) and in the reversed directions.

To simplify notations, we further use symbols p, ρ, and v instead of $\bar{p}$, $\bar{\rho}$, and $\bar{v}$, respectively. Substituting (4.4.27) into (4.4.26), we obtain the well-known momentum balance equation for the fluid flow in a pipe [*Wiley and Streeter*, 1978; *Charudhry*, 1987]:

$$\frac{\partial v}{\partial t} + \frac{v}{\rho}\frac{\partial p}{\partial t} + \frac{1}{\rho}\frac{\partial p}{\partial x} + g\sin\theta + \frac{f}{2D}v|v| = 0 \quad (\rho_1 << \rho) \tag{4.4.28}$$

where $D = 2a$ is the pipe diameter.

For turbulent flow, the friction factor f is a function of the Reynolds number and the relative roughness of the pipe wall [*Janna*, 1993]. The friction factor, f is often determined from the Moody diagram shown in Figure 4.11 [*Janna*, 1993]. If the Reynolds number is less than 2100, then fluid flow is laminar. As the Reynolds number increases beyond 4000, fluid flow becomes turbulent. Between the two regimes, a transition zone exists [*Janna*, 1993]. In this zone, the flow can be either laminar or turbulent, and it is difficult to predict the flow regime. For turbulent flow, the friction factor f in (4.4.28) is often assumed constant (to the first order) [*Charudhry*, 1987]. For laminar flow of a viscous liquid, the friction factor f can be calculated as [*Janna*, 1993]

$$f = \frac{64}{\mathrm{Re}} \tag{4.4.29}$$

where $\mathrm{Re} = \dfrac{\rho v D}{\mu}$ is the Reynolds number of the fluid flow in a pipe and μ the dynamic viscosity of the fluid [*Janna*, 1993]. Inserting (4.4.29) into (4.4.28) results in

$$\frac{\partial v}{\partial t}+\frac{v}{\rho}\frac{\partial p}{\partial t}+\frac{1}{\rho}\frac{\partial p}{\partial x}+g\sin\theta+\frac{32\mu}{\rho D^2}v=0 \qquad (\rho_1 << \rho) \qquad (4.4.30)$$

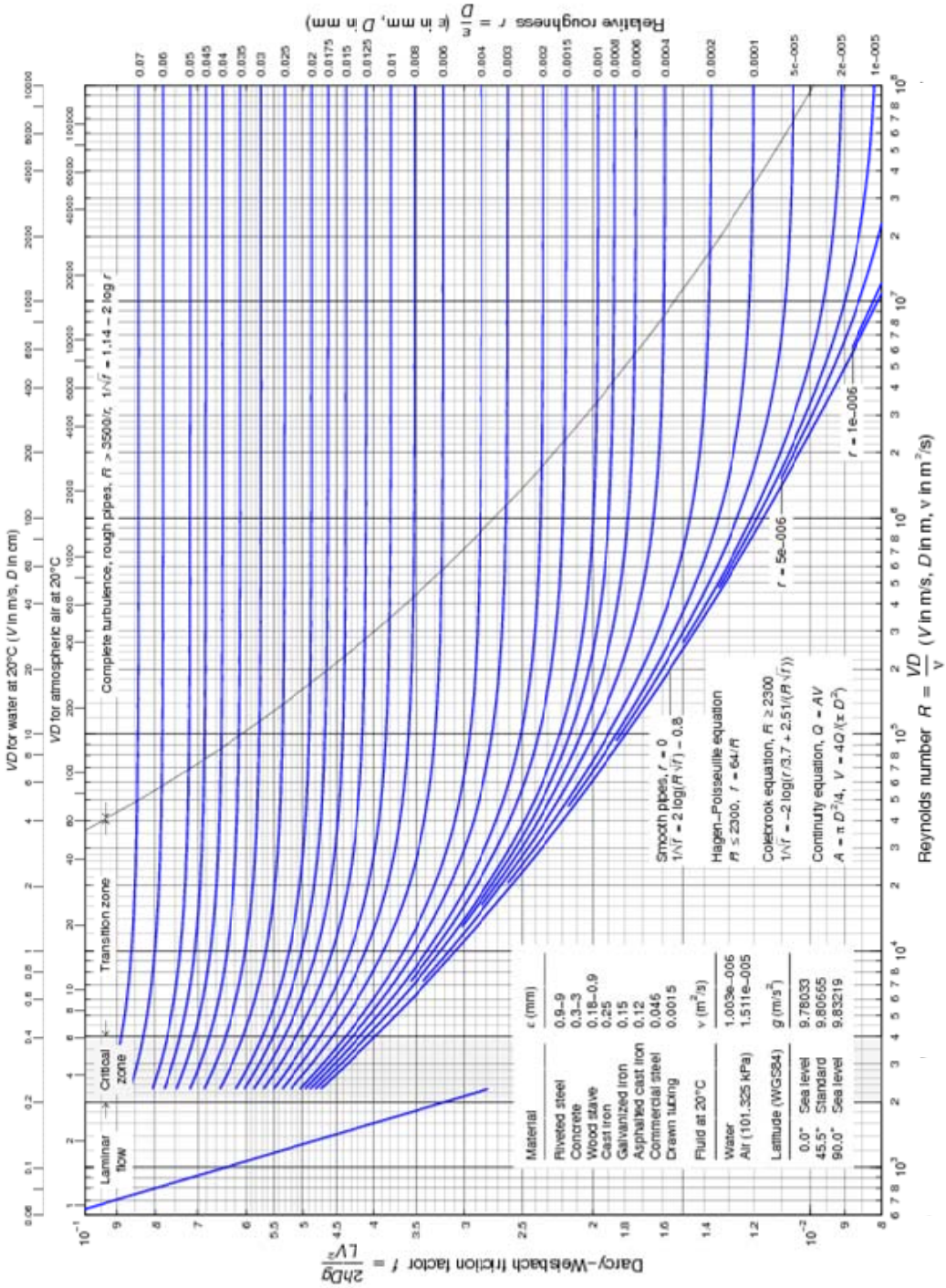

Figure 4.11 Moody diagram [*Janna*, 1993]

4.5 Linearization of Governing Equations

For a transient flow in a pipe, let p be the scale of pressure that changes over the length of scale L along the pipe during the time of scale τ. Let the corresponding scale of the flow velocity change be v and assume that initially (i.e., before perturbation) the fluid pressure is p_0, flow velocity is v_0, and the fluid density is ρ_0. Then, the mass balance equation (4.3.46) for an internally loaded pipe scales as

$$\frac{|p-p_0|}{\tau}+v\frac{|p-p_0|}{L}+\rho_0 a_w^2\frac{|v-v_0|}{L}=0 \tag{4.5.1}$$

The second term in (4.5.1) is much smaller than the third one if condition

$$|p-p_0| << \rho_0 a_w^2 \tag{4.5.2}$$

is satisfied. In this case, the convective term in the mass balance equation (4.3.46) can be ignored, and it can be written as

$$\frac{\partial p}{\partial t}+\rho_0 a_w^2\frac{\partial v}{\partial x}=0 \tag{4.5.3}$$

When the pipe is also loaded by external pressure, p_e, (4.3.58) scales as

$$\frac{|p-p_0|-c_1|p_e-p_0^e|}{\tau}+(|p-p_0|-c_1|p_e-p_0^e|)\frac{|v-v_0|}{L}+\rho_0 a_w^2\frac{|v-v_0|}{L}=0 \tag{4.5.4}$$

where p_0^e is the initial external pressure outside the pipe. Similar to (4.5.1), the second term in (4.5.4) is much smaller than the third one if condition

$$\left|p - p_0 - c_1(p_e - p_0^e)\right| << \rho_0 a_w^2 \tag{4.5.5}$$

is satisfied. But $\left|p - p_0 - c_1(p_e - p_0^e)\right| \le \left|p - p_0\right| + c_1\left|p_e - p_0^e\right|$, where c_1 is generally smaller than 1.0 (Section 4.3). Hence, (4.5.5) will be satisfied if both (4.5.2) and

$$\left|p_e - p_0^e\right| << \rho_0 a_w^2 \tag{4.5.6}$$

are valid. This is assumed everywhere below. Then, the convective terms in (4.3.58) can be ignored, and we have

$$\frac{\partial p}{\partial t} + \rho_0 a_w^2 \frac{\partial v}{\partial x} = c_1 \frac{\partial p_e}{\partial t} \qquad (\left|p - p_0\right| << \rho_0 a_w^2,\ \left|p_e - p_0^e\right| << \rho_0 a_w^2) \tag{4.5.7}$$

Using (4.3.36), rewrite (4.5.2) and (4.5.6) as

$$\left|p - p_0\right|,\ \left|p_e - p_0^e\right| << \frac{K_0}{1 + \dfrac{K_0 CD}{hE}} < K_0 \tag{4.5.8}$$

in the case of the fluid flow in a pipe. For the transient fluid flow in a cavern, a similar condition is obtained by inserting (4.3.45) into (4.5.2):

$$\left|p - p_0\right| << \frac{K_0}{1 + \dfrac{K_0}{G}} < K_0 \tag{4.5.9}$$

Combining (4.5.8) and (4.5.9), we then obtain condition

$$\frac{|p - p_0|}{K_0} << 1, \quad \frac{|p_e - p_0^e|}{K_0} << 1 \tag{4.5.10}$$

which are sufficient for satisfying (4.5.2) and (4.5.6). For the sake of briefness, we further write

$$\frac{|p - p_0|}{K_0} << 1 \tag{4.5.11}$$

instead of two inequalities in (4.5.10). By doing this, however, we still assume that both of them are satisfied when applicable. It is usually clear from the context and cannot be lead to confusion. For example, if only internal fluid flow in the pipe is considered, and $p_e = 0$, then (4.5.11) means only the first condition in (4.5.10).

Assuming that the pressure change is much smaller than the liquid bulk modulus, hereafter, condition (4.5.11) will be further considered satisfied. In a practical sense, it is not too restrictive for many liquids. For example, for water, $K_0 \sim 10^9$ Pa [*Levy et al.*, 2000], and pressure perturbations $|p - p_0|$ and $|p_e - p_0^e|$ can be as high as 10 - 100 MPa. Condition (4.5.11) is adopted in many works [e.g., *Wiley and Streeter*, 1978; *Charudhry*, 1987] because it allows linearizing the pressure-density dependence (4.3.31). Keeping first two leading terms in (4.3.31), the linearized pressure-density relationship for the fluid in the pipe can be written as

$$\rho = \rho_0\left(1 + \frac{p - p_0}{K_0}\right) \qquad \left(|p - p_0| / K_0 << 1\right) \tag{4.5.12}$$

Hence, if condition (4.5.11) is satisfied, the linear pressure-density dependence (4.5.12) for the fluid can be used instead of (4.3.31). Furthermore, this dependence is often used as a definition of a slightly compressible fluid [*Barenblatt et al.*, 1990]. It implies that

$$\frac{\rho-\rho_0}{\rho_0}<<1 \qquad \left(\left|p-p_0\right|/K_0<<1\right) \tag{4.5.13}$$

In this case,

$$\left|\frac{v}{\rho}\frac{\partial\rho}{\partial t}\right|<<\left|\frac{\partial v}{\partial t}\right| \tag{4.5.14}$$

in expressions (4.4.28) and (4.4.30) because the left and right sides in (4.5.14) scales as $(v/\rho_0)[(\rho-\rho_0)/\tau]$ and v/τ, respectively (since $v_0 = 0$). Therefore, the second term in the momentum balance equations (4.4.28) and (4.4.30) can be omitted, and they can be expressed as

$$\frac{\partial v}{\partial t}+\frac{1}{\rho_0}\frac{\partial p}{\partial x}+g\sin\theta+\frac{f}{2D}v|v|=0 \qquad \left(\left|p-p_0\right|/K_0<<1\right) \tag{4.5.15}$$

for the turbulent flow and as

$$\frac{\partial v}{\partial t}+\frac{1}{\rho_0}\frac{\partial p}{\partial x}+g\sin\theta+\frac{32\mu}{\rho_0 D^2}v=0 \qquad \left(\left|p-p_0\right|/K_0<<1\right) \tag{4.5.16}$$

for the laminar flow. Per (4.5.12), we also replaced ρ with ρ_0 in both equations as the difference contributes only to the higher order terms.

We further assumes that initial velocity, v_0, and pressure, p_0, satisfy the governing equations (4.5.3), (4.5.15), or (4.5.16), and hence, can be chosen as functions v_0 and p_0. This means that in the case of turbulent flow, functions v_0 and p_0 satisfy equations

$$\frac{\partial p_0}{\partial t}+\rho_0 a^2\frac{\partial v_0}{\partial x}=0 \tag{4.5.17}$$

and

$$\frac{\partial v_0}{\partial t} + \frac{1}{\rho_0}\frac{\partial p_0}{\partial x} + g\sin\theta + \frac{f}{2D}v_0|v_0| = 0 \tag{4.5.18}$$

Consider deviations v_1 and p_1 from v_0 and p_0, respectively. Then,

$$v = v_0 + v_1, \quad p = p_0 + p_1 \tag{4.5.19}$$

and inserting (4.5.19) into (4.5.3) and (4.5.15), we have

$$\frac{\partial(p_0 + p_1)}{\partial t} + \rho_0 a_w^2 \frac{\partial(v_0 + v_1)}{\partial x} = 0 \tag{4.5.20}$$

$$\frac{\partial(v_0 + v_1)}{\partial t} + \frac{1}{\rho_0}\frac{\partial(p_0 + p_1)}{\partial x} + g\sin\theta + \frac{f}{2D}|v_0 + v_1|(v_0 + v_1) = 0 \tag{4.5.21}$$

where f is assumed constant for the turbulent flow regime. Subtracting (4.5.17) from (4.5.20) and (4.5.18) from (4.5.21), obtain mass balance equation

$$\frac{\partial p_1}{\partial t} + \rho_0 a_w^2 \frac{\partial v_1}{\partial x} = 0 \tag{4.5.22}$$

and momentum balance equation

$$\frac{\partial v_1}{\partial t} + \frac{1}{\rho_0}\frac{\partial p_1}{\partial x} + \frac{f}{2D}(v_0 + v_1)|v_0 + v_1| - \frac{f}{2D}v_0|v_0| = 0 \tag{4.5.23}$$

for turbulent flow.

In the next chapter, we use fluid transients method when the flow in the pipe-cavern system is initially at rest. In this case, the initial velocity, v_0 is zero and we have v =

v_1. To simplify notations, we replace v_1 and p_1 by v and p, respectively. Then, from (4.5.22) and (4.5.23), we finally obtain the governing equations for the turbulent flow

$$\begin{cases} \dfrac{\partial p}{\partial t} + \rho_0 a_w^2 \dfrac{\partial v}{\partial x} = 0 \\ \dfrac{\partial v}{\partial t} + \dfrac{1}{\rho_0}\dfrac{\partial p}{\partial x} + \dfrac{f}{2D} v|v| = 0 \quad (v_0 = 0) \end{cases} \tag{4.5.24}$$

where p and v are the perturbations of pressure and fluid velocity from the steady-state case ($v_0 = 0$). These perturbations satisfy the linearized equations for total v and p.

In the same manner, let v_0 and p_0 be a solution of (4.5.3) and (4.5.16) for laminar flow. We then have

$$\begin{cases} \dfrac{\partial p_0}{\partial t} + \rho_0 a^2 \dfrac{\partial v_0}{\partial x} = 0 \\ \dfrac{\partial v_0}{\partial t} + \dfrac{1}{\rho_0}\dfrac{\partial p_0}{\partial x} + g\sin\theta + \dfrac{32\mu}{\rho_0 D^2} v_0 = 0 \end{cases} \tag{4.5.25}$$

Inserting (4.5.19) into (4.5.25) obtains

$$\begin{cases} \dfrac{\partial (p_0 + p_1)}{\partial t} + \rho_0 a_w^2 \dfrac{\partial (v_0 + v_1)}{\partial x} = 0 \\ \dfrac{\partial (v_0 + v_1)}{\partial t} + \dfrac{1}{\rho_0}\dfrac{\partial (p_0 + p_1)}{\partial x} + g\sin\theta + \dfrac{32\mu}{\rho_0 D^2}(v_0 + v_1) = 0 \end{cases} \tag{4.5.26}$$

Subtracting (4.5.25) from (4.5.26) and taking into account that the initial velocity, v_0, is zero, we have the governing equations for laminar flow

$$\begin{cases} \dfrac{\partial p}{\partial t} + \rho_0 a_w^2 \dfrac{\partial v}{\partial x} = 0 \\ \dfrac{\partial v}{\partial t} + \dfrac{1}{\rho_0}\dfrac{\partial p}{\partial x} + \dfrac{32\mu}{\rho_0 D^2} v = 0 \qquad (v_0 = 0) \end{cases} \tag{4.5.27}$$

where again we used notations p and v for p_1 and v_1, respectively. In other words, p and v in (4.5.27) are the perturbations of pressure and velocity. Note that the mass balance equation in (4.5.27) is the same as that in (4.5.24). Hereafter, we use (4.5.24) and (4.5.27) instead of (4.3.37), (4.4.28), and (4.4.30).

It is often convenient to use the flow rate, Q, as an unknown instead of the flow velocity, v. Then, expressions (4.5.24) and (4.5.27) can be rewritten as

$$\begin{cases} \dfrac{\partial p}{\partial t} + \dfrac{\rho_0 a_w^2}{A}\dfrac{\partial Q}{\partial x} = 0 \\ \dfrac{\partial Q}{\partial t} + \dfrac{A}{\rho_0}\dfrac{\partial p}{\partial x} + \dfrac{f}{2DA} Q|Q| = 0 \qquad (Q_0 = 0) \end{cases} \tag{4.5.28}$$

for turbulent flow and as

$$\begin{cases} \dfrac{\partial p}{\partial t} + \dfrac{\rho_0 a_w^2}{A}\dfrac{\partial Q}{\partial x} = 0 \\ \dfrac{\partial Q}{\partial t} + \dfrac{A}{\rho_0}\dfrac{\partial p}{\partial x} + \dfrac{32\mu}{\rho_0 D^2} Q = 0 \qquad (Q_0 = 0) \end{cases} \tag{4.5.29}$$

for laminar flow, respectively. Here, $Q = vA$, $Q_0 = v_0 A$, and $A = \pi a^2$ is the pipe cross-sectional area. As before, we ignored the change of the cross-sectional area because it only contributes to the higher order terms.

Similarly, for a pipe loaded both by external pressure, p_e, and internal pressure, p, the mass balance equation (4.3.58) can be expressed as

$$\frac{\partial p}{\partial t}+\frac{\rho_0 a_w^2}{A}\frac{\partial Q}{\partial x}=c_1\frac{\partial p_e}{\partial t} \tag{4.5.30}$$

while the momentum balance equation used together with (4.5.30) for governing equations remains the same as those for (4.5.28) and (4.5.29). In (4.5.30), p_e is the perturbation of the external pressure from its initial value p_e^0.

Governing equations for fluid transients are summarized in Table 4.1. The conventional governing equations, including mass and momentum balance equations, can be used for transient fluid flow in a pipe when the impact of the external pressure is negligible on the flow. For fluid flow in pipes subjected to both internal and external pressures, we developed a mass balance equation in this work shown in Table 4.1. Table 4.1 shows appropriate governing equations to describe the fluid flow in pipes and caverns for the cases of interest. In Table 4.1, we use the type of the flow conduit (e.g., pipe or cavern) and loading conditions (external or internal pressure) to determine the corresponding mass balance equation, while we chose a suitable momentum balance equation based on the fluid flow regime (e.g., turbulent and laminar flow).

Table 4.1 Governing equations to describe the fluid flow in pipes and caverns

Condition	Mass balance equation	
	General	Linearized
Internal pressure only	$\frac{\partial p}{\partial t}+v\frac{\partial p}{\partial t}+\rho_0 a_w^2\frac{\partial v}{\partial x}=0$	$\frac{\partial p}{\partial t}+\rho_0 a_w^2\frac{\partial v}{\partial x}=0$
Both internal and external pressure*	$\frac{\partial p}{\partial t}+v\frac{\partial p}{\partial x}+\rho_0 a_w{}^2\frac{\partial v}{\partial x}=c_1\left(\frac{\partial p_e}{\partial t}+v\frac{\partial p_e}{\partial x}\right)$	$\frac{\partial p}{\partial t}+\rho_0 a_w^2\frac{\partial v}{\partial x}=c_1\frac{\partial p_e}{\partial t}$
	Momentum balance equation	
	General	Linearized
Turbulent flow	$\frac{\partial v}{\partial t}+\frac{1}{\rho_0}\frac{\partial p}{\partial x}+g\sin\theta+\frac{f}{2D}v\lvert v\rvert=0$	$\frac{\partial v}{\partial t}+\frac{1}{\rho_0}\frac{\partial p}{\partial x}+\frac{f}{2D}v\lvert v\rvert=0$
Laminar flow	$\frac{\partial v}{\partial t}+\frac{1}{\rho_0}\frac{\partial p}{\partial x}+g\sin\theta+\frac{32\mu}{\rho_0 D^2}v=0$	$\frac{\partial v}{\partial t}+\frac{1}{\rho_0}\frac{\partial p}{\partial x}+\frac{32\mu}{\rho_0 D^2}v=0$
	Wave speed	
Pipe	$a_w^2=\frac{K_0/\rho_0}{1+\frac{K_0 CD}{Eh}}=\frac{a_0^2}{1+\frac{K_0 CD}{Eh}}$	
Cavern*	$a_w^2=\frac{K_0/\rho_0}{1+\frac{K_0}{G}}=\frac{a_0^2}{1+\frac{K_0}{G}}$	
	Coefficient	
	C	c_1
Plane* stress	1	$c_1=\frac{1}{1+\frac{hE}{K_0 D}}$
Plane* strain	$1-\nu^2$	$c_1=\frac{1}{1+\frac{hE}{K_0 D(1-\nu^2)}}$

*Obtained in this work

4.6 Conclusions

The topic of this chapter is related to the factors affecting the geometry and, hence, the mechanical stability of caverns excavated in carbonate rock formations for natural gas storage. Characterization of the cavern shape is required to understand stress changes during the cavity excavation, which can destabilize the cavern. In this work, we propose to characterize the geometry of the cavern by generating pressure waves in a pipe extending into the cavern, and measuring the reflected waves at various locations in another adjacent pipe. Conventional governing equations describe fluid transients in pipes loaded only by internal pressure (such as in the water hammer effect). To model the pressure wave propagation for realistic geometries, we derived new governing equations for pressure transients in pipes subjected to changes in both internal and external (confining) pressures. This is important because the internal pressure (used in the measurement) is changing in response to the perturbation of the external pressure when the pipe is contained in the cavern filled with fluids. If the pressure in the cavern is perturbed, the perturbation creates an internal pressure wave in the submerged pipe that has a signature of the cavern geometry. We showed that the classic equations are included in our formulation as a particular case, but they have limited validity for some practically important combinations of the controlling parameters.

The linearized governing equations are used in the next chapter (Chapter V) to model fluid transients in a gas storage cavern.

LIST OF SYMBOLS

A	Cross-sectional area of a pipe
a	Inner radius of a pipe
a	Wave speed in a fluid contained in a pipe
a_0	Sound wave speed in a fluid
b	Outer radius of a pipe
C	Constant
c_1	Coefficient
D	Inner diameter of a pipe
E	Young's modulus
F	Resultant force applied to a system
f	Darcy-Weisbach friction factor
G	Shear modulus
g	Acceleration of gravity
h	Pipe wall thickness
I_f	Force impulse by friction
I_g	Force impulse by gravitational force
I_p	Force impulse by pressure
K_0	Bulk modulus of a fluid for a reference pressure
L	Pipe length
M_{CO_2}	Molar mass of CO_2
m	Mass
p	Fluid pressure in a pipe

p_c	Characteristic pressure
p_e	External pressure applied on the outside of pipe
p_0	Initial pressure
p_0^e	Initial external pressure outside a pipe
$\overline{p}$	Average pressure in a given cross-section of a pipe
Q	Fluid flow rate
Q_0	Initial fluid flow rate
q	Mass flow rate
$\overline{q}$	Average flux of momentum through a cross-section of a pipe
R	Universal gas constant
Re	Reynolds number
r	Radial distance from the center of a cross-section of a pipe
T	Temperature
t	Time
V	Volume of a domain
v	Fluid velocity
v_0	Initial fluid velocity
$\overline{v}$	Average fluid velocity in a given cross-section of a pipe
x	Distance along a pipe
Z	Compressibility factor
α	Angle from a horizontal line
ε_{xx}	Axial strain
$\varepsilon_{\theta\theta}$	Tangential strain
θ	Inclination of a pipe

μ	Dynamic viscosity of a fluid
ν	Poisson's ratio of a material
ρ	Fluid density
ρ_{CO_2}	CO_2 density
ρ_0	Initial fluid density
ρ_1	Density perturbation
$\overline{\rho}$	Average density in a given cross-section of a pipe
ρ_1^*	Density perturbation at a given point
σ_{rr}	Radial stress
σ_{xx}	Axial stress
$\sigma_{\theta\theta}$	Tangential stress
τ	Shear traction from friction
τ	Time scale
$\overline{\tau}$	Averaged shear traction

References

Atteberry, J.T. (2005), *An assessment of carbonate formations in the Appalachian basin for gas storage using acid dissolution*, Clemson University, Clemson, SC.

Badie, A., and M.C. Wang (1990), Stability of underground cavity subjected to surface loads, *Proceedings of international symposium on unique underground structures*, CSM Press, Denver.

Barenblatt, G.I., V.M. Entov, and V.M. Ryzhik (1990), *Theory of fluid flows through natural rocks*, Kluwer Academic Publishers.

Barla, G., and M. Barla (2001), Numerical simulation of squeezing behavior in tunnels, *Proceedings of second international FLAC symposium*, A.A. Balkema, Lyon, France.

Bartle R.G. (2000), *Introduction to real analysis*, Wiley and Sons.

Bauer, S.J., B.L. Ehgartner, B.L. Levin and J.K. Linn (1998), *Waste disposal in horizontal solution mined caverns considerations of site location, cavern stability, and development considerations*, Underground Storage Technology, Department 6113, Sandia National Laboratories, Albuquerque, NM, USA.

Broch, E. (1989), Use of the underground in Norway, *Proceedings of the International Conference on Storage of Gases in Rock Caverns*, Rotterdam, A.A. Balkema, Trondheim, 26-28 June 1989.

Browne, M. (1999), *Physics for Engineering and Science*, McGraw-Hill.

Castle, J.W., D.A. Bruce, S.E. Brame, D.A. Brooks, R.W. Falta, and L.C. Murdoch (2004), Design and feasibility of creating gas-storage caverns by using acid to dissolve carbonate rock formations, SPE 91436, *Proceedings of SPE Eastern Regional Meeting*, Charleston, WV, USA, 15-17 September, 2004.

Castle, J.W., R.W. Falta, D.A. Bruce, L.C. Murdoch, J. Foley, S.E. Brame, and D.A. Brooks (2005), *Fracture dissolution of carbonate rock: an innovative process for gas storage*, Topical report, USDOE Projection ID: DE-FC26-02NT41299.

Coates, G.K., C.A. Lee, W.C. McClain, P.E. Senseny (1981), *Failure of man-made cavities in salt and surface subsidence due to sulfur mining*, SAND81-7145, RE/SPEC, Inc. Contract Report to Sandia National Laboratories, Albuquerque, NM.

Chaudhry, M.H. (1987), *Applied hydraulic transients*, Van Nostrand Reinhold Company.

Dake, L.P. (1978), *Fundamentals of reservoir engineering*, Elsevier.

Dean, J.R. (Ed.) (1993), *Application of supercritical fluids in industrial Analysis*, Blackie Academic & Professional.

Dussaud, M. (1989*)*, *Review of World Wide Storage Projects, in Underground Storage of Natural Gas: Theory and Practice*, edited by M.R. Tek, 23-29, Dorecht, Kluwer Academic Publishers.

Dietert J.A. and D.A. Pursell (2000), *Underground natural gas storage*, http://www.simmonsco-intl.com/files/63.pdf

EIA (2005), *Monthly energy review*, Energy information administration, Office of energy markets and end use, U.S. Department of Energy, Washington, D.C., http://www.eia.doe.gov/mer/pdf/mer.pdf.

EIA (2009), *Basics of underground natural gas storage*, http://www.eia.doe.gov/pub/oil_gas/natural_gas/analysis_publications/storagebasics/storagebasics.html

Falta, R.W., L.C. Murdoch, and G.K. Chambers (2004), Review of Current Technology for Acid Dissolution and Hydraulic Fracturing (Task 5), *Technical Report prepared for US DOE*.

Foley, J.M.S. (2006), *An analysis of cavern stability and hydraulic fractures in relation to natural gas storage in limestone formation*, MS thesis, Clemson University.

Froise, S. (1987), Hydrocarbon storage in unlined rock caverns: Norway's use and experience*, Tunneling and Underground Space Technology*, 2, 265-268.

Gere, J.M. and S.P. Timoshenko (1992), *Mechanics of materials, 3rd ed.*, Chapman & Hall.

Goodman, R.E. (1989), *Introduction to rock mechanics*, John Wiley & Sons.

Hardy, H.R., Jr. (1982), *Basic studies associated with the design of salt caverns for the storage of pressurized fluids, in Rock Mechanics: caverns and pressure shafts*, edited by W. Wittke, 903-921, Balkema, Rotterdam.

Hoek, E., and E. T. Brown (1980), *Underground excavation in rock*, The institution of mining and metallurgy, London.

Hofstrand, D. (2008), *Natural gas and coal measurements and conversions*, http://www.extension.iastate.edu/agdm/wholefarm/html/c6-89.html.

Holzhausen, G.R. and H.N. Egan (1986), Fracture diagnostics in east Text and western Colorado using the Hydraulic-Impedance method, *Proceedings of Unconventional Gas Technology Symposium*, SPE 15215, Society of Petroleum Engineering, Lousiville, KY, USA, 18-21 May, 1986.

Holzhausen, G.R. and R.P. Gooch (1985a), The effect of hydraulic fracture growth of free oscillations of wellbore pressure, *Proceedings of the 26th US Symposium on Rock Mechanics*, Rapid City, SD, USA, 26-28 Jun, 1985.

Holzhausen, G.R. and R.P. Gooch (1985b), Impedance of hydraulic fractures: its measurement and use for estimating fracture closure pressure and dimensions, SPE/DOE 13982, *Proceedings of SPE/DOE Low permeability gas reservoirs*, Denver, Colorado, 19-22 May, 1985.

Hu, Y. (1997), Buckling failure analysis of a cavern in jointed rock, *International journal of rock mechanics and mining science*, 34, 704.

Janna, W.S. (1993), *Introduction to fluid mechanics*, International Thomson Publishing.

Lake, L.W. (1989), *Enhanced oil recovery*, Prentice Hall, Englewood Cliffs, NJ.

Levy, M., H. Bass, and R. Stern (2000), *Handbook of elastic properties of solids, liquids and gases*, Academic Press.

Lide, D.R. (2004), *CRC handbook of Chemistry and Physics*, CRC Press LLC.

Lindblom, U. (1989), The development of hydrocarbon storage in hard rock caverns, *Proceedings of the International Conference on Storage of Gases in Rock Caverns*, Rotterdam, A.A. Balkema, Trondheim, 26-28 June 1989.

Menzel, W. and W. Schreiner (1989), Geomechanical aspects for the establishment and the operation of gas cavern stores in salt formations of the GDR, *Proceedings of the International Conference on Storage of Gases in Rock Caverns*, Rotterdam, A.A. Balkema, Trondheim.

NGSA (2004*), Natural Gas Supply Association*, http://www.naturalgas.org.

NETL (2005), *Transmission, Distribution & Storage: Natural Gas Storage, National Energy Technology Laboratory: Strategic Center for Natural Gas & Oil*, U.S. Department of Energy, http://www.netl.doe.gov/scngo/NaturalGas/.

NIST (2006), *NIST Chemistry WebBook*, http://webbook.nist.gov/.

Oebro, H. (1989), *Underground gas storage in Denmark - An overview, in Underground Storage of Natural Gas: Theory and Practice*, edited by M.R. Tek, 31-44, Kluwer Academic Publishers, Dorecht.

Paige, R.W., L.R. Murray, and J.D.M. Roberts (1995), Field application of hydraulic impedance testing for fracture measurement, *SPE Production & Facilities*, 10(1), 7-12.

Paige, R.W., J.D.M. Roberts, L.R. Murray, and D.W. Mellor (1992), Fracture management using hydraulic impedance testing, SPE 24824, *Proceedings of the 67th annual technical conference and exhibition of the Society of Petroleum Engineers*, Washington, D.C, USA, 4-7 October, 1992.

Powell, J. (2006), Liquefied natural gas – market challenges and opportunities for innovation, *Hydrocarbon World*, December, 1-3.

Pruess, K. (2005), *Numerical studies of fluid leakage from a geologic disposal reservoir for CO_2 show self-limiting feedback between fluid flow and heat transfer*, LBNL-57362, Lawrence Berkeley National Laboratory.

Reid, R.C., J.M. Prausnitz, and B.E. Poling (1987), *The properties of gases and liquids, 4th ed.*, McGraw-Hill, New York.

Silvani, C., S. Bonelli, P. Phillippe, and T. Desoyer (2008), Buoyancy and local friction effects on rockfill settlements: A discrete modeling, *Computers and Mathematics with Applications*, 55, 208-217.

Soliman, M.Y. and M. Azari (1998), Effect of friction and leak-off on fracture parameters calculated from hydraulic impedance testing, *Proceedings of SPE India Oil and Gas Conference and Exhibition*, New Delhi, India, 17-19 February. 1998.

Streeter, V.L. and E.B. Wylie (1967), *Hydraulic transients*, McGraw-Hill Book Company.

Thompson, P.A. (1972), *Compressible-fluid dynamics*, McGraw-Hill.

Thorley, A.R.D. (1991), *Fluid Transients in Pipeline Systems*, The American Society of Mechanical Engineers.

Tijsseling, A.S. (2007), Water hammer with fluid-structure in thick-walled pipes, *Computers and Structures*, 85, 844-851

Timoshenko, S.P. and J.N. Goodier (1970), *Theory of elasticity*, McGraw-Hill Book Co.

Toelcke, W. (1989), *Use of Pulse Test Technique and Reservoir Simulation for Developing Aquifer Storage, in Underground Storage of Natural Gas: Theory and Practice*, edited by M.R. Tek, 159-167, Kluwer Academic Publishers, Dordrecht.

U.S. Department of Energy (2009), *How is LNG shipped and stored?*, http://fossil.energy.gov/programs/oilgas/storage/lng/feature/howisitshipped.html.

Wiggert, D.C., R.S. Otwell, and F.J. Hatfield (1985), The effect of elbow restraint on pressure transients, *Journal of Fluid Engineering*, 107, 402-406.

Wylie, E.B. and V.L. Streeter (1978), *Fluid transients*, McGraw-Hill International Book Company.

Yang, Y. (2004), *GIS analysis of carbonate formations in six northeastern states for a suitability assessment of using new technology to develop natural gas storage*, MS thesis, Clemson University, Clemson, SC.

CHAPTER V

CHARACTERIZATION OF GAS STORAGE CAVERNS USING FLUID TRANSIENTS

5.1 Introduction

Despite linearization, it is still not straightforward to obtain analytical solutions for the set of equations (4.5.28) to (4.5.30) since the geometry of the problem is complex and the material properties change because several fluids exist in the problem domain. Therefore, numerical analysis methods are generally used to solve such equations. Among these methods, the finite difference method (FDM), the method of characteristics, and the finite element method (FEM) are widely used [*Chaudhry*, 1987].

In general, the FEM can be divided into two categories: explicit and implicit. In the *explicit* FDM, partial derivatives in the partial differential equation are replaced by finite difference approximations. The solutions at each time step are calculated directly from the solution at the previous time step. For the accuracy and stability of the solution, the time steps need to be sufficiently small [*Wang and Anderson*, 1980].

In the *implicit* FDM, spatial derivatives in the partial differential equation are evaluated using weighted averages of approximations between the current and the next time steps. The solution of the current time step is not expressed explicitly in terms of known solutions of the previous time step. Therefore, an iterative method is used instead to obtain the solutions [*Wang and Anderson*, 1980]. The advantage of the *implicit* FDM is that the time step can be greater than the time step of the *explicit* FDM. There still is a restriction for the time step, accordingly to which the Courant number

$$C_N = a_w \frac{\Delta t}{\Delta x} \tag{5.1}$$

must be maintained close to 1.0 [*Holloway and Chaudhry*, 1985]. Here a_w is the wave speed, Δt is the time step, and Δx is the size of the spatial finite difference grid. If condition $C_N \approx 1$ is not satisfied, artificial high frequency oscillations behind a steep wave front may be generated [*Chaudhry*, 1987]. Due to these limitations, the *implicit* FDM has not been popular for the analysis of transients in closed pipes [*Chaudhry*, 1987].

In the method of characteristics, the two partial differential equations are converted into two ordinary differential equations called compatibility equations. Then, the two compatibility equations are solved along the characteristic lines using FDM [*Streeter and Wylie*, 1967]. The main disadvantage of this method is that the size of the time step is restricted due to the same reason as for the *explicit* FDM. In addition, interpolations may be necessary when the pipe's diameter varies, which leads to the variation of the wave speed. In such a case, it is difficult to keep the Courant number close to 1. Consequently this method may produce numerical diffusion [*Szymkiewicz and Mitosek*, 2005].

In this work, we used the FEM-based numerical code COMSOL Multiphysics [*COMSOL*, 2005] to solve the governing equations. The FEM can have greater time steps than the method of characteristics and the *explicit* FDM [*Arfaie and Anderson*, 1991]. The disadvantage of the FEM is that it requires a greater degree of computational sophistication than the FDM does [*Istok*, 1989]. In the FEM, the subdomain is partitioned into smaller meshes called elements. For example, the subdomain is divided into several line elements in 1-D problems, and triangular or quadrilateral elements in 2-D problems. The dependent variables at each point in the elements are approximated using a shape function.

Consider a 1-D element composed of two nodes. Then, the dependent variable can be approximated as [*COMSOL*, 2005]

$$u_m = \sum_i U_i \varphi_i^m \tag{5.2}$$

where u is the dependent variables to be calculated, m is the element number, U_i is the value of u at node i (i = 1, 2), and φ_i is the shape function. The shape functions are known (i.e., chosen) functions. The governing equation, $\Pi(u)$, is expressed in the functional form given by [*Istok*, 1989]

$$\Pi(u) = \int_V f(u(x))dV \tag{5.3}$$

where V is the volume of the domain and f is a differential operator. For a structure analysis, for example, Π is the potential energy of the system. If u in (5.3) is the exact solution, $\Pi(u)$ is zero. Since we use an approximate solution, however, $\Pi(u)$ cannot be zero. Then, by inserting (5.2) into (5.3), the governing equation (5.3) becomes

$$\Pi(u) = \sum_m \int_{V_m} f(\sum_i U_i \varphi_i^m)dV_m \tag{5.4}$$

where V_m is the volume of the element m.

The FEM objective is to obtain an approximate solution by minimizing $\Pi(u)$, which is usually done by using condition [*Bathe*, 1996]

$$\frac{\partial \Pi}{\partial U_i} = 0 \tag{5.5}$$

This condition results in the following matrix equation:

$$KU = F \tag{5.6}$$

where K is the stiffness matrix, U is the vector of dependent variables at each node, and F is the force vector given by boundary conditions.

By solving the system of equations (5.6), the unknown vector of dependent variables U at each node can be determined, and represents an approximate solution of (5.3) [*Bathe*, 1996].

Later in this chapter, in Section 5.2, we suggest a basic model based on a simplified geometry of a gas storage cavern. We adopted simplified boundary conditions for the simplicity of the analysis. The results of modeling based on the geometry, boundary conditions, and parameters are presented in Section 5.3. In Section 5.4, we suggested three cases. The first two cases represent the two extremes of the third case with a borehole (which represents the geometry in the real world). That is, by changing a parameter (discussed in Section 5.4), the results from the third case approach to those from one of the two extreme cases. We adopted this approach for the better understanding of the results for the third case. In Section 5.4, although the geometry for the third case is similar to that in the real world, parameters such as the diameter and the length of the borehole are not realistic. By using these unrealistic parameters, we can make it easier to analyze the results of calculation. Similar to Section 5.4, in Section 5.5, we also proposed three case, but with more realistic parameters. Thus, based on the knowledge obtained in Section 5.4, we can improve the understanding of the wave propagation through a gas storage cavern system in the field conditions in Section 5.5.

5.2 Problem Description

5.2.1 Geometry of the Problem

We use pressure transients to characterize the gas storage cavern during the acid injection stage: a perturbation is generated by changing the injection rate of the acid. The created pressure wave propagates through the acid. If the created wave due to perturbation meets any interface, reflection and transmission of the wave occurs at the interface. By analyzing the characteristics of the reflected and transmitted waves at the wellhead, the geometry of the gas storage cavern can be characterized.

The pressure wave propagation through the system can be considered as a transient fluid flow in a pipe. Hence, the entire system shown in Figure 4.1 is modeled by 1-D transient fluid flow in three pipes named acid injection pipe, cavity-with-mixture (cavern), and brine pipe shown in Figure 5.1.

The acid injection pipe is composed of steel. The injected acid flows through this pipe. Below the acid injection pipe, a cavern called cavity-with-mixture created by the dissolution of carbonate rock is connected to the acid injection pipe (Figure 5.1). The upper part of the cavity-with-mixture is filled with a mixture of acid, supercritical CO_2, and brine. The dissolution process occurs in this region. The lower part of the cavity-with-mixture is filled only with brine. Since the density of brine is greater than that of CO_2, brine settles to the bottom of the cavity-with-mixture. The brine pipe is a steel pipe. Brine is collected at the bottom of the brine pipe through which it is pumped out. The lower part of the brine pipe that contacts brine is loaded externally by the pressure of brine (Figure 5.1) since this part is located in the cavern. This pipe is also loaded by the internal pressure of brine. In the field, the brine pipe is placed inside the cavern. In this work, the brine pipe is modeled separately from the cavern, but, by applying appropriate boundary conditions, we can simulate the wave propagation through it.

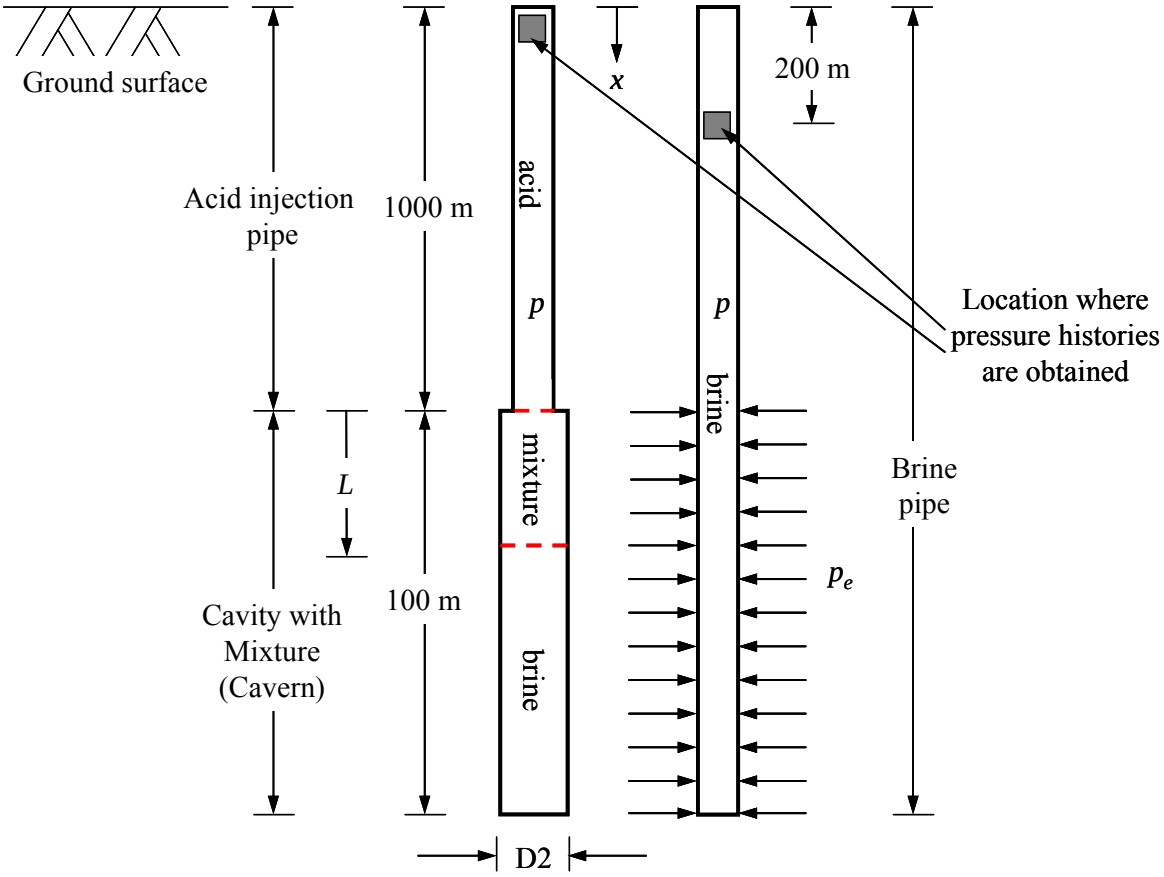

Figure 5.1 Modeling of acid injection process as a fluid flow through a pipe composed of an acid injection pipe, cavity-with-mixture, and brine pipe. Acid injection pipe is composed of steel pipe. It is filled with acid. A cavern called cavity-with-mixture is filled with mixture and brine. The brine pipe is composed of steel and filled with brine. In this figure, L is the location of the mixture-brine interface in the cavity-with-mixture (i.e., thickness of the mixture layer), D2 is the cavern diameter, p is the internal fluid pressure in the pipes, and x is the depth from the ground surface. Part of the brine pipe is loaded by the external pressure p_e as well as the internal pressure of the brine. This figure is not to scale.

We assumed that the length of the acid injection pipe is 1000 m. The length of the cavity-with-mixture is 100 m (Figure 5.1). The location of the mixture-brine interface (Figure 5.1) changes during the injection process. The diameter of both the acid injection pipe and the brine pipe is 0.04 m. The initial diameter of the cavity-with-mixture was

assumed to be 0.15 m. Its diameter increases as the dissolution process continues. In addition, we also assumed that the diameter of the cavity-with-mixture is constant along its length during the wave propagation. Thus, the cavity-with-mixture has a cylindrical shape with constant diameter along its length. In addition, the length of the cavity-with-mixture is much greater than its diameter in this model.

5.2.2 Initial and Boundary Conditions

For the simplicity of the calculations and the analysis, we assumed that the characterization of a cavern using fluid transients is conducted in a zero initial flow rate condition. Therefore, (4.5.28) to (4.5.30) are used. In the field, the acid injection rate can be decreased slowly to zero to create a zero initial flow rate condition. Due to the slow decrease of the injection rate, no significant pressure wave would be created. To create perturbation, acid is injected within short time period, and the injection is stopped abruptly. Such an injection creates a pressure wave in the pipe. Since we use (4.5.28) to (4.5.30) as governing equations to describe transient fluid flow, the initial pressure distribution does not affect the results of the calculation. Therefore, only for solving the governing equations, we set the initial flow rate and the pressure distribution as all zero, along the entire domain, although pressure is not zero in the field.

For the acid injection pipe, we used (4.5.28) since this pipe is under only internal pressure and fluid flow is always turbulent. For the mixture contained in the cavity-with-mixture, we used the mass balance equation in (4.5.28) with the definition of wave speed (4.3.45) because the cavity-with-mixture is located in a carbonate rock formation. We used the momentum balance equation in (4.5.28) since fluid flow in the mixture is always turbulent (Section 5.3.4). In the same manner, we used the mass balance equation in (4.5.29) with (4.3.45) in the brine in the cavity-with-mixture. In contrast to the mixture in the cavity-with-mixture, fluid flow in the brine in the cavity-with-mixture is laminar flow (Section 5.3.4), so that we used the momentum balance equation in (4.5.29) instead of that

in (4.5.28). In the brine pipe, we used (4.5.30) and the momentum balance in (4.5.29) because this pipe is under both external and internal pressures and fluid flow in the pipe is laminar.

For boundary conditions, the flow rate at the top of acid injection pipe (x = 0 m) is controlled. The injection rate is given in Figure 5.2. At the junction of the acid injection pipe and the cavity-with-mixture, the flow rate is continuous. At the top of brine pipe (x = 0 m), the pressure is maintained at zero during the calculation. We also assumed that the pressure and the flow rate at the bottom of the cavity-with-mixture and the brine pipe (x = 1100 m) are continuous. Hence, the pressure at the bottom of the cavity-with-mixture is the same as that at the bottom of the brine pipe. Similar to the pressure, the flow rate at the bottom of the brine pipe is the same as that at the bottom of the cavity-with-mixture.

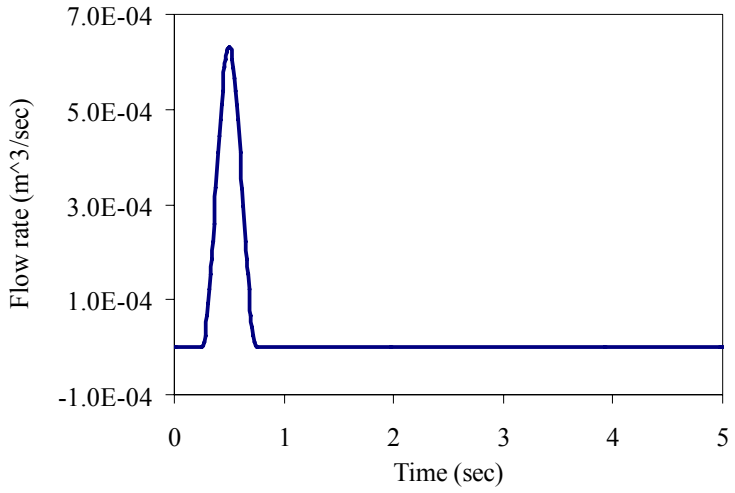

Figure 5.2 Flow rate at x = 0 m in the acid injection pipe.

5.2.3 Material Properties

We assumed that the pipe material is steel. The material properties of steel and the characteristics of the pipe are shown in Table 5.1. The cavern is constructed in a limestone formation. The material properties of limestone are shown in Table 5.2. The material properties of the acid (HCl) and the brine are shown in Table 5.3.

The mixture in the cavity-with-mixture is composed of acid, brine, and CO_2. Therefore, its properties are dependent upon the component ratio of each material. The component ratio of each material is not known. In this work, we assumed that the material properties of the mixture are the same as those of CO_2.

Table 5.1 Material properties of steel and characteristics of pipe [*Gere and Timoshenko*, 1992; *Janna*, 1993]

Material Property	Value
Young's modulus of steel	200×10^{9} Pa
Poisson's ratio of steel	0.28
Internal diameter of pipe	0.04 m (≈1.5 inch)
Pipe wall thickness	0.005 m (assumed)
Pipe wall roughness	4.6×10^{-5} m

Table 5.2 Material properties of limestone [*Goodman*, 1989; *Janna*, 1993]

Material Property	Value
Young's modulus of limestone	56×10^{9} Pa
Poisson's ratio of limestone	0.3
Wall roughness	3.0×10^{-4} m (assumed)

Table 5.3 Material properties of acid (HCl) and brine [*Bisgaard et al.*, 1987; *Levy et al.*, 2000; *Lide*, 2004]

Material property	Acid (HCl)	Brine
Density (kg/m^3)	1180	1230
Bulk modulus (Pa)	2.72×10^{9}	2.35×10^{9}
Dynamic viscosity (Pa·sec)	1.9×10^{-3}	4.9×10^{-3}

Since CO_2 layer (i.e., mixture in the cavity-with-mixture in Figure 5.1) is located at 1000 m below the ground surface (Figure 5.1), it is in a supercritical state. A supercritical fluid has both liquid-like and gas-like properties. Due to the high density of supercritical CO_2, we consider it to be a liquid with low compressibility. If supercritical CO_2 is considered to be a liquid, its bulk modulus and density are required.

Provided that the pressure-density curve for CO_2 is linear, a constant bulk modulus can be used instead of a non-linear bulk modulus. To obtain material properties of supercritical CO_2, consider a CO_2 layer located at the depth h = 1000 m below the ground surface (Figure 5.1). To estimate the material properties of supercritical CO_2, consider a hydrostatic pressure distribution in the entire domain. Then, the pressure at the top of the CO_2 layer is given by

$$p_{CO_2} = \rho_{acid} gh \tag{5.7}$$

where p_{CO_2} is the pressure at the top of the CO_2 layer, ρ_{acid} is the acid density, and g is the gravity acceleration. By assuming that ρ_{acid} is 1180 kg/m^3, the pressure at the top of the CO_2 layer is 11.57 MPa. The pressure-density curve for CO_2 in the range of 10 to 15 MPa is shown in Figure 5.3. From Figure 5.3, it seems that the pressure-density curve for CO_2 in the range of 10 to 15 MPa is non-linear. The pressure change in CO_2 due to the perturbation can be estimated by assuming frictionless flow in a pipe [*Wylie and Streeter*, 1978]

$$\Delta p = \rho a_w \Delta v \tag{5.8}$$

where Δp is the pressure change due to the perturbation, ρ is the fluid density, a_w is the wave speed in the fluid, and Δv is the change of fluid velocity due to the perturbation.

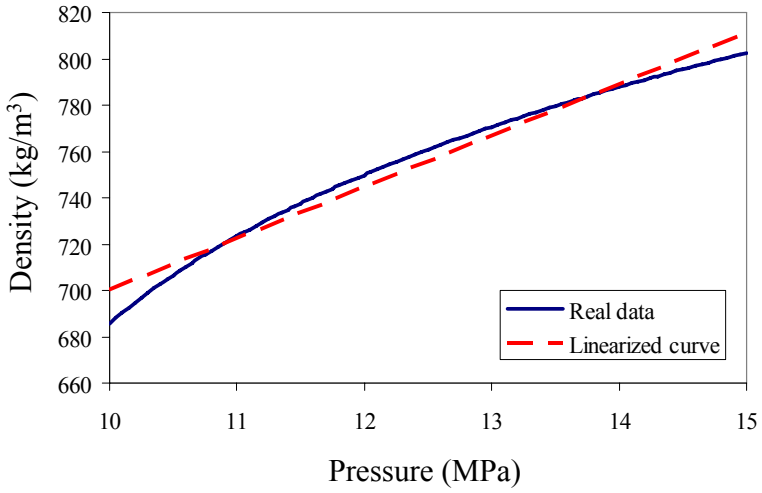

Figure 5.3 Relationship between pressure and density of CO_2. In the range of pressure between 10 to 15 MPa, the correlation of the linearized curve is 0.9765 (temperature = 310 K) [*NIST*, 2006].

Suppose that the density and the wave speed of supercritical CO_2 are 656 kg/m^3 and 1000 m/sec, respectively. If the injection rate is 10 gal/min, Δv is 0.036 m/sec for a cavern with diameter of 0.15 m. Hence, Δp is 2.36×10^4 Pa, and the CO_2 pressure changes approximately from 11.57 to 11.59 MPa due to the perturbation. The real pressure change would be smaller due to the reflection of the wave at the acid-mixture interface and the friction loss. The pressure-density curve in the range of 11 to 12 MPa is shown in Figure 5.4. From Figure 5.4, it appears that the pressure-density curve in the range of 11 to 12 MPa can be considered to be linear, which means that we can use a constant bulk modulus for CO_2. The bulk modulus of CO_2 can be obtained from the linearized curve using (4.5.12). In addition, based on (4.5.13), a constant density is used for (4.5.28) and (4.5.29). The material properties of CO_2 used in this work are shown in Table 5.4.

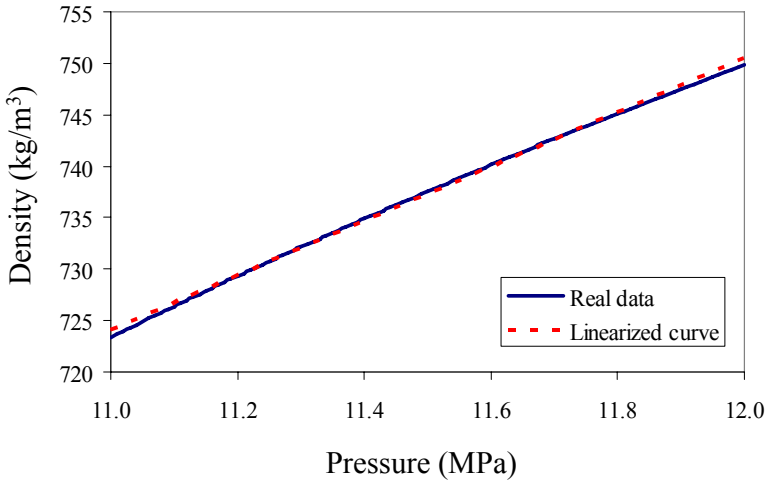

Figure 5.4 Relationship between pressure and density of CO_2 in the range of pressure between 11 and 12 MPa [*NIST*, 2006]. The correlation of the linearized curve is 0.9987 (temperature = 310 K).

Table 5.4 Material properties of CO_2 [*Bisgaard et al.*, 1987; *Arai et al.*, 2002; *NIST*, 2006]

Material Property	Value
Density (kg/m^3)	740
Bulk modulus (Pa)	2.8×10^7
Dynamic viscosity (Pa·sec)	6.1×10^{-5}

As a reference, the density and the bulk modulus of air are 1.2 kg/m^3 and 1.0×10^5 Pa at 25 °C and 1 atm, respectively. By comparing these values with those of supercritical CO_2 (Table 5.4), we confirm that supercritical CO_2 is much heavier and less compressible. Thus, we may consider it to be a liquid in this work.

For the friction factor in the momentum balance equation, the Darcy-Weisbach friction factor f for steady-state fluid flow is generally used for transient fluid flow [*Chaudhry*, 1987; *Adamkowski*, 2003]. From the preliminary calculations, we found that fluid flow in an acid injection pipe is turbulent, and fluid flow in a brine pipe is laminar. The flow regime in CO_2 depends on the diameter of the diameter of the cavity-with-mixture. As it increases greater than 1.0 m, fluid flow becomes laminar flow.

For turbulent flow, (4.5.29) is used. It seems reasonable to use a constant friction factor for each fluid since the change of wave speed in a pipe is expected to be small. If the fluid flow is laminar, in contrast, we can use (4.5.28). The impact of the friction factor is discussed in Section 5.3.4.

5.2.4 Analysis Cases

A gas storage cavern during the acid injection stage is characterized by fluid transients. Accordingly, the cavern characteristics are obtained by measuring the pressure histories at the wellhead in both the acid injection pipe and the brine pipe (Figure 5.1). The initial perturbation is generated by injecting acid within a short time at the wellhead in the acid injection pipe. Since (4.5.28) to (4.5.30) are used as the governing equations assuming zero initial flow rate and pressure along the entire domain, the pressure histories at the wellhead in acid injection pipe and brine pipe represent the history of the pressure difference between total pressure and initial pressure. Therefore, only the pressure histories induced by perturbation are presented.

The pressure histories may be affected by three factors: the diameter change of the cavity-with-mixture (cavern), the material properties of the fluids in this system, and the location of the mixture-brine interface in the cavity-with-mixture. In the early stage of acid injection, the diameter of the cavity-with-mixture is not fully developed, and the amounts of byproducts (i.e., CO_2 and brine) are relatively small. Hence, we can assume that the cavity-with-mixture is filled with only acid. The major concern in the early stage is the diameter change of the cavity-with-mixture.

As the acid injection continues, the mixture and the brine layers will be created in the cavity-with-mixture. In this stage, the detection of a mixture layer and the diameter change of the cavity-with-mixture are the major concerns. We assumed that the main component of the mixture is supercritical CO_2. The interface location L (Figure 5.1) between mixture and brine in the cavity-with-mixture can change during the acid injection.

The detection of the change of the interface location is performed by analyzing the pressure histories at the wellhead.

5.3 Calculation Results

The calculated pressure histories at $x = 0$ m in the acid injection pipe and at $x = 200$ m in the brine pipe (Figure 5.1) are plotted, because in the field, the pressure histories could be measured near the wellhead of both pipes. The pressure measurement at $x = 0$ m in the brine pipe (Figure 5.1) is not appropriate since the constant pressure boundary condition is specified at this point.

5.3.1 Effect of Diameter Change of Cavern at Early Stage of Creation

During the early stage of the acid injection, the cavern (i.e., cavity-with-mixture in the subsequent stages of the acid injection) is not fully developed. Therefore, its diameter is smaller than the final value. Also, the amount of the byproducts would be relatively small. Hence, the material properties of the fluids in the entire domain must be similar to those of acid. Accordingly, at this stage, we call the created cavern as “cavern” instead of cavity-with-mixture. The pressure histories at the wellhead will be affected only by the diameter change of the cavern. In the subsequent stages of the acid injection, after the mixture of byproducts occupies the part of the cavern, we will call it cavity-with-mixture.

In Figure 5.5, the pressure histories at $x = 0$ m in the acid injection pipe are presented for different diameters (D2) of the cavern. The first peak for each case in Figures 5.5a and 5.5b is the input perturbation created by the change of the flow rate in Figure 5.2. The second peaks are the reflected waves at the interface of the pipe and the cavern. The third and the fourth peaks are created by the reflection of waves at the wellhead, and the interface between acid injection pipe and the cavern.

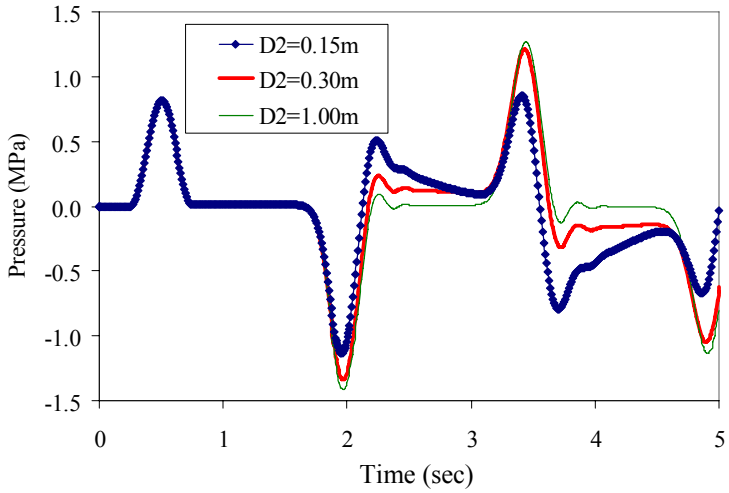

(a)

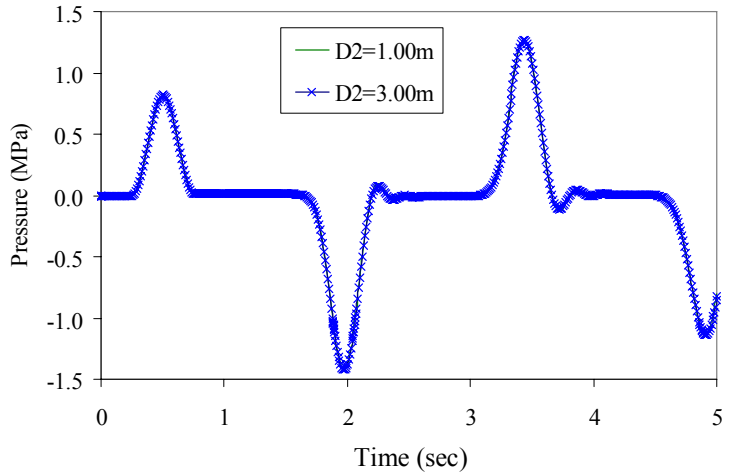

(b)

Figure 5.5 Pressure histories at x = 0 m in the acid injection pipe for different diameters (D2) of the cavern: (a) diameter changes from 0.15 m to 1.0 m and (b) diameter changes from 1.0 m to 3.0 m.

In Figure 5.5a, as the cavern diameter increases, the magnitude of the second peak also increases. However, in Figure 5.5b, there is a slight difference in the magnitude of the second peak for D2 = 1.0 m and 3.0 m. The increase in the diameter cannot be detected by monitoring the pressure history at the wellhead in the acid injection pipe if the cavern

diameter increases to greater than 1.0 m. The pressure histories at x = 200 m in the brine pipe in Figure 5.6 show a different tendency from Figures 5.5a and 5.5b.

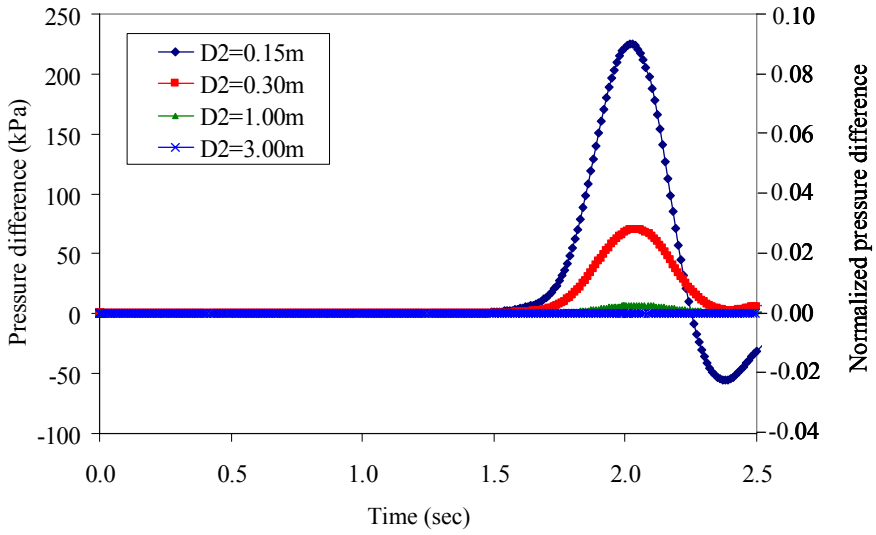

Figure 5.6 Pressure histories at x = 200 m in the brine pipe for different diameters, D2, of the cavern. In this case, the cavity-with-mixture is filled only with acid. Therefore, it is called as a cavern. The normalized pressure difference is the pressure difference divided by the hydrostatic pressure of brine at a depth of 200 m.

In Figure 5.6, the pressure histories to 2.5 sec are plotted to exclude the reflected waves from the wellhead in the brine pipe. The diameter change of the cavern can be clearly detected from the decrease of the peak value of the pressure histories. As the cavern diameter increases from 0.15 m to 3.0 m, the peak pressure difference at x = 200 m in the brine pipe decreases.

The results from Figures 5.5 and 5.6 are summarized in Figure 5.7, which shows the peak pressure with respect to the cavern diameter. Figure 5.7a shows the second peak pressure values from Figure 5.5. As the cavern diameter increases from 0.15 m to 1.0 m, the peak values increase significantly, so we infer it from this curve. However, as the diameter increases beyond 2.0 m, the peak pressure does not increase significantly. The

difference of the peak pressure for the diameter between 2.0 m and 3.0 m is too small compared to the peak values for smaller diameters of the cavern. Thus, it becomes difficult to determine the cavern diameter only from this diagram when it increases beyond 2.0 m (Figure 5.7).

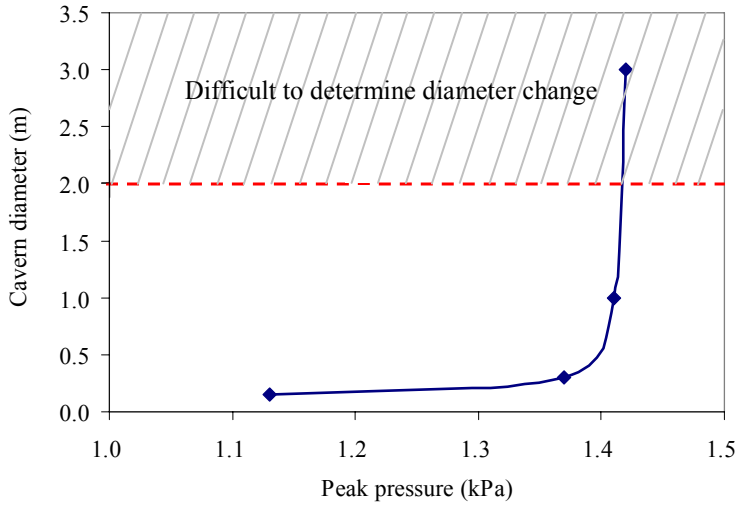

(a)

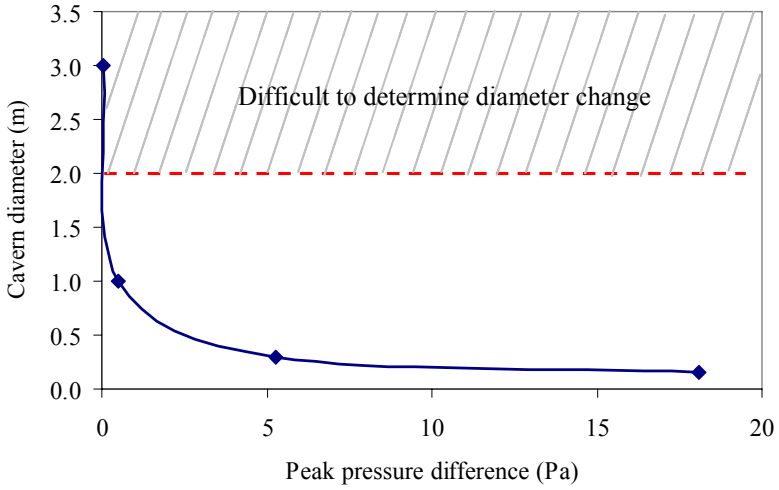

(b)

Figure 5.7 Effect of cavern diameter change on peak pressure difference in the brine pipe: (a) at x = 0 m in the acid injection pipe and (b) at x = 200 m in the brine pipe. The cavern is filled only with acid.

Figure 5.7b shows a different tendency. As the cavern diameter increases from 0.15 m to 1.0 m, the peak pressure values at x = 200 m in a brine pipe decrease. After the cavern diameter increases beyond 2.0 m, the diameter change of the cavern becomes smaller. This result can be explained from the transmission and reflection coefficient of the pressure wave propagation. By assuming that the two pipes in Figure A5.1 in Appendix A5 are filled with acid, consider three cases: the diameter of Pipe 2 in Figure A5.1 is increased from 0.2 m to 5.0 m. The diameter of Pipe 1 remains constant at 0.1 m for the three cases shown in Table 5.5.

Table 5.5 Fluid and pipe diameter for Cases 1, 2, and 3

Case No.	Pipe No.	Fluid	Pipe diameter (m)
1	Pipe 1	Acid	0.1
	Pipe 2	Acid	0.2
2	Pipe 1	Acid	0.1
	Pipe 2	Acid	1.0
3	Pipe 1	Acid	0.1
	Pipe 2	Acid	5.0

Using (A5.31) and (A5.32) in Appendix A5, we obtain the transmission and reflection coefficients of the pressure wave propagation using the same material properties shown in Tables 5.1 to 5.3. The calculated values are given in Table 5.6. Table 5.6 shows that the reflection coefficient changes from -0.630 to -0.988 as the Pipe 2 diameter increases from 0.2 m to 1.0 m. Therefore, the Pipe 2 diameter change significantly affects the reflection coefficient. As the Pipe 2 diameter increases from 1.0 m to 5.0 m, the reflection coefficient changes only from -0.988 to -0.9998. At the same time, the transmission coefficient decreases significantly as the Pipe 2 diameter increases beyond 1.0 m. These results explain that as the cavern diameter increases, peak value of the pressure histories in the acid injection pipe increases while the peak in the brine pipe decreases.

Table 5.6 Estimated reflection and transmission coefficients

Case No.	Reflection coefficient	Transmission coefficient
1	-0.630	0.370
2	-0.988	0.012
3	-0.9998	0.0002

5.3.2 Effect of Supercritical CO_2

As the injection of acid continues, the carbonate rock formation at the surface of the cavern is dissolved and the amount of byproducts of the chemical process increases. Therefore, the interface location between mixture (i.e., CO_2 in this work) and brine in the cavity-with-mixture also changes, and the effect of the two layers would appear in the pressure histories. This effect can be observed in Figure 5.8, in which two cases are compared. In the first case, the acid injection pipe, the cavity-with-mixture, and the brine pipe are filled only with acid. In the second case, the mixture and the brine exist in the cavity-with-mixture. The brine pipe is filled with brine. The location of mixture-brine interface L (Figure 5.1) is 20 m. In both cases, the diameter (D2) of the cavity-with-mixture is 0.15 m.

Figure 5.8a shows the pressure histories at $x = 0$ m in the acid injection pipe. If CO_2 and brine layers exist in the cavity-with-mixture, the magnitude of the reflected wave from the pipe-cavern interface (i.e., the second peaks in the pressure histories) is greater than that when the acid injection pipe and the brine pipe are filled only with acid. Using (4.3.45), the wave speed in the CO_2 in the cavity-with-mixture with a diameter of 0.15 m is 183 m/sec. The wave speed in the acid in the steel pipe with a diameter of 0.04 m is 1442 m/sec (Appendix B5). Thus, if CO_2 exists in the cavity-with-mixture, due to the great difference in the wave speed, more wave energy is reflected back to the wellhead compared to the case wherein the entire domain is filled only with acid. The material properties of brine are similar to those of acid. Therefore, the effect of brine on the wave propagation is small compared to that of CO_2.

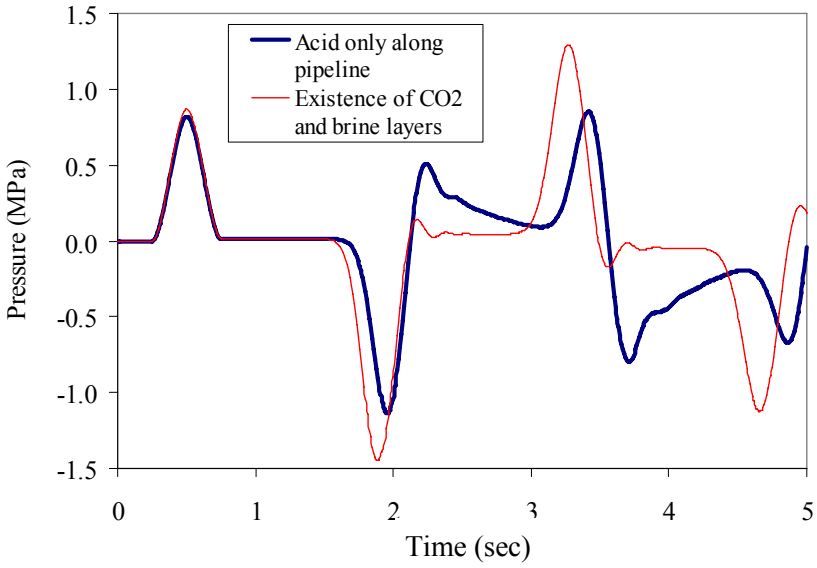

(a)

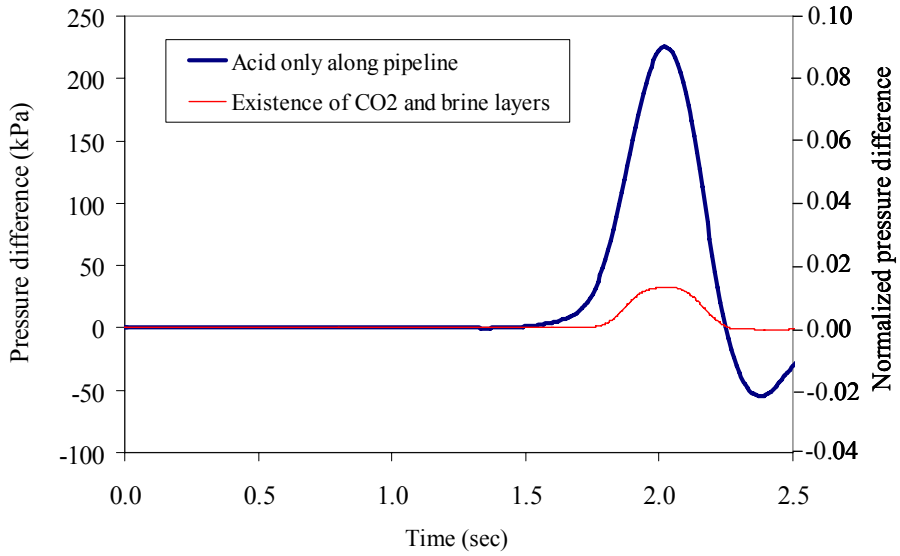

(b)

Figure 5.8 Comparison of pressure histories of two cases: (a) pressure histories at $x = 0$ m in the acid injection pipe and (b) pressure histories at $x = 200$ m in the brine pipe. The normalized pressure difference is the pressure difference divided by the hydrostatic pressure of brine at a depth of 200 m.

The existence of CO_2 in the cavity-with-mixture can also affect the pressure histories at x = 200 m in the brine pipe (Figure 5.8b). The peak value from the case of the entire domain filled with only acid is 225 kPa. The peak from the case with CO_2 in cavity-with-mixture is 32.7 kPa. If CO_2 exists in the cavity-with-mixture, most of the wave energy is reflected back to the wellhead in the acid injection pipe. Therefore, the peak value of the pressure wave arriving at x = 200 m in the brine pipe is much smaller than the case of the entire domain filled only with acid.

After the creation of CO_2 in the cavity-with-mixture, its diameter can still change due to dissolution. Hence, its effect must be investigated together with the effect of CO_2. This case is shown in Figure 5.9, in which the location of mixture-brine interface (L) in Figure 5.1 is 20 m. Figure 5.9a shows the pressure histories at x = 0 m in the acid injection pipe. It also shows that the diameter change of the cavity-with-mixture does not significantly affect the pressure histories at x = 0 m in the acid injection pipe. It appears that the effect of CO_2 is greater than that of the diameter change of the cavity-with-mixture. This indicates that after the creation of the supercritical CO_2 layer in the cavity-with-mixture, it becomes very difficult to detect the diameter change from the measurement of the pressure history in the acid injection pipe.

In contrast, the pressure histories at x = 200 m in the brine pipe are definitely affected by the diameter change of the cavity-with-mixture (Figure 5.9b) even after the appearance of CO_2. In Figure 5.9b, as the diameter of the cavity-with-mixture increases from 0.15 m to 3.0 m, the peak value of pressure histories decrease from 32.6 kPa to 0.1 kPa. Hence, the diameter change after the appearance of CO_2 can be detected by measuring the pressure histories in the brine pipe instead of those in the acid injection pipe.

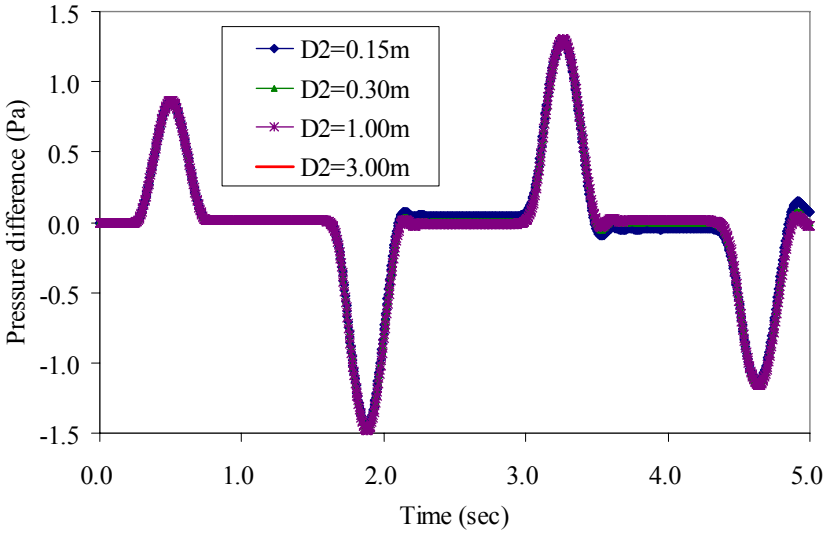

(a)

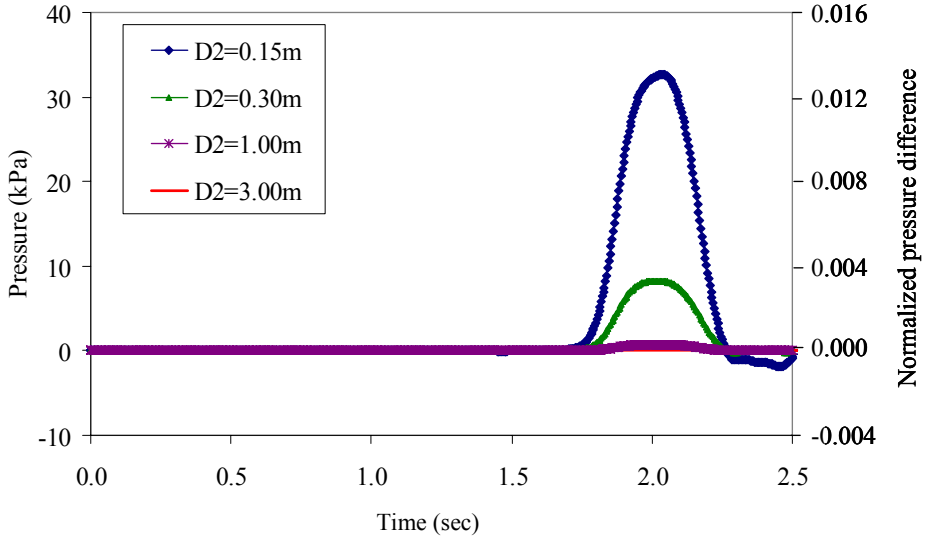

(b)

Figure 5.9 Pressure histories in the acid injection pipe and the brine pipe for different diameter of the cavity-with-mixture with L = 20 m: (a) pressure histories at x = 0 m in the acid injection pipe and (b) pressure histories at x = 200 m in the brine pipe. The normalized pressure difference is the pressure difference divided by the hydrostatic pressure of brine at depth 200 m.

This tendency can also be explained using reflection and transmission coefficients of the pressure wave at the interface of the two pipes in Figure A5.1 in Appendix A5. Consider three cases presented in Table 5.7. Using (4.3.36) and (4.3.45) with material properties and parameters from Tables 5.1, 5.3, 5.4 and 5.7, we obtain the wave speeds in acid and CO_2 contained in steel pipes. For example, wave speed in acid contained in a steel pipe with a diameter of 0.1 m is 1346 m/sec, whereas that in CO_2 contained in a steel pipe with a diameter of 0.2 m is 194 m/sec. The calculated reflection and transmission coefficients from (A5.31) and (A5.32) are given in Table 5.8. From Table 5.8, we can observe that due to the difference of the wave speed in acid and in supercritical CO_2 contained in steel pipes, the change of the reflection coefficient is very small as the diameter of Pipe 2 increases from 0.2 m to 5.0 m. At the same time, the transmission coefficient decreases by two orders of magnitude.

Table 5.7 Fluid and pipe diameter for Cases 1, 2, and 3

Case No.	Pipe No.	Fluid	Pipe diameter(m)
1	1	Acid	0.1
	2	CO_2	0.2
2	1	Acid	0.1
	2	CO_2	1.0
3	1	Acid	0.1
	2	CO_2	5.0

Table 5.8 Estimated reflection and transmission coefficients

Case No.	Reflection coefficient	Transmission coefficient
1	-0.93	0.07
2	-0.997	0.003
3	-0.9999	0.0001

Thus, Table 5.8 explains that due to CO_2 in the cavity-with-mixture, the pressure histories in the acid injection pipe do not change significantly with respect to the diameter change of the cavity-with-mixture. At the same time, the pressure signal in the brine pipe

changes considerably responding the diameter change even after CO_2 is created in the cavity-with-mixture.

From Figure 5.9b, it appears that the magnitude of the peak pressure becomes much smaller as the diameter of the cavity-with-mixture increases. So, it becomes difficult to determine the diameter change from this plot. In the field, as an alternative, we may drop a tube with a small diameter to a depth of 200 m, fill this tube with brine, and attach a pressure transducer to the top of the tube. When the brine is flowing, the transducer will read the pressure drop caused by the friction in the flow, in addition to the pressure perturbation due to the difference in densities between brine and the fluid in the drop tube. These pressures will be small compared to the pressure at the bottom of the drop tube. As a result, we can use a sensitive transducer at the ground surface to measure the pressure change at the end of our drop tube at a depth of 200 m. This approach should be feasible to detect a pulse with an amplitude of 0.1 kPa [*Murdoch*, 2007].

We assumed that the mixture in the cavity-with-mixture has material properties of supercritical CO_2. In field conditions, however, this mixture is composed of acid, supercritical CO_2, and brine. Therefore, its material properties are determined by the ratio of each component, but currently, the ratio is unknown. If the amount of acid or brine in the mixture increases, the reflection at the acid-mixture interface or the mixture-brine interface will decrease since the bulk modulus and the density of supercritical CO_2 are smaller than those of acid or brine. In addition, acid and brine have similar material properties in terms of bulk modulus and density (Table 5.3). Thus, more energy would be transmitted through the interfaces, and the peak value calculated in the brine pipe would increase.

Each component in the mixture would move due to the difference in density. In other words, acid sinks in the acid injection pipe due to injection, and supercritical CO_2 rises due to buoyancy. Brine settles to the bottom of the cavern. The moving components will create reflection waves or change the characteristics of the waves propagating through

them. It is still unknown, however, how the moving fluids would affect the wave propagation in field conditions. It requires further investigation in laboratory and field tests.

5.3.3 Effect of Interface Location

During the acid injection, the location of the mixture-brine interface L (Figure 5.1) can change. This affects the wave propagation. For sensitivity analysis, we changed the location of the mixture-brine interface changes from 20 m, to 50 m and 80 m. The calculated pressure histories for L = 50 m and 80 m are shown in Figure 5.10 and 5.11, respectively.

Similar to the case of L = 20 m, the diameter change of the cavity-with-mixture has a small effect on the pressure histories at x = 0 m in the acid injection pipe (Figures 5.10a and 5.11a). Its effect can be clearly observed in the pressure histories at x = 200 m in the brine pipe (Figures 5.10b and 5.11b). As the diameter of the cavity-with-mixture increases, the magnitude of the peak value of the pressure wave decreases significantly. Such effects of the diameter change on the peak pressure in the brine pipe for L = 20 m, 50 m, and 80 m are summarized in Figure 5.12.

In Figure 5.12, if the diameter of the cavity-with-mixture is fixed, the magnitude of the peak pressure decreases as the location of the interface moves from L = 20 m to 80 m. In addition, if the interface location is fixed, the peak value of the pressure wave decreases as the diameter of the cavity-with-mixture increases from 0.15 m to 3.0 m.

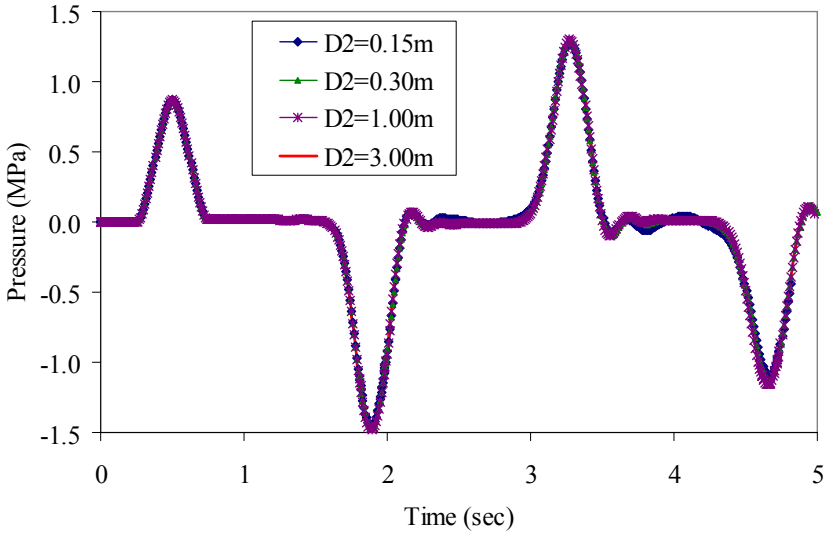

(a)

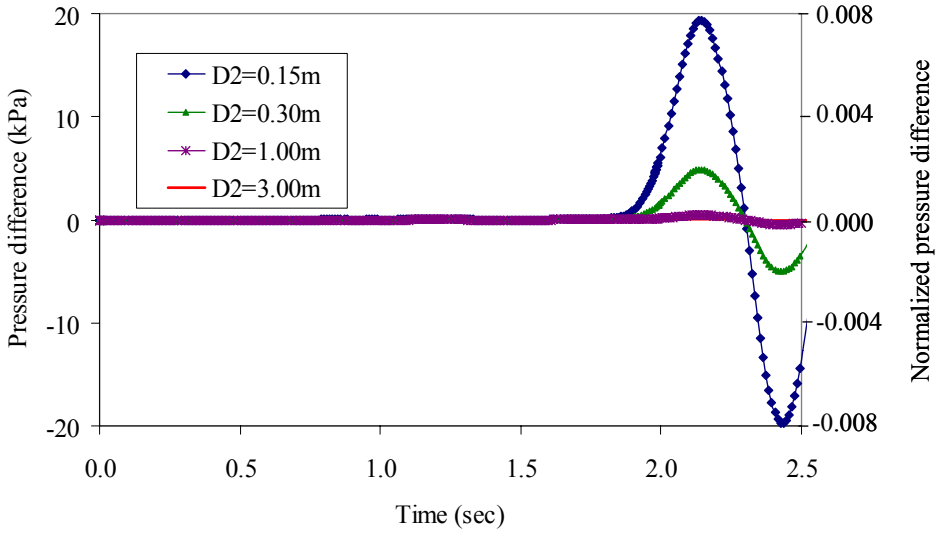

(b)

Figure 5.10 Pressure histories in the acid injection pipe and the brine pipe for different diameter of the cavity-with-mixture for L = 50 m: (a) pressure histories at x = 0 m in the acid injection pipe and (b) pressure histories at x = 200 m in the brine pipe. The normalized pressure difference is the pressure difference divided by the hydrostatic pressure of brine at depth 200 m.

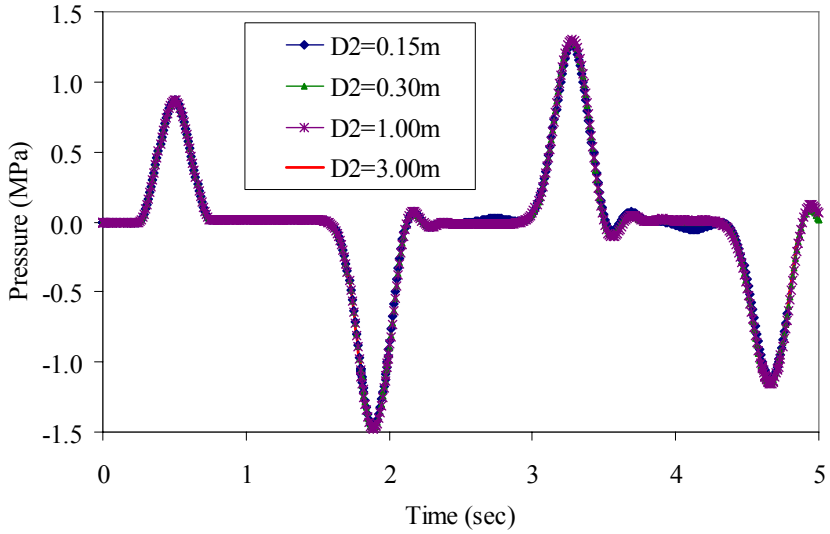

(a)

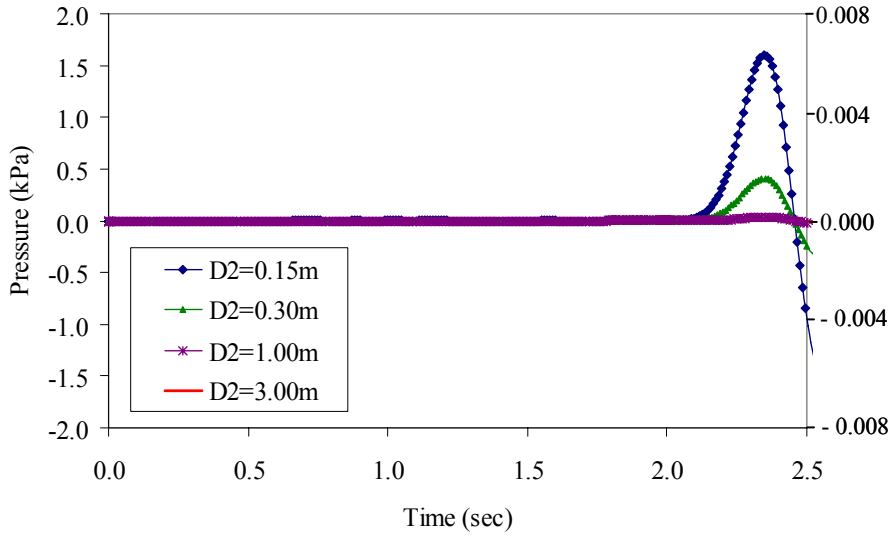

(b)

Figure 5.11 Pressure histories at wellhead in the acid injection pipe and the brine pipe for different diameter of the cavity-with-mixture for L = 80 m: (a) pressure histories at x = 0 m in acid injection pipe and (b) pressure histories at x = 200 m in brine pipe. The normalized pressure difference is the pressure difference divided by the hydrostatic pressure of brine at depth 200 m.

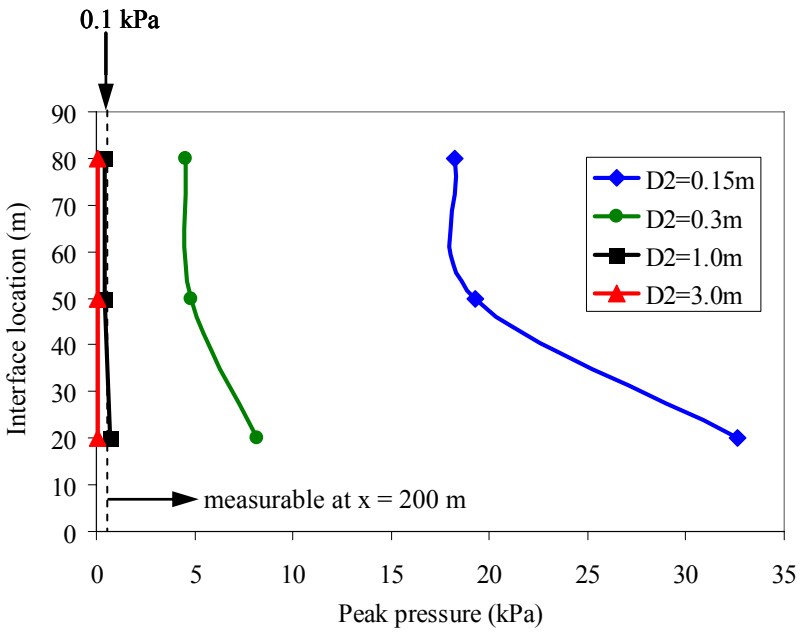

Figure 5.12 Peak pressure values at depth 200 m in the brine pipe for different interface location *L* (Figure 5.1) and diameter (D2) of the cavity-with-mixture. The dashed line shows the realistic limit of measurable magnitude of pressure wave, which corresponds to 0.1 kPa (Section 5.3.2).

The minimum measurable pressure would be 0.1 kPa (Section 5.3.2). This indicates that it may be difficult to determine the diameter change of a cavern from the pressure measurements at a depth of 200 m as it increases beyond 1.0 m. Therefore, to determine the diameter change beyond 1.0 m, we need different techniques. Based on the results of our calculations, we suggest installing pressure transducers at different depths (including depths greater than 200 m). In this case, we should be able to detect the diameter change beyond 1.0 m from different pressure transducers with various measuring ranges.

The arrival time of the peak at x = 200 m in the brine pipe changes due to the change of the interface location shown in Figure 5.13. Although only one curve is presented in Figure 5.13, it represents three different cases: i.e., the interface location changes 20 m, 50 m, and 80 m. The wave speed in CO_2 is determined from (4.3.45). It is a

function of only the material properties of the fluid and the cavern material, and not its diameter. Therefore, the diameter change of the cavity-with-mixture does not affect the arrival time of the pressure wave. The change of the interface location from 20 m to 80 m (i.e., the increase of the thickness of the mixture layer in the cavity-with-mixture) delays the arrival time of the peak since the wave speed in CO_2 (i.e., mixture in this work) is much smaller than those in acid and in brine.

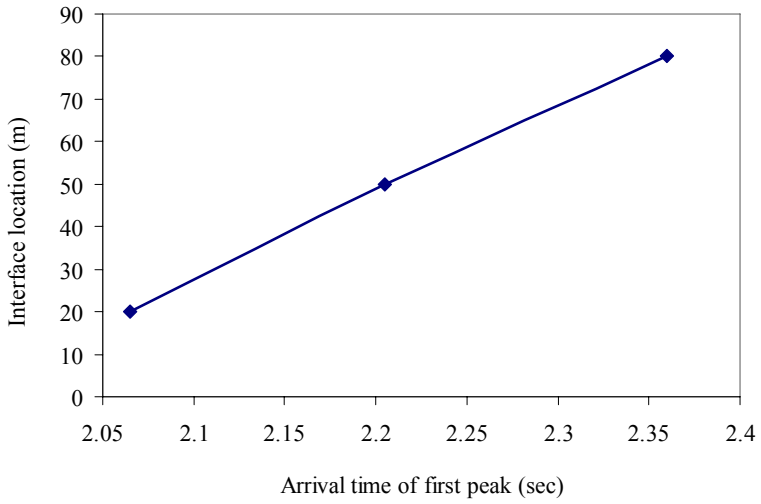

Figure 5.13 Arrival time of the peak pressure for different location of the mixture-brine interface.

5.3.4 Verification of Assumptions in Governing Equations

In Chapter IV and this chapter, we made several assumptions to derive the governing equations and to model the wave propagation process. We now verify the effect of four assumptions on the results: i) effect of the pipe diameter change during wave propagation, ii) validity of the linearized governing equations, iii) flow regime, and iv) 1-D fluid flow.

First, we verify the effect of the diameter change of the pipe and the cavity-with-mixture on the wave propagation. In Section 4.2, we assumed that the diameter of the pipe is constant. If the diameter change is sufficiently large, we have to include its effect in the governing equations. As a first step, we estimate the radial displacement of the pipe. The radial displacement of the acid injection pipe under the internal pressure is given by [*Timoshenko and Goodier*, 1970]

$$u_r = \frac{(D/2)^2 p}{Eh} \tag{5.9}$$

where u_r is the radial displacement, D is the pipe diameter, p is the internal pressure in the pipe, E is the Young's modulus of the pipe material, and h is the pipe wall thickness. From Figure 5.9a, we estimate the internal pressure change as 2.0 MPa. For other parameters, we use values from Tables 5.1, 5.3, and 5.4. The calculated radial displacement is 8×10^{-7} m, so that the ratio of the displacement to the radius of the pipe is 4×10^{-5} ($=2\times8\times10^{-7}$ m/0.04 m). Compared to the pipe diameter, the radial displacement is very small, so we do not have to consider it in our case.

Then, we verify the effect of radial displacement on the wave speed in a pipe. It is given by (4.3.36). If the pipe radius is 0.02 m, the wave speed is ≈1442 m/sec (Appendix B5). With the increased diameter calculated above, the wave speed is also ≈1442 m/sec. In (4.5.24) or (4.5.27), the effect of the diameter change on the mass balance equation is

included only in the wave speed. Since the effect of the diameter change on the wave speed is very small, its effect on the mass balance equation can be considered negligible.

As a next step, we scale the left hand side of the momentum balance equation (4.5.24) as

$$\frac{|v|}{\tau}+\frac{1}{\rho_0}\frac{|p|}{L_p}+\frac{f}{2D}v^2 \tag{5.10}$$

where v is the fluid velocity, τ is the time, ρ_0 is the fluid density (constant), L_p is the pipe length, and f is the Darcy-Weisbach friction factor. From the wave length, wave speed, and pipe length in our case, we assumed that time and length are 1.0 sec and 1000 m, respectively. For scaling, the friction factor was assumed to be 0.01, which is rather large value.

The magnitudes of each term in (5.10), i.e., $\frac{|v|}{\tau}$, $\frac{1}{\rho_0}\frac{|p|}{L_p}$, and $\frac{f}{2D}v^2$ are 0.036 m/sec^2, 1.695 m/sec^2, and 4.25×10^{-5} m/sec^2. The magnitude of the term $\frac{f}{2D}v^2$ compared to the other terms is very small. This indicates that the effect of the pipe diameter change on the momentum balance equation is insignificant. In addition, although we used a rather large friction factor, the magnitude of the term containing it is relatively small. Thus, we also conclude that we do not have to consider the dynamic change of the friction factor during wave propagation.

On the other hand, we assumed above that the cavern diameter is constant along its longitude. This assumption is reasonable since our work is to show that fluid transients can be used to characterize the gas storage cavern. Thus, we adopted a simple model in this work. In the future study, we can consider the impact of the non-constant cavern diameter along its longitude on the wave propagation.

Second, the prerequisite of (4.5.28) to (4.5.30) is (4.5.6) to be satisfied. Using (4.3.36), (4.5.6) can be expressed as

$$\frac{|p - p_0|}{K_0} << \frac{1}{1 + \dfrac{K_0 CD}{hE}} \tag{5.11}$$

where p_0 is the initial pressure, K_0 is the bulk modulus of the fluid for a reference pressure, and C is the constant defined by (4.3.25).

We introduce a ratio A

$$A = \frac{|p - p_0|}{K_0} \Big/ \frac{1}{1 + \dfrac{K_0 CD}{hE}} \tag{5.12}$$

From (5.11) and (5.12), the ratio A must satisfy

$$A << 1 \tag{5.13}$$

Hence, to use (4.5.28) to (4.5.30), (5.13) must be satisfied. We plot the distribution of the ratio A along the length of the acid injection pipe and the brine pipe at time t = 2.505 sec for L = 20 m (Figure 5.14). The time t = 2.505 sec was chosen because at this time the magnitude of the pressure distribution along the entire domain is greatest. In Figure 5.14, the ratios A in both the acid injection and the brine pipes are less than 10^{-3}, so that the ratios A in both pipes satisfy (5.13). Therefore, we can use (4.5.28) to (4.5.30). In addition, in Figure 5.14, we can see that there are several fluctuations of the ratio A along the length of the pipe. In (5.12), the only variables are $|p - p_0|$ and D. If the fluctuation occurs at x = 1000 m, it is caused by the diameter change at the interface of the acid injection pipe and

the cavity-with-mixture. Elsewhere, the fluctuation should be induced by the $|p - p_0|$ term in (5.12). Several waves propagate along the length of the pipe due to the reflection and the transmission at the interfaces. Thus, due to the existence of several waves, the $|p - p_0|$ term should change along the pipe, which leads to the fluctuations of the ratio *A*.

Third, we also have to determine whether we use momentum balance equation in (4.5.28) or (4.5.29). By plotting the Reynolds number with respect to time, we can confirm that the fluid flow at a point in the pipe is turbulent or laminar. Thus, we show the histories of Reynolds number at x = 500 m, 1010 m, and 1060 m in the acid injection pipe and the cavity-with-mixture, and at x = 500 m in the brine pipe. These points represent the center points of the acid section, the CO_2 section, and the brine sections. The histories of the Reynolds number in each case are shown in Figure 5.15 for L = 20 m and D2 = 0.15 m.

In Figure 5.15a, we can consider the fluid flow in the acid injection pipe and in the cavity-with-mixture to be turbulent since the Reynolds number is greater than 2000 for both of them. The fluid flow in the cavity-with-mixture and the brine pipe are laminar because their Reynolds number is less than 2000 (Figure 5.15b).

For D2 = 3.0 m in Figure 5.16, the Reynolds number in the acid injection pipe is greater than 8000. Reynolds number in CO_2 in the cavity-with-mixture is greater than 2000. Therefore, in these two cases, we can consider the fluid flow to be turbulent. Figure 5.16b shows the Reynolds number in brine in the cavity-with-mixture and the brine pipe. In both cases, the Reynolds number is less than 10. Therefore, the fluid flow is laminar.

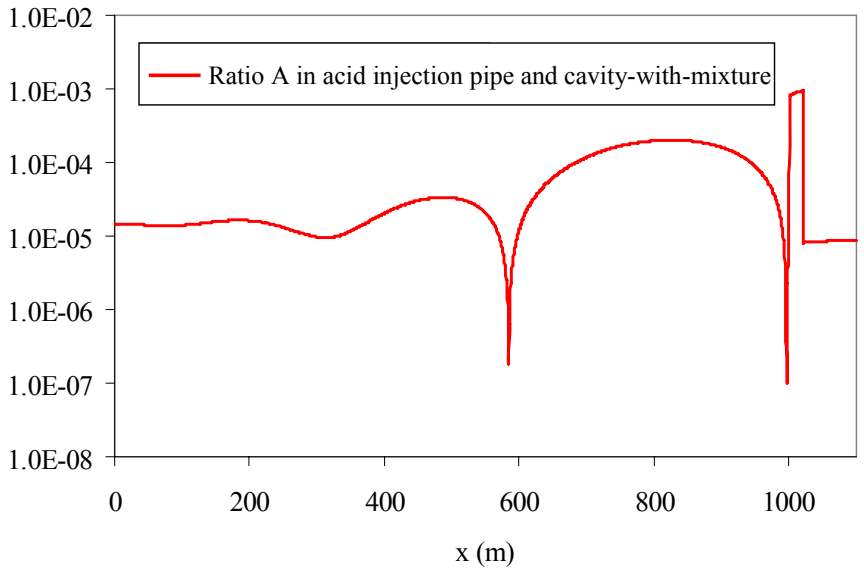

(a)

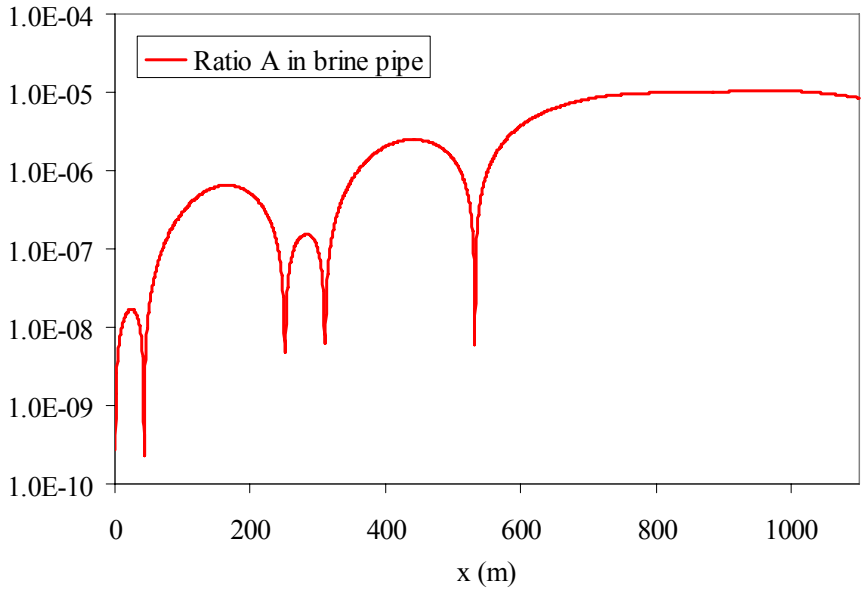

(b)

Figure 5.14 Distribution of ratio A (5.12) at time $t = 2.505$ sec for $L = 20$ m: (a) in the acid injection pipe and in the cavity-with-mixture and (b) in the brine pipe. Fluctuations of ratio A are caused by pressure distribution along the pipes due to the wave propagation.

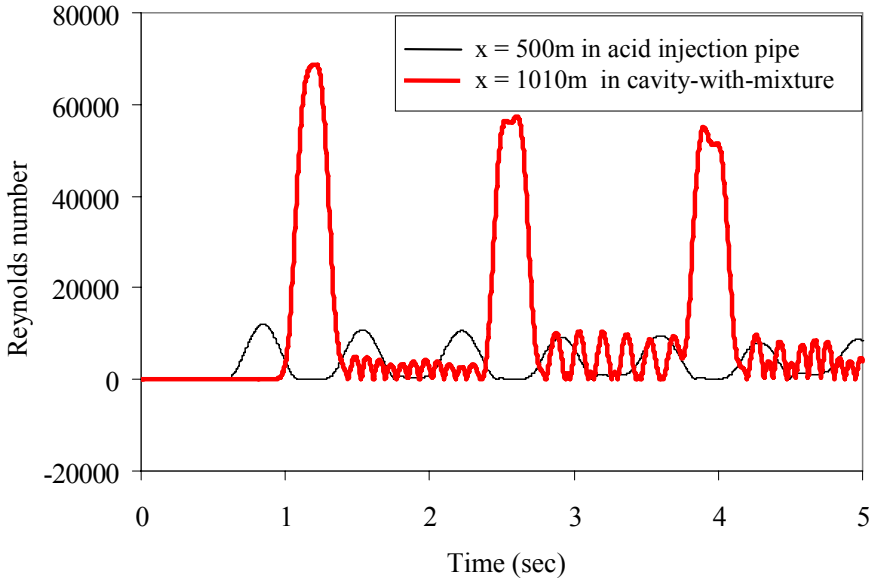

(a)

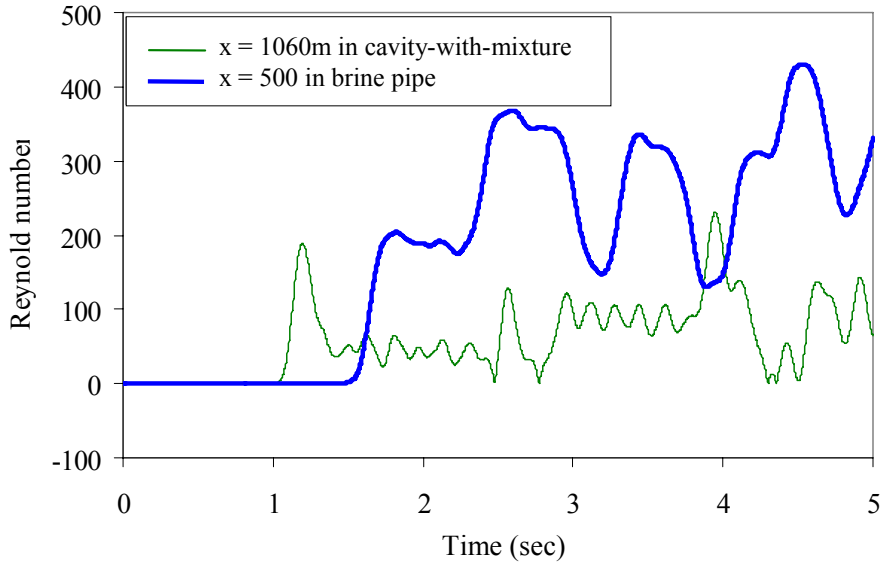

(b)

Figure 5.15 Reynolds number for L = 20 m and D2 = 0.15 m: (a) at x = 500 m in the acid injection pipe and at x = 1010 m in CO_2 in the cavity-with-mixture and (b) at x = 1060 m in brine in the cavity-with-mixture and at x = 500 m in the brine pipe.

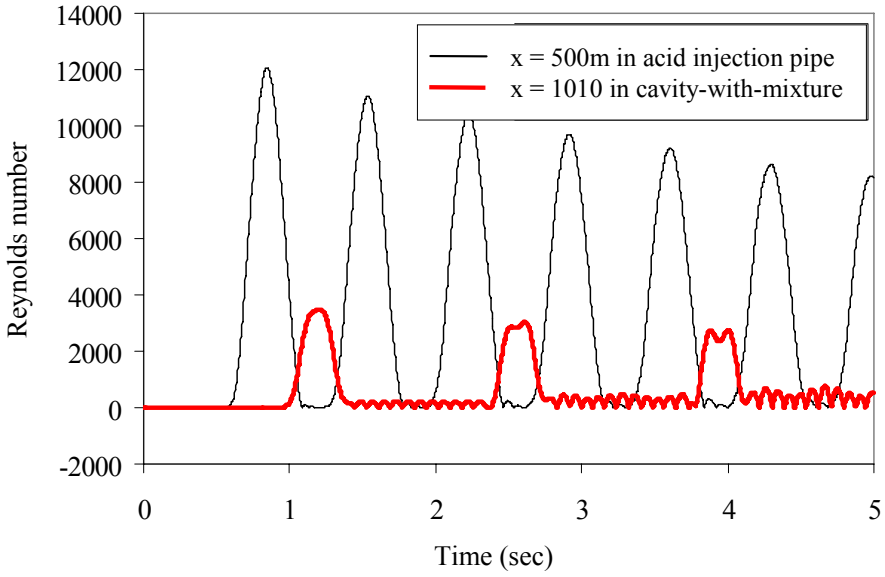

(a)

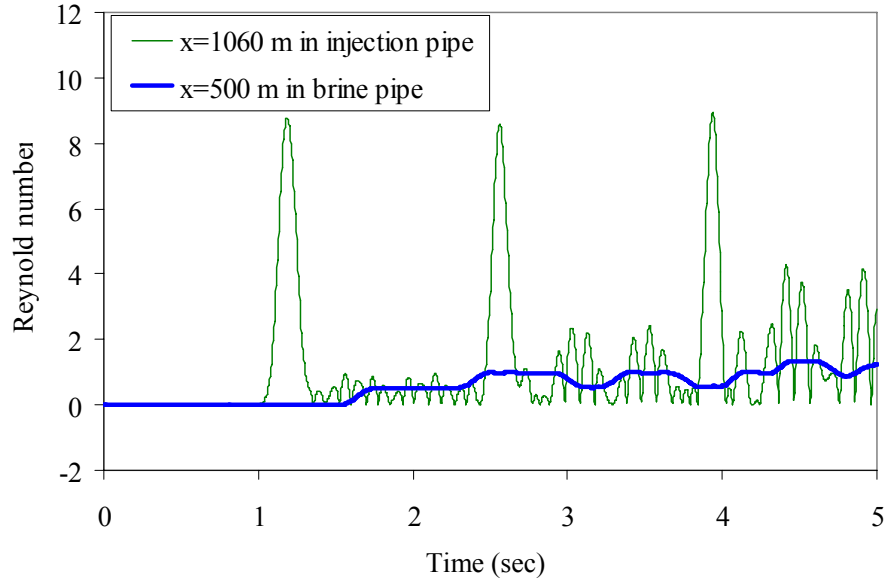

(b)

Figure 5.16 Reynolds number for L = 20 m and D2 = 3.0 m: (a) at x = 500 m in the acid injection pipe and at x = 1010 m in CO_2 in the cavity-with-mixture and (b) at x = 1060 m in brine in the cavity-with-mixture and at x = 500 m in the brine pipe.

Fourth, we only consider 1-D fluid flow in pipes and a cavern. Fluid flow, especially in caverns, may not be 1-D. In caverns, injected acid, CO_2, and brine are mixed. In addition, carbonated rock is dissolved. Thus, the fluid flow pattern in this zone would be complex. It appears that fluid flow in the cavern is probably 2-D (or 3-D) instead of 1-D. Such a 2-D (or 3-D) fluid flow may affect the wave propagation. Although this effect is not considered in this work, it would be worthwhile for future investigations to consider the effect of the 2-D (or 3-D) fluid flow on the wave propagation.

5.4 Effect of External Pressure on the Wave Propagation in the Brine Pipe

5.4.1 Model Description

The wave propagation in the field test would be more complicated than the simple model in Section 5.3. In the field, a borehole is drilled, and pipes are installed in it. Since the injection point changes to maintain the shape of the cavity-with-mixture (cavern), the lower end of the original borehole will likely extend below the bottom of the cavity-with-mixture. For characterization, the extension of the borehole beneath the bottom of the cavity-with-mixture may have a significant impact on the wave propagation in the brine pipe. Hence, corresponding boundary conditions need to be considered to address this effect.

The assumed boundary conditions at the cavity bottom in Section 5.3 correspond to the negligible wave reflection at the bottom of the cavity-with-mixture. Specifically, it was assumed in Section 5.3 that there is a continuous flow rate and pressure between the bottom of the cavity-with-mixture and the brine pipe. Therefore, only the pressure waves due to the inflow into the brine pipe are dominant in the pressure histories in the brine pipe (which will be mentioned later in this section). Also, the extended borehole beneath the bottom of the cavity-with-mixture is not included in the model in Section 5.3. Thus, the impact of the extended borehole on the pressure histories in the brine pipe was not able to

investigate. Due to the these limitations, a new approach is required to allow for the existence of multiple pressure waves propagating in the brine pipe in response to both pressure fluctuations applied externally to the brine pipe and to the reflected wave from the bottom of the cavity, considering the extended borehole as well.

In this section, we consider three cases:

Case A: brine pipe plugged at the bottom of the cavity-with-mixture

Case B: brine pipe open at the bottom of the cavity-with-mixture

Case C: brine pipe open in a borehole extending beneath the cavity-with-mixture

The Cases A and B have the same geometry as in Section 5.3. Case C includes a borehole beneath the cavity-with-mixture. The geometry of Case C is most realistic, but the Cases A and B are the extremes of Case C. That is, if the borehole length in Case C is greater than a certain length (discussed below), the results from Case C should approach those from Case A. In contrast, if the borehole length is asymptotically reduced to zero, the results from Case C should be identical to those from Case B. We adopted this approach since it matches the analyses of the calculation results from Case C more transparently. Case C represents complexities of wave propagations in the field condition, and by comparing the results from Case C with those from the two extreme cases (Cases A and B), helps understand more complicated effects of the wave propagation in Case C. The derivation of the reflection and transmission coefficients used in this section is given in Appendix A5. The calculation of the wave speed is described in Appendix B5.

The objectives of the three cases are as follows

1. Case A models no fluid flow into the brine pipe. The brine pipe is plugged at the bottom, so that there is no inflow due to reflection at the bottom of the

cavity-with-mixture into the brine pipe. Thus, only the external pressure on the surface of the brine pipe creates pressure waves in the brine pipe.

2. Case B considers both reflection at the bottom of the cavity-with-mixture and inflow into the brine pipe. Contrary to Case A, the bottom of the brine pipe is open, so that the reflected wave may enter it. Thus, both the external pressure and the inflow into the brine pipe can create pressure waves in the brine pipe. For Cases A and B, the geometry of the problem is the same as that of the model in Section 5.3 (Figure 5.1), whereas their boundary conditions are different from each other.
3. Case C includes an actual borehole located beneath the bottom of the cavity-with-mixture. To create a gas storage cavern, a borehole is drilled, and acid is injected into the borehole. Due to the dissolution of surrounding carbonate rock, the borehole diameter increased and the enlarged part of the borehole becomes the cavern (cavity-with-mixture in the model). By changing the injection depth of the acid, the shape of the cavern is controlled. The original borehole could remain beneath the bottom of the cavern, and the brine pipe can be lowered into the borehole to pump out brine (Figure 5.17). This case would be more close to the field condition than Cases A and B, and the model in Section 5.3.

The geometry of the model in this section, especially in Case C, enables us to use the same acid injection rate used in Section 5.3. Hence, we can compare the results from this section with those from Section 5.3 for a better understanding of the characteristics of the pressure pulses for the new boundary conditions. The results from this section will also improve the understanding of the pressure pulses with a more realistically scaled geometry, which will be discussed in Section 5.5.

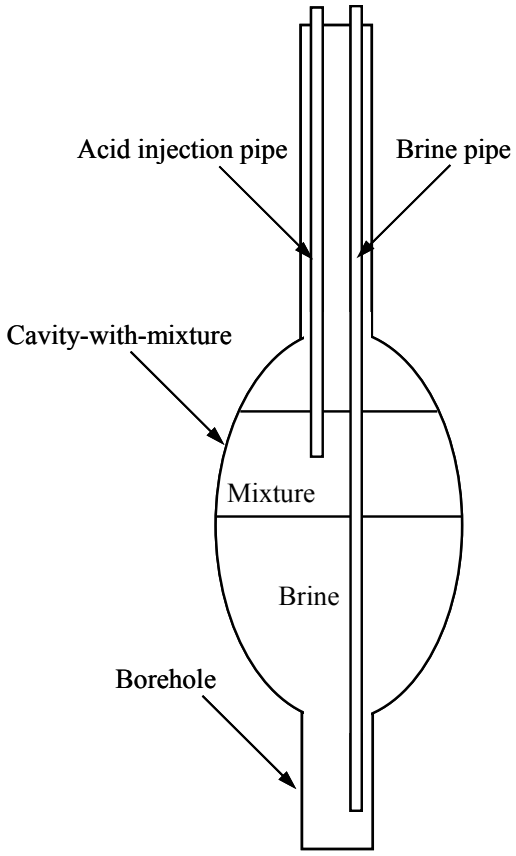

Figure 5.17 Schematic of Case C. In contrast to the model in Section 5.3, an actual borehole is located beneath the cavity-with-mixture. The bottom of the brine pipe is lowered downward into the borehole to pump out brine. This figure is not to scale.

Due to the difference of the diameter between the cavity-with-mixture and the borehole (Figure 5.17), an incident pressure wave into this interface creates reflected and transmitted waves. The bottom part of the cavity-with-mixture and the entire borehole is filled with brine (Figure 5.17). Using (A5.31) and (A5.32) in Appendix A5 and assuming the diameter of the cavity-with-mixture and the borehole to be 0.15 m and 0.05 m, respectively, we estimate the reflection R = 0.8 and transmission T = 1.8 coefficients. According to the estimates, the reflected wave at the interface between the cavity-with-mixture and the borehole has approximately the same magnitude as that of the incident wave into this interface since R = 0.8.

Due to the fluctuations of the external pressure on the brine pipe, a pressure wave is created in this pipe, which propagates upward. At this moment, there is no inflow into the bottom of the brine pipe, since its bottom is extended downward to the bottom of the borehole.

After the transmitted wave through the interface meets the bottom of the borehole, a reflected wave is created, and it enters into the brine pipe. Thus, there is a time difference between the pressure wave due to the external pressure and that due to the inflow into the brine pipe. This indicates that the two waves could be separated as long as the borehole length is sufficiently long.

Case A is used to investigate the impact of the external pressure on the pressure histories in the brine pipe, excluding the pressure wave due to the inflow into the brine pipe. With Case B, we can consider simultaneously the pressure histories in the brine pipe due to the external pressure and the inflow into the brine pipe. With Case C, we can investigate the impact of the borehole beneath the cavity-with-mixture on the pressure histories in the brine pipe.

5.4.2 New Models with COMSOL Multiphysics

Case A is modeled with the same geometry as the model in Section 5.3 (Figure 5.1). In this case, the boundary conditions at the bottom of the cavity-with-mixture and the brine pipe are zero flow rates, to simulate a plugged brine pipe and the reflection of the waves at the bottom of the cavity-with-mixture.

The boundary conditions of Case B are continuous flow rate and pressure at the bottom of the cavity-with-mixture and the brine pipe. At the same time, an incident wave is reflected at the bottom of the cavity-with-mixture. To simulate such a wave reflection at the bottom of the cavity-with-mixture, the flow rate must be zero at this point. However, COMSOL Multiphysics does not allow zero flow rate at the bottom of the cavity-with-mixture and continuous flow into the brine pipe, based on the geometry shown in Figure 5.1. Thus, to incorporate these boundary conditions into a COMSOL Multiphysics model, we use a geometry shown in Figure 5.18.

In Case B, in contrast to the model in Section 5.3, a virtual borehole is located beneath the cavity-with-mixture (Figure 5.18). We assumed that the diameter and the length of the virtual borehole are 0.01 m and 10 m, respectively (Figure 5.18). We also assumed that the virtual borehole is filled with brine. The flow rate between the cavity-with-mixture and the virtual borehole is continuous. The diameter of the virtual borehole is determined to simulate the reflection of the wave at the bottom of the plugged cavity-with-mixture. Due to the difference between the diameter of the cavity-with-mixture and that of the virtual borehole, an incident wave into this interface creates reflection and transmitted waves. With (A5.31) and given diameters of the cavity-with-mixture and the borehole, the reflection coefficient at this interface is $R \approx 1.0$.

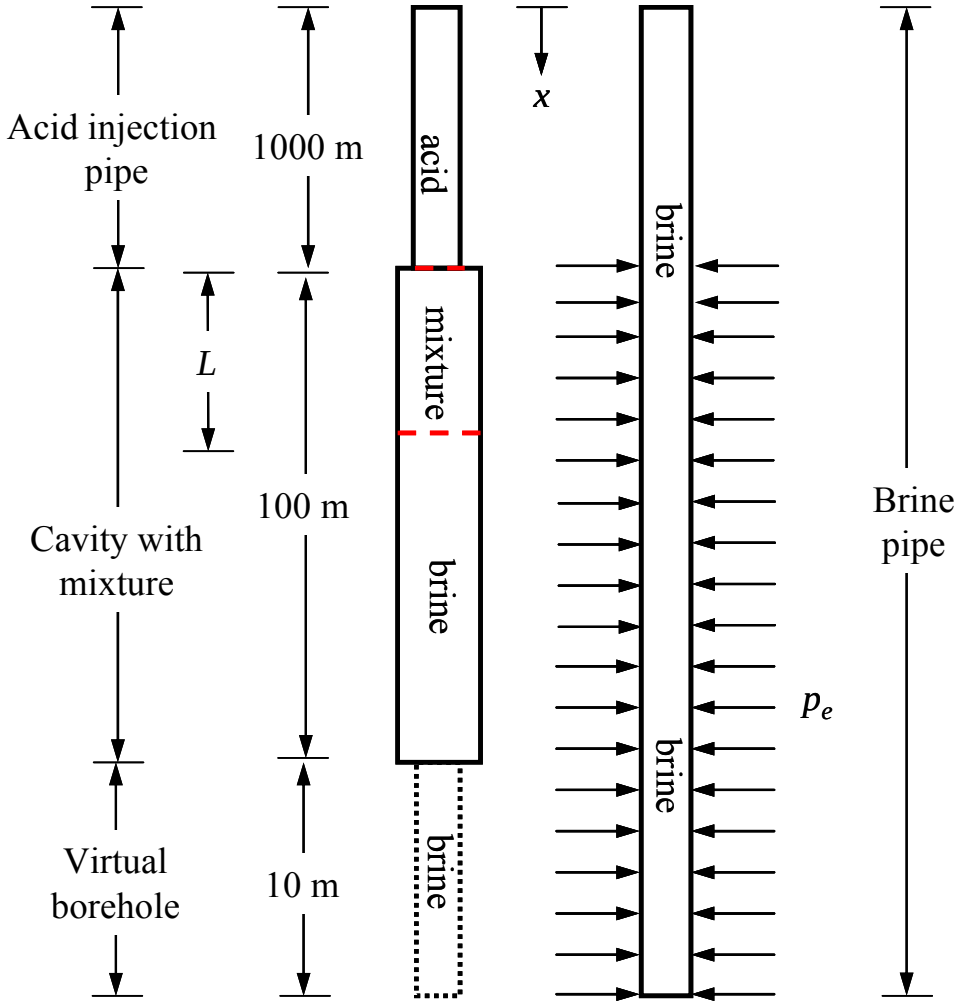

Figure 5.18 Schematic of Case B. In contrast to the model in Section 5.3, a virtual borehole is located beneath the cavity-with-mixture. The length and the diameter of the virtual borehole are 10 m and 0.01 m, respectively. The virtual borehole is displayed by dashed line to emphasize that it does not actually exist in the field. This figure is not to scale.

At the bottom of the cavity-with-mixture with a borehole, R = 1.0. Hence, we conclude that the interface between the cavity-with-mixture and the virtual borehole can simulate the reflection of a wave at the bottom of a cavity-with-mixture without a borehole.

In Case B, the bottom of the brine pipe is lowered downward toward the bottom of the virtual borehole. Thus, the length of the brine pipe is 1110 m (Figure 5.18). We set the flow rate and the pressure at the bottom of the brine pipe to be the same as those at the bottom of the virtual borehole to simulate the inflow into the brine pipe. Thus, by using these boundary conditions, we simulate the wave reflection at the bottom of the cavity-with-mixture and the inflow into the brine pipe simultaneously.

To evaluate the effect of the virtual borehole, consider the wave length in this system. The wave length, L_w, can be calculated as

$$L_w = a_w T \tag{5.14}$$

where a_w is the wave speed and T is the period of the wave. In this case, the wave speed in the brine contained in a borehole is 1312 m/sec and period is 0.5 sec. The period of the wave is assumed to be the same as that of the wave shown in Figure 5.2. The calculated wave length is 656 m. This indicates that a virtual borehole with a length of 10 m in our model would not significantly affect the wave propagation in this system: i.e., the time difference in the pressure histories due to the virtual borehole is 0.015 sec (= 2×10 m / 1312 m/sec).

To incorporate the boundary conditions of Case C into our model, the geometry in Figure 5.19 was used. In this case, an actual borehole is located beneath the bottom of the cavity-with-mixture. The diameter of the borehole was assumed to be 0.05 m. Since the borehole is located beneath the cavity-with-mixture, it is filled with brine. The bottom of the brine pipe extends downward towards the bottom of the borehole. For the boundary conditions, pressure is continuous between the bottom of the borehole and the brine pipe.

Flow rate is scaled by the ratio of the cross-sectional area. This setup simulates the reflection of a pressure wave at the bottom of the cavity-with-mixture and the inflow into the brine pipe.

In Cases A, B, and C, the governing equations used are essentially the same as those used in the model in Section 5.3. For the acid injection pipe, we used (4.5.28) for the governing equations, since it is under only internal pressure and fluid flow is always turbulent. For the mixture contained in the cavity-with-mixture, we used the mass balance equation in (4.5.28) with the definition of wave speed of (4.3.45). We also used the momentum balance equation in (4.5.28) for the mixture in the cavity-with-mixture as the fluid flow in the mixture is turbulent (Section 5.3.4). In the same manner, we used the mass balance equation in (4.5.29) with (4.3.45) in the brine in the cavity-with-mixture because the fluid flow in the brine in the cavity-with-mixture is laminar (Section 5.3.4). Therefore, we used the momentum balance equation in (4.5.29) instead of that in (4.5.28). We assumed that the borehole is a cavern with smaller diameter. Thus, we used the mass balance equation in (4.5.29) with (4.3.45), whereas the momentum balance equation in (4.5.29) is used for the fluid flow in the borehole, since fluid flow in the borehole is laminar. In the brine pipe, we used (4.5.30) and the momentum balance in (4.5.29) since the brine pipe is under both the external and the internal pressures. The fluid flow in the brine pipe is laminar flow.

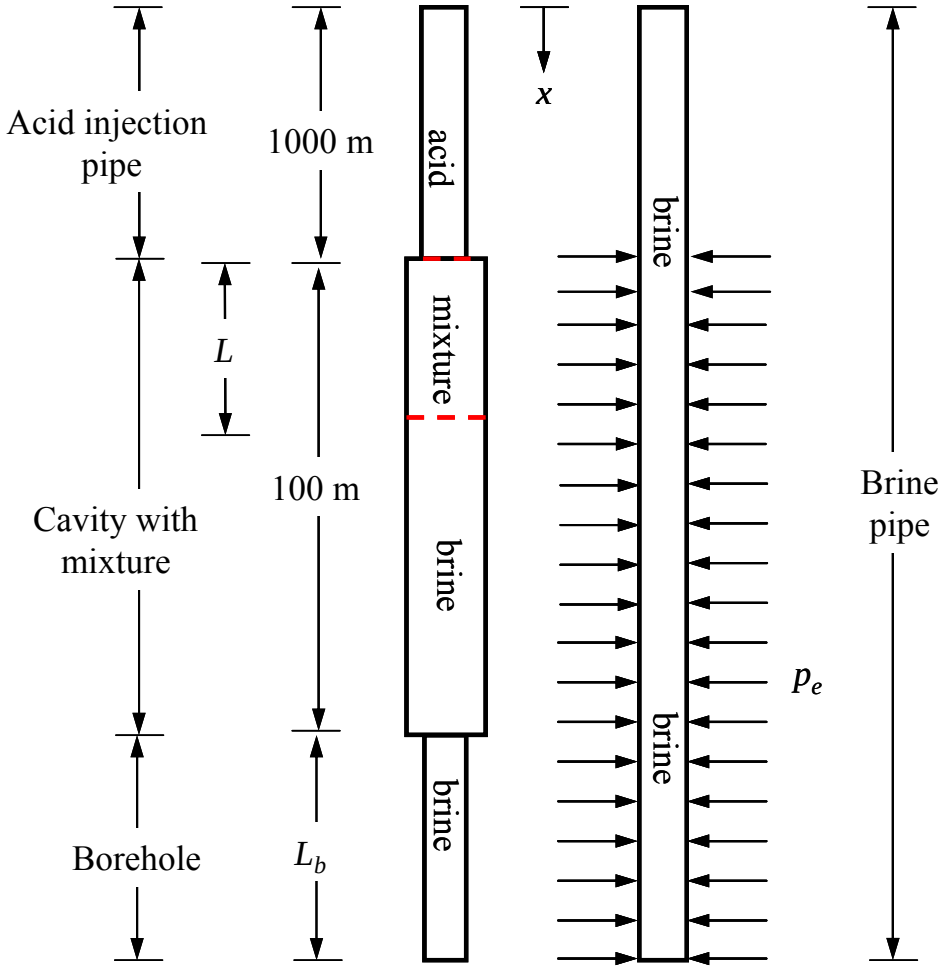

Figure 5.19 Schematic of Case C. In this case, an actual borehole is located beneath the cavity-with-mixture. The borehole length is denoted by L_b. The lower part of the brine pipe is under both the external and the internal (not shown in this figure) pressures. This figure is not to scale.

5.4.3 Results of Calculation from Case A

In Case A, there is no inflow into the brine pipe, so that only the external pressure on the surface of the brine pipe creates pressure waves in the interior of the brine pipe. By comparing the results from Case A with those from the model in Section 5.3, we investigate the effect of the external pressure on the wave the wave propagation in the problem domain. We set a base case based on the model in Section 5.3 (Figure 5.1) with D2 = 0.15 m and L = 20 m. The base case also has the same boundary conditions as the model in Section 5.3. Thus, basically, the base case is identical to the model in Section 5.3. The results of the calculation from the base case and Case A are compared in Figure 5.20. Similar to the presented results in Section 5.3, the pressure histories at x = 0 m in the acid injection pipe and at x = 200 m in the brine pipe are plotted in this section.

Figure 5.20a shows that there is no significant difference between the pressure histories at x = 0 m in the acid injection pipe from the base case and Case A. Since the effects of the change of the diameter and the fluid (from acid in the acid injection pipe to CO_2 in the cavity-with-mixture) are dominant for the wave propagation, we cannot detect the effect of the reflected wave at the bottom of the cavity-with-mixture. That is, the effect of the difference of the boundary condition at the bottom of the cavity-with-mixture and the brine pipe is negligible in the acid injection pipe. Therefore, only the pressure histories in the brine pipe will be presented hereafter.

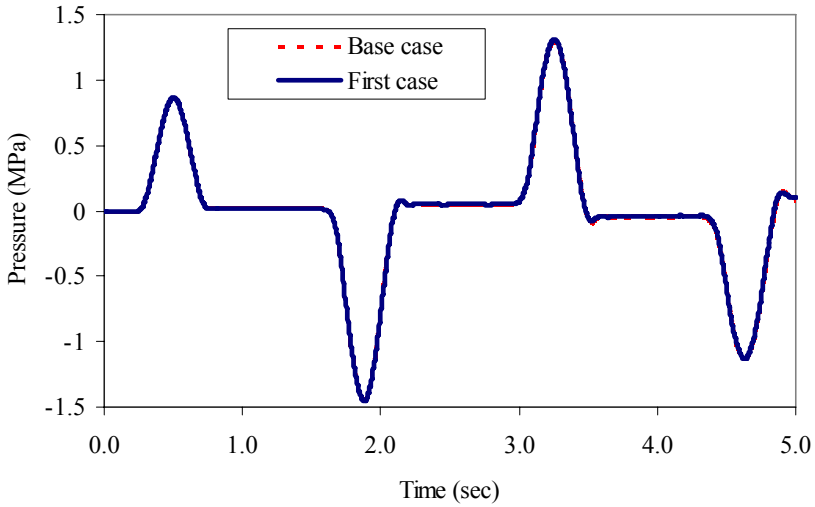

(a)

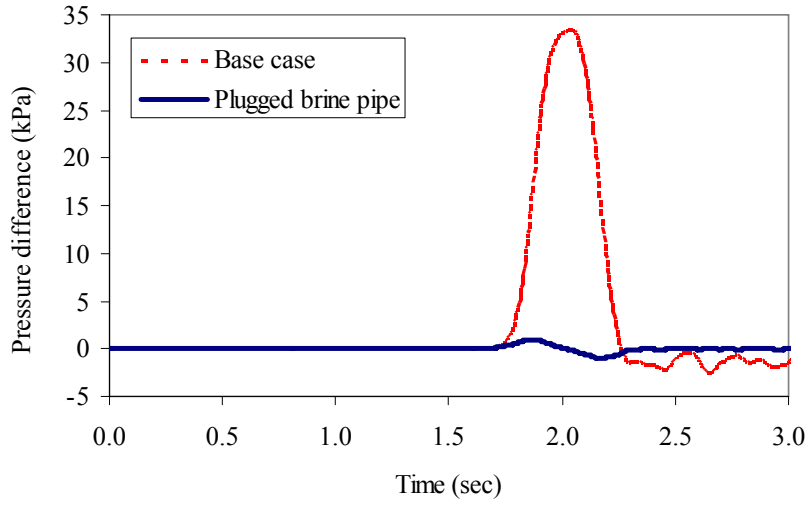

(b)

Figure 5.20 Comparison of pressure histories from Case A with those from the base case (based on the model used in Section 5.3) with D2 = 0.15 m and L = 20 m (Figure 5.1): (a) pressure histories at x = 0 m in the acid injection pipe and (b) pressure histories at x = 200 m in the brine pipe.

There is a significant difference between the two cases in Figure 5.20b. The peak magnitude of the pressure wave from the base case is 33.4 kPa, whereas that from Case A is 1.0 kPa. For the base case with continuous flow rate and pressure, the peak pressure is mainly created by the inflow into the brine pipe. In contrast, the peak pressure with plugged brine pipe (Case A) is induced by the external pressure. This means that the magnitude of the pressure waves due to the external pressure is approximately 30 times smaller than that of the inflow into the brine pipe in this system. This phenomenon is caused by the coefficient c_1 in (4.5.30), which is given by (4.3.56). Using the parameters in Tables 5.1 and 5.3, we estimate $c_1 = 0.09$ for a brine pipe. The calculated value suggests that the contribution of a pressure wave in a brine pipe due to the external pressure to (4.5.30) should be at least one order of magnitude smaller than that due to the inflowing pressure wave into the bottom of the brine pipe, if the magnitudes of the external pressure and the inflowing pressure wave are the same.

We also conducted a series of sensitivity analyses with different diameter of the cavity-with-mixture to investigate its impact on the pressure histories in the brine pipe. In Figure 5.21, pressure histories at $x = 200$ m in the brine pipe are shown. Similar to the pressure histories (Figure 5.10b) in Section 5.3, the magnitude of the peak pressure decreases as the diameter of the cavity-with-mixture increases. The reduction of peak pressure is caused by the decrease of the magnitude of the transmitted wave beyond the interface (Figure 5.1) between the acid injection pipe and the cavity-with-mixture. This can be explained by (A5.32) in Appendix A5: that is, if the cross-sectional area of Pipe 1 A_1, the wave speed in Pipe 1 a_1, and the wave speed in Pipe 2 a_2 (Figure A5.1) are fixed, the transmission coefficient T decreases as the cross-sectional area of Pipe 2 A_2 increases.

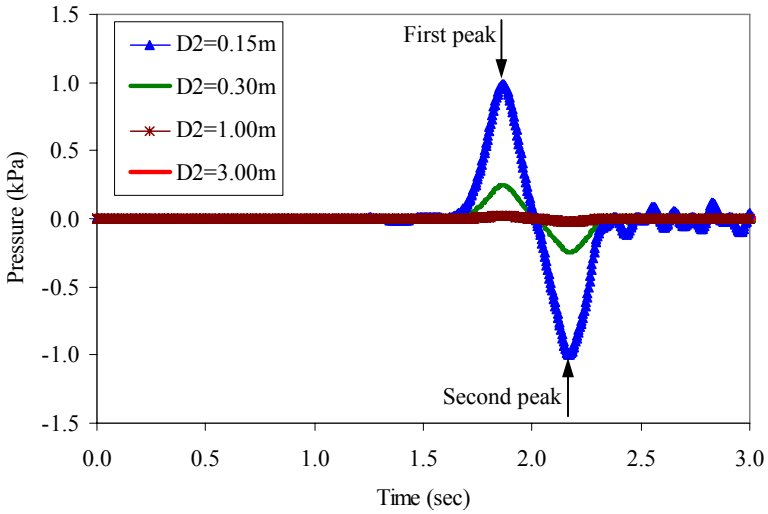

Figure 5.21 Pressure histories at x = 200 m in the brine pipe from Case A. Diameter of the cavity-with-mixture changes from 0.15 m to 3.0 m. The pressure in this figure represents only the pressure difference from the initial value.

From 5.21, we can also observe that there are two peaks in the pressure histories. The first one is caused by an incident pressure wave into the point at x = 200 m. The second one is created by the reflection of the incident pressure wave at the top of the brine pipe. Since the boundary condition at the top of the brine pipe is constant pressure, the phase of the reflected wave is reversed. Thus, the second peak has a negative sign with the same magnitude as that of the first peak, since the pressure in this figure represents only the pressure difference from the initial value.

To confirm this, we compared the time difference between the two peaks from pressure histories with a theoretical estimate. The time difference between the two peaks in Figure 5.21 is 0.304 sec (= 2.168 sec – 1.864 sec). The wave speed in the brine pipe is approximately 1321 m/sec. Since the distance that the reflected wave traversed to appear in the pressure histories is 400 m (= 200 m×2), the theoretical time difference between the two peaks is 0.303 sec (= 400 m/ 1321 m/sec). The two values are in good agreement. This indicates that the second peak in Figure 5.21 is caused by the reflection at the top of the brine pipe.

5.4.4 Results of Calculation from Case B

In Case B, the bottom of the borehole is open in contrast to Case A, so that fluid can flow into the bottom of the brine pipe. The results of the calculation are shown in Figure 5.22, which shows the comparison of the pressure histories at x = 200 m in the brine pipe from Case B with those from the base case.

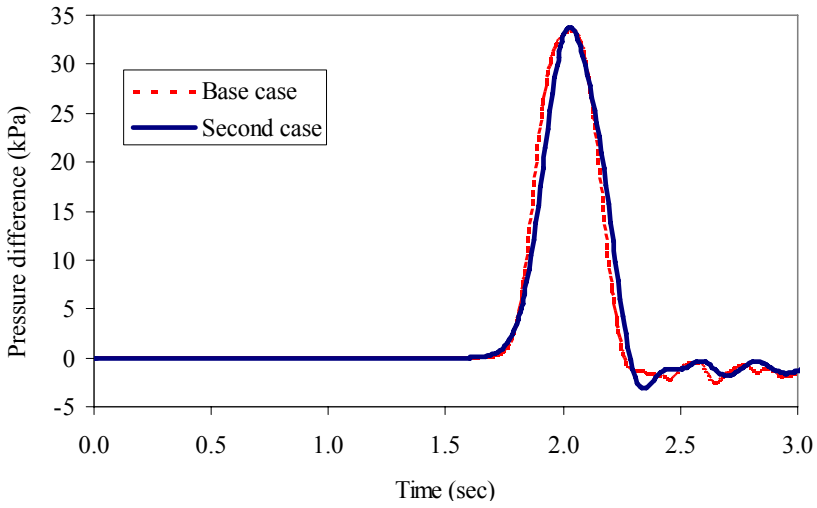

Figure 5.22 Comparison of the pressure histories at x = 200 m in the brine pipe from Case B with those from the base case.

In Figure 5.22, it appears that two curves are almost identical. In Figure 5.20b, the magnitude of the pressure wave due to the inflow into the brine pipe is approximately 30 kPa, whereas that due to the external wave is of the order of kPa. This means that the contribution of the inflow on the pressure history is greater than that of the external pressure. We may detect the pressure wave due to the external pressure on the surface of the brine pipe with conventional equipment (Section 5.3.2). Therefore, the pressure pulses due to the external pressure can be analyzed to characterize the cavern geometry, if we can separate them from those due to the inflow into the brine pipe. A change in the boundary conditions may enable such a separation, which is discussed in Section 5.4.5.

5.4.5 Results of Calculation from Case C

In Case C, an actual borehole exists beneath the bottom of the cavity-with-mixture. We assumed that the lower part of the brine pipe is also under external pressure from the brine in the borehole. We also assumed that the diameter of the cavity-with-mixture and L in Figure 5.19 are 0.15 m and 20 m, respectively. In addition, the borehole diameter was assumed to be 0.05 m. Since the diameter of the brine pipe is 0.04 m, we assumed that flow rate through the bottom of the borehole is scaled down as 0.64 (= $0.04^2/0.05^2$) by the ratio of the cross-sectional areas between the borehole (diameter = 0.05 m) and the brine pipe (diameter = 0.04 m).

We set the borehole length L_b in Figure 5.19 to be 1000 m to separate a pressure wave due to the external pressure from that due to the inflow into the brine pipe. In other words, if the borehole length is sufficiently long compared to wave length, the pressure waves due to the external pressure and the inflow would appear separately in the pressure histories in the brine pipe. The unrealistically long borehole allows us to get better understanding of the wave propagation in the brine pipe due to both the external pressure and the inflow into the brine pipe. For the results of the modeling, Figure 5.23 shows the pressure histories at x = 200 m in the brine pipe.

In Figure 5.23, there are two peaks in pressure histories. The first peak is induced by the external pressure applied on the surface of the brine pipe. The second peak is created by the inflow into the brine pipe at the bottom of the borehole. The magnitudes of the first and second peaks are 0.77 kPa and 30.1 kPa, respectively. The difference of the magnitudes of the two peaks is already mentioned in Section 5.4.3 for Case A. The time difference between the two peaks is 1.625 sec (= 3.540 sec – 1.915 sec). The wave speeds in the brine contained in the cavern and the pipe are 1312 m/sec and 1321 m/sec, respectively. Since the borehole length is 1000 m, the theoretical time difference between

the peaks is 1.640 sec. Thus, the two values are in good agreement. This estimation of the time difference confirms the origin of the two peaks.

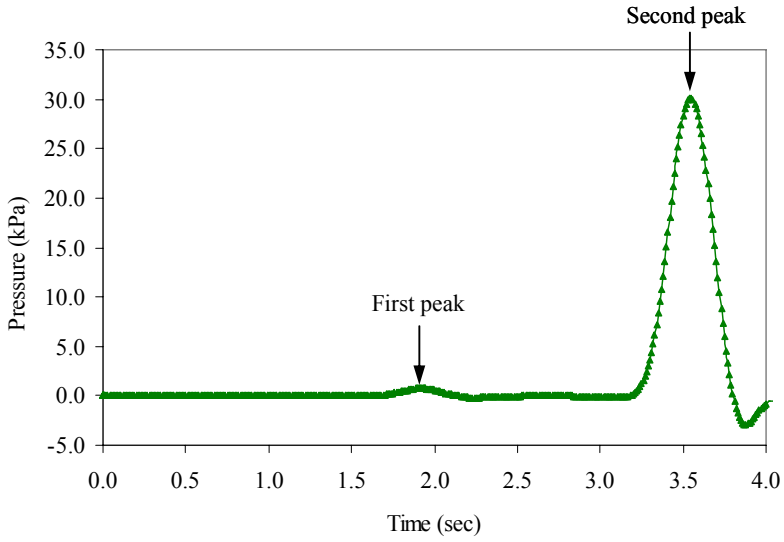

Figure 5.23 Pressure histories at x = 200 m in the brine pipe from Case C. Borehole length L_b (Figure 5.19) is 1000 m. The first peak is induced by external pressure on the brine pipe, whereas the second one is created by the inflow into the bottom of the brine pipe.

We also compared the pressure histories at x = 200 m in the brine pipe from Case C with those from Case A. The comparison is presented in Figure 5.24, where the pressure histories are shown until 3.0 sec to exclude the pressure wave due to the inflow into the brine pipe in Case C. In Figure 5.24, the magnitude of the peak pressure from Case C is 0.77 kPa, whereas that from Case A is 0.99 kPa. The peaks of the pressure histories from both cases are the same order of magnitude. The pressure pulses due to the external pressure are sufficiently large to detect with conventional equipment, so that we can use them to estimate the geometry of the cavern.

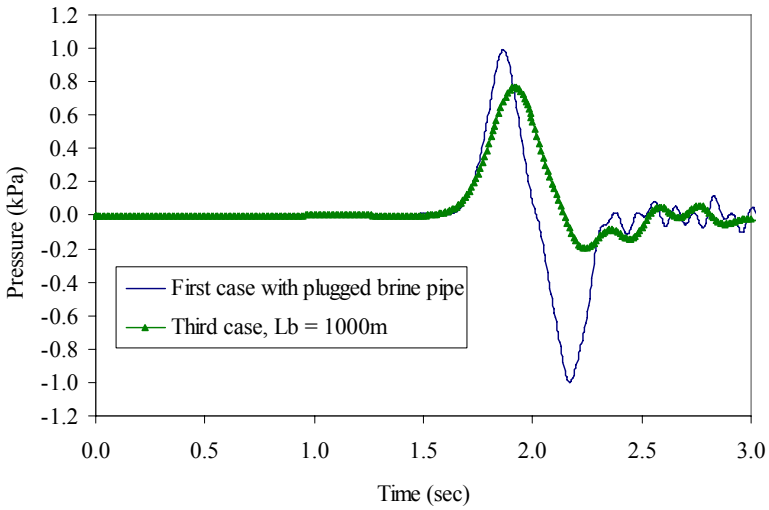

Figure 5.24 Comparison of the pressure histories at x = 200 m in brine pipe from Case C with those from Case A. The pressure histories are shown until 3.0 sec to exclude the pressure wave due to the inflow into the brine pipe in Case C.

To investigate the effect of the borehole length L_b on the pressure histories in the brine pipe, we changed L_b from 1000 m to 500 m, 300 m, and 100 m. The results are shown in Figure 5.25. For the cases of L_b = 1000 m, 500 m, and 300 m, we can identify the pressure peak due to the external pressure at t = 1.915 sec. The second peaks of the pressure waves due to the inflow into the brine pipe for L_b = 1000 m, 500 m, and 300 m appear at t = 3.54 sec, 2.75 sec, and 2.47 sec, respectively. This indicates that the second peak of a pressure wave due to the inflow into the brine pipe arrives earlier as the borehole length decreases.

For L_b = 100 m, we cannot observe the first peak due to the external pressure in Figure 5.25. That is, at t = 1.915 sec, the pressure wave due to the inflow into the brine pipe already arrived because the borehole length is too short for the wave propagation. Thus, the existence of the pressure wave due to the external pressure is masked. This may explain the results from Case B. In Case B, we cannot identify the existence of a pressure wave due to the external pressure. In this case, the pressure waves due to the external

pressure and the inflow into the brine pipe occur approximately at the same time. Case B is an extreme of Case C as the borehole length approaches zero. Moreover, since the magnitude of the pressure wave due to the inflow is greater than that due to the external pressure, we cannot locate the pressure wave due to the external pressure. In this work, the pressure wave length is approximately 660 m (= 1321 m/sec × 0.5 sec). This result suggests that the borehole length should exceed 300 m (i.e., half of the wave length) to identify the existence of a pressure wave due to the external pressure.

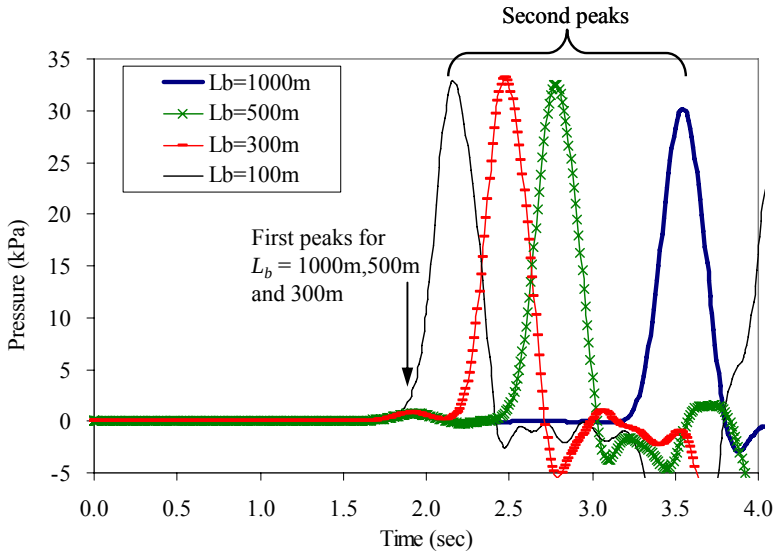

Figure 5.25 Effect of the borehole length L_b on the pressure histories at x = 200 m in the brine pipe. Diameters of the cavity-with-mixture and the borehole are 0.15 m and 0.05 m, respectively. The borehole length L_b changes from 1000 m to 100 m. The arrow of the figure indicates the first peaks for the cases with L_b = 1000 m, 500 m, and 300 m.

The results in this section show that we can separate the pressure pulses due to the external pressure from those due to the inflow into the brine pipe if the borehole length is sufficiently large. Also, the magnitude of the pressure pulses due to the external pressure is sufficiently large to detect with conventional equipment if we can separate it from the

pressure pulses due to inflow into the brine pipe. If it is the case, such pulses can be analyzed to characterize the geometry of the caverns.

5.5 Realistically Scaled Model

In Section 5.4, we showed the effect of the external pressure as well as the various boundary conditions on the pressure histories. Based on the knowledge about the characteristics of the pressure pulses due to the external pressure and boundary conditions used in Section 5.4, we investigated their effects on the pressure pulses with more realistically scaled model. In Section 5.4, we assumed that the borehole length is greater than that of the cavity-with-mixture. However, a borehole longer than a cavity-with-mixture is not realistic in the field. The actual borehole length should be less than that of the cavity-with-mixture.

To consider a more realistically scaled case that fits the actual geometry and configuration of actual solution cavities, we use a borehole with geometry in Figure 5.19 used in Section 5.4.5 (Case C in Section 5.4). In this section, the diameter and the length of the borehole are 0.15 m and 100 m, respectively. The pipe diameter is 0.04 m. These parameters should represent the field conditions. For the boundary conditions, the pressure is continuous between the bottom of the borehole and the brine pipe, whereas the flow rate into the brine pipe is assumed to be 7% ($= 0.04^2/0.15^2$) of that in the bottom of the borehole. That is, the flow rate into the brine pipe is scaled down by the ratio of the cross-sectional area between a borehole with diameter of 0.15 m and a brine pipe with diameter of 0.04 m.

In addition to the case with a realistically scaled geometry, we also studied other two cases: the first case with the geometry shown in Figure 5.1 and the second case shown in Figure 5.18: i.e., similar geometries used in Cases A and B in Section 5.4. In this section, we consider three cases:

Case I: plugged brine pipe (Figure 5.1)

Case II: open brine pipe and a virtual borehole (length of the virtual borehole is 1.0 m) beneath the cavity-with-mixture (Figure 5.18)

Case III: actual borehole beneath the cavity-with-mixture (Figure 5.19).

Similar to Section 5.4, if the borehole length in Case III is greater than half of the wave length, the results from this case would approach those from Case I. If the borehole length is reduced to zero, the results from Case III would be similar to those from Case II. We adopted this approach to improve the understanding of the wave propagation in Case III with realistically scaled geometries.

The acid injection rate into the acid injection pipe is shown in Figure 5.26. In contrast to the acid injection rate used in Sections 5.3 and 5.4, considering the reduced borehole length, we decreased the period of the wave to 0.1 sec (one fifth of the period of the wave in Figure 5.2). Thus, wave length due to a given injection rate is approximately 132 m (= 1321 m/sec × 0.1 sec).

The governing equations used for Cases I, II, and III in this section are the same as those for the three cases in Section 5.4. In this section, the diameter and the length of the cavity-with-mixture are 0.3 m and 100 m, respectively. Also, the location of the mixture layer (L in Figures 5.1, 5.18, and 5.19) in the cavity-with-mixture is assumed to be 20 m.

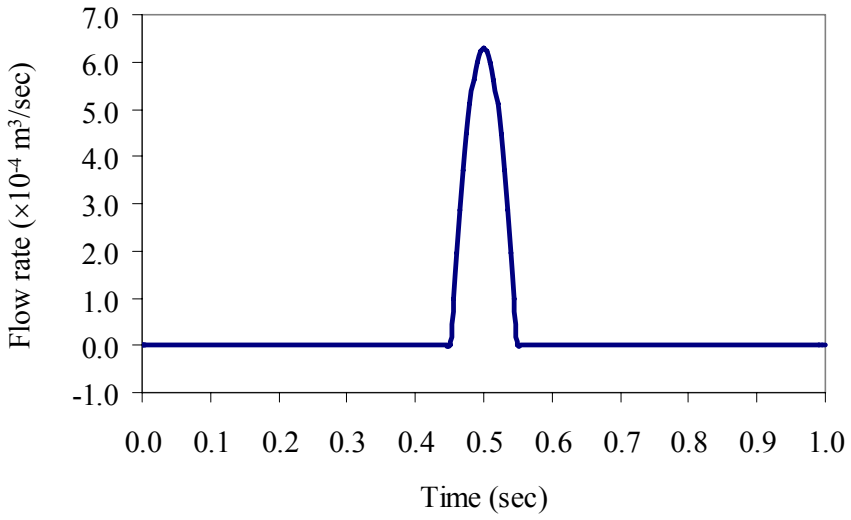

Figure 5.26 The acid injection rate used in this section. In contrast to the acid injection rate used in Sections 5.3 and 5.4, the period of the wave is reduced to 0.1 sec (one fifth of the period of the wave in Figure 5.2).

In this section, similar to Section 5.4, only the pressure histories at x = 200 m in the brine pipe are discussed since pressure histories at x = 0 m in the acid injection pipe are not affected by the change of the geometry and the boundary conditions. Figure 5.27 shows the pressure histories from Cases I and II.

In Case I, the arrival time of the first peak is 1.97 sec (Figure 5.27a), whereas it is 2.05 sec in Case II (Figure 5.27b). As mentioned in Section 5.4.3, the peak pressure from Case I is induced by the arrival of the wave due to the external pressure. In Case II, the inflow into the brine pipe creates the first peak in the pressure histories. Also, the magnitude of the peak value from Case I (Figure 5.27a) is approximately two orders of magnitude smaller than that from Case II (Figure 5.27b).

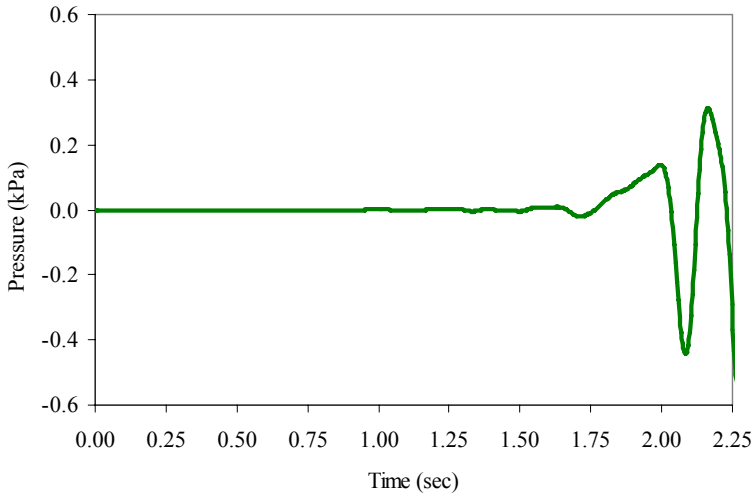

(a)

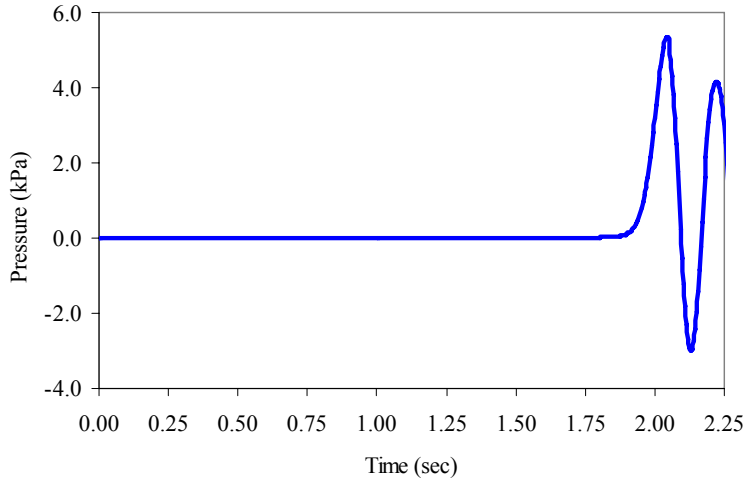

(b)

Figure 5.27 Pressure histories at x = 200 m in the brine pipe: (a) from Case I and (b) from Case II.

In Case III, we changed the borehole length from 100 m to 5 m to investigate its effect on the pressure histories in the brine pipe. In Section 5.4.5, we demonstrate that, as long as the borehole length is sufficiently long compared to half of the wave length of a wave, the pressure waves due to the external pressure on the brine pipe can be identified separately from those due to the inflow into the brine pipe. In contrast, if the borehole length decreases to less than half of the wave length, the pressure wave due to the inflow into the brine pipe masks those due to the external pressure.

Figure 5.28 shows the pressure histories at x = 200 m in the brine pipe from Case III for different borehole length, L_b. For the three cases (L_b = 100 m, 80 m, and 60 m) in Figure 5.28, we can observe that the peak (due to the fluctuation of the external pressure) in the pressure histories occurs at approximately 1.95 sec, which is very close to the arrival time of the first peak (= 1.97 sec) due to the external pressure on the brine pipe (Figure 5.27a). The magnitude of the peaks is approximately 0.1 kPa, and this value is of the same order as that from Figure 5.27a.

For the pressure histories with L_b = 60 m, we can see the pressure increase at 2.0 sec. It is caused by the arrival of the pressure wave due to the inflow into the brine pipe. This indicates that we cannot detect the pressure wave due to the external pressure in the brine pipe as the borehole length decreases less than 60 m. This result can be explained by the wave length of a wave propagating through the system. As mentioned above, the wave length in this section is approximately 132 m. According to the results from Section 5.4.5, the borehole length should be longer than 66 m (= 132 m/2) to capture the existence of the pressure wave due to external pressure, which is very close to the value from the results of the calculation (i.e., 60 m).

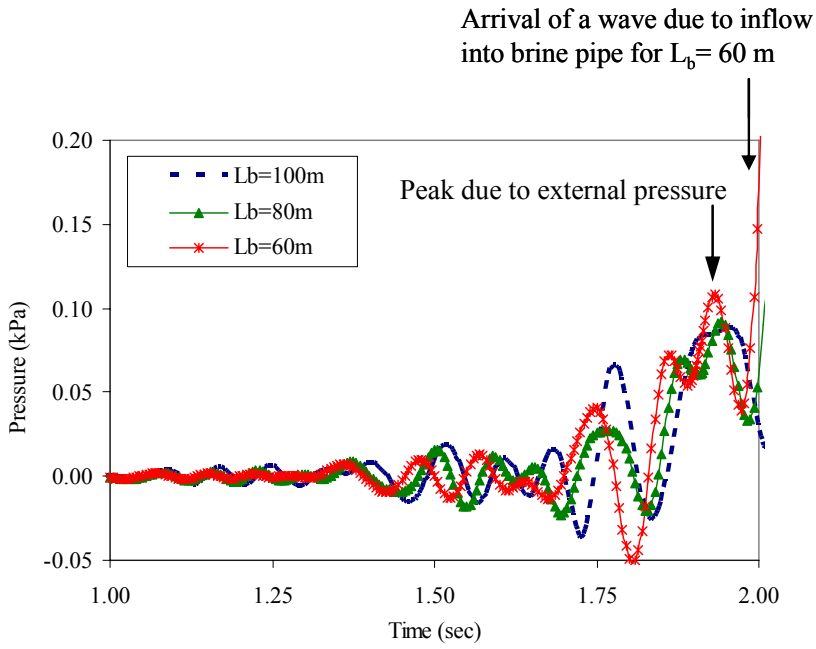

Figure 5.28 Pressure histories at x = 200 m in the brine pipe as the borehole length (L_b) decreases from 100 m to 60 m from Case III. To exclude the pressure waves due to the inflow into the brine pipe, pressure histories until 2.0 sec are presented.

In Figure 5.29, the pressure histories from Case III for different borehole length are presented. Figure 5.29 also shows that the pressure history from Case II, which is the same as in Figure 5.27b. As the borehole length decreases from 100 m to 5 m, the shapes of the curves approach that from Case II. That is, the time for the peaks due to the inflow into the brine pipe approaches 2.05 sec in Case II. In Figure 5.29, the pressure history for L_b = 5.0 m matches well that from Case II. This indicates that the pressure histories for boreholes with a length less than 5.0 m would look similar to those from Case II.

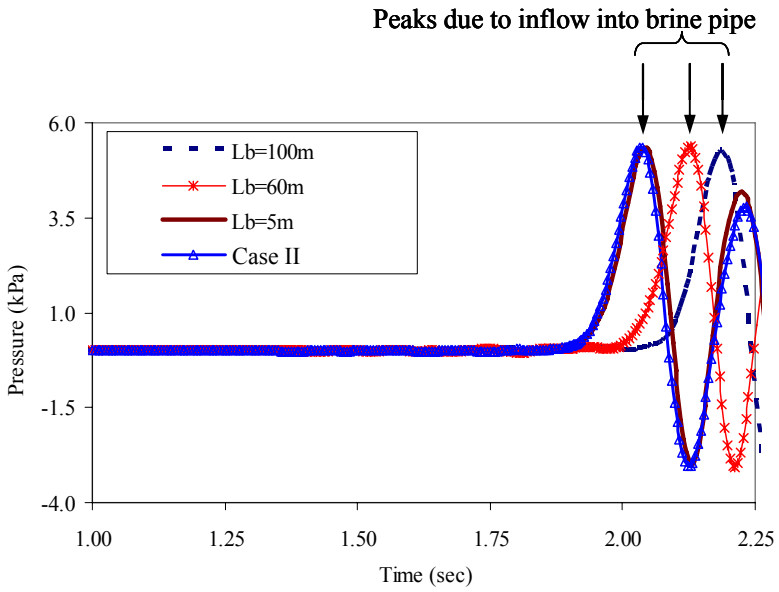

Figure 5.29 Pressure histories from Case III for different borehole length (L_b). Pressure history from Case II is also presented, which is the same curve as in Figure 5.27b.

These results suggest that, similar to the results in Section 5.4, the ratio of the borehole length to the wave length has considerable impact on the pressure histories in the brine pipe. If the borehole is longer than half of the wave length, the existence of the pressure wave due to the external pressure on the brine pipe can be detected. As the borehole length decreases to smaller than half of the wave length, the existence of the pressure wave due to the external pressure is masked by the wave induced by the inflow into the brine pipe.

5.6 Conclusions

Storage facilities are required to store natural gas when supply exceeds demand during the winter months. In many places (such as New England or the Great Lakes region) where no salt domes are available to create gas storage caverns, it is possible to create cavities in limestone employing the acid injection method. In this method, carbonate rock is dissolved, while CO_2 and calcium chloride brine appear as products of the

carbonate dissolution reactions. Driven by the density difference, CO_2 rises towards the ceiling whereas the brine sinks to the bottom of the cavern. A zone of mixed CO_2, acid, and brine forms near the source of acid injection, whereas the brine sinks to the bottom of the cavern.

Characterization of the cavern shape is required to understand stress changes during the cavity excavation, which can destabilize the cavern. It is also important to determine the position of the mixture-brine interface to select the acid injection location. In this work, we propose to characterize the geometry of the cavern and the location of the mixture-brine interface by generating pressure waves in a pipe extending into the cavern, and measuring the reflected waves at various locations in another adjacent pipe. We employed the linearized governing equations (Chapter IV) and formulated appropriate boundary and initial conditions. Using a finite element method, we solved the obtained boundary value problem for a system of pipes and a cavern filled with various characteristic fluids such as aqueous acid, calcium chloride brine, and supercritical CO_2. We found that the pressure waves of moderate amplitudes would create measurable pressure pulses in the submerged pipe. Furthermore, we determined the wavelengths required for resolving the cavern diameter from the pressure history. Our results suggest that the pressure transient technique can indeed be used for characterizing the geometry of gas storage caverns and the movement of the mixture-brine interface.

LIST OF SYMBOLS

A	Ratio related to the linearity of governing equations
A_i	Cross-sectional area of a pipe, i
a_{acid}	Wave speed in acid
a_{brine}	Wave speed in brine
a_{CO2}	Wave speed in CO_2
a_i	Wave speed in the fluid contained in a pipe, i
a_w	Wave speed in the fluid contained in a pipe
C	Constant
C_N	Courant number
c_1	Coefficient
D	Inner diameter of a pipe
E	Young's modulus
F	Force vector
F	Function
F_i	Function
f	Darcy-Weisbach friction factor
f	Differential operator
f_i	Function
G_i	Function
g	Acceleration of gravity
g_i	Function
h	Pipe wall thickness
K	Stiffness matrix

K_0	Bulk modulus of a fluid for a reference pressure
L	Thickness of the mixture layer in a cavity-with-mixture
L_b	Borehole length
L_p	Pipe length
L_w	Wave length
p	Fluid pressure in a pipe
p_0	Initial pressure
p_{CO2}	Pressure at the top of the CO_2 layer
p_e	External pressure applied on the outside of a pipe
Δp	Pressure change due to perturbation
R	Reflection coefficient
T	Transmission coefficient
T	Period of a wave
t	Time
Δt	Time step
U	Vector of dependent variables
U_i	Value of a calculated variable at node i
u	Dependent variable to be calculated
u_r	Radial displacement
V	Volume of a domain
v	Fluid velocity
Δv	Fluid velocity change due to perturbation
x	Distance along a pipe
Δx	Size of a spatial finite difference grid

ν	Poisson's ratio
Π	Governing equation as a form of functional
ρ	Fluid density
ρ_0	Initial fluid density
ρ_{acid}	Acid density
τ	Time
φ_i	Shape function

References

Adamkowski, A. (2003), Analysis of transient flow in pipes with expanding or contracting sections, *Journal of Fluids Engineering*, 125, 716-722.

Arai, Y., T. Sako, and Y. Takebayashi (2002), *Supercritical fluid; Molecular interactions, physical properties, and new applications*, edited by Y. Arai, et al., Springer.

Arfaie, M. and A. Anderson (1991), Implicit finite-differences for unsteady pipe flow, *Mathematical Engineering in Industry*, 3, 133-151.

Bathe, K. J. (1996), *Finite element procedures*, Prentice-Hall.

Bisgaard, C., H.H. Sorensen, and S. Spangenberg (1987), A finite element method for transient compressible flow in pipelines, *International Journal for Numerical Methods in Fluids*, 7, 291-303.

Chaudhry, M.H. (1987), *Applied hydraulic transients*, Van Nostrand Reinhold Company.

COMSOL (2005), *COMSOL Multiphysics User's Guide*, COMSOL AB.

Falta, R.W., L.C. Murdoch, and G.K. Chambers (2004), Review of Current Technology for Acid Dissolution and Hydraulic Fracturing (Task 5), *Technical Report prepared for US DOE*.

Gere, J.M. and S.P. Timoshenko (1992), *Mechanics of materials, 3rd ed.*, Chapman & Hall.

Goodman, R.E. (1989), *Introduction to rock mechanics*, John Wiley & Sons.

Holloway, M.B. and M.H. Chaudhry (1985), Stability and accuracy of waterhammer analysis, *Advances in water resources*, 8, 121-128.

Istok, J.D. (1989), *Groundwater modeling by the finite element method*, American Geophysical Union.

Janna, W.S. (1993), *Introduction to fluid mechanics*, International Thomson Publishing.

Levy, M., H. Bass, and R. Stern (2000), *Handbook of elastic properties of solids, liquids and gases*, Academic Press.

Lide, D.R. (2004), *CRC handbook of Chemistry and Physics*, CRC Press LLC.

Murdoch, L.C. (2007), Personal communication, Clemson University, SC.

NIST (2006), *NIST Chemistry WebBook*, http://webbook.nist.gov/.

Streeter, V.L. and E.B. Wylie (1967), *Hydraulic transients*, McGraw-Hill Book Company.

Szymkiewicz, R. and M. Mitosek (2005), Analysis of unsteady pipe flow using the modified finite element method, *Communication in numerical methods in engineering*, 21, 189-199.

Timoshenko, S.P. and J.N. Goodier (1970), *Theory of elasticity*, McGraw-Hill Book Co.

Wang, H.F. and M.P. Anderson (1980), *Introduction to groundwater modeling: Finite Difference and Finite Element Methods*, W.H. Freeman and Company.

Wylie, E.B. and V.L. Streeter (1978), *Fluid transients*, McGraw-Hill International Book Company.

APPENDIX A5

Transmission and Reflection Coefficients at the Pipe Joint

We follow *Chaudhry* [1987] to differentiate the wave propagation through a place where two different pipes are connected. The pipes can have different diameter and/or material properties and can be filled by different liquids. If the pipe connection place is small compared to the characteristic wave length and we are not interested in details of wave propagation in the connection vicinity, the connection can be viewed as a discontinuity between the pipes (Figure A5.1). Below, we assume that the frictional resistance between the fluid and the conduit wall is negligible, and derive the wave equation from (4.5.15) and (4.5.30). Then, by solving the wave equation for fluid in pipe, we obtain the magnitude of reflected and transmitted waves at a discontinuity.

Inserting $Q = vA$ into (4.5.30) and differentiating the result with respect to time, t, give

$$\frac{\partial^2 p}{\partial t^2} + \rho_0 a_w^2 \frac{\partial^2 v}{\partial x \partial t} = c_1 \frac{\partial^2 p_e}{\partial t^2} \tag{A5.1}$$

where p_e is the external pressure applied outside the pipe (Figure 4.9). Differentiating the momentum balance equation in (4.5.15) with respect to x yields

$$\frac{\partial^2 v}{\partial x \partial t} + \frac{1}{\rho_0}\frac{\partial^2 p}{\partial x^2} + \frac{f}{2D} sign(v) 2v \frac{\partial v}{\partial x} = 0 \tag{A5.2}$$

where

$$sign(v) = \begin{cases} +1 & if \quad v \geq 0 \\ -1 & if \quad v < 0 \end{cases} \tag{A5.3}$$

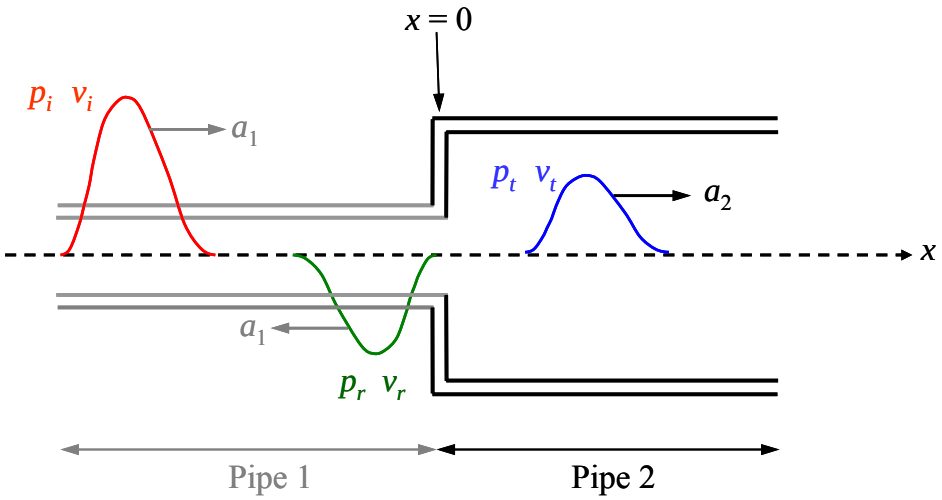

Figure A5.1 Wave propagation through a junction of Pipes 1 and 2. The x-coordinate of the junction is $x = 0$. Here, p is the pressure of the fluid, v is the fluid flow velocity, and a is the wave speed. Subscripts i, r, and t represent incident, reflected, and transmitted waves, respectively. Subscripts 1 and 2 represent Pipes 1 and 2, respectively.

By combining (A5.1) and (A5.2), we obtain

$$\frac{\partial^2 p}{\partial t^2} - a^2 \frac{\partial^2 p}{\partial x^2} = c_1 \frac{\partial^2 p_e}{\partial t^2} + \frac{f \rho_0 a^2}{D} sign(v) v \frac{\partial v}{\partial x} \tag{A5.4}$$

If the conduit is not loaded by external pressure, $p_e = 0$ in (A5.4), and for $f = 0$, (A5.4) becomes a conventional wave equation

$$\frac{\partial^2 p}{\partial t^2} = a_w^2 \frac{\partial^2 p}{\partial x^2} \tag{A5.5}$$

Inserting $Q = vA$ into (4.5.30) and differentiating the result with respect to x, we further have

$$\frac{\partial^2 p}{\partial x \partial t} + \rho_0 a_w^2 \frac{\partial^2 v}{\partial x^2} = c_1 \frac{\partial^2 p_e}{\partial t \partial x} \tag{A5.6}$$

Differentiating (A5.2) with respect to t results in

$$\frac{\partial^2 v}{\partial t^2} + \frac{1}{\rho_0} \frac{\partial^2 p}{\partial x \partial t} + \frac{f}{2D} sign(v) 2v \frac{\partial v}{\partial t} = 0 \tag{A5.7}$$

and combining (A5.6) and (A5.7) gives

$$\frac{\partial^2 v}{\partial t^2} - a^2 \frac{\partial^2 v}{\partial x^2} = -\frac{c_1}{\rho_0} \frac{\partial^2 p_e}{\partial t \partial x} - \frac{f \rho_0 a^2}{D} sign(v) v \frac{\partial v}{\partial t} \tag{A5.8}$$

For $p_e = 0$ and $f = 0$, (A5.8) also becomes a regular wave equation

$$\frac{\partial^2 v}{\partial t^2} = a_w^2 \frac{\partial^2 v}{\partial x^2} \tag{A5.9}$$

Consider next a junction of two pipes in the water hammer problem (Figure A5.1) and take into account that quantities p and v in (A5.5) and (A5.9) represent pressure and velocity perturbations, respectively. Let us denote velocities by

$$v_i = f_1(x - a_1 t) \tag{A5.10}$$

$$v_r = g_1(x + a_1 t) \tag{A5.11}$$

$$v_t = f_2(x - a_2 t) \tag{A5.12}$$

and pressures by

$$p_i = F_1(x - a_1 t) \tag{A5.13}$$

$$p_r = G_1(x + a_1 t) \tag{A5.14}$$

$$p_t = F_2(x - a_2 t) \tag{A5.15}$$

where subscripts i, r, and t represent incident, reflected, and transmitted waves, respectively, while subscripts 1 and 2 represent pipes 1 and 2, respectively. By inserting (A5.10) and (A5.13), (A5.11) and (A5.14), and (A5.12) and (A5.15) into (4.5.3), we have

$$F_1' = \rho_1 a_1 f_1' \tag{A5.16}$$

$$G_1' = -\rho_1 a_1 g_1' \tag{A5.17}$$

$$F_2' = \rho_2 a_2 f_2' \tag{A5.18}$$

where prime sign stands for differentiation. The boundary conditions are given by mass conservation

$$\rho_1 A_1 (v_i + v_r) = \rho_2 A_2 v_t \tag{A5.19}$$

and pressure balance

$$p_i + p_r = p_t \tag{A5.20}$$

at the interface $x = 0$, where A_i is the cross-sectional area of pipe i ($i = 1, 2$).

The solution of (A5.9) and (A5.5) is given by

$$v(x,t)=\begin{cases} f_1(x-a_1t)+g_1(x+a_1t) & (x<0) \\ f_2(x-a_2t) & (x>0) \end{cases} \tag{A5.21}$$

and

$$p(x,t)=\begin{cases} F_1(x-a_1t)+G_1(x+a_1t) & (x<0) \\ F_2(x-a_2t) & (x>0) \end{cases} \tag{A5.22}$$

respectively. Integrating (A5.16), (A5.17), and (A5.18) with respect to t gives

$$\begin{aligned} -\frac{f_1(x-a_1t)}{a_1} &= -\frac{F_1(x-a_1t)}{\rho_1 a_1^2}+C_1 \\ \frac{g_1(x+a_1t)}{a_1} &= -\frac{G_1(x+a_1t)}{\rho_1 a_1^2}+C_2 \\ -\frac{f_2(x-a_2t)}{a_2} &= -\frac{F_2(x-a_2t)}{\rho_2 a_2^2}+C_3 \end{aligned} \tag{A5.23}$$

and inserting (A5.23) into (A5.19) results in

$$\frac{A_1}{a_1}(F_1-G_1)=\frac{A_2}{a_2}F_2-\rho_2 A_2 C_3+\rho_1 A_1(C_1-C_2) \qquad (x=0) \tag{A5.24}$$

Substantiating (A5.13), (A5.14), and (A5.15) into (A5.20), we find

$$F_1+G_1=F_2 \qquad (x=0) \tag{A5.25}$$

and inserting (A5.25) into (A5.24) gives

$$G_1 = \frac{A_1 a_2 - A_2 a_1}{A_1 a_2 + A_2 a_1} \frac{A_1}{a_1} F_1 + \frac{\rho_1 A_1 (C_2 - C_1) + \rho_2 A_2 C_3}{A_1 a_2 + A_2 a_1} \tag{A5.26}$$

At time $t = 0$, both F_1 and G_1 are zero because there is no propagating wave in the pipes. Therefore, constant of (A5.26) should be zero. Therefore, we obtain

$$G_1 = \frac{A_1 a_2 - A_2 a_1}{A_1 a_2 + A_2 a_1} F_1 \qquad (x = 0) \tag{A5.27}$$

Inserting (A5.27) into (A5.25) gives

$$F_2 = \frac{2 A_1 a_2}{A_1 a_2 + A_2 a_1} F_1 \qquad (x = 0) \tag{A5.28}$$

Inserting (A5.13), (A5.14), and (A5.15) into (A5.27) and (A5.28) results in

$$p_r = \frac{A_1 a_2 - A_2 a_1}{A_1 a_2 + A_2 a_1} p_i \qquad (x = 0) \tag{A5.29}$$

and

$$p_t = \frac{2 A_1 a_2}{A_1 a_2 + A_2 a_1} p_i \qquad (x = 0) \tag{A5.30}$$

respectively, where p in (A5.29) and (A5.30) is the perturbation. Then, in the case of $p_e = 0$ and $f = 0$, the magnitudes of the reflected and transmitted waves can be estimated if the magnitude of the incident wave is known.

From (A5.29) and (A5.30), we obtain reflection

$$R = \frac{p_r}{p_i} = \frac{A_1 a_2 - A_2 a_1}{A_1 a_2 + A_2 a_1} \quad (x = 0, \;\; p_e = 0, \;\; f = 0) \qquad \text{(A5.31)}$$

and transmission

$$T = \frac{p_t}{p_i} = \frac{2A_1 a_2}{A_1 a_2 + A_2 a_1} \quad (x = 0, \;\; p_e = 0, \;\; f = 0) \qquad \text{(A5.32)}$$

coefficients of the pressure wave propagating through the interface between two pipes (Figure A5.1).

APPENDIX B5

Wave Speeds in Cavity-Pipe System

Wave speeds in a pipe and in a cavern are given by (4.3.36), and (4.3.45), respectively. Using parameters from Tables 5.1, 5.2, 5.3, and 5.4, we can calculate the wave speeds for different cases.

For a steel pipe with acid that has a diameter of 0.04 m, the wave speed is given by (4.3.36):

$$a_{acid} = \sqrt{\frac{K_0 / \rho_0}{1 + \frac{K_0 CD}{Eh}}} = 1442 \ \ m/\sec \tag{B5.1}$$

where K_0 is the bulk modulus of fluid, ρ_0 is the density of fluid, C is the constant given by (4.3.25), D is the pipe diameter, E is the Young's modulus of the pipe material, and h is the pipe wall thickness.

In a pipe of the same diameter 0.04 m but containing brine, the wave speed is also given by (4.3.36):

$$a_{brine} = \sqrt{\frac{K_0 / \rho_0}{1 + \frac{K_0 CD}{Eh}}} = 1321 \ \ m/\sec \tag{B5.2}$$

For a cavern containing supercritical CO_2, the wave speed is calculated using (4.3.45)

$$a_{CO2} = \sqrt{\frac{K_0 / \rho_0}{1 + \frac{K_0}{E/2(1+\nu)}}} = 195 \ \ m/\sec \tag{B5.3}$$

where E and ν are the Young's modulus and is the Poisson's ratio of the rock, respectively.

In a borehole with brine, the wave speed is also computed using (4.3.45)

$$a_{brine} = \sqrt{\frac{K_0 / \rho_0}{1 + \frac{K_0}{E / 2(1+\nu)}}} = 1312 \ \ m/\sec \tag{B5.4}$$

CHAPTER VI

CONCLUSIONS AND RECOMMENDATIONS

6.1 Conclusions

This dissertation addresses two topics in subsurface geomechanics: (1) modeling sand production mechanisms and (2) characterizing the geometry of gas storage caverns formed by acid dissolution of carbonate rock formations.

The results of studying sand production mechanisms are summarized as follows:

1. From the results of physical experiments designed to model sand production in a reservoir-layer into wells, we found that at sufficiently high flow rate, the sand production begins almost immediately after the fluid injection starts. The accumulated weight of the produced sand increases, but sand production stops after a certain time.
2. We conducted a total of eight large-scale (~1 m) experiments, and in every experiment, we observed the formation of a cavity and a surface flow channel. Monitoring the surface of the sand layer shows that after cavity formation, a surface flow channel is initiated. It also shows that the cavity and the surface flow channel are stabilized when sand production stops.
3. From the measurements of the weight of the sand particles in the collection tank and those estimated from the volume of a cast of the cavity and the flow channel (our base case), we found that most of the produced sand particles are from the cavity and the surface flow channel. An experiment with layers of dyed sand particles showed that there is no visible infiltration of particles into the interior of the sand layer or piping (wormholes) during the experiment.

4. Using scale analysis, we estimated the critical fluid velocity required to induce the erosion of particles at the cavity surface, which is in general agreement with the observed fluid velocity in our experiments.
5. Based on the observations and analysis of our experiments, we suggested a conceptual model that describes our results. This model adopts the cavity erosion mechanism rather than the plastic flow of disintegrated particles. In this model, the particle production results in a cavity that forms around the borehole due to erosion of particles. As the cavity grows till it reaches the maximum size, a flow channel begins forming at the edge of the cavity. As the channel starts growing, it continues to propagate towards the sample perimeter. At this stage, the channel is filled by fluidized sand (slurry) and the channel formation is characterized by the propagation of the fluidization erosion front. Once formed, the cavity and the flow channel then become the dominant conduit for fluid flow due to their greater hydraulic conductivity than that of the sand layer.
6. Under constant fluid flow rate, the cavity and channel eventually stabilize and particle production stops. The cavity is stabilized because of the radial effect in fluid flow resulting in decreasing fluid velocity with increasing cavity size. The stabilization of the surface channel, however, may be due to the limiting size of the experimental setup.
7. The discrete element method codes PFC^{2D} and PFC^{3D}, were used to model the results of our experiments. The 2-D model constructed using PFC^{2D} demonstrated that a cavity and a surface flow channel are formed in the vicinity of an excavated volume created by the production of sand particles. Because the 3-D, radial effect of fluid flow is not considered in our 2-D model, the fluid velocity at the cavity surface does not reduce as the cavity propagates. As a result, particles are removed intensively at the surface of the cavity. Our 2-D results indicate that the mechanism of channel formation could be attributed to the subsidence due to the lateral

deformation of the sand layer. This can be substantiated by continued production of particles from the toe of the slope and possibly from the surface at the cavity and channel. The removal of the particles leads to the cavity collapse, and the fluid flow is concentrated above the subsided part of the sand layer where cavity collapse was initiated. As these processes repeat, the cavity and the surface flow channel do not stabilize in 2-D.

8. The 3-D model, based on PFC^{3D}, shows that a cavity is formed around an opening area, and that the rate of particle production decreases with time. This indicates that the assembly of particles stabilizes with a given flow rate when the sand production domain has limited dimension, which is also observed in our laboratory experiments. 3-D model simulations show that the erosion process from the top of the sample may be an important mechanism contributing to the formation of the surface flow channel developed in the laboratory experiments.

The characterization of gas storage caverns using fluid transients is summarized as follows:

1. To facilitate the characterization of gas storage caverns created by the acid injection method within limestone or dolomite formations, we introduced an approach based on observations of pressure transients. During acid injection, the geometry of a cavern can be characterized by generating a downward propagating pressure wave at the wellhead and measuring the history of the returning reflected waves at several positions in the wells.
2. The conventional governing equations (often called “water-hammer equations”) describe the case that the wave propagation in the thin-walled pipe filled with liquid when the pipe is not loaded from the outside, and only experiences pressure fluctuation of the fluid inside. In order to characterize a cavern, however, pressure

waves are triggered to propagate through pipes loaded both internally and externally as well as through a cavern which can be viewed as a pipe with thick walls (in fact, infinitely thick). This is important where internal pressure is changing in response to the perturbation of the external pressure, when a pipe is contained in another pipe with greater diameter, and both pipes are filled with fluids. Accordingly, we developed appropriate mass balance equations for transient fluid flows in a pipe loaded by both internal and external pressures. In contrast to the mass balance, the conventional momentum balance equation can be used for both pipes loaded by internal and external pressure as well as in the case of a cavern. We model the entire system composed of an acid injection pipe, a cavity-with-mixture (i.e., a cavern), and a brine pipe. By solving the governing equations, we simulate wave propagation through the pipe-cavity system.

3. The modeling results show that, at the early stage of the dissolution process, most of the pipe and the cavern are filled only with acid. Thus, at this stage, the cavern diameter change has the major geometrical effect on wave parameters.
4. Our forward modeling demonstrates that the time dependant histories of pressure waves can be used to estimate the cavern diameter change. As the cavern diameter increases, the magnitude of the reflected wave at the interface between the acid injection pipe and the cavern increases too. The magnitude of the pressure histories at the wellhead in the acid injection pipe increases accordingly. Our results suggest that the cavern diameter changes can be detected more clearly from the pressure histories in the brine (withdrawal) pipe, which show different effect compared to the acid injection pipe: that is, as the cavern diameter increases, the magnitude of the peak value of the pressure histories in the brine pipe decreases.
5. We also calculated the change in the returning reflected pressure waves at the wellhead after a layer of supercritical CO_2 appears in the cavern. The amplitude of these waves at the wellhead in the acid injection pipe decreased after the creation

of a CO_2 layer in the cavern. This is observed even if the cavern diameter does not change. The CO_2 layer also affects pressure histories in the brine pipe. In particular, the CO_2 layer reduces the magnitude of the wave peak pressure in the brine pipe.

6. We concluded that it may be difficult to use the pressure histories near at the wellhead in the acid injection pipe for monitoring the cavern diameter after the creation of a CO_2 layer in it. Instead, we suggest using the pressure histories in the brine pipe. The peak values of the pressure histories in the brine pipe are noticeably reduced as the cavern diameter increases. In contrast, the peak values in the acid injection pipe do not change considerably.
7. We showed that the thickness change of the mixture layer (assumed as supercritical CO_2 in this work) changes the peak value of the pressure histories and the arrival time of the transmitted wave in the brine pipe. The arrival time of the transmitted wave is delayed as the mixture layer thickness increases. Peak pressure value in the brine pipe reduces with the increase in thickness of the mixture layer. These effects indicate that the thickness of the mixture layer in a cavern can be evaluated by monitoring the arrival time of the pressure wave in the brine pipe.
8. It is still difficult, however, to determine the cavern diameter from the pressure histories in the brine pipe. Yet, the relative changes of the diameter can be identified reliably.
9. Our calculations show that as expected, the magnitudes of the pressure wave pulses induced in response to the fluctuations in the external pressure are much less (at least two orders of magnitude) than those due to the pressure waves induced by the inflow into the brine pipe. Nevertheless, the pressure pulses induced by the external pressure are of the order of 1 kPa for a range of practical condition we considered. Such pulses are sufficiently large to be detected with conventional equipment, and can be analyzed to characterize the geometry of the cavern.

10. The wave length of the induced pressure wave is the key factor in detecting the pressure wave due to the external pressure fluctuations. Specifically, the borehole length should be longer than the half of the wave length for such a detection in the brine pipe to be reliable.

6.2 Recommendations for Future Work

Our recommendations for future work on sand production mechanisms include:

1. Conducting additional experimental work using different boundary conditions rather than those (controlled injection rate) used in this study. For example, applying a specified fluid pressure to the external boundary of the model. Such a boundary condition probably comes closest to the real boundary condition that exists in the field and is presumably controlled by the far field fluid pressure. If it is the case, then adopting a controlled fluid pressure boundary instead of a controlled injection flow rate would result in a more realistically scaled model.
2. Developing a more precise method to capture information on the development of the cavity and the surface flow channel. This may require using a high-resolution video imaging as well as more advanced image processing software. Improved dynamic imaging of the evolution of the physical geometry of cavities and channels would result in a better understanding of sand production phenomenon.
3. Using an extensive array of sensors to monitor the state of the interior of the sand layer including installation of P- and S-wave transducers to monitor the elastic compliances of particle aggregate in the vicinity of a wellbore, pore pressure transducers to monitor pressure distribution in the sand layer, and flow meters to measure the flow rate distribution in the sand layer. These sensors would make it possible to investigate the interior of the sand layer more clearly during

experiments and in real time. Such sensors could be installed in the sand layer beyond the region where a cavity is expected to be formed.

4. Performing more developed parametric study with discrete element modeling. Especially in the 3-D model, we could not reliably capture the existence of a surface flow channel due to the limited number of particles. This would most probably require employing high-performance computing. Such an approach would enable investigation of more detailed features of the sand production phenomenon.
5. Performing numerical modeling with a range of different boundary conditions (including pressure controlled boundaries or changing fluid velocity). This approach would require the development of new configurations for the experimental setup.
6. Utilizing other numerical techniques such as the finite element method (FEM) or finite difference methods (FDM) to model these phenomena at a larger scale. The discrete element method is appropriate to model deformation near the wellbore whereas the FEM and FDM approaches are better able to model the conditions in the formation further away from the well. The FEM and FDM domains could be matched at an independent scale which would make the multi-scale approach feasible and would make it possible to address the behavior of petroleum reservoirs at a larger scale and in a more realistic manner.

For future work on the characterization of gas storage caverns, we recommend the following:

1. Deriving new governing equations that are appropriate for models in which the initial condition involves a non-zero flow rate. The governing equations used in this work require the initial condition with zero flow rates. Applying these governing equations to field cases would necessitate stopping the acid injection. In

other words, for the sake of characterization, while measuring pressure histories, the acid injection would be stopped. Therefore, the cavern creation process may be delayed by the measurements. Using the governing equations with a non-zero flow rate initial condition, however, would allow monitoring and characterization in real time.

2. Implementing solutions to the inverse problem technique to approach extracting the cavern geometry from field measurements. In this work, only forward problems have been solved. By changing the geometry of the caverns we were able to obtain the trend of the calculated pressure histories. We were thus able to demonstrate the viability of using fluid transients for the characterization of the cavern geometry. For realistic field applications, however, we would need to estimate the geometry of the cavern from pressure measurements by utilizing inverse modeling. The inverse modeling approach also is useful to resolve the uncertainty in the computed parameters.
3. Obtaining more accurate properties for the mixture in caverns. The material properties of each component (i.e., acid, supercritical CO_2, and brine) of the mixture are known. The mixture properties, however, would depend on the fraction of each component and can only be estimated at this time.
4. We assumed that supercritical CO_2 behaves as a liquid. Its behavior, however, may be affected by the wave propagation, which needs to be included in the modeling.
5. Since the cavern diameter is likely to be not constant in the field, it may affect the pressure wave histories. Accordingly, this effect my allow determining the cavern geometry more accurately.
6. In the cavern, injected acid, CO_2, and brine are mixed. In addition, carbonated rock is dissolved. Thus, the fluid flow pattern in the cavern could be quite complex. Such a 2-D (or 3-D) fluid flow may affect the characterization of wave

propagation. This effect was not considered in our work. To improve our understanding of wave propagation in cavern, the effect of the 2-D (or 3-D) fluid flow on fluid transients should be investigated.